ULTRASENSITIVE ELECTROMETRY AT THE SINGLE-PHOTON LEVEL

A Thesis
Submitted to the Faculty
in partial fulfillment of the requirements for the
degree of

Doctor of Philosophy

in

Physics and Astronomy

by Benjamin Lorsch Brock

Guarini School of Graduate and Advanced Studies
Dartmouth College
Hanover, New Hampshire
July 2021

Examining Committee:

Alexander J. Rimberg, Chair

Miles P. Blencowe

Chandrasekhar Ramanathan

Lorenza Viola

Britton L. T. Plourde

F. Jon Kull, Ph.D.
Dean of the Guarini School of Graduate and Advanced Studies

Abstract

In this thesis we introduce the cavity-embedded Cooper pair transistor (cCPT), a device which behaves as a nonlinear charge- and flux-tunable microwave cavity. We use the charge-tunability to operate the cCPT as a charge sensor, culminating in a demonstration of ultrasensitive electrometry using 16 attowatts of power, corresponding to the single-photon level of the cavity [1, 2]. This is the first ultrasensitive electrometer reported to operate at the single-photon level and we measure a dispersive charge sensitivity of 14 $\mu e/\sqrt{\text{Hz}}$, which is comparable to the sensitivity of rf-SETs while using about 5 orders of magnitude less power. This low-power operation enables the cCPT to be integrated with near quantum-limited amplifiers and could help facilitate the multiplexed readout of quantum-dot-based qubits. Furthermore, our results support the feasibility of using the cCPT to mediate an optomechanical interaction that reaches the single-photon strong coupling regime [3].

Underpinning this charge sensitivity measurement is a detailed experimental characterization of the cCPT [4] with an emphasis on the effects of $1/f$ charge and flux noise, which couple to the resonant frequency of the cCPT via its tunability. In particular, we observe an oblong deformation of our measured resonance circles due to frequency fluctuations induced by this $1/f$ noise, in accordance with our theoretical predictions [5]. Since tunable microwave cavities have become ubiquitous in the field of circuit quantum electrodynamics, we expect the techniques we've developed for characterizing these systems to be broadly relevant.

Acknowledgments

First and foremost, I would like to thank my advisor Alex Rimberg for his guidance over the last six years, both inside the lab and out, and for affording me the freedom to explore my own ideas. I also thank Miles Blencowe, who became like a second advisor to me, for all of his help on the theoretical side of my research. I'm grateful to my labmates Juliang Li, Bhargava Thyagarajan, Sisira Kanhirathingal, Billy Braasch, and Chunyang Tang, for all of their help and camaraderie over the years. I'm particularly indebted to Juliang, not only for fabricating the sample I studied but also for teaching me the practical, hands-on skills required for experimental work.

I would also like to thank Chandrasekhar Ramanathan and Lorenza Viola for agreeing to be on my committee and for their advice over the years. I also thank Britton Plourde for taking the time out of his schedule to be on my committee.

Finally, I'd like to thank my family for always encouraging me to pursue my interests, and my partner Laura for all of her love and support over the years.

Contents

List of Figures

List of Tables

Chapter 1

Introduction

In this thesis we introduce the cavity-embedded Cooper pair transistor (cCPT), a device that consists of a quarter-wavelength ($\lambda/4$) coplanar waveguide cavity with a Cooper pair transistor connected between its voltage antinode and the ground plane, as shown in Figure 1.1. The CPT is made up of two Josephson junctions (JJs) separated by an island, which can be gated with a voltage V_g via the capacitance C_g. The cavity and CPT form a closed loop, which is superconducting when cooled to base temperature in a dilution refrigerator. This SQUID loop is L-shaped, as shown in Figure 1.1(b). The vertical segment of the loop runs parallel to a transmission line carrying the current I_Φ, which threads flux through the loop, while the horizontal segment runs parallel to the cavity. Embedded in this way, the CPT behaves as a Josephson inductance L_J in parallel with the cavity that can be tuned by both the number of electrons $n_g = C_g V_g/e$ gating the island and the flux Φ_{ext} threading the SQUID loop. Since the Josephson junctions are nonlinear circuit elements, the Josephson inductance is nonlinear as well. Thus, the system as a whole behaves as a nonlinear, charge- and flux-tunable microwave cavity.

This thesis is centered around two main projects. The first project consists of a detailed characterization of the cCPT, which has both theoretical [5] and experimental [4] components. On the theoretical side, we develop a model for how frequency fluctuations comparable to the cavity linewidth may arise in tunable and nonlinear microwave cavities (due to classical fluctuations in the tuning parameters and quantum fluctuations in the intracavity field, respectively), and how these frequency fluctuations affect the measurement of scattering matrix elements (such as the reflection and transmission coefficients). Since the measurement of scattering matrix elements is a standard method for extracting the damping rates of microwave cavities

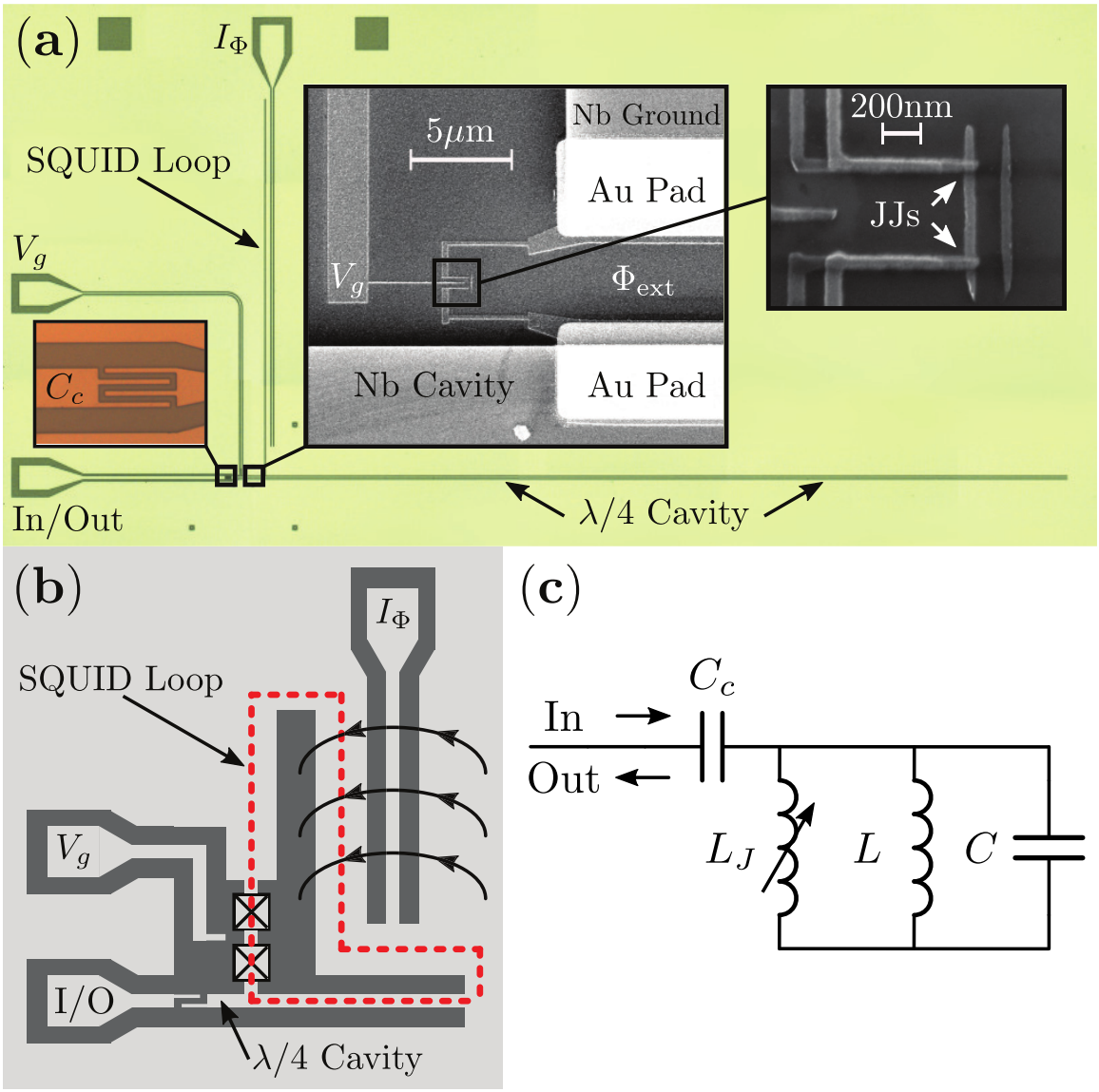

Figure 1.1: (a) Sample images of the cCPT. (b) An illustration of the chip layout of the cCPT; the dashed red line depicts the SQUID loop, and the black arcs depict the magnetic field lines generated by the current I_Φ. (c) An equivalent-circuit schematic of the cCPT. The $\lambda/4$ cavity behaves as a parallel LC circuit when operated near its fundamental frequency $\omega_{\lambda/4} = 1/\sqrt{LC}$ [6], and the CPT behaves as a tunable Josephson inductance L_J in parallel with the cavity

[7, 8], one must use this model that accounts for the effect of frequency fluctuations to accurately determine the damping rates of these cavities. On the experimental side, we use this theoretical model to characterize the cCPT. We observe key signatures of frequency fluctuations predicted by our model, and describe in detail the experimental techniques used to measure and corroborate the effects of frequency fluctuations.

We expect this work to be broadly relevant to the community working on tunable and nonlinear microwave cavities, which have become ubiquitous in the field of circuit quantum electrodynamics. Tunable cavities have been used as parametric oscillators to achieve single-shot readout of superconducting qubits [9, 10], as quantum buses for selective qubit coupling [11], as broadband filters [12], and as platforms for investigating the dynamical Casimir effect [13, 14, 15]. Many such cavities are also nonlinear due to the presence of embedded Josephson junctions, but nonlinear microwave cavities on their own have found wide-ranging applications as well. For example, they have been used as a platform for generating Schrodinger cat states [16] and as amplifiers operating near the quantum limit of added noise [17, 18, 19]. By using our theoretical model for the effect of frequency fluctuations on measurements of scattering matrix elements, we expect that these devices can be characterized more accurately moving forward.

The second project consists of benchmarking the cCPT's performance as a dispersive electrometer. The method of operating the cCPT as a charge sensor is straightforward: the gate charge n_g is encoded in the resonant frequency ω_0 of the cCPT, such that changes in n_g yield a change in the phase of a signal reflected off of the cCPT. This work again has both theoretical [2] and experimental [1] components. Sisira Kanhirathingal led the theoretical side of this project, which consists of a first-principles derivation of the charge sensitivity of the cCPT, including a detailed analysis of the fundamental sources of noise limiting the cCPT's performance as an electrometer. This derivation predicts the best possible sensitivity attainable by the cCPT subject to limitations imposed by quantum mechanics (i.e., the quantum-limited performance), which provides a basis of comparison for our experimental results. On the experimental side, we demonstrate ultrasensitive dispersive charge detection with the cCPT: using 16 attowatts of power, corresponding to the single-photon level of the cavity, we measure a minimum charge sensitivity of 14 $\mu e/\sqrt{\text{Hz}}$. This is the first ultrasensitive electrometer reported to operate at the single-photon level and its sensitivity is comparable to rf-SETs [20], which typically require picowatts of power. Relative to theory, we find that the cCPT operates within a factor of 5 of its quantum-limited

sensitivity.

Fast and ultrasensitive electrometers have been instrumental to the advancement of basic science. They have been used to detect in real time the tunneling of electrons in a quantum dot [21], determine the tunneling rates of quasiparticles in superconducting devices [22], and search for signatures of Majorana zero modes in nanowires [23]. In addition, the rapid detection of single electrons is crucial for the readout of quantum-dot-based qubits [24], for which operating at lower photon numbers reduces measurement backaction [25]. In this same vein, ultrasensitive electrometers are at the heart of many schemes for sensing the displacement of charged mechanical resonators [26, 27, 28], as well as for coherently coupling mechanical resonators to microwave cavities [3, 29, 30]. To observe and take advantage of quantum effects in such hybrid systems it is often essential that their coupling be strong at the single-photon level, a regime that has been achieved for quantum dots [31, 32] but not yet for mechanical resonators despite significant effort [33, 34, 35, 36]. Reaching the single-photon strong optomechanical coupling regime, where a single cavity photon causes sufficient radiation pressure to displace the mechanical resonator by more than its zero-point uncertainty, would enable the generation of nonclassical states of both light and motion [37, 38], as well as provide a rich platform for studying the quantum-to-classical transition and other fundamental physics [39].

Electrometers based on the single electron transistor (SET) are among the fastest and most sensitive reported in the literature to date. Radio-frequency single electron transistors (rf-SETs) are the best known of these devices, having achieved sensitivities below 1 $\mu e/\sqrt{\text{Hz}}$ [40] and bandwidths greater than 100 MHz [20]. The rf-SET functions by encoding the charge gating the SET in the power dissipated by the SET, which is embedded in a tank circuit to enable radio-frequency readout of this dissipation. This dissipative detection typically requires picowatts of power, corresponding to hundreds of thousands of photons in the tank circuit, which renders the rf-SET unsuitable for some of the aforementioned applications and makes it impossible to integrate the rf-SET with modern near-quantum-limited parametric amplifiers [17, 41, 42] (which typically saturate well below the picowatt scale). Dispersive electrometers based on the SET have also been developed, which encode the gate charge in the resonant frequency of a tank circuit. Such electrometers have been operated using femtowatts of power [43, 22], corresponding to tens or hundreds of photons, and have achieved charge sensitivities as low as 30 $\mu e/\sqrt{\text{Hz}}$ [44]. More recently, dispersive gate-based sensors have been developed [45] that have surpassed the per-

formance of SET-based electrometers. These devices have achieved sensitivities as low as 0.25 $\mu e/\sqrt{\text{Hz}}$ with detection bandwidths approaching 1 MHz while using only 100 attowatts of power, corresponding to hundreds of photons [46].

Our demonstration of ultrasensitive charge detection at the single-photon level thus advances the state of the art of electrometry. As mentioned above, this low-power operation enables the cCPT to be integrated with near quantum-limited amplifiers and could help facilitate the multiplexed readout of quantum-dot-based qubits. Furthermore, our results support the feasibility of using the cCPT to mediate an optomechanical interaction that reaches the single-photon strong coupling regime [3].

In order to properly contextualize these two projects we also present background material necessary to understand them. The bulk of this background material is aimed at understanding the two key building blocks of the cCPT: the $\lambda/4$ microwave cavity and the Cooper pair transistor. We use this background material to understand the Hamiltonian of the cCPT, as well as its dynamics. We present this material at a level that assumes some knowledge of quantum optics. An understanding at the level of Gerry and Knight [47] should suffice; for a more advanced text we recommend Schleich's "Quantum Optics in Phase Space" [48].

This thesis is organized as follows. In Chapter 2 we develop the theoretical framework for understanding the dynamics of microwave cavities, including cavities that are tunable and nonlinear, and provide relevant experimental examples along the way. In Chapter 3 we develop the theoretical framework for understanding the Hamiltonian of Josephson junctions, which we use to understand the energy levels of the Cooper pair transistor. In Chapter 4 we introduce the physical realization of the cCPT, briefly discuss how it was fabricated (this was done by Juliang Li [49]), and present a simple derivation of the cCPT Hamiltonian. In Chapter 5 we describe the cryogenic circuitry used to experimentally study the cCPT and discuss several important measurement schemes. In Chapter 6 we both characterize the cCPT experimentally and present our theoretical analysis of the effects of frequency fluctuations on scattering measurements, which is necessary to model several of the measurements used in the experimental characterization. In Chapter 7 we present our experimental measurements of the charge sensitivity of the cCPT.

In addition to these chapters we've included several appendices that contain interesting measurements and analysis, but which are not necessary to understand the central results of this thesis. In Appendix A we discuss how the cCPT's nonlinearity can be exploited to enhance charge sensitivity. In Appendix B we discuss

parametric resonance in the cCPT. In Appendix C we present several miscellaneous measurements that make use of the cCPT's nonlinearity, including an observation of hysteresis and a proof-of-principle measurement showing how the cCPT can be operated as a Josephson parametric amplifier (JPA). In Appendix D we present a first-principles derivation of the open-system dynamics of the cCPT, which complements the theoretical analysis in Ref. [2].

Chapter 2

Microwave Cavities

One of the building blocks of the cCPT is the cavity, in the form of a microwave-frequency quarter-wavelength coplanar waveguide cavity. In order to better understand this component of our device, it is useful to first consider it on its own. The purpose of this chapter is therefore to provide the background theory relevant to understanding our microwave cavity. We begin by discussing the quantization of electrical circuits. We then introduce input-output theory, which we use to model a transmission line coupled to a microwave cavity; coupling to this transmission line is neccessary to drive and measure the cavity, but this coupling also introduces noise and dissipation, as we will see. Finally, we use input-output theory to analyze the dynamics of a linear cavity, a frequency-modulated cavity, and a cavity with a Kerr nonlinearity. Interspersed throughout are relevant experimental examples.

This chapter is centered around specific examples relevant to our experiments, rather than a general overview. For further reading on circuit quantization we recommend Devoret's Les Houches lecture notes [50] (and the updated version of these notes [51]), Lev Bishop's thesis [52], and Yurke and Denker's paper on quantum network theory [53]. For further reading on input-output theory we recommend the textbook by Gardiner and Zoller [54] and Clerk's review article [55]. For classical microwave engineering, Pozar is the go-to source [6]. Finally, for an introductory treatment of quantum optics we recommend Gerry and Knight [47], and for an advanced treatment we recommend Schleich [48].

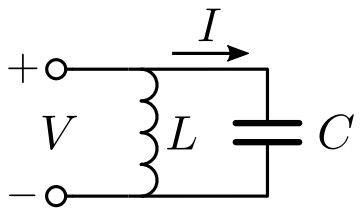

Figure 2.1: Schematic of a lumped-element LC circuit, with inductance L and capacitance C. The voltage V and current I indicate the sign conventions used in the analysis.

Section 2.1

Circuit Quantization

2.1.1 LC Circuit

The simplest possible resonant electrical circuit consists of an inductor and capacitor, as depicted schematically in Fig. 2.1. In order to treat this system quantum mechanically, we will derive the equation of motion of the system using Kirchhoff's laws, backtrack to find a Lagrangian consistent with this equation, Legendre transform to find the corresponding Hamiltonian, and finally impose the canonical commutation relations. This is essentially the same method we'll eventually use to find the Hamiltonian of the full cCPT.

From Kirchhoff's voltage law we have

$$V = -L\dot{I} = \frac{Q}{C} \tag{2.1}$$

where V is the voltage drop across each circuit element and I is the current running through them, and from Kirchhoff's current law we have

$$I = \dot{Q}. \tag{2.2}$$

For reasons that will become clear when we introduce Josephson junctions into our circuit, we now define a 'branch flux' variable [50]

$$\Phi(t) \equiv \int_{-\infty}^{t} V(t')dt' \tag{2.3}$$

such that $\Phi = -LI$ is related to the effective flux through the inductor. Plugging

this definition into Kirchhoff's laws, we arrive at the equation of motion for the flux

$$C\ddot{\Phi} = -\frac{\Phi}{L}. \tag{2.4}$$

It is straightforward to verify that the Lagrangian

$$\mathscr{L}(\Phi, \dot{\Phi}) = \frac{1}{2}C\dot{\Phi}^2 - \frac{1}{2L}\Phi^2 \tag{2.5}$$

is consistent with this equation of motion. Choosing Φ to be our canonical position, we now find our canonical momentum to be

$$p_\Phi \equiv \frac{\partial \mathscr{L}}{\partial \dot{\Phi}} = C\dot{\Phi} = Q \tag{2.6}$$

such that the flux Φ through the inductor and the charge Q on the capacitor are canonically conjugate variables. Before proceeding, it is worth noting that the Lagrangian can also be expressed in the form

$$\mathscr{L} = \frac{1}{2}CV^2 - \frac{1}{2}LI^2 \tag{2.7}$$

from which it's clear that in this case the energy stored in the capacitor plays the role of kinetic energy, whereas that stored in the inductor plays the role of potential energy. These roles are a matter of convention, however; if we had chosen the charge on the capacitor to be our canonical position, these roles would be reversed.

We now perform a Legendre transformation to arrive at our Hamiltonian

$$H(\Phi, Q) = \dot{\Phi}\frac{\partial \mathscr{L}}{\partial \dot{\Phi}} - \mathscr{L} = \frac{Q^2}{2C} + \frac{\Phi^2}{2L} \tag{2.8}$$

such that the flux Φ and the charge Q obey the canonical commutation relation

$$[\Phi, Q] = i\hbar. \tag{2.9}$$

To arrive at the standard form for the Hamiltonian of a harmonic oscillator, we now

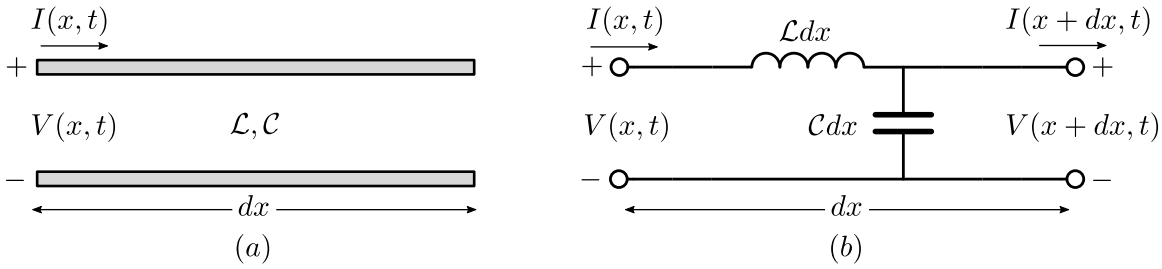

Figure 2.2: Illustration (a) and schematic (b) of an infinitessimal length dx of a transmission line cavity with inductance per unit length $\mathcal{L}$ and capacitance per unit length $\mathcal{C}$. In (a), the two planes of the physical transmission line are depicted. In (b), the equivalent lumped-element circuit is depicted.

introduce the creation and annihilation operators

$$\begin{aligned} a &= \sqrt{\frac{1}{2\hbar Z}}\left(\Phi + iZQ\right) \\ a^\dagger &= \sqrt{\frac{1}{2\hbar Z}}\left(\Phi - iZQ\right) \end{aligned} \tag{2.10}$$

where $Z = \sqrt{L/C}$ is the characteristic impedance of the circuit and $[a, a^\dagger] = 1$. For completeness, the canonical coordinates can be expressed in terms of the creation and annihilation operators as

$$\begin{aligned} \Phi &= \sqrt{\frac{\hbar Z}{2}}\left(a + a^\dagger\right) \\ Q &= -i\sqrt{\frac{\hbar}{2Z}}\left(a - a^\dagger\right). \end{aligned} \tag{2.11}$$

Finally, in terms of the creation and annihilation operators the Hamiltonian can be expressed as

$$H = \hbar\omega_0\left(a^\dagger a + \frac{1}{2}\right) \tag{2.12}$$

where $\omega_0 = 1/\sqrt{LC}$ is the resonant frequency of the circuit.

2.1.2 Transmission Line Cavity

A slightly more complicated electrical resonator, which serves as a good model for our microwave cavity, consists of inductances and capacitances distributed continuously over the length of a transmission line, as depicted in Fig. 2.2. Such a description

of our system in terms of distributed rather than lumped elements becomes necessary when the wavelengths of the electromagnetic waves of interest are comparable to or smaller than the size of the circuit elements, so that the voltage and current associated with these waves will vary significantly over the length of the circuit elements, as is the case for waves in the microwave frequency range [6]. To find the Hamiltonian for this transmission line cavity, we proceed along the same lines as the previous section.

Kirchhoff's voltage law for the infinitessimal length dx of the transmission line is

$$V(x,t) - \mathcal{L}dx\frac{\partial I(x,t)}{\partial t} - V(x+dx,t) = 0 \tag{2.13}$$

while Kirchhoff's current law is

$$I(x,t) - \mathcal{C}dx\frac{\partial V(x+dx,t)}{\partial t} - I(x+dx,t) = 0. \tag{2.14}$$

Dividing both equations through by dx and taking the limit as $dx \to 0$ yields the differential equations

$$\begin{aligned}\frac{\partial V(x,t)}{\partial x} &= -\mathcal{L}\frac{\partial I(x,t)}{\partial t} \\ \frac{\partial I(x,t)}{\partial x} &= -\mathcal{C}\frac{\partial V(x,t)}{\partial t}\end{aligned} \tag{2.15}$$

known as the telegrapher equations [6]. We again introduce a flux variable

$$\phi(x,t) = \int_{-\infty}^{t} V(x,t')dt' \tag{2.16}$$

and, assuming all voltages and currents vanish as $t \to -\infty$, these differential equations can be written concisely as

$$\frac{\partial^2\phi(x,t)}{\partial t^2} = v^2\frac{\partial^2\phi(x,t)}{\partial x^2} \tag{2.17}$$

which is a wave equation for $\phi(x,t)$ with phase velocity $v = 1/\sqrt{\mathcal{LC}}$. Using the separation of variables technique, the general solution to this wave equation can be expressed as

$$\phi(x,t) = \sum_k A_k \cos(kx + \alpha_k)\cos(kvt + \beta_k) \tag{2.18}$$

where A_k, α_k, and β_k are constants to be determined.

At this point we've shown that a generic transmission line supports traveling wave solutions; to make this system a resonator we must impose boundary conditions that yield a discrete set of standing wave solutions. For a quarter-wavelength cavity of length ℓ, our boundary conditions are that the transmission line is open at $x = 0$ and shorted to ground at $x = \ell$, which can be written mathematically as

$$\begin{aligned} \left.\frac{\partial\phi(x,t)}{\partial x}\right|_{x=0} &= 0 \\ \phi(x,t)|_{x=\ell} &= 0. \end{aligned} \tag{2.19}$$

These conditions yield the constraints

$$\begin{aligned} &\alpha_k = 0 \quad \forall k \\ &k \in \left\{ k_n = \frac{(2n-1)\pi}{2\ell} : n = 1, 2, 3, ... \right\} \end{aligned} \tag{2.20}$$

such that the general solution for $\phi(x,t)$ can now be written

$$\phi(x,t) = \sum_{n=1}^{\infty} A_n \cos(k_n x)\cos(k_n v t + \beta_n) \tag{2.21}$$

which is now a discrete sum over the standing waves that correspond to the normal modes of the system. We note that the wavelength of the fundamental mode is related to the length of the cavity according to

$$\ell = \frac{\lambda_1}{4} \tag{2.22}$$

where $\lambda_1 = 2\pi/k_1$, giving rise to the 'quarter-wavelength' nomenclature.

It is straightforward to verify that the Lagrangian

$$\mathscr{L}[\phi, \partial_x\phi, \dot{\phi}] = \int_0^{\ell} \left[\frac{\mathcal{C}\dot{\phi}(x,t)^2}{2} - \frac{\left(\partial_x\phi(x,t)\right)^2}{2\mathcal{L}} \right] dx \tag{2.23}$$

is consistent with the wave equation of Eq. (2.17), where $\partial_x = \partial/\partial x$. The one thing

worth noting here is that the Euler-Lagrange equation for our case is

$$\frac{d}{dt}\frac{\partial \mathscr{L}}{\partial \dot{\phi}} + \frac{d}{dx}\frac{\partial \mathscr{L}}{\partial \phi'} - \frac{\partial \mathscr{L}}{\partial \phi} = 0 \tag{2.24}$$

which can be derived by minimizing the action with respect to a Lagrangian that depends on $\phi(x,t)$, $\dot{\phi}(x,t)$, and $\phi'(x,t)$. Plugging in the general solution from Eq. (2.21), we can perform this integral explicitly to find

$$\mathscr{L}[\{\Phi_n, \dot{\Phi}_n\}] = \sum_{n=1}^{\infty}\left[\frac{\ell\mathcal{C}}{4}\dot{\Phi}_n^2 - \frac{k_n^2\ell}{4\mathcal{L}}\Phi_n^2\right] \tag{2.25}$$

where we've introduced the normal mode coordinates

$$\Phi_n(t) = A_n\cos(k_n v t + \beta_n). \tag{2.26}$$

Comparing this Lagrangian to that of a simple LC circuit, as given by Eq. (2.5), we express our Lagrangian as

$$\mathscr{L}[\{\Phi_n, \dot{\Phi}_n\}] = \sum_{n=1}^{\infty}\left[\frac{C_n}{2}\dot{\Phi}_n^2 - \frac{1}{2L_n}\Phi_n^2\right] \tag{2.27}$$

which is equivalent to the Lagrangian of a collection of uncoupled LC circuits with effective inductances

$$L_n = \frac{2\mathcal{L}}{k_n^2\ell} = \frac{8\ell\mathcal{L}}{\pi^2(2n-1)^2} \tag{2.28}$$

and effective capacitances

$$C_n = \frac{\ell\mathcal{C}}{2}. \tag{2.29}$$

From here we can proceed exactly as we did in the case of a single LC circuit. We find the conjugate momenta to be

$$Q_n = \frac{\partial \mathscr{L}}{\partial \dot{\Phi}_n} = C_n\dot{\Phi}_n \tag{2.30}$$

which again take the form of effective charge coordinates. Performing a Legendre

transformation, we now arrive at the Hamiltonian

$$\begin{aligned} H(\{\Phi_n, Q_n\}) &= \sum_{n=1}^{\infty} \left[\dot{\Phi}_n \frac{\partial \mathscr{L}}{\partial \dot{\Phi}_n} \right] - \mathscr{L} \\ &= \sum_{n=1}^{\infty} \left[\frac{Q_n^2}{2C_n} + \frac{\Phi_n^2}{2L_n} \right] \end{aligned} \tag{2.31}$$

where the charge and flux coordinates obey the canonical commutation relations

$$\begin{aligned} [\Phi_n, Q_m] &= i\hbar\delta_{nm} \\ [\Phi_n, \Phi_m] &= 0 \\ [Q_n, Q_m] &= 0. \end{aligned} \tag{2.32}$$

Here we again introduce the creation and annihilation operators

$$\begin{aligned} a_n &= \sqrt{\frac{1}{2\hbar Z_n}} \left(\Phi_n + i Z_n Q_n \right) \\ a_n^\dagger &= \sqrt{\frac{1}{2\hbar Z_n}} \left(\Phi_n - i Z_n Q_n \right) \end{aligned} \tag{2.33}$$

where $Z_n = \sqrt{L_n/C_n}$ is the characteristic impedance of the nth mode of the cavity and we have the commutation relations

$$\begin{aligned} [a_n, a_m^\dagger] &= \delta_{nm} \\ [a_n, a_m] &= 0 \\ [a_n^\dagger, a_m^\dagger] &= 0. \end{aligned} \tag{2.34}$$

Once again, for completeness, the inverse transformation from creation and annihilation operators back to charge and flux operators is given by

$$\begin{aligned} \Phi_n &= \sqrt{\frac{\hbar Z_n}{2}} \left(a_n + a_n^\dagger \right) \\ Q_n &= -i \sqrt{\frac{\hbar}{2Z_n}} \left(a_n - a_n^\dagger \right). \end{aligned} \tag{2.35}$$

Finally, the Hamiltonian of the quarter-wavelength transmission line cavity can be

expressed in its standard form

$$H = \hbar \sum_{n=1}^{\infty} \omega_n \left(a_n^\dagger a_n + \frac{1}{2} \right) \tag{2.36}$$

where $\omega_n = 1/\sqrt{L_n C_n}$ is the resonant frequency of the nth mode of the cavity.

2.1.3 Infinite Transmission Line

We next consider an infinite transmission line, or more realistically a transmission line far longer than the wavelengths of interest such that the normal modes are well-approximated by a continuum. This is essentially the same system we considered in the previous section, but without boundary conditions. The infinite transmission line is a good model for the coaxial cable that we couple to our cavity, which provides the means of both driving and measuring the cavity. This system is also the main thermal bath coupled to the cavity.

We start from the Lagrangian density for a transmission line

$$\mathscr{L}[\phi, \partial_x \phi, \dot{\phi}] = \frac{\mathcal{C}\dot{\phi}(x,t)^2}{2} - \frac{\left(\partial_x \phi(x,t)\right)^2}{2\mathcal{L}} \tag{2.37}$$

derived in the previous section (Eq. 2.23), except in these case we leave it as a density rather than integrating. We proceed to quantize this scalar field [56, 53], where the conjugate momentum is the charge density field

$$q(x,t) = \frac{\partial \mathscr{L}}{\partial \dot{\phi}} = \mathcal{C}\dot{\phi}(x,t), \tag{2.38}$$

which obeys the canonical commutation relations

$$\begin{aligned} [\phi(x,t), q(x',t)] &= i\hbar\delta(x-x') \\ [\phi(x,t), \phi(x',t)] &= 0 \\ [q(x,t), q(x',t)] &= 0. \end{aligned} \tag{2.39}$$

Performing a Legendre transformation, the Hamiltonian density is

$$\mathcal{H} = \frac{q(x,t)^2}{2\mathcal{C}} + \frac{\left(\partial_x \phi(x,t)\right)^2}{2\mathcal{L}}. \tag{2.40}$$

As we did in the case of a transmission line cavity, we now decompose the general

solution to this system into its normal modes; the difference is that we now have a continuum of such modes rather than a countably-infinite set. The Euler-Lagrange equation corresponding to the above Lagrangian density is simply the wave equation

$$\frac{\partial^2\phi(x,t)}{\partial t^2} = v^2\frac{\partial^2\phi(x,t)}{\partial x^2} \tag{2.41}$$

for the flux field $\phi(x,t)$, where $v = 1/\sqrt{\mathcal{LC}}$. The general solution to this wave equation can be decomposed into left-going and right-going parts

$$\phi(x,t) = \phi_L\left(t + \frac{x}{v}\right) + \phi_R\left(t - \frac{x}{v}\right) \tag{2.42}$$

which can each in turn be expanded in its normal modes

$$\phi_L\left(t + \frac{x}{v}\right) = \sqrt{\frac{\hbar\mathcal{Z}}{4\pi}}\int_0^\infty \frac{d\omega}{\sqrt{\omega}}\left(b_L(\omega)e^{-i\omega(t+x/v)} + b_L^\dagger(\omega)e^{i\omega(t+x/v)}\right) \tag{2.43}$$

$$\phi_R\left(t - \frac{x}{v}\right) = \sqrt{\frac{\hbar\mathcal{Z}}{4\pi}}\int_0^\infty \frac{d\omega}{\sqrt{\omega}}\left(b_R(\omega)e^{-i\omega(t-x/v)} + b_R^\dagger(\omega)e^{i\omega(t-x/v)}\right) \tag{2.44}$$

where $\mathcal{Z} = \sqrt{\mathcal{L}/\mathcal{C}}$ is the characteristic impedance of the transmission line.

We note that the factor of $1/\sqrt{\omega}$ in the integrand may look strange, but it simply anticipates the desired commutation relations for the operators $b(\omega)$, as we will see shortly. Using this form of the general solution for $\phi(x,t)$, the charge density field takes the form

$$q(x,t) = q_L\left(t + \frac{x}{v}\right) + q_R\left(t - \frac{x}{v}\right) \tag{2.45}$$

where the left and right-going parts of the solution can be expanded in normal modes

$$q_L\left(t + \frac{x}{v}\right) = -i\mathcal{C}\sqrt{\frac{\hbar\mathcal{Z}}{4\pi}}\int_0^\infty d\omega\sqrt{\omega}\left(b_L(\omega)e^{-i\omega(t+x/v)} - b_L^\dagger(\omega)e^{i\omega(t+x/v)}\right) \tag{2.46}$$

$$q_R\left(t - \frac{x}{v}\right) = -i\mathcal{C}\sqrt{\frac{\hbar\mathcal{Z}}{4\pi}}\int_0^\infty d\omega\sqrt{\omega}\left(b_R(\omega)e^{-i\omega(t-x/v)} - b_R^\dagger(\omega)e^{i\omega(t-x/v)}\right). \tag{2.47}$$

Using these expressions and the identity

$$\int_{-\infty}^{\infty} e^{i(\omega-\omega')x/v}dx = 2\pi v\delta(\omega-\omega') \tag{2.48}$$

we can invert the above expressions and solve for the creation and annihilation operators in terms of the field operators

$$b_L(\omega) = \frac{1}{v}\sqrt{\frac{\omega}{4\pi\hbar\mathcal{Z}}}\int_{-\infty}^{\infty}\left(\phi(x,t)+\frac{i}{\omega\mathcal{C}}q(x,t)\right)e^{i\omega(t+x/v)}dx \tag{2.49}$$

$$b_R(\omega) = \frac{1}{v}\sqrt{\frac{\omega}{4\pi\hbar\mathcal{Z}}}\int_{-\infty}^{\infty}\left(\phi(x,t)+\frac{i}{\omega\mathcal{C}}q(x,t)\right)e^{i\omega(t-x/v)}dx. \tag{2.50}$$

where we've also used the fact that the domain of ω is the non-negative reals to drop terms containing $\delta(\omega+\omega')$ which are always zero over this domain. From these expressions it is straightforward to derive the commutation relations for the creation and annhilation operators

$$[b_L(\omega), b_L^\dagger(\omega')] = \delta(\omega-\omega') \tag{2.51}$$

$$[b_R(\omega), b_R^\dagger(\omega')] = \delta(\omega-\omega') \tag{2.52}$$

$$[b_L(\omega), b_R(\omega')] = 0 \tag{2.53}$$

$$[b_L(\omega), b_R^\dagger(\omega')] = 0 \tag{2.54}$$

using the above identity and the canonical commutation relation between the cavity flux and charge density fields.

We now seek to express the Hamiltonian in terms of these creation and annihilation operators. First, we note that

$$\begin{aligned}\phi'(x,t) &= \frac{1}{v}\left[\dot{\phi}_L\left(t+\frac{x}{v}\right)-\dot{\phi}_R\left(t-\frac{x}{v}\right)\right]\\ &= \frac{1}{\mathcal{C}v}\left[q_L\left(t+\frac{x}{v}\right)-q_R\left(t-\frac{x}{v}\right)\right]\end{aligned} \tag{2.55}$$

such that the Hamiltonian density can be expressed

$$\begin{aligned}\mathcal{H} &= \frac{1}{2\mathcal{C}}\left(q_L + q_R\right)^2 + \frac{1}{2\mathcal{C}}\left(q_L - q_R\right)^2 \\ &= \frac{1}{\mathcal{C}}\left(q_L^2 + q_R^2\right).\end{aligned} \tag{2.56}$$

It is now straightforward to find the Hamiltonian by integrating this expression over all space, yielding the Hamiltonian

$$H = \int_0^\infty \hbar\omega \left(b_L^\dagger(\omega) b_L(\omega) + b_R^\dagger(\omega) b_R(\omega)\right) d\omega \tag{2.57}$$

where we've dropped an overall constant (though infinite) term arising from the commutation relations for the creation and annihilation operators.

Rather than keeping the left-going and right-going modes as separate operators, the left-going modes can be associated with negative frequencies (i.e., negative wavenumbers) and the right-going modes with positive frequencies. Thus, the Hamiltonian for the infinite transmission line can be written compactly as

$$H = \int_{-\infty}^\infty \hbar\omega b^\dagger(\omega) b(\omega) d\omega. \tag{2.58}$$

As we will see shortly, this is identical to the bath Hamiltonian considered in input-output theory.

Section 2.2

Input-Output Theory

We now introduce input-output theory, which provides a model for how our cavity couples to its environment. As we will show, it is a unified framework for modeling how driving fields couple into the cavity, how energy is dissipated in the cavity, and how the state of the cavity is measured.

2.2.1 Simplified Analysis

To derive the quantum Langevin equation, one of the two key results of input-output theory, we follow the same line of reasoning as Gardiner and Collett [57] but

do not aim to reproduce the generality of their results. For the sake of clarity, we make several simplifying assumptions right from the beginning. First, we specify that our system of interest is an oscillator (not necessarily a linear one), and so its system operators are the creation and annihilation operators a and $a^\dagger$. Second, we assume a definite form for the interaction Hamiltonian, which amounts to adopting a particular convention for the form of the resulting quantum Langevin equation. Third, we assume that the strength of the coupling between the cavity and its bath is constant as a function of frequency.

Thus, our starting point is the Hamiltonian

$$H = H_{\text{sys}} + H_{\text{bath}} + H_{\text{int}} \tag{2.59}$$

describing our system and its interaction with a bath consisting of a continuum of harmonic oscillators, such that

$$H_{\text{bath}} = \int_{-\infty}^{\infty} \hbar\omega b^\dagger(\omega) b(\omega) d\omega \tag{2.60}$$

$$H_{\text{int}} = i\hbar\sqrt{\frac{\kappa}{2\pi}} \int_{-\infty}^{\infty} \left[a^\dagger b(\omega) - b^\dagger(\omega) a\right] d\omega \tag{2.61}$$

where $b(\omega)$ are the annihilation operators of the bath, each associated with a mode of frequency ω, which satisfy the commutation relations

$$[b(\omega), b^\dagger(\omega')] = \delta(\omega - \omega') \tag{2.62}$$

$$[b(\omega), b(\omega')] = 0 \tag{2.63}$$

and κ is the strength of the coupling. We stress that for each frequency ω, $b(\omega)$ is a function of time; it is not an operator in Fourier space. The Heisenberg equations of motion for the operators $b(\omega)$ and a are therefore

$$\dot{b}(\omega) = -i\omega b(\omega) - \sqrt{\frac{\kappa}{2\pi}} a \tag{2.64}$$

$$\dot{a} = \frac{i}{\hbar}\left[H_{\text{sys}}, a\right] + \sqrt{\frac{\kappa}{2\pi}} \int_{-\infty}^{\infty} b(\omega) d\omega. \tag{2.65}$$

We approach Eq. (2.64) by plugging in the ansatz

$$b(\omega, t) = f(t)e^{-i\omega t} \tag{2.66}$$

which leads to the differential equation

$$\dot{f}(t) = -\sqrt{\frac{\kappa}{2\pi}} a e^{i\omega t} \tag{2.67}$$

that we can integrate from initial time t_0 to the present time t, yielding the solution

$$b(\omega) = b_0(\omega)e^{-i\omega(t-t_0)} - \sqrt{\frac{\kappa}{2\pi}} \int_{t_0}^{t} a(t')e^{-i\omega(t-t')}dt' \tag{2.68}$$

where $b_0(\omega)$ is the operator $b(\omega)$ at $t = t_0$. We now define an 'input' operator

$$b_{\text{in}}(t) = \frac{1}{\sqrt{2\pi}} \int_{-\infty}^{\infty} b_0(\omega)e^{-i\omega(t-t_0)}d\omega \tag{2.69}$$

that satisfies the commutation relation

$$[b_{\text{in}}(t), b_{\text{in}}^{\dagger}(t')] = \delta(t - t') \tag{2.70}$$

and in terms of which we can express

$$\sqrt{\frac{\kappa}{2\pi}} \int_{-\infty}^{\infty} b(\omega)d\omega = \sqrt{\kappa}b_{\text{in}}(t) - \frac{\kappa}{2\pi} \int_{t_0}^{t} dt' a(t') \int_{-\infty}^{\infty} d\omega e^{-i\omega(t-t')} \tag{2.71}$$

$$= \sqrt{\kappa}b_{\text{in}}(t) - \frac{\kappa}{2}a(t) \tag{2.72}$$

where we've used the fact that

$$\int_{t_0}^{t} dt' a(t')\delta(t - t') = \frac{a(t)}{2} \tag{2.73}$$

for appropriately smooth functions. Plugging back into Eq. (2.65), we find

$$\dot{a}(t) = \frac{i}{\hbar} [H_{\text{sys}}, a(t)] - \frac{\kappa}{2}a(t) + \sqrt{\kappa}b_{\text{in}}(t) \tag{2.74}$$

which is the quantum Langevin equation for the operator a. This amounts to the usual Heisenberg equation of motion for the operator a with the addition of a damping term of strength $\kappa/2$ and a driving field in the form of b_{in} that couples into the system at a rate determined by κ. Thus, we see that dissipation and measurement are intimately linked; in order to drive and measure the oscillator we must couple it to an external bath, which also serves as a loss channel.

Instead of integrating Eq. (2.64) from past time t_0 to current time t, we could have equivalently integrated it from future time t_1 back to the present time t. This yields the solution

$$b(\omega) = b_1(\omega)e^{-i\omega(t-t_1)} + \sqrt{\frac{\kappa}{2\pi}}\int_t^{t_1} a(t')e^{-i\omega(t-t')}dt' \tag{2.75}$$

where $b_1(\omega)$ is the operator $b(\omega$ at $t = t_1$. Analogously, we define an 'output' operator

$$b_{\text{out}}(t) = \frac{1}{\sqrt{2\pi}}\int_{-\infty}^{\infty} b_1(\omega)e^{-i\omega(t-t_1)}d\omega \tag{2.76}$$

in terms of which Eq. (2.65) can also be expressed

$$\dot{a}(t) = \frac{i}{\hbar}\left[H_{\text{sys}}, a(t)\right] + \frac{\kappa}{2}a(t) + \sqrt{\kappa}b_{\text{out}}(t). \tag{2.77}$$

Combining Eqs. (2.74) and (2.77), we find

$$b_{\text{out}}(t) - b_{\text{in}}(t) = -\sqrt{\kappa}a(t) \tag{2.78}$$

relating the input and output fields of the bath to the internal field of the cavity.

2.2.2 Quantum Damped, Driven Harmonic Oscillator

The quantum Langevin equation and input-output relations may seem intimidating and opaque at first glance, but they are actually quite intuitive. To develop this intuition we consider the simple case of a linear harmonic oscillator, for which we will find correspondence with the classical damped, driven harmonic oscillator. In this case, our system Hamiltonian is given by

$$H_{\text{sys}} = \hbar\omega_0 a^\dagger a \tag{2.79}$$

such that Eq. (2.74) takes the form

$$\dot{a}(t) = \left(-i\omega_0 - \frac{\kappa}{2}\right) a(t) + \sqrt{\kappa} b_{\text{in}}(t). \tag{2.80}$$

To solve this equation, we make the ansatz

$$a(t) = f(t) e^{(-i\omega_0 - \kappa/2)t} \tag{2.81}$$

leading to the differential equation

$$\dot{f}(t) = \sqrt{\kappa} b_{\text{in}}(t) e^{(i\omega_0 + \kappa/2)t} \tag{2.82}$$

that we can integrate from 0 to t to find the general solution

$$a(t) = a(0) e^{(-i\omega_0 - \kappa/2)t} + \sqrt{\kappa} \int_0^t b_{\text{in}}(t') e^{(-i\omega_0 - \kappa/2)(t-t')} dt' \tag{2.83}$$

which takes the form of a linear response of $a(t)$ to the driving field $b_{\text{in}}(t)$.

Now let us suppose that $b_{\text{in}}(t)$ is a sinusoidal drive, which we express in the form

$$b_{\text{in}}(t) = \frac{\varepsilon}{\sqrt{\kappa}} e^{-i\omega t} \Theta(t) + \delta b_{\text{in}}(t) \tag{2.84}$$

where ε is the complex amplitude of the driving field, $\Theta(t)$ is the step function, and $\delta b_{\text{in}}(t)$ is the operator corresponding to the fluctuations in the drive that are necessary to satisfy the commutation relation of Eq. (2.70). Plugging back into the general solution of Eq. (2.83), we find

$$\begin{aligned} a(t) = a(0) e^{(-i\omega_0 - \kappa/2)t} &+ \frac{\varepsilon}{i(\omega_0 - \omega) + \kappa/2} \left[e^{-i\omega t} - e^{(-i\omega_0 - \kappa/2)t}\right] \\ &+ \sqrt{\kappa} \int_0^t \delta b_{\text{in}}(t') e^{(-i\omega_0 - \kappa/2)(t-t')} dt'. \end{aligned} \tag{2.85}$$

The expectation value of this mode is

$$\langle a(t) \rangle = \frac{\varepsilon}{i(\omega_0 - \omega) + \kappa/2} \left[e^{-i\omega t} - e^{(-i\omega_0 - \kappa/2)t}\right] \tag{2.86}$$

where we've assumed an initial ground state. This is in correspondence with the

classical damped driven harmonic oscillator under the assumption that $\omega - \omega_0 \ll \omega_0$.

We next show that the steady state of this solution (2.85) is a coherent state. In the steady state ($t \to \infty$), the expectation value of the annihilation operator undergoes sinusoidal oscillation at the drive frequency with a constant amplitude

$$\langle a(t) \rangle = \alpha e^{-i\omega t} \quad ; \quad \alpha = \frac{\varepsilon}{i(\omega_0 - \omega) + \kappa/2}. \tag{2.87}$$

What remains is to show that $a(t)$ is a minimum-uncertainty state. More precisely, we aim to show that fluctuations in the dimensionless position and momentum (quadrature) operators

$$x = a^\dagger + a \tag{2.88}$$

$$p = i\left(a^\dagger - a\right) \tag{2.89}$$

are minimized according to the generalized uncertainty relation

$$\Delta x \Delta p \geq \frac{1}{2} |\langle [x, p] \rangle| = 1 \tag{2.90}$$

and equally distributed between the two quadrature operators, such that

$$\Delta x = \sqrt{\left\langle \left(x - \langle x \rangle \right)^2 \right\rangle} = 1 \tag{2.91}$$

$$\Delta p = \sqrt{\left\langle \left(p - \langle p \rangle \right)^2 \right\rangle} = 1. \tag{2.92}$$

Fluctuations in the mode operator a take the form

$$a(t) - \langle a(t) \rangle = a(0) e^{(-i\omega_0 - \kappa/2)t} + \sqrt{\kappa} \int_0^t \delta b_{\text{in}}(t') e^{(-i\omega_0 - \kappa/2)(t-t')} dt' \tag{2.93}$$

such that the fluctuations in x take the form

$$(\Delta x)^2 = \left\langle a(0) a^\dagger(0) \right\rangle e^{-\kappa t} + \kappa e^{-\kappa t} \int_0^t dt' \int_0^t dt'' \left\langle \delta b_{\text{in}}(t') \delta b_{\text{in}}^\dagger(t'') \right\rangle e^{i\omega_0 (t' - t'')} e^{\kappa(t' + t'')/2} \tag{2.94}$$

where almost all of the cross-terms vanish since the expectation value is taken with

respect to the ground state. Using the fact that $\left\langle a(0)a^\dagger(0)\right\rangle = 1$ and

$$\left\langle \delta b_{\text{in}}(t')\delta b_{\text{in}}^\dagger(t'')\right\rangle = \left\langle [b_{\text{in}}(t'), b_{\text{in}}^\dagger(t'')]\right\rangle = \delta(t'-t''), \tag{2.95}$$

we find that $(\Delta x)^2 = 1$. The fluctuations in p are identical to those in x

$$(\Delta p)^2 = \left\langle a(0)a^\dagger(0)\right\rangle e^{-\kappa t} + \kappa e^{-\kappa t}\int_0^t dt' \int_0^t dt'' \left\langle \delta b_{\text{in}}(t')\delta b_{\text{in}}^\dagger(t'')\right\rangle e^{i\omega_0(t'-t'')}e^{\kappa(t'+t'')/2} \tag{2.96}$$

such that the minimum uncertainty relation

$$\Delta x = \Delta p = 1 \tag{2.97}$$

holds for all time. Thus, the steady state solution of the damped, driven quantum harmonic oscillator is a coherent state.

Section 2.3

Lossy Quarter-wavelength Cavity

In this section we analyze the dynamics of a quarter-wavelength ($\lambda/4$) microwave cavity in the presence of loss. We consider two forms of loss: that due to coupling to an external transmission line, which also provides the means of driving and measuring the cavity, and that due to internal loss in the cavity. Our analysis is focused around the reflection coefficient of the cavity, and we show that the classical and quantum treatments (based on microwave engineering and input-output theory, respectively) are in correspondence with one another.

2.3.1 Classical Treatment

Near its fundamental frequency, the input impedance of our quarter-wavelength cavity is approximately [6]

$$Z_{\text{in}} \approx \frac{Z_0}{\alpha\ell + i\pi\Delta/2\omega_0} \tag{2.98}$$

where $\Delta = \omega - \omega_0$ is the detuning from the fundamental frequency ω_0, α is the cavity's attenuation constant, ℓ is its length, Z_0 is its characteristic impedance, and we've assumed both low loss ($\alpha\ell \ll 1$) and small detuning ($\Delta \ll \omega_0$). This input

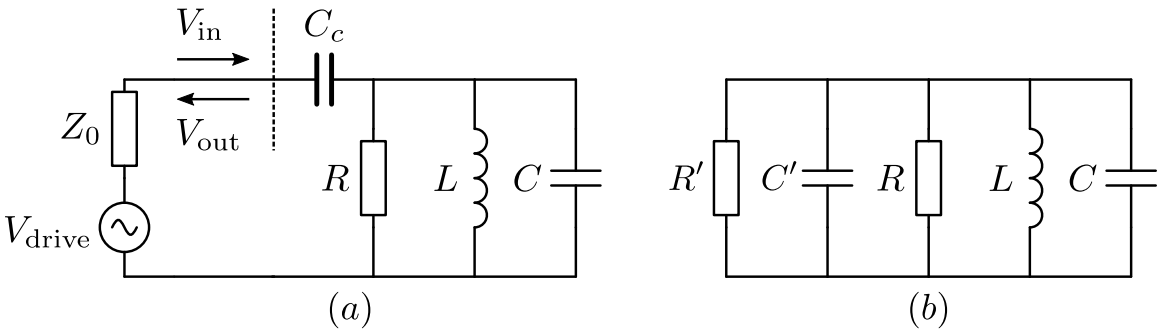

Figure 2.3: Schematics representing our quarter-wavelength cavity and its external environment. In (a), the external elements Z_0 and C_c are in series with the cavity, as they are in the experiment, and the plane of the sample (at which the reflection coefficient will be analyzed) is marked by a dashed line. In (b), the external elements are represented by their parallel equivalents: resistance R' and capacitance C'.

impedance is equivalent to that of a parallel RLC resonator

$$Z_{in} \approx \frac{1}{(1/R) + 2i\Delta C} \tag{2.99}$$

near its resonant frequency ($\Delta \ll \omega_0$), with effective lumped elements

$$R = \frac{Z_0}{\alpha \ell} \tag{2.100}$$

$$L = \frac{1}{\omega_0^2 C} \tag{2.101}$$

$$C = \frac{\pi}{4\omega_0 Z_0} \tag{2.102}$$

that depend on the resonant frequency of the cavity. We couple to this system with a series capacitance C_c and measure it by connecting it to a network analyzer with the same characteristic impedance $Z_0 = 50\Omega$ that provides the incoming voltage and measures the outgoing voltage for reflection measurements. The loaded cavity can therefore be approximated by the circuit shown in Figure 2.3(a).

To simplify things [58], we can replace the series combination of Z_0 and C_c by an equivalent combination of R' and C' in parallel, as shown in Figure 2.3(b). We find R' and C' with the constraint

$$Z_0 - \frac{i}{\omega C_c} = \left(\frac{1}{R'} + i\omega C'\right)^{-1} \tag{2.103}$$

that yields the solutions

$$\begin{aligned} R' &= Z_0 \left(1 + \frac{1}{\omega^2 Z_0^2 C_c^2}\right) \\ C' &= C_c \left(\frac{1}{1 + \omega^2 Z_0^2 C_c^2}\right). \end{aligned} \tag{2.104}$$

Using the fact that $C_c \ll C$, since we have designed our system so the majority of the capacitance comes from the cavity itself, and the effective capacitance of our cavity given by Eq. 2.102, we can infer that $C_c \omega_0 Z_0 \ll 1$. We can therefore approximate

$$\begin{aligned} R' &\approx \frac{1}{\omega^2 Z_0 C_c^2} \\ C' &\approx C_c \quad . \end{aligned} \tag{2.105}$$

where we've used $\omega \approx \omega_0$ since we've constrained ourselves to working very close to the fundamental frequency.

Internal and External Quality Factors. Drawing the circuit in this way allows us to easily analyze the internal and external quality factors of our system, since the internal quality factor Q_{int} is due to dissipation in R and the external quality factor Q_{ext} is due to dissipation in R'. The most general definition of quality factor at resonance is [6]

$$Q \equiv \omega_0 \frac{\text{average energy stored}}{\text{energy loss/second}} \tag{2.106}$$

where the average energy stored in a cycle is a combination of the electrical energy $W_e = (C_{\text{tot}})|V_{\text{in}}|^2/4 \approx (C+C_c)|V_{\text{in}}|^2/4$ and the magnetic energy W_m (which equals W_e at resonance), and the average energy loss per second in a cycle (due to the resistance R_{loss}) is $P_{\text{loss}} = |V_{\text{in}}|^2/2R_{\text{loss}}$. Putting these expressions together, our internal and external quality factors take the form

$$\begin{aligned} Q_{\text{int}} &= \omega_0 R\,(C + C_c) \\ Q_{\text{ext}} &= \frac{C + C_c}{\omega_0 Z_0 C_c^2} \end{aligned} \tag{2.107}$$

and the total, or 'loaded', quality factor is given by

$$Q_{\text{tot}} = \left(\frac{1}{Q_{\text{int}}} + \frac{1}{Q_{\text{ext}}}\right)^{-1} = \frac{\omega_0 R\,(C + C_c)}{1 + \omega_0^2 R Z_0 C_c^2}. \tag{2.108}$$

Lastly, we define effective angular damping rates $\kappa = \omega_0/Q$ which take the form

$$\begin{aligned}\kappa_{\text{int}} &= \frac{1}{R\left(C + C_c\right)} \\ \kappa_{\text{ext}} &= \frac{\omega_0^2 Z_0 C_c^2}{\left(C + C_c\right)} \\ \kappa_{\text{tot}} &= \frac{1 + \omega_0^2 R Z_0 C_c^2}{R\left(C + C_c\right)}.\end{aligned} \tag{2.109}$$

Since the effective capacitance C is a function of the resonant frequency ω_0 of the fundamental mode of the cavity, according to Eq. (2.102), so too are these damping rates

$$\kappa_{\text{int}}(\omega_0) \approx \frac{4\omega_0 Z_0}{\pi R} \tag{2.110}$$

$$\kappa_{\text{ext}}(\omega_0) \approx \frac{4}{\pi}\omega_0^3 Z_0^2 C_c^2 \tag{2.111}$$

$$\kappa_{\text{tot}}(\omega_0) = \kappa_{\text{int}}(\omega_0) + \kappa_{\text{ext}}(\omega_0) \tag{2.112}$$

where we've used $C_c \ll C$ to simplify the above expressions.

Reflection Coefficient. We now turn to the analysis of reflection measurements off the cavity into the characteristic impedance Z_0 [59]. In this case we consider everything other than Z_0 to be part of the resonant circuit, so we include the series coupling capacitance C_c. The impedance of the cavity is then

$$Z_{\text{cav}} = \frac{1}{i\omega C_c} + \left(\frac{1}{R} + \frac{1}{i\omega L} + i\omega C\right)^{-1} \tag{2.113}$$

which gives rise to the reflection coefficient

$$\begin{aligned}S_{11} = \frac{V_{\text{out}}}{V_{\text{in}}} &= \frac{Z_{\text{cav}} - Z_0}{Z_{\text{cav}} + Z_0} \\ &= \frac{1 - \omega^2\left[L\left(C + C_c\right) - \frac{Z_0 C_c L}{R}\right] + i\omega\left[\frac{L}{R} - Z_0 C_c\left(1 - \omega^2 LC\right)\right]}{1 - \omega^2\left[L\left(C + C_c\right) + \frac{Z_0 C_c L}{R}\right] + i\omega\left[\frac{L}{R} + Z_0 C_c\left(1 - \omega^2 LC\right)\right]}\end{aligned} \tag{2.114}$$

which requires significant simplification. First, note that $Z_0/R = \pi/4Q_{\text{int}} \ll 1$, and let $x = \omega/\omega_0$ where $\omega_0 = 1/\sqrt{L(C+C_c)}$, allowing us to write

$$S_{11} = \frac{1 - x^2 + ix\omega_0 \left[\frac{L}{R} - Z_0 C_c \left(1 - x^2 \frac{C}{C+C_c}\right)\right]}{1 - x^2 + ix\omega_0 \left[\frac{L}{R} + Z_0 C_c \left(1 - x^2 \frac{C}{C+C_c}\right)\right]} \tag{2.115}$$

We now express R and Z_0 in terms of Q_{int} and Q_{ext}, respectively, yielding

$$S_{11} = \frac{1 - x^2 + ix \left[\frac{1}{Q_{\text{int}}} - \frac{C+C_c}{C_c Q_{\text{ext}}} \left(1 - x^2 \frac{C}{C+C_c}\right)\right]}{1 - x^2 + ix \left[\frac{1}{Q_{\text{int}}} - \frac{C+C_c}{C_c Q_{\text{ext}}} \left(1 - x^2 \frac{C}{C+C_c}\right)\right]} \tag{2.116}$$

Next we reiterate that the operating frequency must be very close to the resonant frequency for this model to hold, so we may write $x = 1 + \delta x$ and keep only the lowest order terms in δx. In addition, as stated before, the coupling capacitance is small compared to the total capacitance, so that $C_c/(C + C_c) \ll 1$. Incorporating these simplifications, we find

$$S_{11} = \frac{-2\delta x + i\left(\frac{1}{Q_{\text{int}}} - \frac{1}{Q_{\text{ext}}}\right)}{-2\delta x + i\left(\frac{1}{Q_{\text{int}}} + \frac{1}{Q_{\text{ext}}}\right)} \tag{2.117}$$

Noting that $\delta x = \Delta/\omega_0$, we multiply through by $-\omega_0/2$ and express the Q's in terms of κ's to obtain

$$S_{11}(\Delta) = \frac{\Delta - i\left(\kappa_{\text{int}} - \kappa_{\text{ext}}\right)/2}{\Delta - i\left(\kappa_{\text{int}} + \kappa_{\text{ext}}\right)/2} \tag{2.118}$$

which is our final result. Using the real and imaginary parts (or equivalently the magnitude and phase) of the reflection coefficient obtained from a network analyzer trace, we can fit this model to our data and obtain best fits for ω_0, κ_{int}, and κ_{ext}. These are crucial to our other theoretical models in which they appear as empirical parameters.

2.3.2 Quantum Treatment

We would like to connect this formalism to that of input-output theory, but first we have to make clear how the reflection coefficient acts upon quadrature operators. Unlike its action on complex-valued voltages, the reflection coefficient acts on quadrature operators by changing their magnitude and inducing a rotation in phase space (rather than simply multiplying by $e^{i\theta}$). To be precise, let's introduce the quadrature

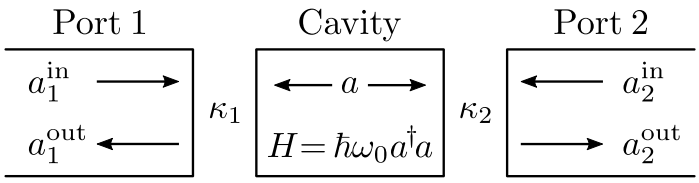

Figure 2.4: Schematic of a two sided linear cavity with decay rates κ_1 and κ_2.

operator

$$X(\theta) = \frac{1}{2}\left(ae^{-i\theta} + a^\dagger e^{i\theta}\right) \tag{2.119}$$

corresponding to the angle θ in phase space. In terms of this quadrature operator, we can now write the action of the complex reflection coefficient S_{11} as

$$X_{\text{out}}(0) = |S_{11}| X_{\text{in}}\left(\arg(S_{11})\right) \tag{2.120}$$

which yields the following relations

$$\begin{aligned} a_{\text{out}} &= S_{11}^* a_{\text{in}} \\ a_{\text{out}}^\dagger &= S_{11} a_{\text{in}}^\dagger \end{aligned} \tag{2.121}$$

for the associated creation and annihilation operators.

For our model system we consider a two-sided cavity, as depicted in Fig. 2.4, where one port is meant to model the physical transmission line capacitively coupled to our cavity and the other port is meant to model an inaccessible internal loss channel. Extending the results of input-output theory to the case of two baths, we relate the fields at the ports of the cavity to the internal field of the cavity according to

$$\begin{aligned} a_1^{\text{out}}(t) - a_1^{\text{in}}(t) &= -\sqrt{\kappa_1} a(t) \\ a_2^{\text{out}}(t) - a_2^{\text{in}}(t) &= -\sqrt{\kappa_2} a(t) \end{aligned} \tag{2.122}$$

where κ_1 and κ_2 are the damping rates associated with their respective ports, such that the internal cavity field obeys the quantum langevin equation

$$\begin{aligned} \dot{a}(t) = -i\omega_0 a(t) - \frac{\kappa_1 + \kappa_2}{2} a(t) + \sqrt{\kappa_1} a_1^{\text{in}}(t) \\ + \sqrt{\kappa_2} a_2^{\text{in}}(t). \end{aligned} \tag{2.123}$$

Scattering Matrix. In scattering experiments we are generally interested in the steady state response of the cavity as a function of drive frequency ω, to which end we Fourier transform Eq. (2.123) and solve for the cavity response algebraically

$$\tilde{a}(\omega) = \frac{\sqrt{\kappa_1}\tilde{a}_1^{\text{in}}(\omega) + \sqrt{\kappa_2}\tilde{a}_2^{\text{in}}(\omega)}{i(\omega_0 - \omega) + (\kappa_1 + \kappa_2)/2} \tag{2.124}$$

where a tilde denotes the Fourier transform of the given mode operator. Plugging this result into the Fourier transform of Eq. (2.122), we find a linear relationship between the input and output mode operators

$$\begin{aligned} \tilde{a}_1^{\text{out}}(\omega) &= \tilde{a}_1^{\text{in}}(\omega) - \frac{\kappa_1\tilde{a}_1^{\text{in}}(\omega) + \sqrt{\kappa_1\kappa_2}\tilde{a}_2^{\text{in}}(\omega)}{i(\omega_0 - \omega) + (\kappa_1 + \kappa_2)/2} \\ \tilde{a}_2^{\text{out}}(\omega) &= \tilde{a}_2^{\text{in}}(\omega) - \frac{\sqrt{\kappa_1\kappa_2}\tilde{a}_1^{\text{in}}(\omega) + \kappa_2\tilde{a}_2^{\text{in}}(\omega)}{i(\omega_0 - \omega) + (\kappa_1 + \kappa_2)/2} \end{aligned} \tag{2.125}$$

that defines the scattering matrix according to

$$\begin{bmatrix} \tilde{a}_1^{\text{out}}(\omega) \\ \tilde{a}_2^{\text{out}}(\omega) \end{bmatrix} = \begin{bmatrix} S_{11}^* & S_{12}^* \\ S_{21}^* & S_{22}^* \end{bmatrix} \begin{bmatrix} \tilde{a}_1^{\text{in}}(\omega) \\ \tilde{a}_2^{\text{in}}(\omega) \end{bmatrix} \tag{2.126}$$

where the complex conjugate of each matrix element is taken for the reasons discussed earlier. The scattering matrix elements therefore take the form

$$S_{11}(\Delta) = \frac{\Delta - i(\kappa_2 - \kappa_1)/2}{\Delta - i(\kappa_1 + \kappa_2)/2} \tag{2.127}$$

$$S_{12}(\Delta) = \frac{i\sqrt{\kappa_1\kappa_2}}{\Delta - i(\kappa_1 + \kappa_2)/2} \tag{2.128}$$

$$S_{21}(\Delta) = \frac{i\sqrt{\kappa_1\kappa_2}}{\Delta - i(\kappa_1 + \kappa_2)/2} \tag{2.129}$$

$$S_{22}(\Delta) = \frac{\Delta - i(\kappa_1 - \kappa_2)/2}{\Delta - i(\kappa_1 + \kappa_2)/2} \tag{2.130}$$

where $\Delta = \omega - \omega_0$ is the detuning, as before.

Quantum-Classical Correspondence. Comparing our classical reflection coefficient from Eq. (2.118) and our quantum reflection coefficient from Eq. (2.127), we

see that they are equivalent if we identify

$$\begin{aligned} \kappa_1 &= \kappa_{\text{ext}} \\ \kappa_2 &= \kappa_{\text{int}} \end{aligned} \tag{2.131}$$

such that port 1 is intepreted as the physical port through which the system is driven and measured, and port 2 is interpreted as an inaccessible port modeling internal losses. Under this interpretation, we therefore find the quantum two-sided cavity to be an accurate model of a lossy quarter-wavelength cavity. In this case it is convenient to rewrite the quantum Langevin equation for our $\lambda/4$ cavity in the form

$$\dot{a}(t) = \frac{i}{\hbar}\left[H_{\text{sys}}, a(t)\right] - \frac{\kappa_{\text{tot}}}{2}a(t) + \sqrt{\kappa_{\text{ext}}}a_{\text{in}}(t) + \sqrt{\kappa_{\text{in}}}b_{\text{in}}(t) \tag{2.132}$$

where a_{in} is the input mode of the physical port, and b_{in} is the noisy input mode of the port modeling internal losses such that $\langle b_{\text{in}}(t)\rangle = 0$.

Furthermore, since the reflection coefficient now admits both of the following interpretations

$$\begin{aligned} V_{\text{out}} &= S_{11}V_{\text{in}} \\ \langle a_{\text{out}}\rangle &= S_{11}^{*}\langle a_{\text{in}}\rangle \end{aligned} \tag{2.133}$$

we can conclude that V_{out} is linearly related to the output mode operators and V_{in} is linearly related to the input mode operators. Thus, we can identify the signal we send into the cavity via the coupling capacitor C_c with the input mode operators, and we can interpret the signal coming out of the cavity via the coupling capacitor C_c with the output mode operators.

2.3.3 Reflection Coefficient

We next analyze some key properties of the reflection coefficient

$$S_{11}(\Delta) = \frac{\Delta - i\left(\kappa_{\text{int}} - \kappa_{\text{ext}}\right)/2}{\Delta - i\left(\kappa_{\text{int}} + \kappa_{\text{ext}}\right)/2} \tag{2.134}$$

and illustrate the importance of this quantity with an experimental example.

Coupling Regimes. It is useful to define a dimensionless coupling ratio

$$\xi = \frac{Q_{\text{int}}}{Q_{\text{ext}}} = \frac{\kappa_{\text{ext}}}{\kappa_{\text{int}}} \tag{2.135}$$

that tells us the fraction of energy entering the cavity that eventually escapes. When $\xi > 1$ the system is said to be over-coupled, and most of the energy that enters the cavity eventually exits (the reflected signal here is mostly due to reflection off the back of the cavity). When $\xi < 1$ the system is said to be under-coupled, and most of the energy that enters the cavity is dissipated inside of it (the reflected signal here is mostly due to reflection off the front of the cavity). When $\xi = 1$ the system is said to be critically-coupled, and there is a balance of energy dissipation. Since we rely on intra-cavity photons leaking out to infer the state of the cavity, the over-coupled regime is preferable in our case.

Trajectory in the Complex Plane. The reflection coefficient takes the form of a parametric curve in the complex plane, parametrized by the detuning Δ, as pictured in Figure 2.5. To analyze this trajectory, it is useful to define another dimensionless parameter $\zeta = (1-\xi)/(1+\xi)$ in terms of which the reflection coefficient can be written in a nondimensional form

$$S_{11}(\Delta) = \frac{(\Delta/\kappa_{\text{tot}}) - i\zeta/2}{(\Delta/\kappa_{\text{tot}}) - i/2}. \tag{2.136}$$

We now show explicitly that this parametric curve traces out a circle in the complex plane. Using the trigonometric substitution $\Delta/\kappa_{\text{tot}} = \tan(\theta/2)/2$ we find

$$\begin{aligned} S_{11}(\theta) &= \sin^2\left(\frac{\theta}{2}\right) + \zeta\cos^2\left(\frac{\theta}{2}\right) + i\,(1-\zeta)\sin\left(\frac{\theta}{2}\right)\cos\left(\frac{\theta}{2}\right) \\ &= \frac{1+\zeta}{2} - \frac{1-\zeta}{2}e^{-i\theta} \end{aligned} \tag{2.137}$$

which is the equation for a circle. In terms of our original variables, we can write

$$S_{11}(\Delta) = \frac{1}{1+\xi} - \frac{\xi}{1+\xi}\exp\left[-2i\arctan\left(\frac{2\Delta}{\kappa_{\text{tot}}}\right)\right] \tag{2.138}$$

which makes clear that the center and radius of this circular trajectory depend only on the coupling ratio ξ, whereas the rate at which the trajectory is traversed depends on the total damping rate κ_{tot}. It is important to note that the magnitude $|S_{11}|$ is

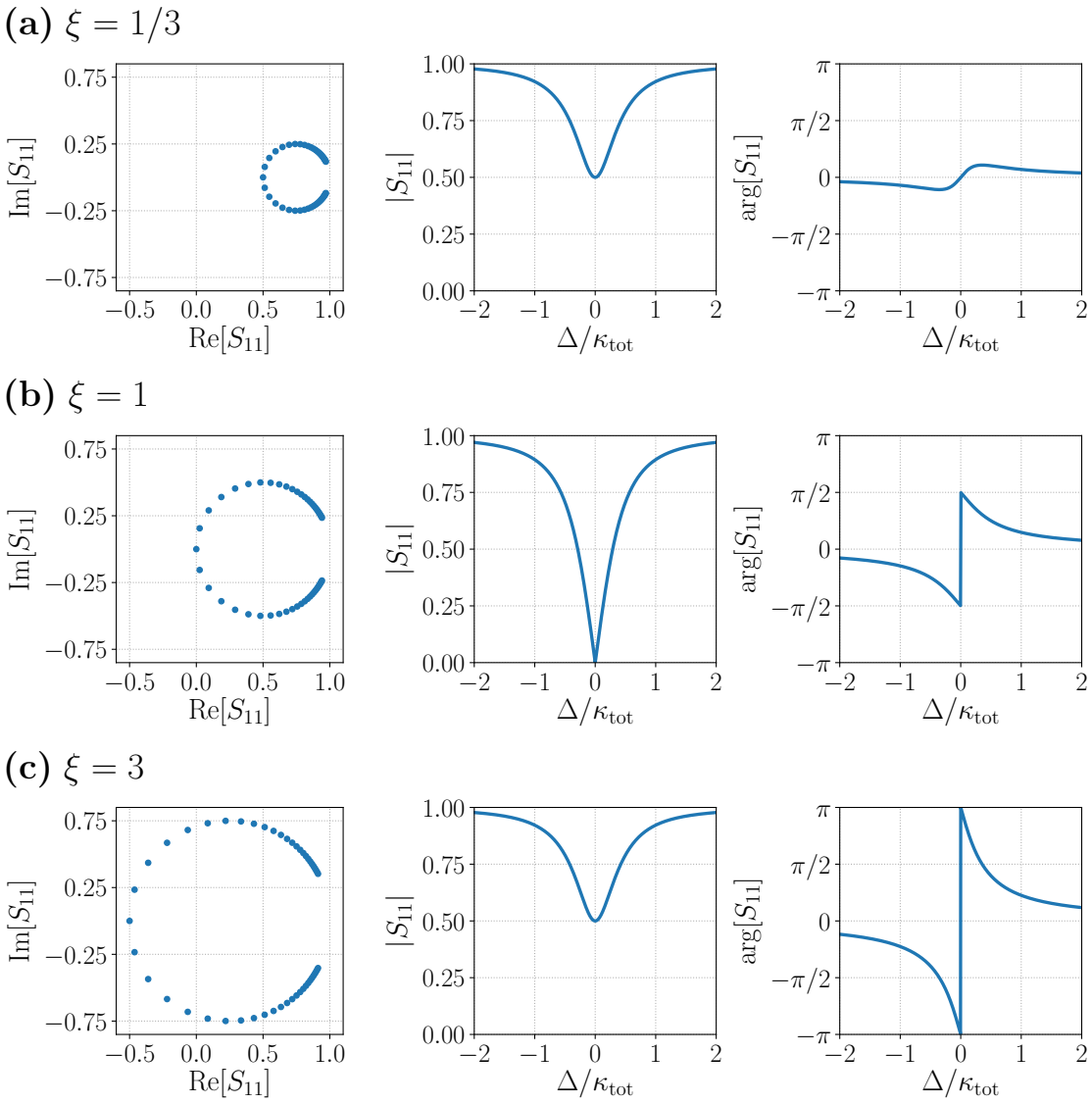

Figure 2.5: Visualization of the linear reflection coefficient, Eq. (2.134), in (a) the under-coupled regime with $\xi = 1/3$, (b) the critically-coupled regime with $\xi = 1$, and (c) the over-coupled regime with $\xi = 3$. The circular path traced out in the complex plane (as a function of detuning) is plotted point by point to visualize the rate at which the path is traversed for a set of linearly-spaced frequencies.

insufficient to determine the internal and external damping rates independently, since it is invariant under $\xi \to 1/\xi$, as can be seen in Fig. 2.5. To extract both damping rates κ_{int} and κ_{ext} it is therefore crucial to use both magnitude and phase data for the reflection coefficient, which is most easily accomplished by treating S_{11} as a trajectory in the complex plane.

Experimental Example. To illustrate the utility of the reflection coefficient for characterizing microwave cavities, it is useful to take a look at some experimental data. Fig. 2.6 shows a measurement of $S_{11}(\Delta)$ for a $\lambda/4$ microwave cavity. By fitting to Eq. (2.134) we are able to determine the resonant frequency ω_0 as well as the damping rates κ_{int} and κ_{ext}. This measurement requires careful calibration of the microwave network used to measure the cavity; we discuss this methodology in detail in Section 5.2 and make use of it extensively in Chapter 6.

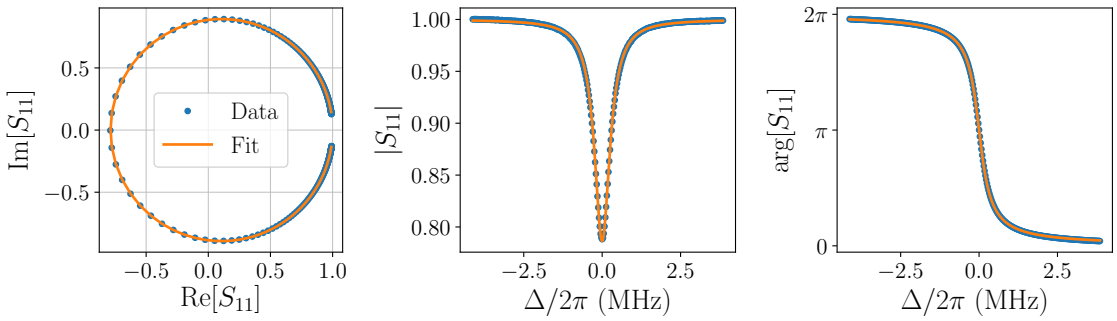

$\omega_0/2\pi$	$\kappa_{\text{int}}/2\pi$	$\kappa_{\text{ext}}/2\pi$	$\kappa_{\text{tot}}/2\pi$
6.01 GHz	68 kHz	565 kHz	633 kHz

Figure 2.6: Measured $S_{11}(\Delta)$ for a $\lambda/4$ cavity and best fit to Eq. (2.134). Best fit parameters are in the table above.

2.3.4 Ringdown Dynamics

We next analyze the transient dynamics of the cavity as it rings down. In this situation, the cavity is first driven to a steady state amplitude, then the drive is abruptly turned off at $t = 0$. As we will see, measuring the rate of decay allows us to determine the total damping rate of the cavity κ_{tot}.

We approach this problem semiclassically by solving for the ensemble-averaged cavity response. To find the steady state amplitude at $t < 0$, we start by taking the

expectation value of the quantum Langevin equation

$$\dot{\alpha}(t) = -i\omega_0\alpha(t) - \frac{\kappa_{\text{tot}}}{2}\alpha(t) + \sqrt{\kappa_{\text{ext}}}\alpha_{\text{in}}(t) \tag{2.139}$$

where $\alpha(t) = \langle a(t)\rangle$ and $\alpha_{\text{in}}(t) = \langle a_{\text{in}}(t)\rangle$. Assuming a sinusoidal input drive $\alpha_{\text{in}}(t) = \alpha_{\text{in}}e^{-i\omega t}$, we plug in the ansatz $\alpha(t) = \alpha e^{-i\omega t}$ for the steady-state cavity response and obtain the solution

$$\alpha(t<0) = \frac{\sqrt{\kappa_{\text{ext}}}}{-i\Delta + \kappa_{\text{tot}}/2}\alpha_{\text{in}}e^{-i\omega t}, \tag{2.140}$$

for the steady-state intracavity field for $t < 0$. At $t = 0$ the input drive is turned off, such that the average cavity field evolves according to the equation

$$\dot{\alpha}(t) = -i\omega_0\alpha(t) - \frac{\kappa_{\text{tot}}}{2}\alpha(t) \tag{2.141}$$

for $t > 0$. The solution to this differential equation is a simple exponential decay, given by

$$\alpha(t>0) = \frac{\sqrt{\kappa_{\text{ext}}}}{-i\Delta + \kappa_{\text{tot}}/2}\alpha_{\text{in}}e^{-i\omega_0 t}e^{-\kappa_{\text{tot}}t/2}, \tag{2.142}$$

where $\alpha(0)$ is determined by our steady-state solution for $\alpha(t < 0)$.

We've now solved for the intracavity field at all times t, but what we're actually interested in is the output field since this is what we can measure directly. Plugging our results into the input-output relationship $\alpha_{\text{out}}(t) - \alpha_{\text{in}}(t) = -\sqrt{\kappa_{\text{ext}}}\alpha(t)$, the amplitude of the average output field takes the form

$$|\alpha_{\text{out}}(t)| = \begin{cases} \left[1 - \dfrac{\kappa_{\text{int}}\kappa_{\text{ext}}}{\Delta^2 + \kappa_{\text{tot}}^2/4}\right]^{1/2} |\alpha_{\text{in}}| & t < 0 \\ \dfrac{\kappa_{\text{ext}}}{\sqrt{\Delta^2 + \kappa_{\text{tot}}^2/4}}|\alpha_{\text{in}}|e^{-\kappa_{\text{tot}}t/2} & t \geq 0 \end{cases} \tag{2.143}$$

which inherits a discontinuity from the input drive when it is turned off at $t = 0$. By measuring the decay of the output field we can determine the total damping rate κ_{tot}.

Experimental Example. An example of a ringdown measurement is shown in Fig. 2.7. This measurement was performed on the same cavity as the reflection coefficient measurement in Fig. 2.6, and we obtain consistent values for κ_{tot} with these two measurements. Furthermore, we see the discontinuous jump in the cavity amplitude when the drive is turned off (though this sharp feature is blurred due to the bandwidth

of our measurement). We discuss this measurement scheme in detail in Section 5.4 and make use of it in Section 6.6.2.

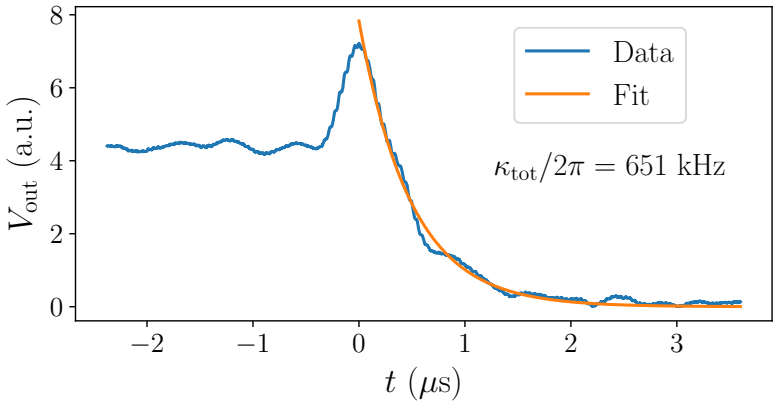

Figure 2.7: Ringdown measurement with a $\lambda/4$ cavity.

Section 2.4

Frequency-modulated Cavity

We next consider the dynamics of a driven two-sided cavity whose resonant frequency is modulated sinusoidally. This analysis serves as a model for an important measurement scheme we will later use to determine both the dispersive charge sensitivity of the cCPT and the power spectra of charge and flux noise that couple to the cCPT's resonant frequency. The idea behind the measurement scheme is straightforward: when driven near resonance, any changes in the resonant frequency of the cavity are encoded as changes in the phase of the reflected signal. If the resonant frequency is modulated sinusoidally then the reflected signal becomes phase-modulated, as we will show. One consequence of this phase modulation is the generation of output power at sideband frequencies, which can easily be measured in the lab. This measurement scheme is discussed in detail in Section 5.3 and implemented experimentally in Section 6.4.

The quantum Langevin equation for the two-sided, frequency-modulated cavity

$$\dot{a} = -i\omega_0(t)a - \frac{\kappa_{\mathrm{tot}}}{2}a + \sqrt{\kappa_{\mathrm{ext}}}a_{\mathrm{in}} + \sqrt{\kappa_{\mathrm{int}}}b_{\mathrm{in}} \tag{2.144}$$

where we assume the resonant frequency is modulated sinusoidally such that

$$\omega_0(t) = \omega_0 + \Omega\cos(\omega_m t). \tag{2.145}$$

We treat the system semiclassically by taking the expectation value of this equation of motion and assuming a sinusoidal drive $\langle a_{\text{in}}(t)\rangle = \alpha_{\text{in}} e^{-i\omega t}$, such that

$$\dot{\alpha} = \left[-i\omega_0 - i\Omega\cos(\omega_m t) - \frac{\kappa_{\text{tot}}}{2}\right]\alpha + \sqrt{\kappa_{\text{ext}}}\alpha_{\text{in}} e^{-i\omega t}. \tag{2.146}$$

We now make an ansatz of the form

$$\alpha(t) = A(t)\exp\left[-i\omega_0 t - i\frac{\Omega}{\omega_m}\sin(\omega_m t) - \frac{\kappa_{\text{tot}}}{2}t\right] \tag{2.147}$$

and find the equation of motion for the amplitude $A(t)$

$$\dot{A} = \sqrt{\kappa_{\text{ext}}}\alpha_{\text{in}}\exp\left[-i\Delta t + i\frac{\Omega}{\omega_m}\sin(\omega_m t) + \frac{\kappa_{\text{tot}}}{2}t\right]. \tag{2.148}$$

where we have introduced the detuning $\Delta = \omega - \omega_0$.

To solve this differential equation we use the Jacobi-Anger expansion

$$e^{iz\sin(x)} = \sum_{n=-\infty}^{\infty} J_n(z)e^{inx} \tag{2.149}$$

where J_n is the nth Bessel function of the first kind. Plugging this identity into our differential equation, we find

$$\dot{A} = \sqrt{\kappa_{\text{ext}}}\alpha_{\text{in}}\sum_{n=-\infty}^{\infty} J_n\left(\frac{\Omega}{\omega_m}\right)\exp\left[-i(\Delta - n\omega_m)t + \kappa_{\text{tot}}t/2\right]. \tag{2.150}$$

This equation can be integrated directly, yielding the solution

$$A(t) = \sqrt{\kappa_{\text{ext}}}\alpha_{\text{in}}\sum_{n=-\infty}^{\infty} J_n\left(\frac{\Omega}{\omega_m}\right)\frac{\exp\left[-i(\Delta - n\omega_m)t + \kappa_{\text{tot}}t/2\right]}{-i(\Delta - n\omega_m) + \kappa_{\text{tot}}/2} \tag{2.151}$$

where we have dropped the constant $A(0)$ since we are interested in the steady state, rather than the transient response. Plugging back into our ansatz, we arrive at the

general solution for the expectation value of the intracavity field

$$\alpha(t) = \sqrt{\kappa_{\text{ext}}}\alpha_{\text{in}} \sum_{n=-\infty}^{\infty} J_n\left(\frac{\Omega}{\omega_m}\right) \frac{\exp\left[-i(\omega - n\omega_m)t - i(\Omega/\omega_m)\sin(\omega_m t)\right]}{-i(\Delta - n\omega_m) + \kappa_{\text{tot}}/2}. \quad (2.152)$$

To make use of this solution it is convenient to simplify it further. First we apply the Jacobi-Anger expansion again to find

$$\alpha(t) = \sqrt{\kappa_{\text{ext}}}\alpha_{\text{in}} \sum_{n=-\infty}^{\infty} J_n\left(\frac{\Omega}{\omega_m}\right) \frac{\exp\left[-i(\omega - n\omega_m)t\right]}{-i(\Delta - n\omega_m) + \kappa_{\text{tot}}/2} \sum_{k=-\infty}^{\infty} J_k\left(\frac{\Omega}{\omega_m}\right) \exp\left[-ik\omega_m t\right]. \quad (2.153)$$

Next we assume the amplitude of the frequency modulation is small, such that $\Omega/\omega_m \ll 1$, and expand to linear order in this small parameter yielding

$$\alpha(t) = \sqrt{\kappa_{\text{ext}}}\alpha_{\text{in}} \Bigg\{ \frac{\exp\left[-i\omega t\right]}{-i\Delta + \kappa_{\text{tot}}/2} + \frac{\Omega}{2} \frac{\exp\left[-i(\omega + \omega_m)t\right]}{\left[-i\Delta + \kappa_{\text{tot}}/2\right]\left[-i\left(\Delta + \omega_m\right) + \kappa_{\text{tot}}/2\right]} + \frac{\Omega}{2} \frac{\exp\left[-i(\omega - \omega_m)t\right]}{\left[-i\Delta + \kappa_{\text{tot}}/2\right]\left[-i\left(\Delta - \omega_m\right) + \kappa_{\text{tot}}/2\right]} \Bigg\}. \quad (2.154)$$

From this expression we see that the cavity primarily responds at the drive frequency ω and the sideband frequencies $\omega \pm \omega_m$.

2.4.1 Output Power Spectrum

We next simplify this expression by evaluating at $\Delta = 0$ (where the response is maximized) and expanding to linear order in Ω/ω_m (which we assume to be much less than one for a weak frequency modulation amplitude), yielding the expression

$$\alpha(t) = \sqrt{\kappa_{\text{ext}}}\alpha_{\text{in}} \left[\frac{2}{\kappa_{\text{tot}}} e^{-i\omega_0 t} - \frac{i\Omega e^{-i(\omega_0 + \omega_m)t}}{\kappa_{\text{tot}}(-i\omega_m + \kappa_{\text{tot}}/2)} - \frac{i\Omega e^{-i(\omega_0 - \omega_m)t}}{\kappa_{\text{tot}}(i\omega_m + \kappa_{\text{tot}}/2)} \right]. \quad (2.155)$$

Finally, we solve for the output field

$$\alpha_{\text{out}} = \alpha_{\text{in}} \left[\left(1 - 2\frac{\kappa_{\text{ext}}}{\kappa_{\text{tot}}}\right) e^{-i\omega_0 t} + \frac{i\kappa_{\text{ext}}\Omega e^{-i(\omega_0 + \omega_m)t}}{\kappa_{\text{tot}}(-i\omega_m + \kappa_{\text{tot}}/2)} + \frac{i\kappa_{\text{ext}}\Omega e^{-i(\omega_0 - \omega_m)t}}{\kappa_{\text{tot}}(i\omega_m + \kappa_{\text{tot}}/2)} \right] \quad (2.156)$$

using the input-output relation $a_{\text{out}} = a_{\text{in}} - \sqrt{\kappa_{\text{ext}}}a$.

Since the ingoing and outgoing voltages are proportional to a_{in} and a_{out}, the

amplitude of the outgoing voltage at each of the sidebands is given by

$$V_{\text{out}}(\omega_0 \pm \omega_m) = \frac{\kappa_{\text{ext}}\Omega}{\kappa_{\text{tot}}\sqrt{\omega_m^2 + \kappa_{\text{tot}}^2/4}} V_{\text{in}} \tag{2.157}$$

such that we can simply read off the power at the sidebands

$$P_{\text{out}}(\omega_0 \pm \omega_m) = \frac{\kappa_{\text{ext}}^2\Omega^2}{\kappa_{\text{tot}}^2(\omega_m^2 + \kappa_{\text{tot}}^2/4)} P_{\text{in}}. \tag{2.158}$$

If the frequency modulation is instead a noisy signal with power spectral density $S_{\Omega\Omega}(\omega)$ rather than a pure tone, the output power spectral density S_{out} will take the form

$$S_{\text{out}}(\omega_0 \pm \omega) = \frac{2\kappa_{\text{ext}}^2}{\kappa_{\text{tot}}^2(\omega^2 + \kappa_{\text{tot}}^2/4)} P_{\text{in}} S_{\Omega\Omega}(\omega) \tag{2.159}$$

where we have picked up an extra factor of two since the power spectral density is defined in terms of RMS modulation amplitude per unit bandwidth. Thus, if we drive the cavity at its resonant frequency we can extract the power spectral density of frequency noise $S_{\Omega\Omega}(\omega)$ by measuring the output power spectral density $S_{\text{out}}(\omega_0 \pm \omega)$ at the corresponding sideband frequencies.

Experimental Example. Examples of two measurements that rely on this theory are shown in Figure 2.8. First, a measurement of the frequency noise spectrum is shown in Fig. 2.8(a). By driving the cavity on resonance and measuring the output noise near the reflected drive, the power spectral density $S_{\Omega\Omega}(\omega)$ of frequency noise can be determined from the output power in excess of the noise floor using Eq. (2.159). This measurement is important for determining the power spectra of charge and flux noise coupling to the resonant frequency of the cCPT. We discuss this measurement methodology in greater detail in Section 5.3.

Second, a measurement of a frequency-modulated cavity is shown in Fig. 2.8(b). By measuring the output power at the sideband frequencies $\omega_0 \pm \omega_m$ we can determine the amplitude Ω of the sinusoidal frequency modulation using Eq. (2.158). This measurement is important for determining the charge sensitivity of the cCPT, which we discuss in detail in Chapter 7.

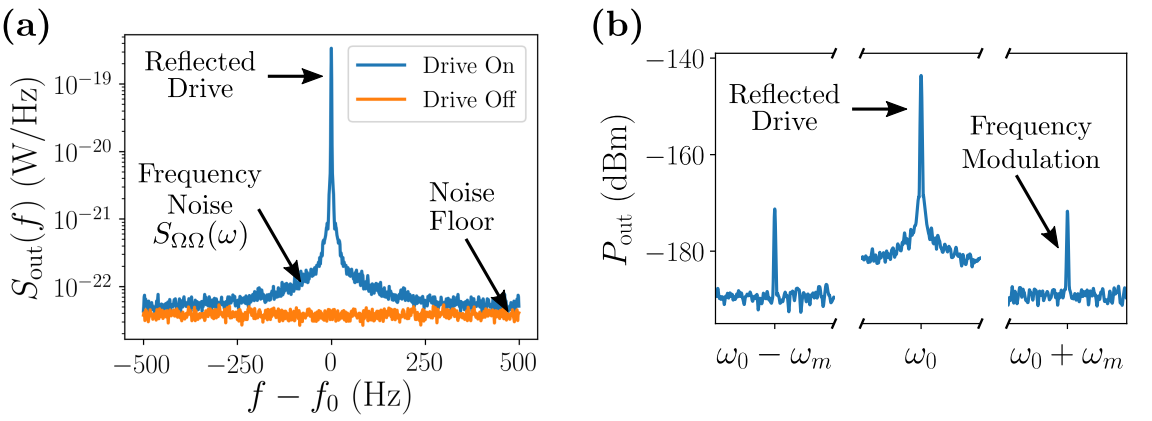

Figure 2.8: Anatomy of (a) frequency noise and (b) frequency modulation measurements.

Section 2.5

Kerr Cavity

We next consider the dynamics of a cavity with a Kerr nonlinearity. As we will see in Chapter 4, this is a good model for the cCPT. In addition, the power-dependent frequency shift induced by the Kerr nonlinearity provides a means for us to calibrate in-situ the power reaching the cCPT.

We begin from the Hamiltonian for a cavity with a Kerr nonlinearity K

$$H = \hbar\omega_0 a^\dagger a + \frac{1}{2}\hbar K a^{\dagger 2} a^2, \tag{2.160}$$

which yields the nonlinear quantum Langevin equation

$$\dot{a}(t) = -i\left[\omega_0 + K a^\dagger(t) a(t)\right] a(t) - \frac{\kappa_{\text{tot}}}{2} a(t) + \sqrt{\kappa_{\text{ext}}}\, a_{\text{in}}(t) + \sqrt{\kappa_{\text{int}}}\, b_{\text{in}}(t). \tag{2.161}$$

Taking the expectation value of this equation, we arrive at

$$\left[i\left(\omega_0 - \omega + K|\alpha|^2\right) + \frac{\kappa_{\text{tot}}}{2}\right] \alpha = \sqrt{\kappa_{\text{ext}}}\, \alpha_{\text{in}} \tag{2.162}$$

which is a nonlinear equation for the magnitude and phase of the intracavity field as a function of the input amplitude and detuning. We proceed to solve this equation for the magnitude and phase separately by first multiplying each side by its complex

conjugate to obtain

$$K^2 n^3 - 2\Delta K n^2 + \left[\Delta^2 + \frac{\kappa_{\text{tot}}^2}{4}\right] n - \kappa_{\text{ext}} \frac{P_{\text{in}}}{\hbar\omega_0} = 0 \tag{2.163}$$

where $n = |\alpha|^2$ is the average number of intra-cavity photons, $P_{\text{in}} = \hbar\omega|\alpha_{\text{in}}|^2$ is the power at the input port of the cavity, and we've used $1/\omega \approx 1/\omega_0$ since $\Delta \ll \omega_0$. If this equation has only one real solution then it is stable and the unique physical solution, whereas if there are three real solutions then one solution will be unstable and there will be bistability in the intracavity amplitude response as a function of detuning [60]. Once a solution for the magnitude of the intracavity amplitude is found, then we can plug back into Eq. (2.162) to find a unique solution for the cavity phase

$$\arg(\alpha) = \arg(\alpha_{\text{in}}) - \arctan\left(\frac{\Delta - Kn}{\kappa_{\text{tot}}/2}\right). \tag{2.164}$$

For the measurements we aim to model (those made with a network analyzer), we are most interested in how the cavity response depends on the input power P_{in} and detuning Δ. For this analysis we therefore consider ω_0, κ_{int}, κ_{ext}, and K to be fixed.

Bifurcation Point. We first analyze the dependence of the cavity response on the input power. In particular, we are interested in the bifurcation point of the Kerr cavity, which occurs at the minimum power such that the response becomes bistable (that is, when there are two stable solutions n for a single value of the detuning Δ). A key feature of this bifurcation is that the response curve $n(\Delta)$ becomes vertical, or equivalently that the derivative of the detuning Δ with respect to the response n becomes zero [61]. We can find this condition by differentiating Eq. (2.163) with respect to n and evaluating at the point n_c where $d\Delta/dn = 0$. This yields the equation

$$3K^2 n_c^2 - 4K\Delta n_c + \Delta^2 + \frac{\kappa_{\text{tot}}^2}{4} = 0, \tag{2.165}$$

which has solutions

$$n_c^{\pm} = \frac{2\Delta}{3K}\left(1 \pm \frac{1}{2}\sqrt{1 - \frac{3\kappa_{\text{tot}}^2}{4\Delta^2}}\right). \tag{2.166}$$

The point at which this solution becomes real defines the onset of bistability and the condition for this is $|\Delta| = \sqrt{3}\kappa_{\text{tot}}/2$, yielding the critical values

$$\begin{aligned} \Delta_c &= \text{sign}(K)\frac{\sqrt{3}}{2}\kappa_{\text{tot}}, \\ n_c &= \frac{\sqrt{3}}{3}\frac{\kappa_{\text{tot}}}{|K|}, \end{aligned} \tag{2.167}$$

where Δ and K must have consistent signs such that n_c remains positive. We further require that this critical response n_c satisfy Eq. (2.163), so we plug back in to find the critical input power

$$P_c = \frac{\sqrt{3}}{9}\frac{\kappa_{\text{tot}}}{|K|}\frac{\kappa_{\text{tot}}}{\kappa_{\text{ext}}}\hbar\omega_0\kappa_{\text{tot}}. \tag{2.168}$$

Thus, a bifurcation occurs when the Kerr cavity is driven with power P_c at the detuning Δ_c, such that for input powers greater than P_c there is a range of detunings Δ where the response $n(\Delta)$ is bistable.

Response Curves. We next analyze the response as a function of detuning, $n(\Delta)$. To do so, it is convenient to rewrite Eq. (2.163) in nondimensional form

$$N^3 - 2\delta N^2 + \left(\delta^2 + \frac{1}{4}\right)N - \frac{\sqrt{3}}{9}\rho_{\text{in}} = 0 \tag{2.169}$$

where the nondimensional response N, detuning δ, and input power ρ_{in} are given by

$$\begin{aligned} N &= |K|n/\kappa_{\text{tot}}, \\ \delta &= (\Delta/\kappa_{\text{tot}})\text{sign}(K), \\ \rho_{\text{in}} &= P_{\text{in}}/P_c. \end{aligned} \tag{2.170}$$

The simulated curve $N(\delta)$ is shown in Figure 2.9. At the bifurcation point $\rho_{\text{in}} = 1$ the response $N(\delta)$ becomes vertical.

2.5.1 Nonlinear Reflection Coefficient

With our solution for $n(\Delta)$ we can plug back into our input-output relationship to find the nonlinear reflection coefficient

$$S_{11}(\omega) = \left(\frac{\alpha_{\text{out}}}{\alpha_{\text{in}}}\right)^* = \frac{i\left[\Delta - Kn(\Delta)\right] + (\kappa_{\text{int}} - \kappa_{\text{ext}})/2}{i\left[\Delta - Kn(\Delta)\right] + \kappa_{\text{tot}}/2}. \tag{2.171}$$

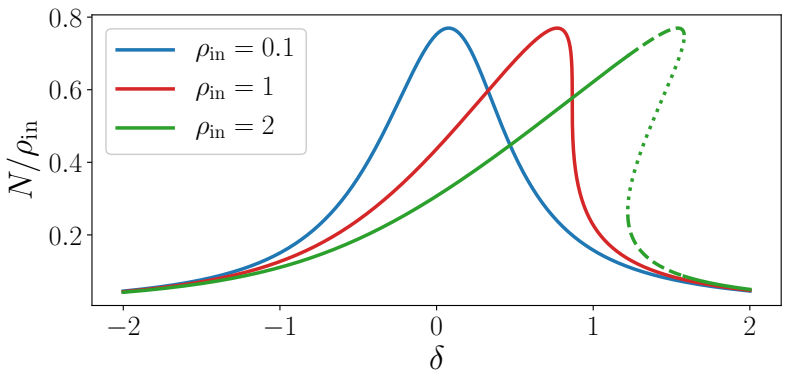

Figure 2.9: Number of photons in the Kerr cavity as a function of detuning at different input powers. Solid lines indicate monostable solutions, dashed lines indicate bistable solutions, and dotted lines indicate unstable solutions.

Using the same line of reasoning as in section 2.3.3, we can express S_{11} as

$$S_{11}(\omega) = \frac{\kappa_{\text{int}}}{\kappa_{\text{tot}}} - \frac{\kappa_{\text{ext}}}{\kappa_{\text{tot}}} \exp\left[-2i \arctan\left(\frac{\Delta - Kn(\Delta)}{\kappa_{\text{tot}}/2}\right)\right] \tag{2.172}$$

so the trajectory of the non-linear reflection coefficient is circular, just as in the linear case. The only difference is the rate at which that trajectory is traversed, as shown in Figure 2.10.

2.5.2 Kerr Shift

By slightly rewriting the Kerr Hamiltonian (2.160),

$$H = \hbar\left(\omega_0 - \frac{K}{2} + \frac{K}{2}a^\dagger a\right) a^\dagger a \tag{2.173}$$

it is clear that the nonlinear term can be interpreted as a frequency shift proportional to the number of photons in the cavity. Another way of seeing this is by noting that the minimum magnitude achieved by the nonlinear reflection coefficient (2.171) occurs at detuning $\Delta_* = Kn(\Delta_*)$ proportional to the average number of photons in the cavity. This condition for the minimum reflection is equivalent to the condition for maximum response n_*, which can be obtained by taking a derivative of Eq. (2.163) with respect to detuning Δ and setting $dn/d\Delta = 0$ at Δ_*. Doing so, we find

$$\Delta_* = Kn(\Delta_*) \tag{2.174}$$

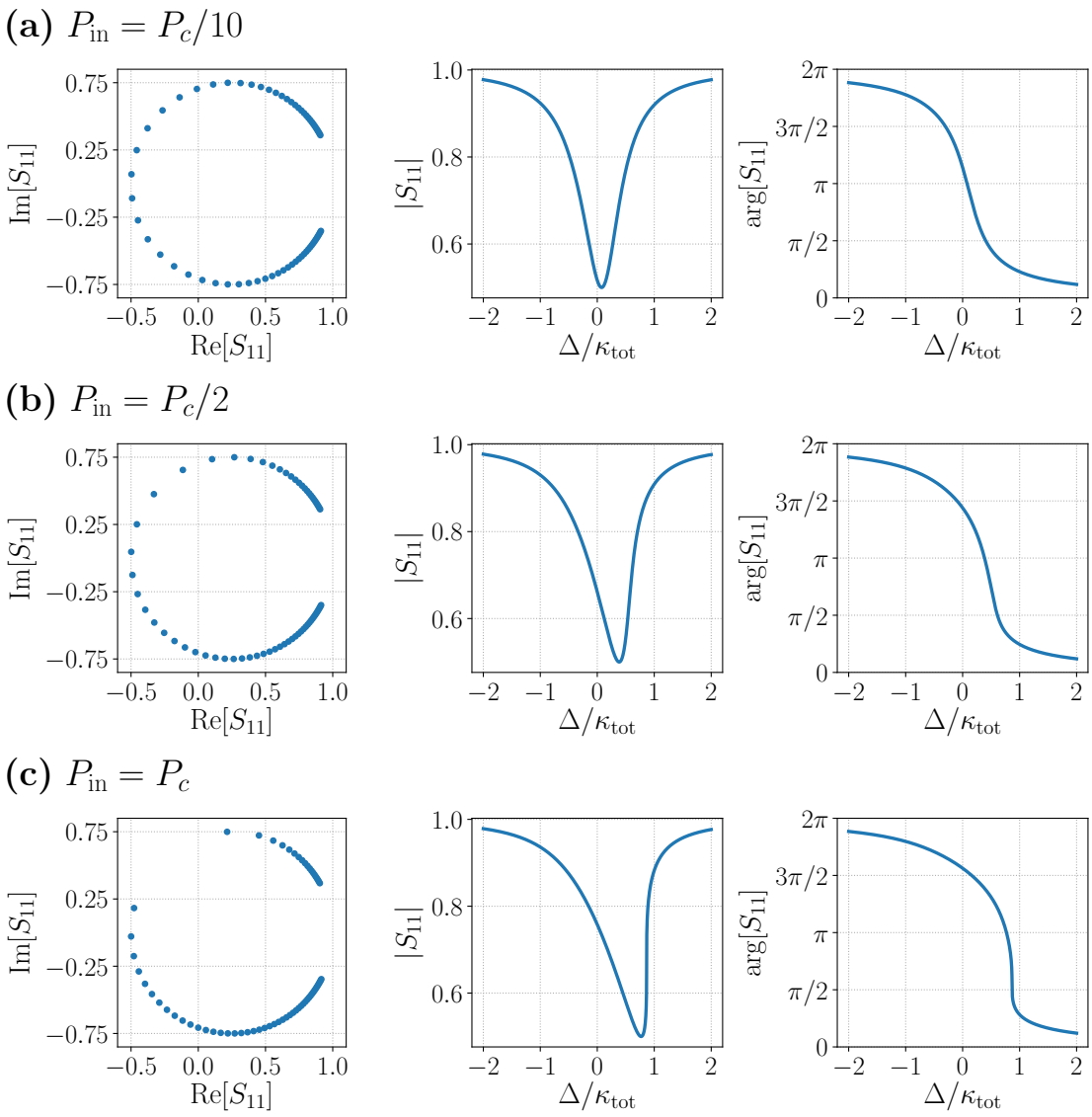

Figure 2.10: Visualization of the nonlinear reflection coefficient (2.171) below the threshold of bistability, with $\kappa_{\text{ext}}/\kappa_{\text{int}} = 3$ and $K > 0$, for three different input powers: (a)$P_{\text{in}} = P_c/10$, (b)$P_{\text{in}} = P_c/2$, and (c)$P_{\text{in}} = P_c$. The circular path traced out in the complex plane as a function of detuning is plotted point by point, for a set of linearly-spaced frequencies, to visualize the rate at which the path is traversed.

in line with our expectations. As this detuning corresponds to both maximum response and absorption it can be viewed as a shift in the effective resonant frequency of the oscillator. What we are primarily interested in, however, is how this frequency depends on the input power P_{in}. Plugging $n = \Delta_*/K$ back into Eq. (2.163), we find

$$\Delta_* = 4K\frac{\kappa_{\text{ext}}}{\kappa_{\text{tot}}}\frac{P_{\text{in}}}{\hbar\omega_0\kappa_{\text{tot}}} \tag{2.175}$$

so the shifted frequency $\omega_* = \omega_0 + \Delta_*$ is proportional to the input power as well, which can be seen in Figure 2.10. It is important to note that this analysis is only precise below the bifurcation point, such that $n(\Delta)$ is single-valued and varies smoothly.

Experimental Example. An example of a measurement utilizing the Kerr shift is shown in Figure 2.11. Here we measure the magnitude of the reflection coefficient S_{11} near resonance using a vector network analyzer (VNA), for a linearly-spaced set of powers P_{VNA}. The VNA traces for each value of P_{VNA} are shown in Fig. 2.11(a). From these traces we determine the shifted resonant frequency ω_* as a function of P_{VNA}, which we plot in Fig. 2.11(b). By fitting a line to this data we can determine the amount of power P_{in} reaching the sample relative to the power supplied by the VNA. Calibrating the power at the plane of the sample enables us to determine the gain and noise of our amplifier chain, which are important for comparing a variety of experimental results with theory. We discuss this methodology in detail in Section 6.5.

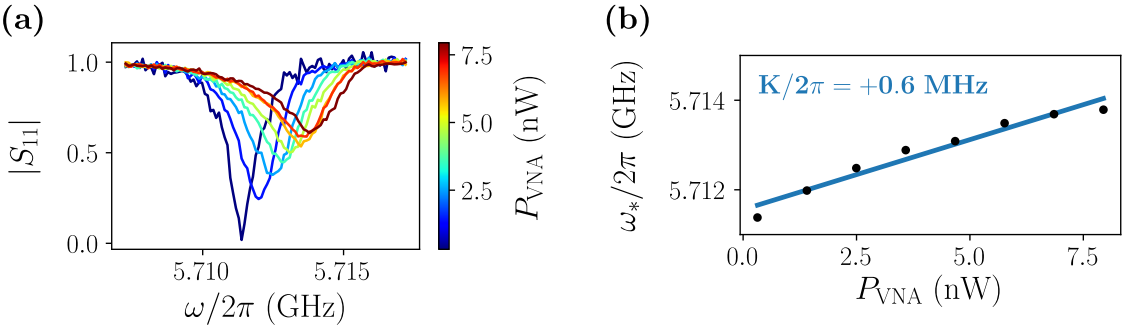

Figure 2.11: Example of a measurement utilizing the Kerr shift. (a) VNA trace of $|S_{11}|$ near resonance as a function of P_{VNA}. (b) The Kerr-shifted resonant frequency ω_* as a function of P_{VNA}, extracted from the traces in (a).

Chapter 3

Josephson Junctions

In this chapter we discuss the second key building block of the cCPT: the Josephson junction (JJ). We first derive the Hamiltonian of a lumped-element JJ and discuss how it behaves as a nonlinear inductance. We next analyze the Hamiltonian and energy levels of the Cooper pair transistor (CPT), which is formed by two JJs in series, and discuss how it behaves as a *tunable* nonlinear inductance. This analysis is crucial to understanding the Hamiltonian of the cCPT.

For further reading on JJs, we recommend the text by Orlando and Delin [62] for an introductory treatment, and the text by Tinkham [63] for a more advanced treatment. For further reading on the CPT, we recommend the theses of Cottet [64] and Joyez [65].

Section 3.1
Lumped Element Josephson Junction

The dynamics of the lumped element Josephson junction, depicted schematically in Fig. 3.1, are governed by the Josephson relations [62]

$$I = I_c \sin(\varphi) \tag{3.1}$$

$$V = \frac{\Phi_0}{2\pi}\frac{\partial \varphi}{\partial t} \tag{3.2}$$

where I_c is the critical current of the junction, φ is the gauge-invariant phase difference across the junction, and $\Phi_0 = h/2e$ is the magnetic flux quantum. Before proceeding, it is worth noting that if we again define an effective flux coordinate as in Chapter 2

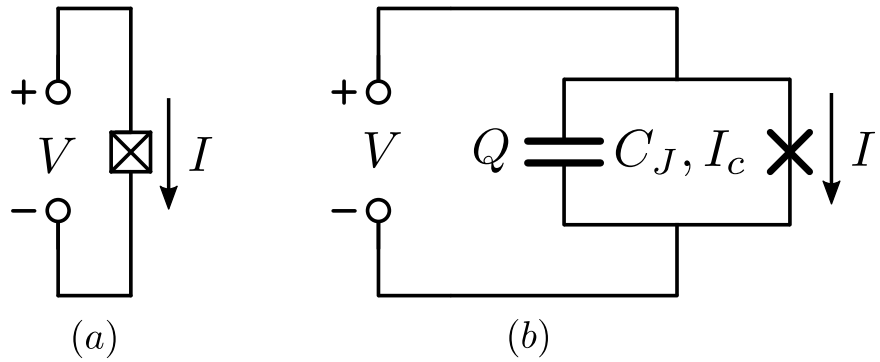

Figure 3.1: Schematics of a lumped-element Josephson junction showing (a) the voltage and current conventions and (b) the equivalent description of the junction as a parallel combination of capacitance C_J and a tunnel junction with critical current I_c.

according to

$$\Phi(t) \equiv \int_{-\infty}^{t} V(t')dt' \tag{3.3}$$

we find in this case

$$\Phi_J(t) = \frac{\Phi_0}{2\pi}\varphi(t) \tag{3.4}$$

such that it is simply the gauge invariant phase across the JJ multiplied by the reduced flux quantum $\Phi_0/2\pi$, and therefore has dimensions of magnetic flux. Thus, writing our equations of motion in terms of these flux coordinates is a natural way of putting JJ's on the same footing as other circuit elements.

We now apply Kirchhoff's laws to this system, yielding the equations

$$V = \frac{Q}{C_J} = \frac{\Phi_0}{2\pi}\frac{\partial\varphi}{\partial t} \tag{3.5}$$

$$I = -\dot{Q} = I_c \sin(\varphi) \tag{3.6}$$

where the sign convention for the current enforces the fact that tunneling is the mechanism by which the effective capacitor discharges. These can be combined into a single equation of motion

$$C_J\frac{\Phi_0}{2\pi}\ddot{\varphi} + I_c\sin(\varphi) = 0 \tag{3.7}$$

equivalent to that of a pendulum. Written in terms of the dimensionful flux coordinate

Φ_J, this equation of motion reads

$$C_J\ddot{\Phi}_J + I_c \sin\left(\frac{2\pi\Phi_J}{\Phi_0}\right) = 0 \tag{3.8}$$

which derives from the Lagrangian

$$\mathscr{L}(\Phi_J, \dot{\Phi}_J) = \frac{1}{2}C_J\dot{\Phi}_J^2 + E_J \cos\left(\frac{2\pi\Phi_J}{\Phi_0}\right) \tag{3.9}$$

where we've defined the Josephson energy E_J according to

$$E_J = \frac{I_c\Phi_0}{2\pi}. \tag{3.10}$$

The momentum conjugate to the effective flux coordinate Φ_J is therefore

$$\frac{\partial\mathscr{L}}{\partial\dot{\Phi}_J} = C_J\dot{\Phi}_J = Q_J \tag{3.11}$$

which we write as the effective charge Q_J. Performing a Legendre transformation, we arrive at the Hamiltonian

$$H(\Phi_J, Q_J) = \frac{\partial\mathscr{L}}{\partial\dot{\Phi}_J}\dot{\Phi}_J - \mathscr{L} = \frac{1}{2C_J}Q_J^2 - E_J\cos\left(\frac{2\pi\Phi_J}{\Phi_0}\right) \tag{3.12}$$

such that the flux and charge obey the canonical commutation relation

$$[\Phi_J, Q_J] = i\hbar. \tag{3.13}$$

Having canonically quantized the system using the dimensionful operators Φ_J and Q_J, it is useful to now return to the dimensionless phase φ and introduce a dimensionless charge N according to

$$N = \frac{Q_J}{2e} \tag{3.14}$$

where e is the elementary charge. In terms of these dimensionless operators, our Hamiltonian takes the form

$$H = 4E_C N^2 - E_J\cos(\varphi) \tag{3.15}$$

where we've defined the charging energy E_C according to

$$E_C = \frac{e^2}{2C_J} \tag{3.16}$$

which is the electrostatic energy associated with charging the capacitor C_J with a single electron. The commutation relation between these new operators is found to be

$$[\varphi, N] = i. \tag{3.17}$$

3.1.1 Hamiltonian in the Phase and Charge Bases

We now seek to express this Hamiltonian in both the phase and charge bases. We are going to be somewhat loose with our notation, since we are assuming the reader is familiar with graduate level quantum mechanics, but we will use hats to represent operators in this section. The phase basis is straightforward, since we have

$$\hat{N} = \frac{-i\hbar}{2e}\frac{\partial}{\partial \Phi_J} = -i\frac{\partial}{\partial \varphi} \tag{3.18}$$

from the canonical commutation relations [66]. As such, the Hamiltonian in the phase basis takes the form

$$\hat{H} = -4E_C\frac{\partial^2}{\partial \varphi^2} - E_J\cos(\hat{\varphi}) \tag{3.19}$$

such that Schrodinger's equation takes the form

$$-4E_C\frac{\partial^2\psi(\varphi)}{\partial \varphi^2} - E_J\cos(\varphi)\psi(\varphi) = E\psi(\varphi). \tag{3.20}$$

We note that this eigenvalue equation can be solved exactly in terms of Mathieu functions [67], but this is primarily useful in the transmon regime for which $E_J \gg E_C$, whereas we are working in the Cooper pair box regime for which $E_C \gtrsim E_J$. Regardless, it is important to be aware of and we discuss it in the next section on the Cooper pair transistor.

To express the Hamiltonian in the charge basis, we need to determine how the operator $\cos(\hat{\varphi})$ acts on the charge basis. To this end, we first note that the eigenkets of the phase operator $\hat{\varphi}$ must be 2π periodic, which can be formally stated as

$$|\varphi\rangle = |\varphi + 2\pi\rangle = e^{-i2\pi\hat{N}}|\varphi\rangle \tag{3.21}$$

where in the last step we've used the fact that $\hat{N}$ is the generator of translations in φ [64]. From this we can infer that the eigenvalues of $\hat{N}$ must be integers. Next, for any function $f(\hat{\Phi}_J)$ we have the commutation relation [66]

$$[\hat{Q}_J, f(\hat{\Phi}_J)] = -i\hbar f'(\hat{\Phi}_J) \tag{3.22}$$

such that

$$[\hat{N}, e^{i\hat{\varphi}}] = e^{i\hat{\varphi}}. \tag{3.23}$$

We apply this commutator to the expression

$$\hat{N}e^{i\hat{\varphi}} |N\rangle = e^{i\hat{\varphi}} \left(\hat{N} + 1\right) |N\rangle \tag{3.24}$$

to find that

$$e^{i\hat{\varphi}} |N\rangle = |N+1\rangle . \tag{3.25}$$

This relationship allows us to express $\cos(\hat{\varphi})$ in the charge basis as

$$\cos(\hat{\varphi}) = \frac{1}{2} \sum_{N\in\mathbb{Z}} \Big(|N+1\rangle\langle N| + |N\rangle\langle N+1| \Big) \tag{3.26}$$

such that the Hamiltonian in the charge basis takes the form

$$\hat{\mathcal{H}} = 4E_C \sum_{N\in\mathbb{Z}} N^2 |N\rangle\langle N| - \frac{E_J}{2} \sum_{N\in\mathbb{Z}} \Big(|N+1\rangle\langle N| + |N\rangle\langle N+1| \Big). \tag{3.27}$$

3.1.2 Josephson Inductance

We may associate an inductance L_J to the JJ according to the relationship $V = L_J \dot{I}$. For the voltage and current given by the Josephson relations, this yields the inductance

$$L_J(\varphi) = \frac{L_J^{(0)}}{\cos(\varphi)} \tag{3.28}$$

where

$$L_J^{(0)} = \frac{\Phi_0}{2\pi I_c} \tag{3.29}$$

is often simply called the Josephson inductance. The effective inductance of this circuit element is nonlinear since it depends on the phase φ, or equivalently the

current I. It can be cast as a function of current explicitly according to

$$L_J(I) = \frac{L_J^{(0)}}{\sqrt{1-(I/I_c)^2}}. \tag{3.30}$$

Similarly, we could have defined the Josephson energy by analogy to the potential energy of an LC circuit

$$U = \frac{\Phi_J^2}{2L_J} = \left(\frac{\Phi_0}{2\pi}\right)^2 \frac{\varphi^2}{2L_J}. \tag{3.31}$$

In this case, the Josephson inductance can be written in the form

$$L_J^{(0)}(\varphi_{\text{eq}}) = \left(\frac{\Phi_0}{2\pi}\right)^2 \left(\frac{\partial^2 U}{\partial \varphi^2}\right)^{-1}\Bigg|_{\varphi=\varphi_{\text{eq}}} \tag{3.32}$$

where we're expanding about the equilibrium position of our effective oscillator, determined by

$$\left.\frac{\partial U}{\partial \varphi}\right|_{\varphi=\varphi_{\text{eq}}} = 0. \tag{3.33}$$

For our Hamiltonian, $\varphi_{\text{eq}} = 0$ and the Josephson inductance is given by

$$L_J^{(0)} = \frac{\Phi_0}{2\pi I_c} \tag{3.34}$$

in agreement with our previous method. We note that with this method the nonlinear contributions to the inductance are obtained by taking higher order derivatives of the effective potential energy with respect to φ.

3.1.3 Josephson Energy

Written in the charge basis, the term in the Hamiltonian corresponding to the Josephson energy

$$H_J = -\frac{E_J}{2}\sum_{N\in\mathbb{Z}}\Big(|N+1\rangle\langle N| + |N\rangle\langle N+1|\Big) \tag{3.35}$$

can be interpreted as the energy associated with tunneling through the junction; it assigns an energy to transitions from a given number N of cooper pairs on the plates of the capacitor C_J to $N \pm 1$. This intuition is reinforced by considering the energy associated with driving a current through a junction according to the I-V

characteristics of the circuit element. From this perspective the energy is simply the power $P = IV$ integrated over time, which can be written

$$E_{\text{Current}}(t) = \int_0^t I(t')V(t')dt'. \tag{3.36}$$

Plugging in the Josephson relations, we find

$$\begin{aligned} E_{\text{Current}}(t) &= \frac{I_c\Phi_0}{2\pi}\int_0^t \sin(\varphi(t'))\frac{\partial\varphi}{\partial t'}dt' \\ &= E_J\int_{\varphi_0}^{\varphi(t)} \sin(\varphi')d\varphi' \\ &= -E_J\Big[\cos(\varphi(t)) - \cos(\varphi_0)\Big] \end{aligned} \tag{3.37}$$

which is the Josephson energy expressed in terms of the phase, up to an overall constant.

Section 3.2

Cooper Pair Transistor

We now consider the Cooper pair transistor, depicted schematically in Fig. 3.2, which consists of two identical JJs separated by a superconducting island to which a gate voltage is applied. Kirchhoff's voltage law for this system yields the equations

$$V_1 - \frac{Q_1}{C_J} = 0 \tag{3.38}$$

$$V_2 - \frac{Q_2}{C_J} = 0 \tag{3.39}$$

$$V_g(t) - \frac{Q_g}{C_g} - \frac{Q_2}{C_J} = 0 \tag{3.40}$$

$$\frac{Q_1}{C_J} + \frac{Q_2}{C_J} - \dot{\Phi}_{\text{ext}}(t) = 0 \tag{3.41}$$

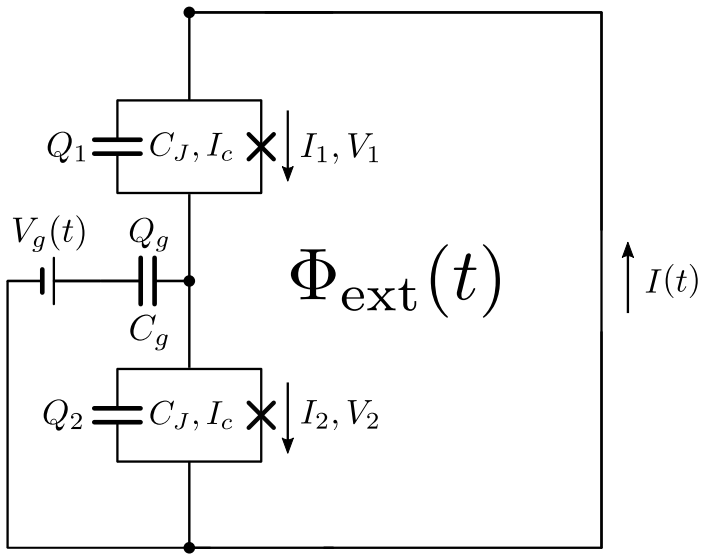

Figure 3.2: Schematic of a Cooper pair transistor, consisting of two identical JJs (each with capacitance C_J and critical current I_c) with a gate voltage V_g applied to the superconducting island between them. They form a closed superconducting loop through which an external flux Φ_{ext} is threaded. In this model the total current $I(t)$ is not controlled externally; it responds to the dynamics of the system.

and Kirchhoff's current law yields the equations

$$\dot{Q}_1 + I_1 + \dot{Q}_g - \dot{Q}_2 - I_2 = 0 \tag{3.42}$$

$$I(t) - \dot{Q}_1 - I_1 = 0. \tag{3.43}$$

We now impose the Josephson relations on the currents through and voltages across each JJ

$$\begin{aligned} I_i &= I_c \sin(\varphi_i) \\ V_i &= \frac{\Phi_0}{2\pi} \frac{\partial \varphi_i}{\partial t} \end{aligned} \tag{3.44}$$

where φ_i is the gauge invariant phase across the i'th JJ and $\Phi_0 = h/2e$ is the magnetic flux quantum. Plugging back in to Eqs. (3.38)-(3.40), we can express the charge

variables in terms of the phases across the JJs according to

$$Q_1 = C_J \frac{\Phi_0}{2\pi} \dot{\varphi}_1 \tag{3.45}$$

$$Q_2 = C_J \frac{\Phi_0}{2\pi} \dot{\varphi}_2 \tag{3.46}$$

$$Q_g = C_g V_g(t) - C_g \frac{\Phi_0}{2\pi} \dot{\varphi}_2. \tag{3.47}$$

Plugging these expressions into Eq. (3.41), we find

$$\frac{\partial}{\partial t} \left[\frac{\Phi_0}{2\pi} (\varphi_1 + \varphi_2) - \Phi_{\text{ext}}(t) \right] = 0 \tag{3.48}$$

which we recognize as the condition that the flux around a closed superconducting loop is constant. Integrating this equation, and absorbing the constant of integration (an integer multiple of Φ_0) into Φ_{ext} as a DC offset, we find

$$\frac{\Phi_0}{2\pi} (\varphi_1 + \varphi_2) = \Phi_{\text{ext}}(t). \tag{3.49}$$

Plugging all these results into Eqs. (3.42) and (3.43), and adding the latter to the former, we find

$$(C_J + C_g) \frac{\Phi_0}{2\pi} \ddot{\varphi}_2 + I_c \sin(\varphi_2) - C_g \dot{V}_g = I(t) \tag{3.50}$$

$$C_J \frac{\Phi_0}{2\pi} \ddot{\varphi}_1 + I_c \sin(\varphi_1) = I(t). \tag{3.51}$$

Using Eq. (3.49) we now introduce the average and relative phase coordinates

$$\overline{\varphi} = \frac{\varphi_1 + \varphi_2}{2} = \frac{\pi}{\Phi_0} \Phi_{\text{ext}} \tag{3.52}$$

$$\delta\varphi = \frac{\varphi_1 - \varphi_2}{2} \tag{3.53}$$

in terms of which Eqs. (3.50) and (3.51) take the form

$$C_J \frac{\Phi_0}{2\pi} \left(\ddot{\overline{\varphi}} - \ddot{\delta\varphi} \right) + I_c \sin(\overline{\varphi} - \delta\varphi) - C_g \dot{V}_g = I(t) \tag{3.54}$$

$$C_J \frac{\Phi_0}{2\pi} \left(\ddot{\overline{\varphi}} + \ddot{\delta\varphi} \right) + I_c \sin(\overline{\varphi} + \delta\varphi) = I(t) \tag{3.55}$$

where we've dropped sub-leading order terms under the assumption that $C_g \ll C_J$.

Taking the sum of and difference between Eqs. (3.54) and (3.55), and dividing the former by two, we find

$$C_J \frac{\Phi_0}{2\pi} \ddot{\overline{\varphi}} + I_c \sin(\overline{\varphi}) \cos(\delta\varphi) - \frac{1}{2} C_g \dot{V}_g = I(t) \tag{3.56}$$

$$C_J \frac{\Phi_0}{\pi} \ddot{\delta\varphi} + 2I_c \cos(\overline{\varphi}) \sin(\delta\varphi) + C_g \dot{V}_g = 0. \tag{3.57}$$

According to Eq. (3.56), the current $I(t)$ responds to our control parameters V_g and Φ_{ext} as well as to the dynamics of $\delta\varphi$. The only undetermined variable in this system is therefore $\delta\varphi$, and its dynamics are governed by the equation of motion Eq. (3.57). As in the previous section, we now introduce the effective flux coordinate

$$\Phi_J = \frac{\Phi_0}{2\pi} \delta\varphi \tag{3.58}$$

such that Eq. (3.57) takes the form

$$2C_J \ddot{\Phi}_J + 2I_c \cos(\overline{\varphi}) \sin\left(\frac{2\pi}{\Phi_0} \Phi_J\right) + C_g \dot{V}_g = 0 \tag{3.59}$$

which derives from the Lagrangian

$$\mathscr{L}(\Phi_J, \dot{\Phi}_J) = C_J \dot{\Phi}_J^2 + C_g V_g \dot{\Phi}_J + 2E_J \cos(\overline{\varphi}) \cos\left(\frac{2\pi}{\Phi_0} \Phi_J\right) \tag{3.60}$$

where we've again introduced

$$E_J = \frac{I_c \Phi_0}{2\pi} \tag{3.61}$$

to be the Josephson energy of a single junction. The conjugate momentum now takes the form of the effective charge variable

$$Q_J = \frac{\partial \mathscr{L}}{\partial \dot{\Phi}_J} = 2C_J \dot{\Phi}_J + C_g V_g. \tag{3.62}$$

Performing a Legendre transformation, we arrive at the Hamiltonian

$$\begin{aligned} H(\Phi_J, Q_J) &= \frac{\partial \mathscr{L}}{\partial \dot{\Phi}_J} \dot{\Phi}_J - \mathscr{L} \\ &= \frac{1}{4C_J} \left(Q_J - C_g V_g\right)^2 - 2E_J \cos(\overline{\varphi}) \cos\left(\frac{2\pi}{\Phi_0} \Phi_J\right) \end{aligned} \tag{3.63}$$

where the operators Φ_J and Q_J obey the canonical commutation relation

$$[\Phi_J, Q_J] = i\hbar. \tag{3.64}$$

We now transform to the dimensionless operators

$$\delta\varphi = \frac{2\pi}{\Phi_0}\Phi_J \tag{3.65}$$

$$N = \frac{1}{2e}Q_J \tag{3.66}$$

$$[\delta\varphi, N] = i \tag{3.67}$$

in terms of which the Hamiltonian can be written

$$H = 4E_C\left(N - \frac{n_g}{2}\right)^2 - 2E_J\cos\left(\frac{\pi}{\Phi_0}\Phi_{\text{ext}}\right)\cos(\delta\varphi) \tag{3.68}$$

where we've defined the charging energy

$$E_C = \frac{e^2}{2C_\Sigma} \approx \frac{e^2}{4C_J} \tag{3.69}$$

in terms of the total capacitance of the island $C_\Sigma = 2C_J + C_g \approx 2C_J$, introduced the dimensionless parameter

$$n_g = \frac{C_g V_g}{e} \tag{3.70}$$

corresponding to the number of electrons gating the island, and substituted $\overline{\varphi} = \pi\Phi_{\text{ext}}/\Phi_0$. Using the results of the previous section, we express this Hamiltonian in the charge basis as

$$\begin{aligned} H \ &= 4E_C\sum_{N\in\mathbb{Z}}\left(N - \frac{n_g}{2}\right)^2 |N\rangle\langle N| \\ &\quad - E_J\cos\left(\frac{\pi}{\Phi_0}\Phi_{\text{ext}}\right)\sum_{N\in\mathbb{Z}}\Big(|N+1\rangle\langle N| + |N\rangle\langle N+1|\Big) \end{aligned} \tag{3.71}$$

which is tunable via both the gate charge n_g and external flux Φ_{ext}.

3.2.1 Energy Levels

We are primarily interested in the lowest few energy levels of this Hamiltonian and their dependence on gate and external flux. In particular, when we later consider

the CPT embedded in a cavity we will see that derivatives of the ground state energy determine the effective dynamics of our cavity modes and excitation of the CPT is something we need to avoid. In this section we therefore discuss several methods of finding the lowest eigenvalues of the CPT Hamiltonian and analyze the properties of the resulting energy bands as a function of gate and flux.

Exact Solution. We first approach the system in the phase basis, which will yield an exact solution for all eigenvalues in terms of Mathieu characteristic numbers. We generally follow Koch's treatment [67], the two differences being our convention for n_g in units of electrons rather than Cooper pairs and our convention for defining the Josephson energy E_J as that of a single junction rather than both. In the phase basis the Hamiltonian is expressed as

$$H = 4E_C \left(i\frac{\partial}{\partial \varphi} + \frac{n_g}{2} \right)^2 - 2E_J \cos\left(\frac{\pi}{\Phi_0} \Phi_{\text{ext}} \right) \cos(\varphi) \tag{3.72}$$

where we've let $\delta\varphi \to \varphi$ for notational convenience, such that Schrodinger's equation takes the form

$$\left[4E_C \left(i\frac{\partial}{\partial \varphi} + \frac{n_g}{2} \right)^2 - 2E_J \cos\left(\frac{\pi}{\Phi_0} \Phi_{\text{ext}} \right) \cos(\varphi) \right] \psi(\varphi) = E\psi(\varphi) \tag{3.73}$$

with boundary condition $\psi(\varphi) = \psi(\varphi + 2\pi)$. We now cast this differential equation in the form of the Mathieu equation by making the substitution

$$\psi(\varphi) = e^{in_g\varphi/2} f\left(\frac{\varphi}{2}\right) \tag{3.74}$$

in terms of which the differential equation takes the form

$$f''(x) + \left(\frac{E}{E_C} + \frac{2E_J \cos(\pi\Phi_{\text{ext}}/\Phi_0)}{E_C} \cos(2x) \right) f(x) = 0. \tag{3.75}$$

where $x = \varphi/2$. The energy eigenvalues of this differential equation take the form

$$E_m(n_g, \varphi_{\text{ext}}) = E_C a_{-n_g + 2k(m,n_g)} \left(\frac{-E_J \cos(\pi\Phi_{\text{ext}}/\Phi_0)}{E_C} \right) \tag{3.76}$$

where $a_\nu(q)$ is Mathieu's characteristic value and $k(m, n_g)$ is an auxiliary function used to properly sort the energy eigenvalues in ascending order. This is given by

$$k(m, n_g) = \sum_{\ell=\pm 1} \Big(\text{int}(n_g + \ell/2) \bmod 2\Big)\Big(\text{int}(n_g/2) + \ell(-1)^m \left[(m+1) \text{ div } 2\right]\Big) \quad (3.77)$$

where int(x) is the integer closest to x and (a div b) is the integer part of the quotient a/b.

We note that our expression for E_m differs slightly from Koch's [67] in the subscript ν of Mathieu's characteristic value, since using Koch's expression as-is ($\nu = n_g + 2k$) yields non-sensical results. We believe ν is meant to be the characteristic exponent derived in the appendix of [67] to be $\nu = -n_g + 2k$, which comes from the periodic boundary condition on $\psi(\varphi)$, and this is also the expression used by Bishop [52]. That being said, most sources use Koch's expression for ν so it's possible they're just using a convention that we've overlooked. For further reading, we recommend Cottet's thesis [64].

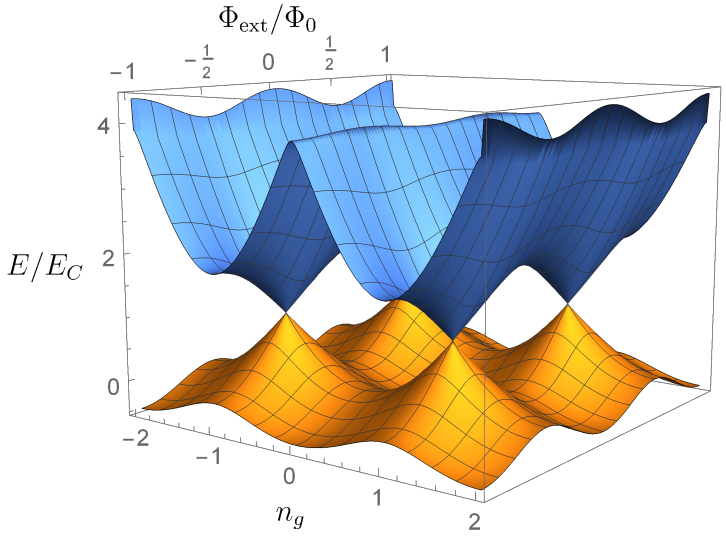

Figure 3.3: The first two energy levels $E_0(n_g, \Phi_{\text{ext}})$ and $E_1(n_g, \Phi_{\text{ext}})$ of the CPT for $E_J/E_C = 1$.

As we mentioned, we are primarily interested in the lowest two energy levels of the CPT, which are plotted in Fig. 3.3 for $E_J/E_C = 1$. At this energy ratio we can see both characteristics of the band structure: parabolic structure as a function of n_g associated with the charging energy E_C, and sinusoidal structure as a function of Φ_{ext} associated with the Josephson energy E_J. In line with this same intuition,

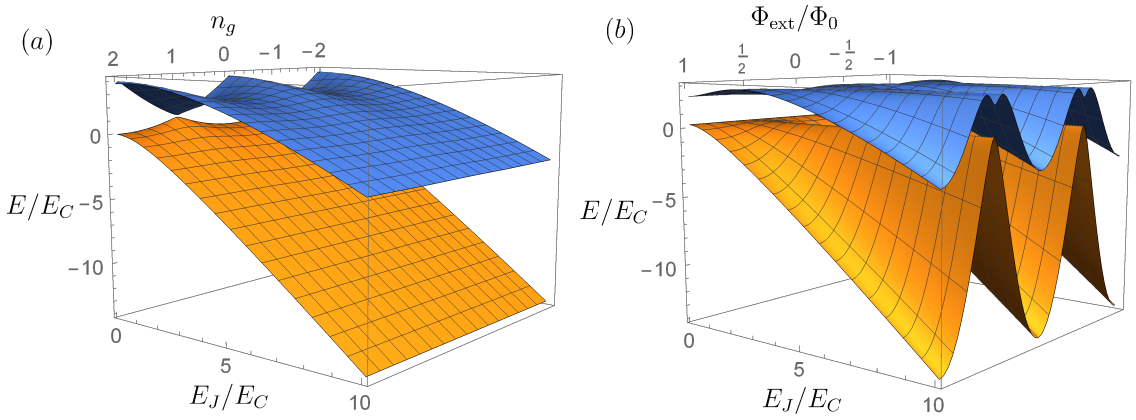

Figure 3.4: Cross-sections of the first two energy levels $E_0(n_g, \Phi_{\text{ext}})$ and $E_1(n_g, \Phi_{\text{ext}})$ of the CPT as a function of E_J/E_C. In (a), the energy levels are evaluated at $\Phi_{\text{ext}} = 0$. In (b), the energy levels are evaluated at $n_g = 1/2$.

when $E_J/E_C \ll 1$ the band structure flattens out as a function of Φ_{ext} and when $E_J/E_C \gg 1$ the band structure flattens out as a function of n_g, as can be seen in Fig. 3.4. It is worth noting that for each value of Φ_{ext}, the minimum energy difference between the bands occurs at charge degeneracy ($n_g = 1 \mod 2$) and is approximately $E_J \cos(\pi\Phi_{\text{ext}}/\Phi_0)$.

Ideally, we would always evaluate the energy levels using this exact solution, but evaluating the Mathieu characteristic values is computationally intensive. In addition, at the time of writing the exact expression for E_m must be evaluated via Mathematica; Python's method of evaluating $a_\nu(q)$ via SciPy can only handle $\nu \in \mathbb{Z}_{\geq 0}$. It may be possible to perform the evaluation numerically in Mathematica, import this data into Python, and use an interpolation routine to simulate the exact energy levels in Python, but this interpolation step is made difficult by the fact that $a_\nu(q)$ has discontinuities as a function of ν. In the transmon regime ($E_J/E_C \gg 1$), one way of circumventing this difficulty is by using asymptotic forms of the characteristic values. In the Cooper pair box regime ($E_J/E_C \lesssim 1$), we can solve for the eigenvalues of a truncated form of the Hamiltonian expressed in the charge basis.

Truncated Charge Expansion. In general, the energy eigenstates $|E_m\rangle$ will be a superposition of many different charge states $|N\rangle$. Since we are working in the Cooper pair box regime ($E_C \gtrsim E_J$), however, the quadratic term dominates and the contribution of charge states with eigenvalues significantly different from $\text{int}(n_g/2)$

will be small for the lowest lying energy levels. We note that it is always possible to set $\mathrm{int}(n_g/2) = 0$ by adding or subtracting an even number, since the whole system is symmetric under $n_g \to n_g + 2k$ for $k \in \mathbb{Z}$, and we do this for convenience. Thus, the eigenvalues of the truncated CPT Hamiltonian

$$\begin{aligned} H \ =& 4E_C \sum_{N=-N_{\mathrm{low}}}^{N_{\mathrm{high}}} \left(N - \frac{n_g}{2}\right)^2 |N\rangle\langle N| \\ &- E_J \cos\left(\frac{\pi}{\Phi_0}\Phi_{\mathrm{ext}}\right) \sum_{N=-N_{\mathrm{low}}}^{N_{\mathrm{high}}} \Big(|N+1\rangle\langle N| + |N\rangle\langle N+1|\Big). \end{aligned} \tag{3.78}$$

are good approximations for the true energy levels. We now have two different ways of approaching the problem of finding the eigenvalues of the truncated Hamiltonian: analytically if fewer than three charge states are included, and numerically if more than three charge states are included.

Truncated to two charge states, the Hamiltonian takes the form

$$H_{CPT} = 2E_C(n_g - 1)\sigma_z - E_J \cos\left(\frac{\pi}{\Phi_0}\Phi_{\mathrm{ext}}\right)\sigma_x + E_C(n_g^2 - 2n_g + 2) \tag{3.79}$$

where the Pauli operators are given by

$$\sigma_z = |0\rangle\langle 0| - |1\rangle\langle 1| \tag{3.80}$$

$$\sigma_x = |0\rangle\langle 1| + |1\rangle\langle 0| \tag{3.81}$$

and we've included the overall constant term so that we can compare this solution method to others on the same footing. This is easily diagonalized to find an expression for the two eigenenergies ($m = 0, 1$)

$$E_m(\varphi_{\mathrm{ext}}, n_g) = E_C(n_g^2 - 2n_g + 2) + (-1)^{m+1}\sqrt{4E_C^2\,(n_g - 1)^2 + E_J^2 \cos^2\left(\frac{\pi}{\Phi_0}\Phi_{\mathrm{ext}}\right)} \tag{3.82}$$

which is valid for $n_g \in (0, 2)$ but most accurate near $n_g = 1/2$. These expressions can be extended to the real axis by letting $n_g \to n_g \bmod 2$, but in doing so one finds energy levels that are not differentiable at $n_g \equiv 0 \bmod 2$ since the $N = n_g \pm 1$ states will contribute equally at this point but only one is included. This cusp at $n_g = 0$ can be seen in Fig. 3.5(a).

Truncated to three charge states, the Hamiltonian in the charge basis can be

represented by the matrix

$$H = \begin{bmatrix} E_C(2+n_g)^2 & -E_J\cos\left(\frac{\pi}{\Phi_0}\Phi_{\text{ext}}\right) & 0 \\ -E_J\cos\left(\frac{\pi}{\Phi_0}\Phi_{\text{ext}}\right) & E_C n_g^2 & -E_J\cos\left(\frac{\pi}{\Phi_0}\Phi_{\text{ext}}\right) \\ 0 & -E_J\cos\left(\frac{\pi}{\Phi_0}\Phi_{\text{ext}}\right) & E_C(2-n_g)^2 \end{bmatrix} \tag{3.83}$$

where the matrix elements are given by $H_{ij} = \langle i|H|j\rangle$. To find the eigenvalues of this matrix, we follow Joyez' treatment [65]. The characteristic equation of this matrix is given by

$$\begin{aligned}\left(E - E_C(n_g+2)^2\right)\left(E - E_C n_g^2\right)\left(E - E_c(n_g-2)^2\right) \\ - E_J^2\cos^2(\frac{\pi}{\Phi_0}\Phi_{\text{ext}})\left(2E - 2E_C(n_g^2+4)\right) = 0\end{aligned} \tag{3.84}$$

which can be solved analytically for the eigenvalues E. We introduce the intermediate quantities

$$\lambda = \frac{16}{3}\left(\frac{1}{3}+n_g^2\right) + \frac{2}{3}\left(\frac{E_J}{E_C}\right)^2\cos^2\left(\frac{\pi}{\Phi_0}\Phi_{\text{ext}}\right) \tag{3.85}$$

$$\mu = \frac{128}{3}\left(\frac{1}{9}-n_g^2\right) + \frac{8}{3}\left(\frac{E_J}{E_C}\right)^2\cos^2\left(\frac{\pi}{\Phi_0}\Phi_{\text{ext}}\right) \tag{3.86}$$

$$\theta = \arccos\left(\frac{-\mu}{2\lambda^{3/2}}\right) \tag{3.87}$$

in terms of which the three eigenvalues can be expressed

$$E_m(n_g,\Phi_{\text{ext}}) = E_C\left[\frac{8}{3}+n_g^2+\sqrt{4\lambda}\cos\left(\frac{\theta+2\pi(m+1)}{3}\right)\right] \quad ; \quad m=0,1,2. \tag{3.88}$$

These expressions are valid for $n_g \in (-1,1)$, but they can be extended to the real axis by letting $n_g \to (n_g+1 \bmod 2)-1$. As was the case for the two charge state approximation, however, this yields energy bands that are not differentiable. This time cusps are present at $n_g = 1 \mod 2$, as can be seen in Fig. 3.5(a).

Comparing Evaluation Methods. To compare these evaluation methods to the exact solution we consider two different energy ratios, $E_J/E_C = 5$ and $E_J/E_C = 0.5$, as depicted in Fig. 3.5. From (a), in which the larger energy ratio $E_J/E_C = 5$ is considered, it's clear that including more charge states yields more accurate energy

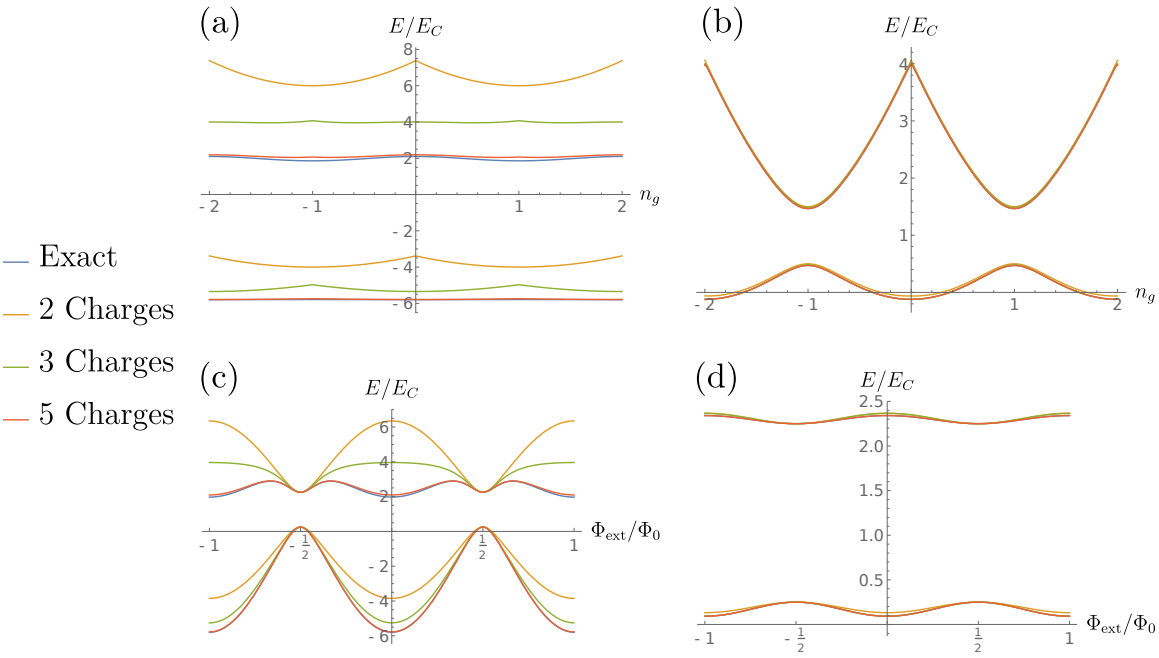

Figure 3.5: Comparing the ground and first excited state of the CPT evaluated using the exact solution and truncations to 2, 3, and 5 charge states. In (a) and (c) $E_J/E_C = 5$, while in (b) and (d) $E_J/E_C = 0.5$. In (a) and (b) the cross-sections are evaluated at $\varphi_{\text{ext}} = 0$, while in (c) and (d) they are evaluated at $n_g = 1/2$.

levels. From (b), in which the smaller energy ratio $E_J/E_C = 0.5$ is considered, it's clear that many fewer charge states are required to achieve the same level of accuracy. In this regime, therefore, the primary reason for using more charge states is to avoid the presence of cusps in the energy levels that make them non-differentiable at certain points, which will be very important for our purposes.

3.2.2 Tunable Josephson Inductance

By analogy to our previous treatment in Section 3.1.2, we now treat the ground state energy of the CPT as an effective potential and define the Josephson inductance as

$$L_J(n_g, \Phi_{\text{ext}}) = \left(\frac{\Phi_0}{2\pi}\right)^2 \left(\frac{\partial^2 E_0(n_g, \phi)}{\partial \phi^2}\right)^{-1}\Bigg|_{\phi = 2\pi\Phi_{\text{ext}}/\Phi_0} \tag{3.89}$$

where the equilibrium coordinate of the total flux is now the tunable via Φ_{ext}. Here we've differentiated with respect to the total phase $\phi = \varphi_1 + \varphi_2$ across the JJs since E_0 is 2π-periodic in this parameter. This is a bit hand-wavy for now, but it will be rigorously derived later on in Chapter 4 to be exactly this quantity that

tunes the resonant frequency of our device. The inverse of this tunable inductance is depicted in Fig. 3.6. We note that we've restricted ourselves to the gate range

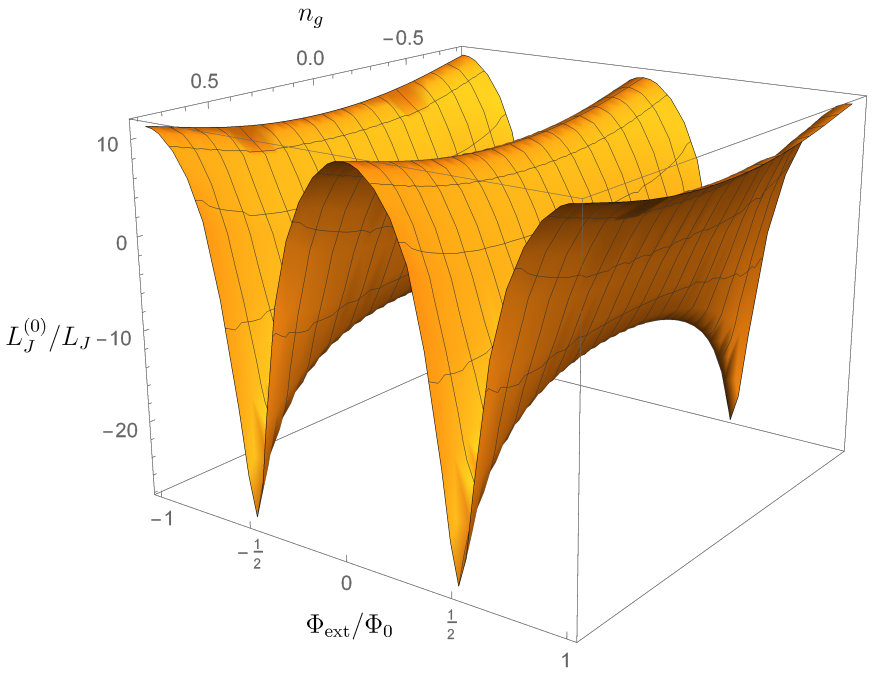

Figure 3.6: The inverse of Josephson inductance $L_J(n_g, \Phi_{\text{ext}})$ expressed in units of $L_J^{(0)} = \Phi_0/2\pi I_c$ for the energy ratio $E_J/E_C = 1$.

$-0.8 < n_g < 0.8$ both because this is the range we are concerned with in practice, and because the derivatives defining the above inductance diverge near the points ($n_g = 1 \mod 2, \Phi_{\text{ext}}/\Phi_0 = 1/2 \mod 1$) in parameter space, indicating that the effective Josephson inductance goes to zero at these points.

It is worthwhile to evaluate the Josephson inductance using the various methods discussed previously and compare them, the results of which are shown in Fig. 3.7. As we found earlier, the differences between the evaluation methods is greater in the case $E_J/E_C > 1$. Unlike evaluating the energy levels, however, there are regions where the three charge state model differs significantly from the exact solution even in the case $E_J/E_C < 1$. Thus, to accurately simulate the Josephson inductance of the CPT one will generally need to use at least five charge states. If one is working far enough away from charge degeneracy, though, the three charge state model may still suffice.

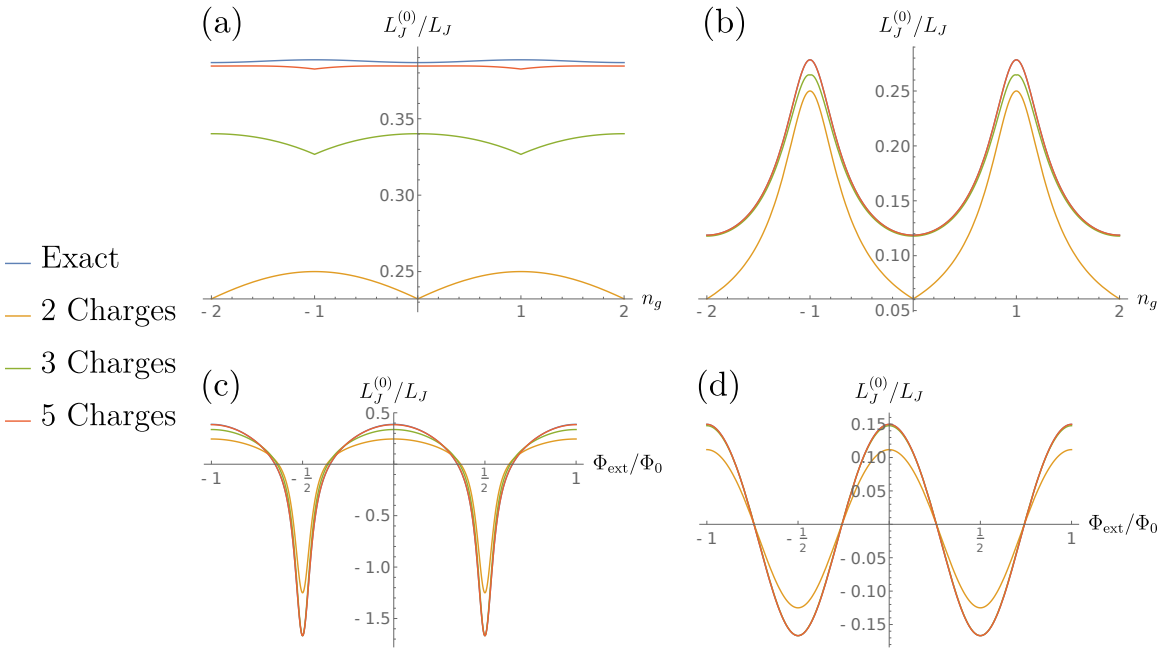

Figure 3.7: Comparing the inverse of the tunable Josephson inductance of the CPT evaluated using the exact solution and truncations to 2, 3, and 5 charge states. In (a) and (c) $E_J/E_C = 5$, while in (b) and (d) $E_J/E_C = 0.5$. In (a) and (b) the cross-sections are evaluated at $\Phi_{\text{ext}} = 0$, while in (c) and (d) they are evaluated at $n_g = 1/2$.

Chapter 4

Cavity-embedded Cooper Pair Transistor

In this chapter we introduce the cavity-embedded Cooper pair transistor (cCPT). First, we discuss the physical realization of the cCPT and how it was fabricated. The device we study was fabricated by Juliang Li, and we refer the reader to his thesis [49] for a much more detailed account of the fabrication process. Another good source of information on this process is Fei Chen's thesis [68], since he and Juliang used many of the same methods. Second, we derive the cCPT Hamiltonian using similar techniques to those used in Chapter 2.

Section 4.1 Sample

The cCPT consists of a quarter-wavelength ($\lambda/4$) coplanar waveguide cavity with a Cooper pair transistor connected between its voltage antinode and the ground plane, as shown in Figure 4.1. The CPT is made up of two Josephson junctions (JJs) separated by an island, which can be gated with a voltage V_g via the capacitance C_g. Here we treat the JJs as identical, since their asymmetry is sufficiently small that it is not necessary to account for our experimental observations. The cavity and CPT form a closed loop, which is superconducting when cooled to base temperature in a dilution refrigerator. This SQUID loop is L-shaped, as shown in Figure 4.1(b). The vertical segment of the loop runs parallel to a transmission line carrying the current I_Φ, which threads flux through the loop, while the horizontal segment runs parallel to the cavity. This design minimizes the coupling between the cavity and the transmission line

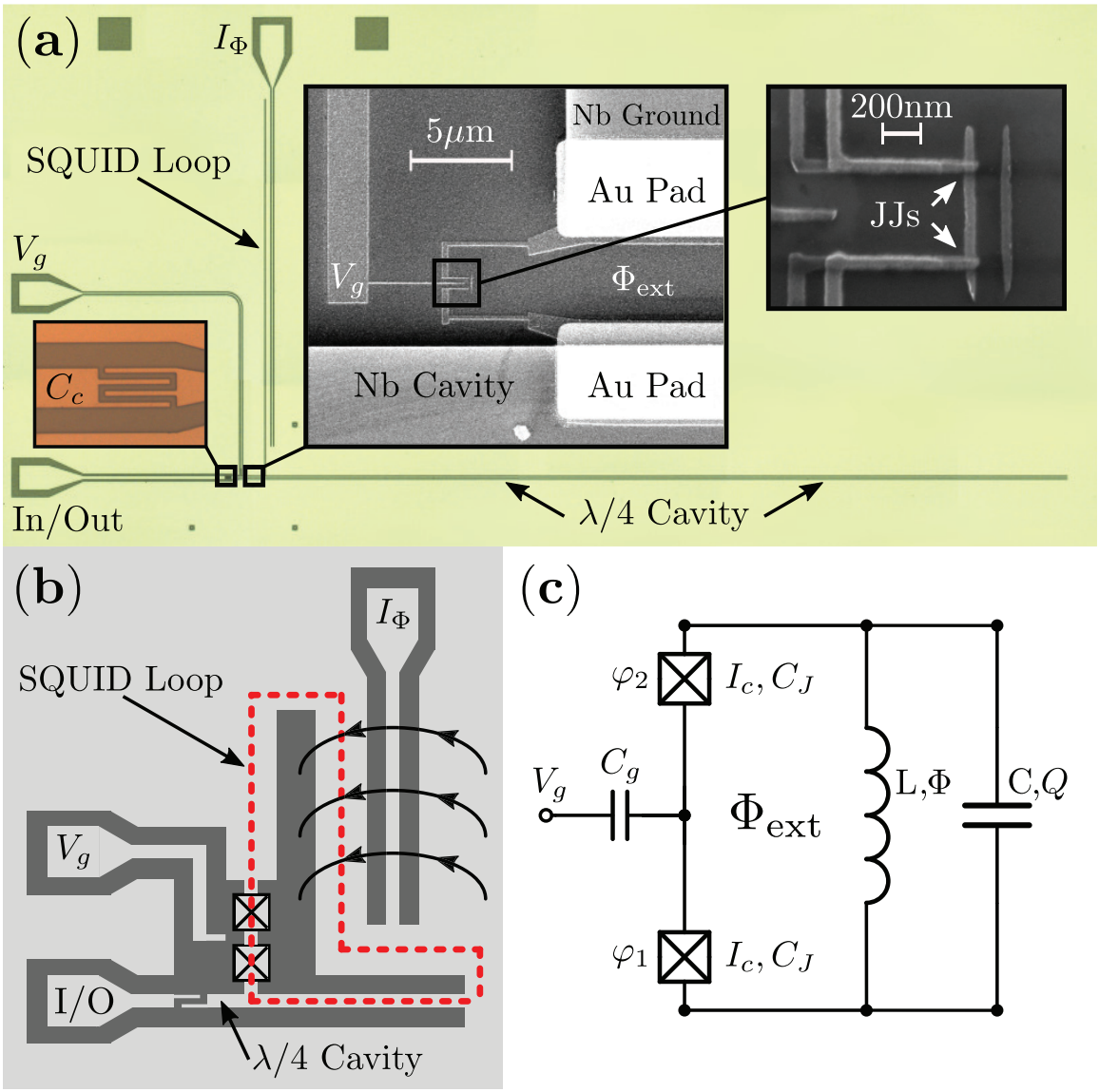

Figure 4.1: (a) Sample images of the cCPT. (b) An illustration of the chip layout of the cCPT; the dashed red line depicts the SQUID loop, and the black arcs depict the magnetic field lines generated by the current I_Φ. (c) An equivalent-circuit schematic of the closed-system cCPT. The $\lambda/4$ cavity behaves as a parallel LC circuit when operated near its fundamental frequency $\omega_{\lambda/4} = 1/\sqrt{LC}$ [6].

carrying I_Φ, such that the effect on the intrinsic cavity damping rate is negligible. The cavity is driven and measured via an external transmission line coupled to its voltage antinode via the interdigitated capacitor C_c. The cavity, input/output line, gate bias line, and flux bias line are all designed to have characteristic impedances of $Z_0 = 50\Omega$. The cavity has a length $\ell = 5135$ μm and bare resonant frequency $\omega_{\lambda/4} = 2\pi \times 5.757$ GHz (of its fundamental mode), which includes the slight renormalization due to the coupling capacitance C_c (see Appendix A of Ref. [4]).

To fabricate the sample, a 100 nm layer of Nb was first sputtered onto an intrinsic high-resistivity silicon substrate. The on-chip transmission lines (cavity, input/output, gate/flux bias lines, and interdigitated coupling capacitor) were then patterned using photolithography, and the Nb in the negative space was removed by reactive-ion etching. Next, the oxide layer on the Nb was removed via ion milling and 10 nm of Au was deposited for contact pads. Finally, the JJs were patterned using electron-beam lithography to have a cross-sectional area of roughly 50×50 nm^2, and Al was deposited using a double layer shadow evaporation with an oxidation step between the layers to form the insulating barrier. The lower layer of Al forming the island, deposited using a cryogenically-cooled stage, is 9 nm thick so as to increase the superconducting gap energy [69, 70] and thereby suppress quasiparticle poisoning [71]. The upper layer of Al connecting to the Au contact pads is 65 nm thick. The superconducting phase around the SQUID loop remains coherent across the Au contact pads due to the proximity effect. The fabrication techniques were similar to those described in Ref. [72], which provides further detail.

Section 4.2

Hamiltonian

In this section we present an intuitive derivation of the closed-system cCPT Hamiltonian, depicted schematically in Fig. 4.2. The Hamiltonian of this system consists of two parts: that due to the cavity, and that due to the CPT. Using the results of

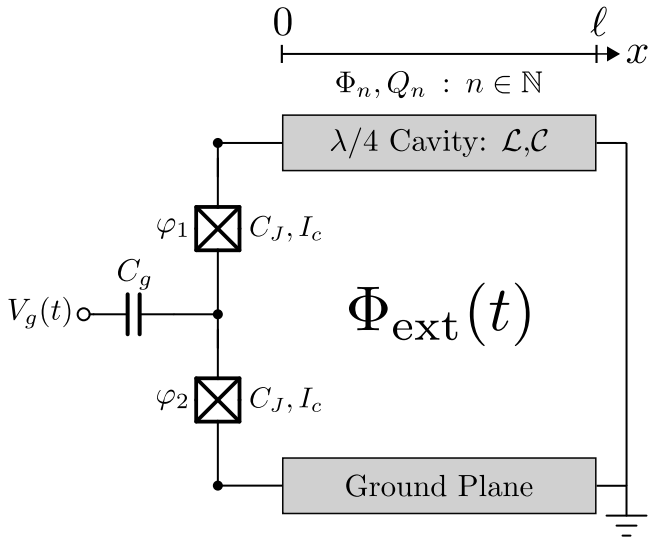

Figure 4.2: Simplified schematic of the closed-system cCPT, consisting of a Cooper pair transistor connected between the voltage antinode and ground plane of a superconducting $\lambda/4$ cavity. A gate voltage $V_g(t)$ is applied to the island between the JJs via the capacitance C_g. An external flux $\Phi_{\text{ext}}(t)$ is threaded through the superconducting loop formed by the series combination of the cavity and the CPT. The JJs are assumed to be identical, each having capacitance C_J and critical current I_c. The cavity is characterized by its inductance per unit length $\mathcal{L}$, its capacitance per unit length $\mathcal{C}$, its length ℓ, and its normal mode coordinates Φ_n, Q_n.

Chapters 2 and 3, we can therefore write

$$H = H_{\text{Cavity}} + H_{\text{CPT}} \tag{4.1}$$

$$H_{\text{Cavity}} = \sum_{n=1}^{\infty} \left[\frac{Q_n^2}{2C_n} + \frac{\Phi_n^2}{2L_n} \right] \tag{4.2}$$

$$H_{\text{CPT}} = 4E_C \sum_{N\in\mathbb{Z}} \left(N - \frac{n_g}{2} \right)^2 |N\rangle\langle N| - E_J \cos(\phi/2) \sum_{N\in\mathbb{Z}} \Big(|N+1\rangle\langle N| + |N\rangle\langle N+1| \Big), \tag{4.3}$$

where $\phi = \varphi_1 + \varphi_2$ is the total phase across the JJs. Since the flux around a closed superconducting loop must be an integer multiple of the flux quantum Φ_0, we also have the constraint

$$\frac{\Phi_0}{2\pi} (\varphi_1 + \varphi_2) - \sum_{n=1}^{\infty} \Phi_n - \Phi_{\text{ext}}(t) = m\Phi_0 \quad ; \quad m \in \mathbb{Z}. \tag{4.4}$$

Absorbing the constant multiple of Φ_0 into $\Phi_{\text{ext}}(t)$ as a DC offset, the total phase across the JJs takes the form

$$\phi = \frac{2\pi}{\Phi_0}\left[\sum_{n=1}^{\infty}\Phi_n - \Phi_{\text{ext}}(t)\right] \tag{4.5}$$

such that the CPT Hamiltonian can be written

$$\begin{aligned} H_{\text{CPT}} =& 4E_C\sum_{N\in\mathbb{Z}}\left(N-\frac{n_g}{2}\right)^2|N\rangle\langle N| \\ &- E_J\cos\left(\frac{\pi}{\Phi_0}\sum_{n=1}^{\infty}\Phi_n + \frac{\pi}{\Phi_0}\Phi_{\text{ext}}\right)\sum_{N\in\mathbb{Z}}\Big(|N+1\rangle\langle N| + |N\rangle\langle N+1|\Big). \end{aligned} \tag{4.6}$$

However, for most of our subsequent analysis it will be convenient to leave H_{CPT} in terms of ϕ, rather than expressing it in terms of the cavity flux coordinates Φ_n and external flux Φ_{ext}. We therefore see that the CPT couples to the cavity modes via their shared flux loop.

Adiabatic Elimination of the CPT. We now make an adiabatic approximation. If we operate the CPT at bias points far enough away from the charge degeneracy $n_g \equiv 1 \,(\text{mod}\, 2)$ then the gap between the ground and first excited state will be on the order of $E_C \sim h \times 50\text{GHz}$, which is much faster than any other relevant frequencies in our system. As we will discuss later, we're actually unable to operate at gate biases in the range $0.7 \lesssim n_g \,(\text{mod}\, 2) \lesssim 1.3$ due to quasiparticle poisoning, in which case the minimum gap between the ground and first excited state of the CPT is about $E_{\text{CPT}}^{0\to1} \gtrsim h \times 75$ GHz. Furthermore, our entire system will be at base temperature in a dilution refrigerator with $T \lesssim 30$ mK, so that $E_{\text{CPT}}^{0\to1} \gg kT$ and thermal excitations will be negligible. Together, these imply that the CPT will remain in its ground state, which will depend on the more slowly varying operators Φ_n and Q_n. It is worth noting that higher harmonics of the cavity may be comparable to the excitation frequency of the CPT, so we must restrict ourselves to the first few harmonics at most.

The effective Hamiltonian of the rest of the system is obtained by taking the expectation value of the total Hamiltonian with respect to the ground state $|g\rangle$ of the CPT, yielding

$$H_{\text{eff}} = H_{\text{Cavity}} + E_{\text{CPT}}(n_g, \phi) \tag{4.7}$$

where $E_{\text{CPT}}(n_g, \phi)$ is the ground state energy of the CPT Hamiltonian (Eq. (4.3)),

and ϕ depends on both the cavity flux coordinates Φ_n and the external flux Φ_{ext}. Thus, the ground state energy of the CPT modifies the effective potential energy of the cavity modes. To evaluate this ground state energy we can use all the same techniques we developed in Chapter 3, the only difference being that ϕ is now a function of our cavity flux operators Φ_n.

Equilibrium Phase Coordinate. Our goal is to understand and describe the dynamics of small oscillations of the cavity mode coordinates about their equilibrium values. To this end, we seek to find the equilibria of the effective potential

$$V_{\text{eff}}(\{\Phi_n\}) = \sum_{n=1}^{\infty} \frac{1}{2L_n}\Phi_n^2 + E_{\text{CPT}}(n_g, \phi). \tag{4.8}$$

The condition defining each mode coordinate's equilibrium Φ_n^{eq} is therefore

$$\frac{\partial V_{\text{eff}}(\{\Phi_m\})}{\partial \Phi_n}\Big|_{\Phi_n^{\text{eq}}} = \frac{1}{L_n}\Phi_n^{\text{eq}} + \frac{2\pi}{\Phi_0}\frac{\partial E_{CPT}(n_g, \phi)}{\partial \phi}\Big|_{\phi=\phi_{\text{ext}}+\phi^{\text{eq}}} = 0 \tag{4.9}$$

where we've introduced the notation

$$\phi_{\text{ext}} = \frac{2\pi}{\Phi_0}\Phi_{\text{ext}} \tag{4.10}$$

$$\phi^{\text{eq}} = \frac{2\pi}{\Phi_0}\sum_{n=1}^{\infty}\Phi_n^{\text{eq}}. \tag{4.11}$$

This is a complicated set of non-linear equations for the Φ_n^{eq} that depend on the bias points n_g and Φ_{ext}, which can be expressed more conveniently as a single equation for ϕ^{eq} by summing over all modes, yielding

$$\phi^{\text{eq}} = -\left(\frac{2\pi}{\Phi_0}\right)^2 \frac{\partial E_{\text{CPT}}(n_g, \phi)}{\partial \phi}\Big|_{\phi=\phi_{\text{ext}}+\phi^{\text{eq}}} \sum_{n=1}^{\infty} L_n. \tag{4.12}$$

Using our expression for the cavity mode inductance $L_n = 8\ell\mathcal{L}/\pi^2(2n-1)^2$ we can evaluate the summation

$$\sum_{n=1}^{\infty} L_n = \sum_{n=1}^{\infty} \frac{8\ell\mathcal{L}}{\pi^2(2n-1)^2} = \ell\mathcal{L} = \frac{\pi^2}{8}L_1 \tag{4.13}$$

analytically, where we've expressed the result in terms of the inductance L_1 of the fundamental cavity mode since this is a convenient quantity to extract experimentally. Plugging back in, our equation for $\bar{\varphi}^{\text{eq}}$ now reads

$$\phi^{\text{eq}} = -L_1 \frac{\pi^2}{8} \left(\frac{2\pi}{\Phi_0}\right)^2 \frac{\partial E_{\text{CPT}}(n_g, \phi)}{\partial \phi}\Big|_{\phi=\phi_{\text{ext}}+\phi^{\text{eq}}}. \tag{4.14}$$

It is worth noting at this point the significance of having a non-zero ϕ^{eq}: its effect is to alter the total phase across the JJs at equilibrium

$$\phi(\Phi_{\text{ext}}, \phi^{\text{eq}}) = \frac{2\pi}{\Phi_0}\Phi_{\text{ext}} + \phi^{\text{eq}}(n_g, \Phi_{\text{ext}}) \tag{4.15}$$

and therefore complicate our ability to freely control this parameter via the external flux Φ_{ext}. We may try to target a particular value of ϕ, but the equilibrium flux at that bias point will also enter into the argument of the cosine in the CPT Hamiltonian, yielding a nonlinear dependence of the parameter we want to tune (ϕ) on the parameter we have access to (Φ_{ext}). On the other hand, if ϕ^{eq} always remains small, we can ignore this effect entirely.

A simple upper bound on the solutions to Eq. (4.14) can be obtained by maximizing over the right hand side, yielding

$$|\phi^{\text{eq}}| \leq L_1 \frac{\pi^2}{8} \left(\frac{2\pi}{\Phi_0}\right)^2 \max_{\{n_g,\phi\}} \left|\frac{\partial E_{CPT}(n_g, \phi)}{\partial \phi}\right| \tag{4.16}$$

which assumes fixed and known values of L_1, E_J and E_C. We can write

$$L_1 = \frac{4\mathcal{Z}}{\pi\omega_1} \tag{4.17}$$

in terms of the cavity's characteristic impedance $\mathcal{Z} = \sqrt{\mathcal{L}/\mathcal{C}}$, designed such that $\mathcal{Z} \approx 50\Omega$, and the bare frequency of the fundamental mode $\omega_1 \approx 2\pi \times 5.76$ GHz. If we want to apply a simplified model (one that neglects the non-zero equilibrium coordinate) to experimental data as a means to extract E_J and E_C, however, we must also maximize over a reasonable range of these parameters. To this end, we maximize

over the space defined by the intervals

$$n_g \in [-0.7, 0.7] \tag{4.18}$$

$$E_C/h \in [50\text{ GHz}, 60\text{ GHz}] \tag{4.19}$$

$$E_J/h \in [10\text{ GHz}, 20\text{ GHz}] \tag{4.20}$$

where the gate n_g is restricted to reflect the practical range over which we can operate due to quasiparticle poisoning (see Section 6.1.2). We perform this maximization using the Mathematica code shown in Fig. 4.3 and find

$$|\phi^{\text{eq}}| \lesssim 0.035 \ll 1. \tag{4.21}$$

Thus, we can safely treat the equilibrium position as being zero for the purposes of modeling our experiments.

```
In[271]:= << NumericalCalculus`

In[272]:= k[m_, ng_] := Sum[Mod[Round[ng + l / 2], 2] * (Round[ng / 2] - l * ((-1) ^m) *
            Quotient[m + 1, 2]), {l, {-1, 1}}];

In[273]:= Ecpt[m_, ng_, ϕ_, Eratio_, Ec_] :=
           Ec * MathieuCharacteristicA[-ng + (2 * k[m, ng]), -1.0 * Eratio * Cos[ϕ / 2]];

In[274]:= h = 6.63 * (10^-34);
          ϕ0 = 2.07 * (10^-15);

In[276]:= Z0 = 50.0;
          ω1 = 2 * Pi * 5.76 * (10^9);
          L1 = (4 * Z0) / (Pi * ω1);

In[279]:= phieqfunction[ng_, ϕ_, Ej_, Ec_] :=
           ND[Ecpt[0, ng, ϕdummy, Ej / Ec, Ec], {ϕdummy, 1}, ϕ];

In[280]:= result = NMaximize[{Abs[phieqfunction[ng, ϕ, Ej, Ec]],
             Ej < h * (20.0 * (10^9)) && Ej > h * (10.0 * (10^9)) && Ec > h * (50.0 * (10^9)) &&
              Ec < h * (60.0 * (10^9)) && -0.7 < ng && ng < 0.7 && ϕ ≥ 0 && ϕ ≤ (2 * Pi)}, {ng, ϕ, Ej, Ec}]

Out[280]= {1.75091 × 10^-24, {ng → 0.522775, ϕ → 1.55505, Ej → 1.326 × 10^-23, Ec → 3.315 × 10^-23}}

In[281]:= (L1 * ((Pi^2) / 8) * (((2 * Pi) / ϕ0) ^2)) * result[[1]]

Out[281]= 0.0350083
```

Figure 4.3: Mathematica code used to bound the equilibrium coordinate.

Effective Cavity Hamiltonian. Having found the equilibrium phase coordinate to be negligibly small, we can now Taylor expand our effective potential about this

point to arrive at our effective Hamiltonian

$$H_{\text{eff}} = \sum_{n=1}^{\infty}\left(\frac{Q_n^2}{2C_n} + \frac{\Phi_n^2}{2L_n}\right) + \sum_{k=2}^{\infty}\frac{1}{k!}\frac{\partial^k E_{\text{CPT}}(n_g,\phi)}{\partial\phi^k}\Big|_{\phi=\phi_{\text{ext}}}\left(\frac{2\pi}{\Phi_0}\sum_{n=1}^{\infty}\Phi_n\right)^k \tag{4.22}$$

where the $k = 0$ term has been dropped since it's an overall constant and the $k = 1$ term vanishes since we are expanding about the approximate equilibrium point of the effective potential. It is worth noting that the condition that this Taylor series is only accurate when the total flux in the cavity is much less than the flux quantum: $|\sum_{n=1}^{\infty}\Phi_n| \ll \Phi_0$. Finally, for notational convenience we adopt the following shorthand for partial differentiation of the CPT ground state energy

$$\partial_\phi^k E_{\text{CPT}}(n_g,\Phi_{\text{ext}}) = \frac{\partial^k E_{CPT}(n_g,\phi)}{\partial\phi^k}\Big|_{\phi=2\pi\Phi_{\text{ext}}/\Phi_0} \tag{4.23}$$

in terms of which the Hamiltonian can be written

$$H_{\text{eff}} = \sum_{n=1}^{\infty}\left(\frac{Q_n^2}{2C_n} + \frac{\Phi_n^2}{2L_n}\right) + \sum_{k=2}^{\infty}\frac{1}{k!}\partial_\phi^k E_{\text{CPT}}(n_g,\Phi_{\text{ext}})\left(\frac{2\pi}{\Phi_0}\sum_{n=1}^{\infty}\Phi_n\right)^k. \tag{4.24}$$

Section 4.3

Dynamics of the Fundamental Mode

We now consider the situation where we drive the cavity near the resonant frequency of its fundamental mode. Applying the RWA we drop all terms that do not tend to oscillate near this resonant frequency such that our effective cavity Hamiltonian becomes

$$H = \frac{Q^2}{2C} + \frac{\Phi^2}{2L} + \sum_{k=2}^{\infty}\frac{1}{k!}\partial_\phi^k E_{\text{CPT}}(n_g,\Phi_{\text{ext}})\left(\frac{2\pi}{\Phi_0}\Phi\right)^k \tag{4.25}$$

where we've written $L = L_1$, $C = C_1$, $Q = Q_1$, and $\Phi = \Phi_1$ for simplicity. We note that there will also be many terms involving higher order modes, but these can be dropped under the assumption that they are in their ground state, which is true to very good approximation. Defining the tunable Josephson inductance $L_J(n_g,\varphi_{\text{ext}})$ according to

$$L_J(n_g,\Phi_{\text{ext}}) = \left(\frac{\Phi_0}{2\pi}\right)^2\left(\partial_\phi^2 E_{\text{CPT}}(n_g,\Phi_{\text{ext}})\right)^{-1} \tag{4.26}$$

and the total inductance L_{tot} as the parallel combination of L and L_J

$$\frac{1}{L_{\text{tot}}(n_g, \varphi_{\text{ext}})} = \frac{1}{L} + \frac{1}{L_J(n_g, \Phi_{\text{ext}})} \tag{4.27}$$

this Hamiltonian can be rewritten

$$H = \frac{Q^2}{2C} + \frac{\Phi^2}{2L_{\text{tot}}(n_g, \Phi_{\text{ext}})} + \sum_{k=3}^{\infty} \frac{1}{k!} \partial_\phi^k E_{\text{CPT}}(n_g, \Phi_{\text{ext}}) \left(\frac{2\pi}{\Phi_0}\Phi\right)^k. \tag{4.28}$$

We now introduce creation and annihilation operators in the usual way

$$\begin{aligned} a &= \frac{1}{\sqrt{2\hbar Z_{\text{tot}}}} \left(\Phi + i Z_{\text{tot}} Q\right) \\ a^\dagger &= \frac{1}{\sqrt{2\hbar Z_{\text{tot}}}} \left(\Phi - i Z_{\text{tot}} Q\right) \end{aligned} \tag{4.29}$$

with inverse transformations given by

$$\begin{aligned} \Phi &= \sqrt{\frac{\hbar Z_{\text{tot}}}{2}} \left(a + a^\dagger\right) \\ Q &= i\sqrt{\frac{\hbar}{2Z_{\text{tot}}}} \left(a^\dagger - a\right). \end{aligned} \tag{4.30}$$

where $[a, a^\dagger] = 1$ and $Z_{\text{tot}} = \sqrt{L_{\text{tot}}/C}$ is the total impedance of the cavity mode, which depends on both n_g and Φ_{ext} in general. Plugging these operators into our Hamiltonian, we find

$$H = \hbar\omega_0 a^\dagger a + \sum_{k=3}^{\infty} \frac{1}{k!} \left(\frac{2\pi}{\Phi_0}\sqrt{\frac{\hbar Z_{\text{tot}}}{2}}\right)^k \partial_\phi^k E_{\text{CPT}}(n_g, \Phi_{\text{ext}}) \left(a + a^\dagger\right)^k \tag{4.31}$$

where $\omega_0 = 1/\sqrt{L_{\text{tot}} C}$ and we've dropped overall constant terms.

4.3.1 Tunable Resonant Frequency

The resonant frequency ω_0 of the cCPT is given by

$$\omega_0(n_g, \Phi_{\text{ext}}) = \sqrt{\frac{1}{C}\left(\frac{1}{L} + \frac{1}{L_J(n_g, \Phi_{\text{ext}})}\right)} = \omega_{\lambda/4}\sqrt{1 + \frac{L}{L_J(n_g, \Phi_{\text{ext}})}} \tag{4.32}$$

where we've introduced the notation $\omega_{\lambda/4}$ for the bare frequency of the fundamental mode of the $\lambda/4$ cavity, for simplicity. From this expression we see that ω_0 can be tuned via n_g and Φ_{ext}. Empirically we know that the resonant frequency can only be tuned by ± 70 MHz, or about 1% of its bare frequency, which means $L/L_J \ll 1$. We may therefore write

$$\omega_0(n_g, \Phi_{\text{ext}}) \approx \omega_{\lambda/4}\left(1 + \frac{L}{2L_J(n_g, \Phi_{\text{ext}})}\right) = \omega_{\lambda/4} + \frac{\phi_{\text{zp}}^2}{\hbar}\partial_\phi^2 E_{\text{CPT}}(n_g, \Phi_{\text{ext}}) \tag{4.33}$$

where we've introduced the dimensionless constant

$$\phi_{\text{zp}} = \frac{2\pi}{\Phi_0}\sqrt{\frac{\hbar Z_{\text{tot}}}{2}}, \tag{4.34}$$

which is related to the zero-point fluctuations of the cavity flux coordinate.

4.3.2 Zero-point Fluctuations

We now consider the zero-point fluctuations of our flux and charge variables

$$\Phi_{\text{zp}} = \sqrt{\langle 0|\Phi^2|0\rangle} = \sqrt{\frac{\hbar Z_{\text{tot}}}{2}} \tag{4.35}$$

$$Q_{\text{zp}} = \sqrt{\langle 0|Q^2|0\rangle} = \sqrt{\frac{\hbar}{2Z_{\text{tot}}}} \tag{4.36}$$

which serve as the natural scales of these variables when operating at low photon numbers. Using the same line of reasoning as above, we expand to first order in L/L_J yielding the expressions

$$\Phi_{\text{zp}} \approx \sqrt{\frac{\hbar Z}{2}}\left(1 - \frac{L}{2L_J(n_g, \Phi_{\text{ext}})}\right), \tag{4.37}$$

$$Q_{\text{zp}} \approx \sqrt{\frac{\hbar}{2Z}}\left(1 + \frac{L}{2L_J(n_g, \Phi_{\text{ext}})}\right), \tag{4.38}$$

which vary with n_g and Φ_{ext}, where $Z = \sqrt{L/C} = 4Z_0/\pi$. As above, however, these quantities only vary from their bare values by about 1% at most, which is too small an effect to observe in practice (unlike the resonant frequency, where 1% of its bare value is 10 to 100 times larger than its linewidth). As such it suffices for our purposes

to approximate them as

$$\Phi_{\text{zp}} \approx \sqrt{\frac{\hbar Z}{2}} \approx 0.028\,\Phi_0 \tag{4.39}$$

$$Q_{\text{zp}} \approx \sqrt{\frac{\hbar}{2Z}} \approx 5.7\,e \tag{4.40}$$

where in the last step we've plugged in our experimental values. The dimensionless constant we introduced earlier

$$\phi_{\text{zp}} = \frac{2\pi}{\Phi_0}\sqrt{\frac{\hbar Z}{2}} \approx 0.176 \tag{4.41}$$

can now be interpreted as the zero-point fluctuations of the total phase across the JJs, induced by the zero-point fluctuations of the cavity field, and to be precise it has units of radians. In terms of this constant, our Hamiltonian can be expressed more simply as

$$H = \hbar\omega_0 a^\dagger a + \sum_{k=3}^{\infty} \frac{1}{k!}\phi_{\text{zp}}^k \partial_\phi^k E_{\text{CPT}}(n_g, \Phi_{\text{ext}}) \left(a + a^\dagger\right)^k . \tag{4.42}$$

from which we can see that the value of ϕ_{zp} is a significant factor determining the strength of the nonlinear terms in our Hamiltonian.

4.3.3 Kerr Nonlinearity

We now consider the leading-order nonlinear term in our Hamiltonian within the RWA, which is that due to the Duffing nonlinearity

$$H_{\text{Duffing}} = \frac{1}{24}\phi_{\text{zp}}^4 \partial_\phi^4 E_{\text{CPT}}(n_g, \Phi_{\text{ext}}) \left(a + a^\dagger\right)^4 . \tag{4.43}$$

We use the "Duffing" nomenclature since the effective potential is proportional to Φ^4, yielding a generalized force proportional to Φ^3. As we will show, however, this is equivalent to a Kerr nonlinearity within the RWA. Applying this approximation, we keep only those terms with an equal number of a's and $a^\dagger$'s, such that

$$\begin{aligned} \left(a + a^\dagger\right)^4 \xrightarrow{\text{RWA}} \quad & a^\dagger a^\dagger a a + a^\dagger a a^\dagger a + a^\dagger a a a^\dagger + a a^\dagger a^\dagger a + a a^\dagger a a^\dagger + a a a^\dagger a^\dagger \\ & = 6 a^{\dagger 2} a^2 + 12 a^\dagger a + \text{constant}. \end{aligned} \tag{4.44}$$

Our Duffing term can therefore be rewritten

$$H_{\text{Duffing}} = \frac{1}{4}\phi_{\text{zp}}^4 \partial_\phi^4 E_{\text{CPT}}(n_g, \Phi_{\text{ext}}) a^{\dagger 2} a^2 + \frac{1}{2}\phi_{\text{zp}}^4 \partial_\phi^4 E_{\text{CPT}}(n_g, \Phi_{\text{ext}}) a^\dagger a \tag{4.45}$$

which contains a term that renormalizes the resonant frequency of the cavity, but this renormalization is smaller than (though on the order of) the linewidth of our cavity (~ 1 MHz) so we drop it. The remaining term can be cast in the conventional form of a Kerr-type Hamiltonian

$$H_{\text{Kerr}} = \frac{\hbar}{2} K a^{\dagger 2} a^2 = \frac{1}{4}\phi_{\text{zp}}^4 \partial_\phi^4 E_{\text{CPT}}(n_g, \Phi_{\text{ext}}) a^{\dagger 2} a^2 \tag{4.46}$$

where the strength of the Kerr nonlinearity is given by

$$K = \frac{1}{2\hbar}\phi_{\text{zp}}^4 \partial_\phi^4 E_{\text{CPT}}(n_g, \Phi_{\text{ext}}), \tag{4.47}$$

which can be tuned via n_g and Φ_{ext}.

4.3.4 Final Hamiltonian

To sum up the results of this section, the Hamiltonian of the cCPT can be cast as that of a Kerr cavity

$$H = \hbar\omega_0 a^\dagger a + \frac{1}{2}\hbar K a^{\dagger 2} a^2 \tag{4.48}$$

where both the resonant frequency and Kerr nonlinearity are tunable according to the expressions

$$\omega_0(n_g, \Phi_{\text{ext}}) = \omega_{\lambda/4} + \frac{\phi_{\text{zp}}^2}{\hbar}\partial_\phi^2 E_{\text{CPT}}(n_g, \Phi_{\text{ext}}) \tag{4.49}$$

$$K(n_g, \Phi_{\text{ext}}) = \frac{1}{2\hbar}\phi_{\text{zp}}^4 \partial_\phi^4 E_{\text{CPT}}(n_g, \Phi_{\text{ext}}) \tag{4.50}$$

and $\phi_{\text{zp}} \approx 0.176$ is the scale of zero point fluctuations in the total phase across the JJs induced by fluctuations in the cavity flux coordinate.

Chapter 5

Experimental Setup

In this chapter we discuss the general features of the measurement setup used to conduct our experiments. First, we discuss the microwave and DC circuitry in our dilution refrigerator, with a particular focus on the factors influencing its design. For the principles underlying the operation of the dilution refrigerator itself, we refer the reader to the introductory text by Betts [73] for a good overview and the texts by Lounasmaa [74] and Pobell [75] for more detail. Second, we discuss several measurement schemes that will be useful for studying the cCPT, with a focus on how raw measurement data must be processed in order to compare results with theory.

Section 5.1

Cryogenic Circuitry

The cCPT is housed in a dilution refrigerator with a base temperature of $T \approx 30$ mK, and the sample box itself is mounted within a magnetic shield made of Cryoperm 10. We measure the sample using the circuitry depicted in Figure 5.1. On the input line, attenuators are distributed such that the input noise at 30 mK is thermalized, and a cryogenic filter is used to suppress high frequency noise. On the output line, a circulator is used to separate the outgoing signal, which passes through two isolators before being amplified by a cryogenic HEMT amplifier and then a room temperature FET amplifier. Stainless steel coaxial cables are used to carry the input signal down to the circulator, giving rise to additional input attenuation, whereas niobium coaxial cables are used between the sample and HEMT to minimize attenuation of the output signal. The gate and flux DC biases are carried by twisted pairs, which are filtered both at room temperature and at cryogenic temperatures using a combination of RC

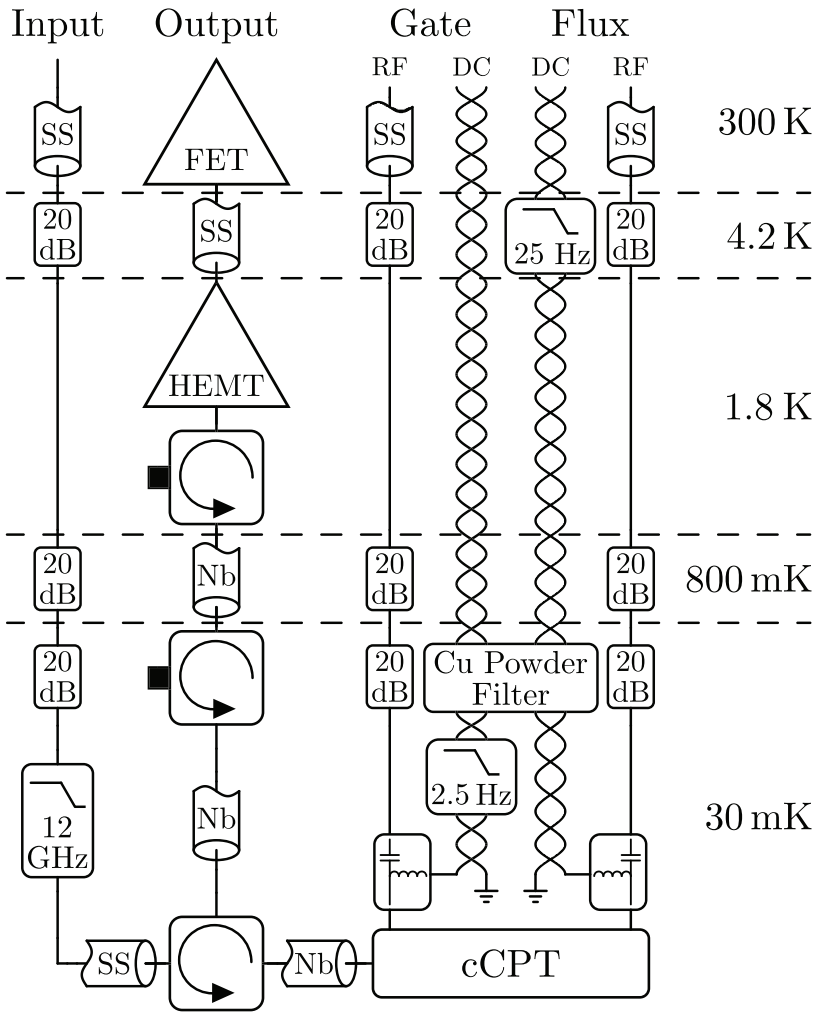

Figure 5.1: Schematic of the circuitry used to measure the cCPT.

filters to suppress 60 Hz noise, and a copper powder filter to suppress radio frequency (RF) noise [76, 77]. The different size and location of the RC filter on the flux line relative to the gate line is due to the resistive heating associated with driving a steady current I_Φ through the flux line, compared to the negligible heating associated with maintaining a voltage V_g across the capacitance C_g. The gate and flux DC lines are combined with their RF counterparts via bias tees. These RF lines can be used to apply parametric drives to the cCPT, and they are designed similarly to the input line.

Section 5.2

Reflection Coefficient Measurements

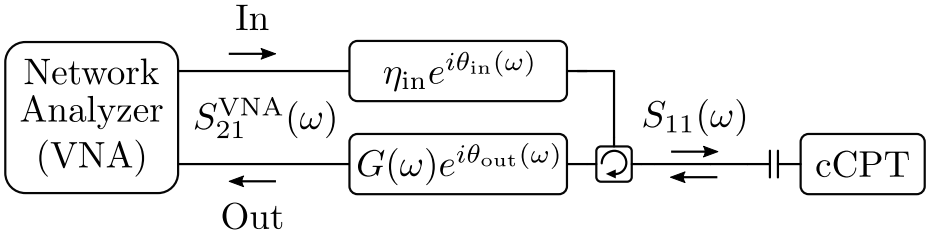

Figure 5.2: Schematic of the microwave network used to measure the reflection coefficient.

To measure the reflection coefficient of the cCPT we use a vector network analyzer (VNA) to measure the transmission from the input to the output of the fridge, as depicted in Fig. 5.2. This measurement can be related to the reflection coefficient at the plane of the sample, as we will see shortly. We use this measurement scheme extensively in Chapter 6 to extract the tunable resonant frequency and damping rates of the cCPT, to observe key signatures of resonant frequency fluctuations in the cCPT, and to determine the power reaching the cCPT in-situ via the Kerr shift. In all these measurements (aside from the Kerr shift) we use input powers corresponding to $n \lesssim 0.25$ photons in the cavity, such that the cCPT responds linearly to good approximation and the fluctuations in the intracavity field follow a central chi-square distribution (see Section 6.2.4).

5.2.1 Background Scattering Profile

When we analyzed the reflection coefficient S_{11} of a microwave cavity in Chapter 2, we always assumed we were driving and measuring the system directly. In reality, however, our sample is embedded in a microwave network that changes both the magnitude and phase of the reflection coefficient. A schematic of the microwave network used to measure the reflection coefficient of the cCPT is shown in Figure 5.2. At the top of the fridge, a VNA is used to measure the transmission coefficient $S_{21}^{\mathrm{VNA}}(\omega)$ from the input to the output port. As the input signal travels from the top of the fridge down to the cCPT it is attenuated by a factor η_{in} and picks up a phase factor of $\theta_{\mathrm{in}}(\omega)$; the signal is then reflected off of the cCPT according to our model for $S_{11}(\omega)$; the output (reflected) signal is then separated from the input signal using a circulator ; finally, as the output signal travels to the top of the fridge it is

amplified by a factor $G(\omega)$ and picks up a phase factor of $\theta_{\text{out}}(\omega)$. We can therefore relate the transmission coefficient measured by the VNA to the reflection coefficient at the plane of the sample according to

$$S_{21}^{\text{VNA}}(\omega) = \sqrt{\frac{G(\omega)}{\eta_{\text{in}}}} e^{i\theta(\omega)} S_{11}(\omega) \tag{5.1}$$

where $\theta = \theta_{\text{in}} + \theta_{\text{out}}$. It is worth noting that we've defined the gain G and attenuation η_{in} relative to the power rather than the amplitude, giving rise to the square root in the above expression. In practice, we typically work with these quantities in terms of decibels, which takes care of this potential ambiguity (e.g., 20 dB of gain means a factor of 100 increase in power and a factor of 10 increase in amplitude).

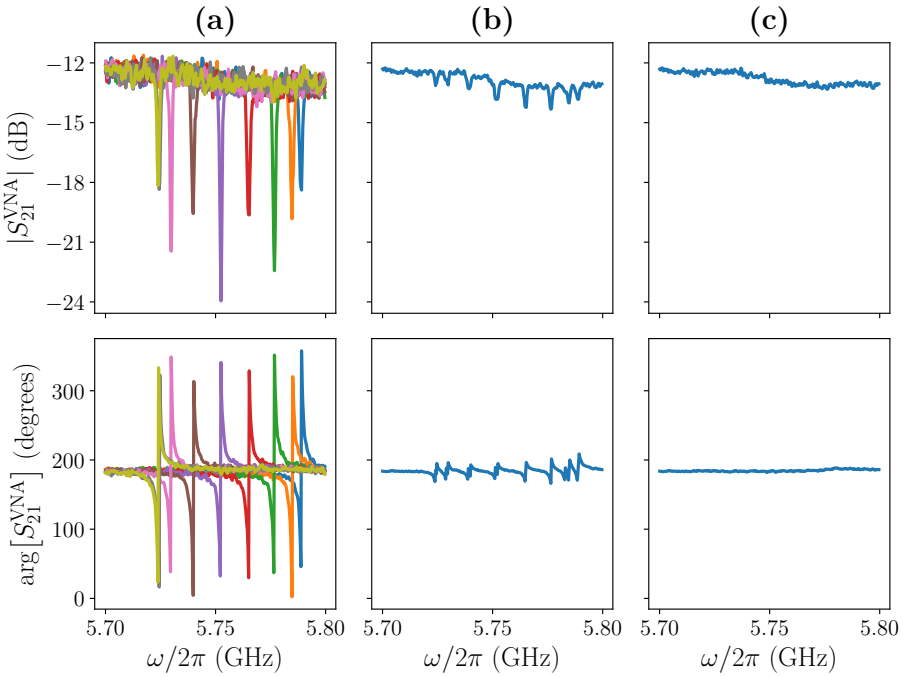

Figure 5.3: Process for determining the background scattering profile to refer reflection measurements to the plane of the sample. (a) Raw traces of the magnitude and phase of S_{21}^{VNA} for a set of different resonant frequencies. (b) The average of all these traces. (c) The average of the off-resonant parts of all these traces; the top panel is the background magnitude $G(\omega)/\eta_{\text{in}}$ and the bottom panel is the background phase $\theta(\omega)$.

We can determine the prefactor relating S_{21}^{VNA} to S_{11}, and thereby refer this measurement to the plane of the sample, using the fact that $S_{11}(\Delta \gg \kappa_{\text{tot}}) \approx 1$ when the

drive frequency ω is far-detuned from resonance. To be precise,

$$S_{21}^{\mathrm{VNA}}(\omega; \Delta \gg \kappa_{\mathrm{tot}}) \approx \sqrt{\frac{G(\omega)}{\eta_{\mathrm{in}}}} e^{i\theta(\omega)}. \tag{5.2}$$

With non-tunable cavities one is forced to infer this prefactor near ω_0 using an off-resonant drive; in our case, we can detune the resonant frequency itself rather than the drive, and thereby perform this calibration at any frequency. To determine this prefactor as a function of frequency we measure S_{21}^{VNA} across our frequency range of interest, for many values of the resonant frequency (this is easily accomplished in our case by sweeping the flux across a full period). We then average all of these traces together, which diminishes the resonant features of each trace and allows us to robustly locate the resonant frequency of each trace even when the background gain profile varies significantly. Finally, we define a window around the resonant frequency of each trace that we exclude from the averaging process, and average all the off-resonant parts of the traces together. This yields the magnitude and phase of the "background" scattering profile, which we can use to refer any subsequent measurement to the plane of the sample, and thereby compare our results with our theoretical model for $S_{11}(\Delta)$. This process of determining the background scattering profile is illustrated in Figure 5.3.

5.2.2 Impedance Mismatches

In our experiments we observe that the trajectories traced out by S_{11} in the complex plane are rotated about the off-resonant point $S_{11} = 1$. This is a sign of impedance mismatching at the sample input, likely due to the self-inductance of wire bonds, which also causes a dilation of the resonance circle [78, 79]. The effect of this rotation can be modeled by the transformation

$$S_{11}(\Delta) \to 1 + [S_{11}(\Delta) - 1]\, e^{i\theta_{\mathrm{IM}}} \tag{5.3}$$

where θ_{IM} is the angle of rotation to be determined empirically. In our case, the angle of rotation remains less than 0.1 radians in magnitude over the full tuning range of the cCPT, which leads to a systematic error in our extracted damping rates of less than 0.5%. Since this is generally smaller than their confidence intervals we can safely ignore this effect. It is also worth noting that this rotation angle can be extracted by finding the tangent to the trajectory at $S_{11} = 1$, which is independent of all other

fitting parameters.

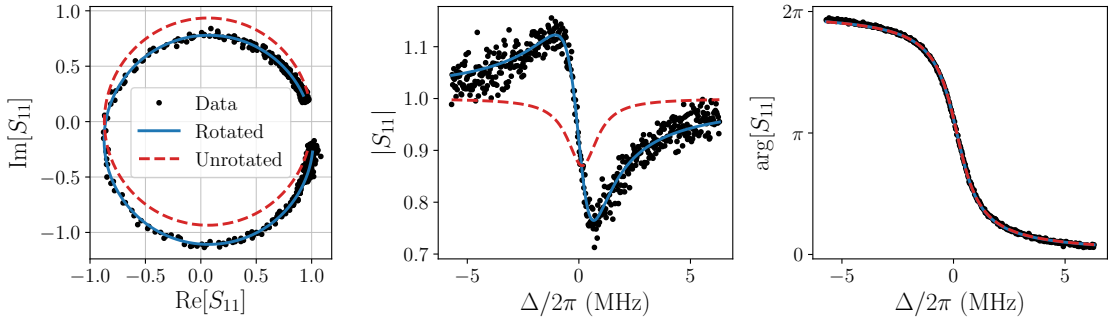

Figure 5.4: Reflection coefficient of a $\lambda/4$ cavity (nominally identical to the bare cavity used to realize our cCPT) showing signs of impedance mismatching. The solid blue curve is the best fit to our model for the reflection coefficient accounting for impedance mismatching, while the dashed red curve is our best fit to the ideal model. The best fit parameters of the blue curve are $\omega_0/2\pi = 5.752$ GHz, $\kappa_{\text{int}}/2\pi = 94$ kHz, $\kappa_{\text{ext}}/2\pi = 1.58$ MHz, and $\theta_{\text{IM}} = -0.18$ rad.

Figure 5.4 shows a measurement of the reflection coefficient of a bare $\lambda/4$ cavity nominally identical to the one used to realize our cCPT sample. As you can see, our measured trajectory for $S_{11}(\Delta)$ is rotated around the point $S_{11}(\Delta)$. The empirical angle of rotation $\theta_{\text{IM}} = -0.18$ rad is larger in this case than we find for the cCPT itself. Although the angle needs to be accounted for to obtain a good fit, this effect does not lead to significant systematic error in our extracted damping rates.

Section 5.3

Frequency Noise Measurements

To measure the power spectral density (PSD) of the cCPT's frequency fluctuations, we drive the cCPT with a carrier signal on resonance and measure the output power near ω_0 using a spectrum analyzer; this setup is depicted schematically in Figure 5.5. This carrier signal will be modulated by the frequency fluctuations, which we assume to have PSD $S_{\Omega\Omega}(\omega)$, such that the PSD S_{out} of the output power at the plane of the sample is given by

$$S_{\text{out}}(\omega_0 \pm \omega) = \frac{2\kappa_{\text{ext}}^2}{\kappa_{\text{tot}}^2(\omega^2 + \kappa_{\text{tot}}^2/4)} P_{\text{in}} S_{\Omega\Omega}(\omega) \tag{5.4}$$

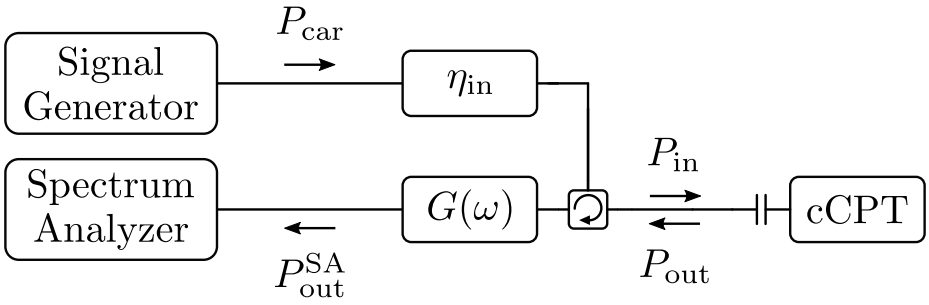

Figure 5.5: Schematic of the microwave network used to measure output power.

as shown in Section 2.4. This can be related to the power spectral density $S_{\text{out}}^{\text{SA}}$ measured by the spectrum analyzer according to

$$S_{\text{out}}^{\text{SA}}(\omega_0 \pm \omega) = \frac{2\kappa_{\text{ext}}^2}{\kappa_{\text{tot}}^2(\omega^2 + \kappa_{\text{tot}}^2/4)} \frac{G(\omega_0 \pm \omega)}{\eta_{\text{in}}} P_{\text{car}} S_{\Omega\Omega}(\omega) \tag{5.5}$$

where G is the gain of the amplifier chain, η_{in} is the input attenuation, and P_{car} is the power of the carrier signal at the fridge input. As discussed in Section 5.2, we can measure the ratio G/η_{in} at any frequency using the off-resonant transmission magnitude $|S_{21}|$ from the input to the output port of the fridge, which allows us to determine S_{out} from $S_{\text{out}}^{\text{SA}}$. In order to determine $S_{\Omega\Omega}(\omega)$ from a measurement of $S_{\text{out}}^{\text{SA}}$, however, we have to first determine the damping rates of the cCPT. This frequency noise measurement will be used in Chapter 6 to determine the power spectral density of frequency fluctuations due to charge, flux, and quantum noise, as well as those due to quasiparticle poisoning.

It is worth noting that the spectrum analyzer measures power integrated over a given resolution bandwidth B. To relate output powers to output power spectral densities, we simply divide by this resolution bandwidth (using linear units like Watts, not logarithmic units like dBm). One can always resolve a pure sinusoidal signal from the noise floor by reducing the resolution bandwidth, which reduces the noise floor but leaves the output power of the signal unchanged. This doesn't work for the output power spectral density due to frequency noise, however. In this case $S_{\text{out}}^{\text{SA}}(\omega_0 \pm \omega)$ must be larger than the noise floor (set by the amplifier noise and vacuum noise in the transmission line) in order to resolve it.

Section 5.4

Homodyne and Heterodyne Detection

We next turn to a different measurement scheme, that of homodyne and heterodyne detection [80]. In this scheme we aim to determine the amplitude and phase of a reflected signal as a function of time. This measurement is akin to measuring the reflection coefficient manually rather than using a VNA, since the VNA is designed for continuous-wave measurements rather than fast time-domain measurements. Rather than working with the amplitude $A(t)$ and phase $\theta(t)$, we often work with the in-phase $I(t)$ and quadrature $Q(t)$ components of the reflected signal instead. The two sets of quantities are just different ways of expressing a sinusoidal signal, according to

$$\begin{aligned} V(t) &= A(t)\cos\left[\omega t + \theta(t)\right] \\ &= I(t)\cos(\omega t) + Q(t)\sin(\omega t). \end{aligned} \tag{5.6}$$

In general, we assume that I and Q vary much slower than the signal frequency ω.

To perform homodyne and heterodyne detection we drive the cCPT, mix the reflected signal down to DC (for homodyne detection) or an intermediate frequency (IF, for heterodyne detection) using a local oscillator (LO), and digitize the resulting signal. This mixing step is necessary since conventional digital electronics aren't fast enough to sample waveforms in the microwave regime ($\sim$ 5 GHz). The mixer multiplies the two signals together (the RF drive and the LO), producing a signal with components at the sum and difference frequencies $\omega_{\mathrm{RF}} \pm \omega_{\mathrm{LO}}$. Finally, we use a low pass filter (LPF) to keep only the low-frequency output of the mixer. Sometimes it's also useful to further amplify the IF signal. It is crucial that all the signals used in this measurement are phase-locked, so the relative phase between the RF and LO signals remains constant over repeated measurements.

In practice we use heterodyne detection rather than homodyne detection, since DC signals are susceptible to low frequency noise and drift. We therefore focus our discussion on heterodyne detection from here on, but the line of reasoning is easily applied to homodyne detection (for which $\omega_{\mathrm{LO}} = \omega_{\mathrm{RF}}$). In our case, ω_{IF} is chosen to be as large as possible (so that changes in the reflected amplitude and phase can be resolved quickly) while being much smaller than the sampling rate of the digitizer (to avoid aliasing effects). We use an AlazarTech ATS9462 digitizer with a sampling rate of 180 MS/s, and therefore use LO signals detuned from ω_{RF} by 10 or 20 MHz.

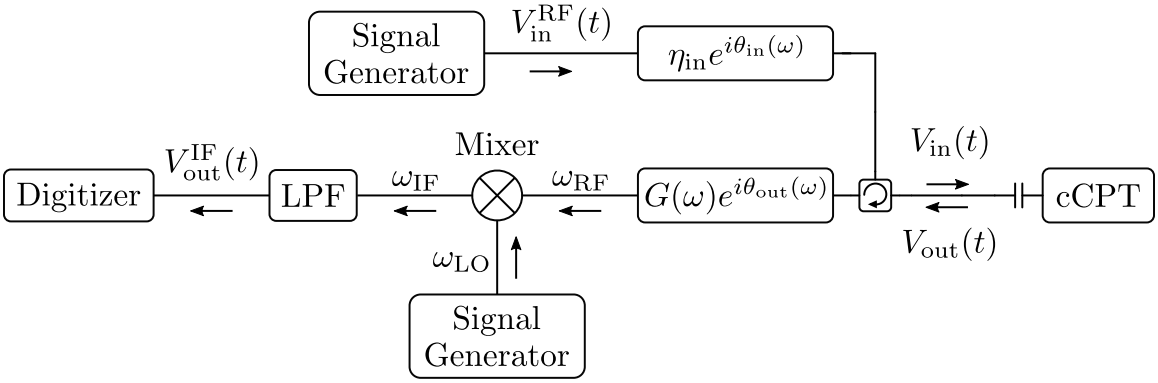

Figure 5.6: Schematic of a heterodyne detection measurement.

A schematic of the setup used to perform heterodyne detection is shown in Figure 5.6. After recording the IF signal

$$V_{\text{out}}^{\text{IF}}(t) = I(t)\cos(\omega_{\text{IF}}t) + Q(t)\sin(\omega_{\text{IF}}t) \tag{5.7}$$

we then mix it down to DC digitally in order to extract the time-averaged quantities $\overline{I}(t)$ and $\overline{Q}(t)$. This is done by multiplying the recorded waveform by a pure sine or cosine and integrating over a full period, according to

$$\overline{I}(t) = \frac{\omega_{\text{IF}}}{\pi} \int_0^{2\pi/\omega_{\text{IF}}} V_{\text{out}}^{\text{IF}}(t)\cos(\omega_{\text{IF}}t)dt \tag{5.8}$$

$$\overline{Q}(t) = \frac{\omega_{\text{IF}}}{\pi} \int_0^{2\pi/\omega_{\text{IF}}} V_{\text{out}}^{\text{IF}}(t)\sin(\omega_{\text{IF}}t)dt. \tag{5.9}$$

It is straightforward to verify that these are equivalent to the quantities $I(t)$ and $Q(t)$ for a pure sinusoidal signal. It's worth noting that this measurement scheme is sometimes called "digital homodyne detection" [80].

In practice we measure the cCPT at the single-photon level or below, which means the output signal will generally have a signal to noise ratio much less than unity (the bandwidth can't be limited too much, otherwise we won't be able to detect fast changes in I and Q). Thus, to resolve our signal from the noise we have to take an ensemble of measurements. If we average together our ensemble of measurements $V_{\text{out}}^{\text{IF}}(t)$, the noise will average out and allow us to resolve our signal.

Chapter 6

Device Characterization

In this chapter we focus on characterizing the cCPT as a function of our gate and flux parameters. Measuring the tunable resonant frequency of the cCPT is straightforward, and we find excellent agreement between our measurements and our theoretical model; however, extracting the damping rates of the cCPT is complicated by the presence of frequency fluctuations comparable in scale to the cavity linewidth. These fluctuations arise due to charge and flux noise coupling into the resonant frequency via its tunability, and quantum fluctuations of the cavity field coupling into the resonant frequency via the Kerr nonlinearity. Such fluctuations deform the ideal resonance circle (i.e., the trajectory traced out by the reflection coefficient $S_{11}(\Delta)$ in the complex plane as a function of detuning Δ) and thereby lead to systematic errors in the extracted damping rates if not properly taken into account [5]. Furthermore, the qualitative features of this deformation depend on the underlying source of frequency fluctuations. Here we report the first observation of this phenomenon both for the Gaussian-distributed frequency fluctuations due to gate and flux noise, and for the chi-square-distributed frequency fluctuations due to quantum fluctuations in the cavity field.

By using our model for the deformed resonance circles as a fitting function for experimental data, we are able to extract both the true damping rates of the cCPT and the standard deviation of frequency fluctuations σ_{ω_0} as a function of gate and flux. We find excellent agreement between σ_{ω_0} and our model for its dependence on the gate and flux parameters, from which we extract the standard deviation of the underlying charge and flux noise. To corroborate these results we directly measure the power spectral density of frequency fluctuations at both a charge-sensitive/flux-insensitive point and a charge-insensitive/flux-sensitive point, from which we determine the un-

derlying power spectral densities of charge and flux fluctuations. These power spectra follow distinct $f^{-\alpha}$ power laws where α is order unity, a common observation in solid state systems [81], likely due to fluctuating two-level systems in the case of charge noise [82, 83] and unpaired surface spins in the case of flux noise [84, 85]. We find that the scales of these power laws are in order-of-magnitude agreement with our results from fitting to the deformed resonance circles, and we discuss several limitations of comparing the two measurement schemes.

We perform most of our characterization measurements at the sub-photon level, since several of the theoretical models we use are only valid in this regime. It is therefore essential for us to determine the number of intracavity photons in-situ, which we do by measuring the power-dependent shift in the resonant frequency induced by the Kerr nonlinearity K [60, 86, 59]. This measurement both enables us to refer our input and output powers to the plane of the sample, and corroborates our model for how K varies with gate and flux.

This chapter is organized as follows. In Section 6.1 we measure the tunable resonant frequency and compare our results with theory. In Section 6.2 we present a theoretical model for how frequency fluctuations in tunable and nonlinear microwave cavities affect the measurement of scattering matrix elements (e.g., the reflection coefficient). In Section 6.3 we study the deformation of our resonance circles induced by frequency fluctuations and determine the internal and external damping rates of the cCPT by accounting for this effect. In Section 6.4 we measure the power spectral densities of charge and flux fluctuations, which corroborate our results from Section 6.3. In Section 6.5 we measure the power-dependent shift in resonant frequency due to the Kerr nonlinearity, which validates several methods used in the preceding measurements. Finally, in Section 6.6 we present some time-domain measurements that provide further insight into the effects of frequency fluctuations.

It is important to note that most of this chapter is derived from our papers: Ref. [5], our theory paper on frequency fluctuations in tunable and nonlinear microwave cavities, and Ref. [4], our experimental paper on the characterization of the cCPT using the results of the theory paper. Large sections of this chapter have been taken from these papers verbatim, but we have included additional detail in some sections and organized the content differently so it is coherent with this thesis as a whole.

Section 6.1

Tunable Resonant Frequency

We begin the characterization process by measuring the resonant frequency of the cCPT as a function of gate and flux. This tunable resonant frequency is both the most important feature of the cCPT and the simplest to measure. By comparing our results with theory we will extract the Josephson and charging energies of the cCPT, E_J and E_C respectively. In addition, this measurement will highlight a key factor limiting the operating range of the cCPT: quasiparticle poisoning.

6.1.1 Gate and Flux Periodicity

In order to compare our measurements of the resonant frequency ω_0 to theory, we must first convert our gate voltage-bias V_g and flux current-bias I_Φ to our gate and flux parameters n_g and Φ_{ext}, respectively. To perform this conversion we need the periodicity of ω_0 with respect to each of these bias parameters (i.e., the voltage difference ΔV_g corresponding to the $2e$-periodicity in n_g and the current difference ΔI_Φ corresponding to the Φ_0-periodicity in Φ_{ext}), and one point of reference for each (the voltage V_g^0 corresponding to $n_g = 0$ and the current I_Φ^0 corresponding to $\Phi_{\text{ext}} = 0$). With this information, we can convert $V_g \to n_g$ and $I_\Phi \to \Phi_{\text{ext}}$ according to

$$n_g = \frac{2e}{\Delta V_g}(V_g - V_g^0) \tag{6.1}$$

$$\Phi_{\text{ext}} = \frac{\Phi_0}{\Delta I_\Phi}(I_\Phi - I_\Phi^0). \tag{6.2}$$

To determine ΔV_g and V_g^0 we measure ω_0 as a function of V_g for fixed I_Φ, as shown in Figure 6.1. As you can see, the smooth $2e$-periodicity is broken by sharp jumps giving rise to a pseudo-$1e$-periodicity. This is due to quasiparticle poisoning, which we will discuss in detail in the next section. In the smoothly-varying parts, we empirically find that $\omega_0(V_g)$ is well-modeled by the quartic function

$$\omega_0(V_g) = A(V_g - V_g^0)^4 + B(V_g - V_g^0)^2 + C. \tag{6.3}$$

By fitting to this function we can extract the minimum-point V_g^0 for each of the two smoothly-varying parts; one of these corresponds to $n_g = 0$, the other to $n_g = 2$, and the difference corresponds to the periodicity ΔV_g. We perform this same process for

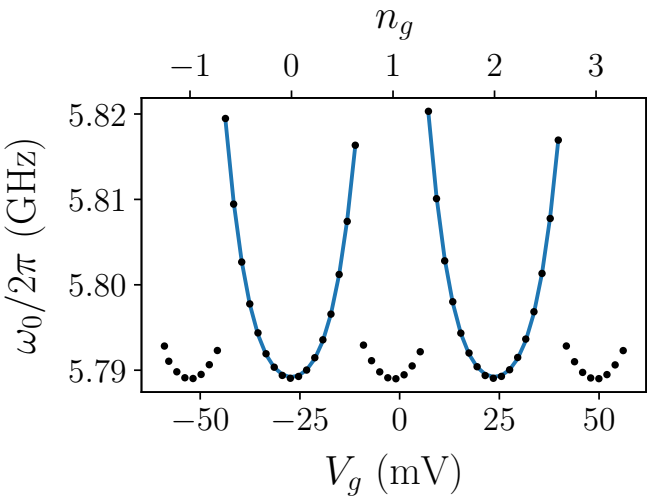

Figure 6.1: Periodicity of ω_0 with respect to the gate voltage V_g. The black dots are measured values, the blue curves are best fits to Eq. (6.3).

a full period of I_Φ to obtain the gate period ΔV_g and gate capacitance $C_g = 2e/\Delta V_g$

$$\Delta V_g = 51\,\text{mV}, \tag{6.4}$$

$$C_g = 6.3\,\text{aF}. \tag{6.5}$$

Similarly, to determine ΔI_Φ and I_Φ^0 we measure ω_0 as a function of I_Φ for fixed V_g, as shown in Figure 6.2. Empirically, we find that $\omega_0(I_\Phi)$ is well-modeled by the sinusoidal function

$$\omega_0(I_\Phi) = \omega_{\lambda/4} + A\cos\left[\frac{2\pi}{\Delta I_\Phi}(I_\Phi - I_\Phi^0)\right], \tag{6.6}$$

where $\omega_{\lambda/4}$ is the bare frequency of our $\lambda/4$ cavity. We fit to this function for each value of V_g (sampling over a full period) and extract the reference point I_Φ^0, the periodicity ΔI_Φ, and the bare cavity frequency $\omega_{\lambda/4}$. In particular, we find the periodicity ΔI_Φ and mutual inductance $M_\Phi = \Phi_0/\Delta I_\Phi$ (between the current-bias line and the SQUID loop) to be

$$\Delta I_\Phi = 49\,\mu\text{A}, \tag{6.7}$$

$$M_\Phi = 42\,\text{pH}, \tag{6.8}$$

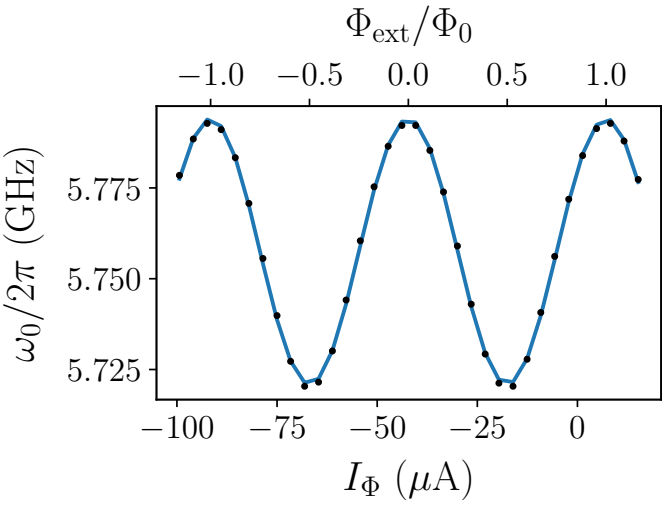

Figure 6.2: Periodicity of ω_0 with respect to the flux current-bias I_Φ. Black dots are measured values, the blue curve is the best fit to Eq. (6.6).

and the bare cavity frequency to be

$$\omega_{\lambda/4} = 2\pi \times 5.757\,\text{GHz}. \tag{6.9}$$

Although these periodicities only have to be determined once, since they are determined by the geometry of the sample, the reference points V_g^0 and I_Φ drift over time and have to be calibrated regularly. Having now detailed how this calibration is performed, we will work in terms of the gate and flux parameters n_g and Φ_{ext} from here on. Our measured values of $\omega_0(n_g, \Phi_{\text{ext}})$, over multiple periods of each parameter, are shown in Figure 6.3.

6.1.2 Quasiparticle Poisoning

As discussed in the previous section, a prominent feature of $\omega_0(n_g, \Phi_{\text{ext}})$ is the presence of sudden jumps when $|(n_g - 1) \mod 2| \approx 0.3$ due to quasiparticle poisoning [22]. Near these points, the decrease in energy obtained from the transition $n_g \to n_g + 1$ is comparable to the energy required for quasiparticles to tunnel onto the island, so quasiparticles can tunnel back and forth [71]. The latter energy scale is the difference between the superconducting gaps of the island and the leads, $\delta\Delta = \Delta_i - \Delta_l$, which arises in our case due to the island's thickness of 9 nm relative to the leads' thickness of 65 nm [69, 70]. We refer to the state with no excess quasiparticles on

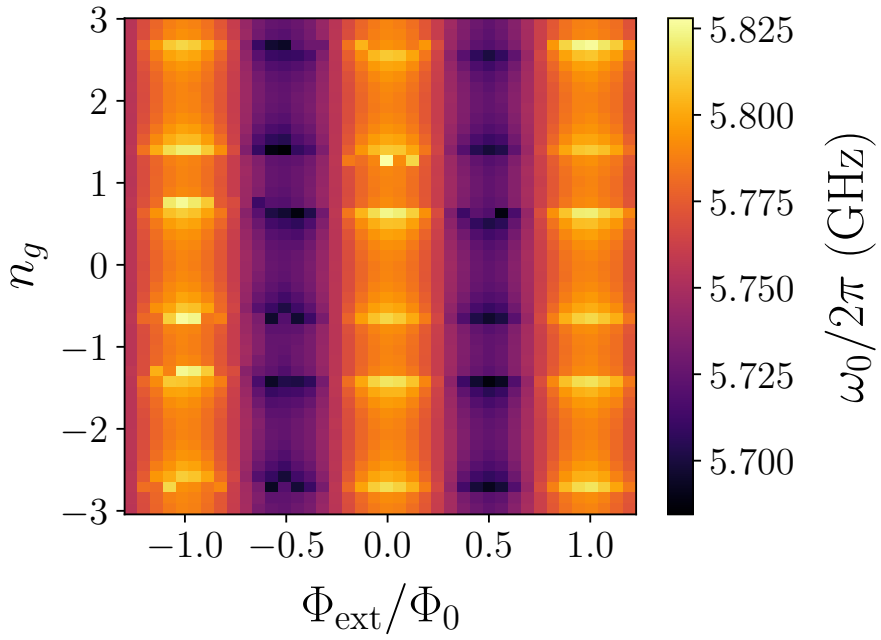

Figure 6.3: Tunable resonant frequency $\omega_0(n_g, \Phi_{\text{ext}})$ over multiple periods of each parameter.

the island as the "even-parity state" and the state with one excess quasiparticle the "odd-parity state." The energies of these two states are given by

$$E_{\text{even}} = E_{\text{CPT}}(n_g, \Phi_{\text{ext}}), \tag{6.10}$$

$$E_{\text{odd}} = E_{\text{CPT}}(n_g \pm 1, \Phi_{\text{ext}}) + \delta\Delta. \tag{6.11}$$

Closer to $n_g \equiv 0 \mod 2$ the even parity ground state is energetically favorable ($E_{\text{even}} \ll E_{\text{odd}}$) and quasiparticles are expelled from the island, whereas closer to $n_g \equiv 1 \mod 2$ the odd parity ground state is energetically favorable ($E_{\text{odd}} \ll E_{\text{even}}$) and quasiparticles are trapped on the island.

The two states become equiprobable at the critical gate charge $n_g^c \approx 0.7$ such that

$$E_{\text{CPT}}(n_g^c, \Phi_{\text{ext}}) - E_{\text{CPT}}(n_g^c \pm 1, \Phi_{\text{ext}}) = \delta\Delta. \tag{6.12}$$

We note that for $E_C > E_J$ the left hand side of the above equation does not vary appreciably with Φ_{ext}, which is why the threshold n_g^c does not vary appreciably with Φ_{ext} either. Near this threshold, random switching occurs between the even and odd parity states. When measured with a VNA, this switching manifests itself as

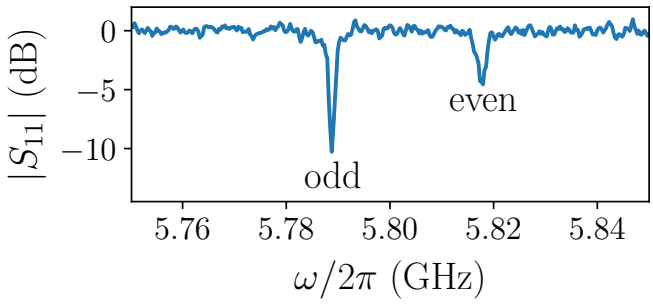

Figure 6.4: VNA trace of $|S_{11}|$ at the quasiparticle poisoning threshold $(n_g, \Phi_{\text{ext}}) = (0.7, 0)$, showing both the even and odd parity resonances.

two visible resonances as shown in Figure 6.4. The blockiness of Fig.6.3 around the transition points $|n_g| \approx 0.7$ is the result of identifying only one of these two resonant frequencies. We can measure the power spectral density of these frequency-switching events using the measurement scheme discussed in Section 5.3; the results of this measurement are presented in Section 6.4, which provides better context.

6.1.3 Josephson and Charging Energies

Thus, quasiparticle poisoning prevents us from operating at gate values above $|n_g| \gtrsim 0.7$. For our remaining measurements we restrict ourselves to the region $-0.65 \leq n_g \leq 0.65$ to avoid the effects of quasiparticle poisoning. In this region we can fit our theoretical model for the tunable resonant frequency

$$\omega_0(n_g, \Phi_{\text{ext}}) = \omega_{\lambda/4} + \frac{\phi_{\text{zp}}^2}{\hbar} \partial_\phi^2 E_{\text{CPT}}(n_g, \Phi_{\text{ext}}) \tag{6.13}$$

to our measurements of $\omega_0(n_g, \Phi_{\text{ext}})$ to extract E_J and E_C. As shown in Figure 6.5, we find excellent agreement between theory and experiment, and obtain the best fit parameters

$$\begin{aligned} E_J/h &= 14.80 \pm 0.04\,\text{GHz} \\ E_C/h &= 54.1 \pm 0.2\,\text{GHz}. \end{aligned} \tag{6.14}$$

It is important to note that given these values for E_J and E_C, the Kerr nonlinearity can now be calculated using Eq. (4.50).

The Josephson energy can be written in terms of the normal-state resistance R_n

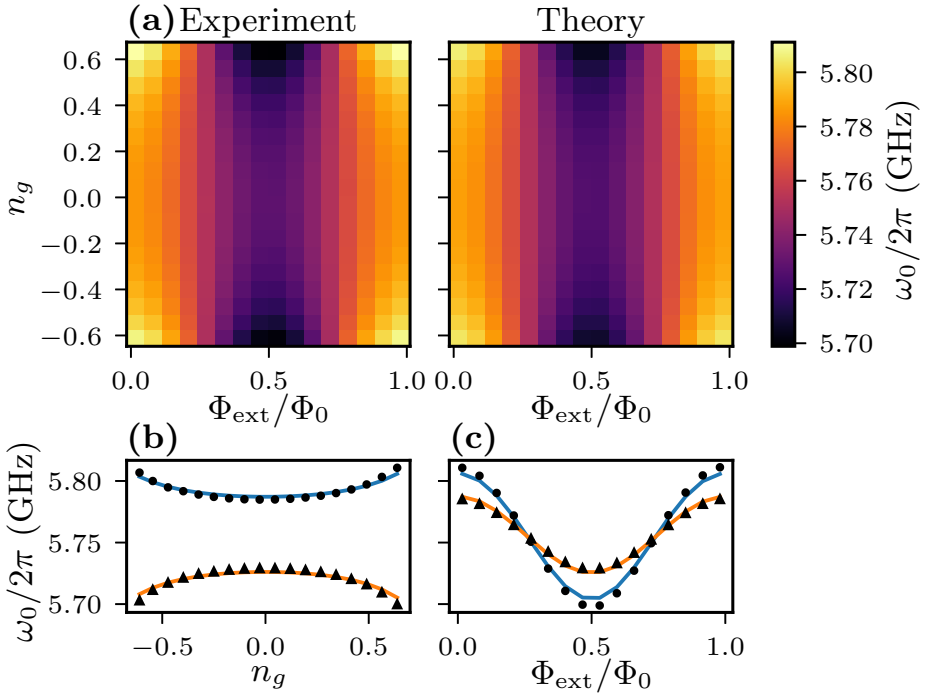

Figure 6.5: (a) Measured resonant frequency $\omega_0(n_g, \Phi_{\text{ext}})$ and the best fit to Eq. (6.13). Cross-sections of (a) are plotted in (b) and (c). In (b), circles correspond to $\Phi_{\text{ext}} = 0$ and triangles correspond to $\Phi_{\text{ext}} = \Phi_0/2$. In (c), circles correspond to $n_g = 0.64$ and triangles correspond to $n_g = 0$. Solid lines are the corresponding cross-sections of the best fit.

of each junction

$$E_J = \frac{h\Delta_{\text{Al}}}{8e^2 R_n} \tag{6.15}$$

using the Ambegaokar-Baratoff formula [63], where Δ_{Al} is the superconducting gap energy of aluminum. This extracted value of the Josephson energy is consistent with the normal resistance of each junction, which is about $10 - 20$ kΩ. This resistance cannot be measured directly on the sample we are studying, since the source and drain of the CPT are shorted with respect to dc signals. Rather, this estimate of the normal resistance is based on devices we made to hone the fabrication recipe, which were designed to allow such a dc measurement. Similarly, the charging energy can be written in terms of the area A and thickness d of the junctions

$$E_C = \frac{e^2}{4}\frac{d}{\epsilon A}, \tag{6.16}$$

where ϵ is the dielectric constant of aluminum oxide. This extracted value of the

charging energy is consistent with 50×50 nm^2 junctions whose oxide layer is about 1 nm thick.

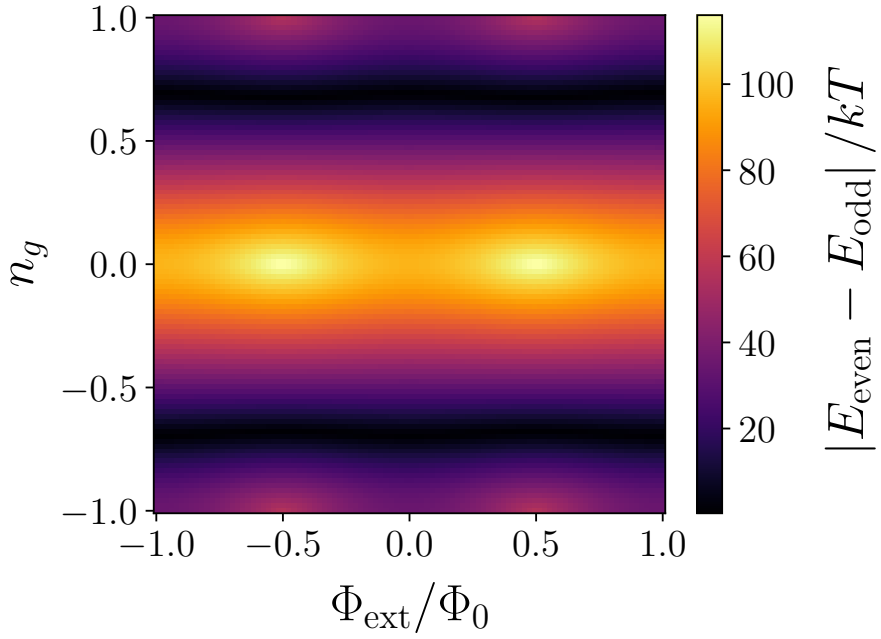

Figure 6.6: Energy difference between the even- and odd-parity states as a function of gate and flux, for $\delta\Delta = 80$ μeV. The scale of thermal fluctuations is set by $T \approx 30$ mK.

This agreement between our expected and extracted values of E_J and E_C also helps to corroborate the value of $\phi_{\text{zp}} \approx 0.176$. If the actual value of ϕ_{zp} differed considerably from 0.176 we would have obtained best fits for E_J and E_C that differed considerably from their expected values as well, since the tunable resonant frequency is proportional to ϕ_{zp}^2. We can further corroborate this value for ϕ_{zp} by plugging our best fit values for E_J and E_C back into Eq. (6.12), which is independent of ϕ_{zp}. Doing so, we estimate the difference between the superconducting gap energies of the island and the leads to be $\delta\Delta \approx 80$ μeV, consistent with our expectations based on the literature [69, 70]. As with the normal resistance, a direct measurement of the superconducting gaps of the island and leads cannot be made via dc transport measurements, since the source and drain of the CPT are shorted with respect to dc signals. The difference in energies between the even- and odd-parity states as a function of n_g and Φ_{ext} is shown in Fig. 6.6 for this value of the gap difference $\delta\Delta$. As you can see, the energy difference goes to zero at our critical gate value $|n_g^c| \approx 0.7$

and the energy difference is only smaller than the scale of thermal fluctuations for a small window around this value, consistent with our observations.

Qualitatively, the polynomial dependence of ω_0 on n_g in Fig. 6.5(b) arises from the charging energy term in the CPT Hamiltonian (Eq. 4.3), while the sinusoidal dependence of ω_0 on Φ_{ext} in Fig. 6.5(c) arises from the Josephson energy term. This behavior underscores our choice of E_C and E_J. The present device was designed to optimize its charge sensitivity by maximizing $\partial\omega_0/\partial n_g$, which tends to increase with the ratio E_C/E_J [2, 44]. We therefore tried to maximize E_C by minimizing the cross-sectional area of the JJs, and aimed for a Josephson energy that satisfies $\hbar\omega_0 < E_J < E_C$ to maintain the validity of the ground-state approximation discussed in Sec. 4.2. For other uses, a different regime of E_C and E_J may be optimal.

Section 6.2

Frequency Fluctuations in Tunable and Nonlinear Cavities

We next seek to determine the damping rates of the cCPT. As we will see, however, the standard method for extracting the damping rates of the cCPT yields values for κ_{int} and κ_{ext} that vary significantly with our tuning parameters n_g and Φ_{ext}. This observation of tuning-dependent damping rates is a common issue in a wide variety of tunable cavities [87, 88, 86, 89, 90, 91]. Although many have attributed this to causes specific to their devices, this trend suggests an underlying mechanism related to the tunability itself. Motivated by this trend, we develop a model for how frequency fluctuations in tunable and nonlinear microwave cavities give rise to inhomogeneous broadening that can easily be mistaken for changes in damping rates, providing a potential explanation of the aforementioned observations in the literature. The model we develop for this effect will enable us to determine both the true damping rates of the cCPT and the scale of frequency fluctuations present in the cCPT. It is important that we determine the two independently, since frequency fluctuations give rise to dephasing rather than energy loss [92], and these have different effects on the dynamics of the cCPT.

Much of this section is taken verbatim from our theory paper on the subject (Ref. [5]), but threaded together to be coherent with the broader scope of this thesis. Here we provide additional experimental data from the cCPT to motivate the work, but we consider generic systems in our theoretical treatment. In Section 6.3 we apply this

theory to measurements of the cCPT.

6.2.1 Apparent Tuning-dependent Loss

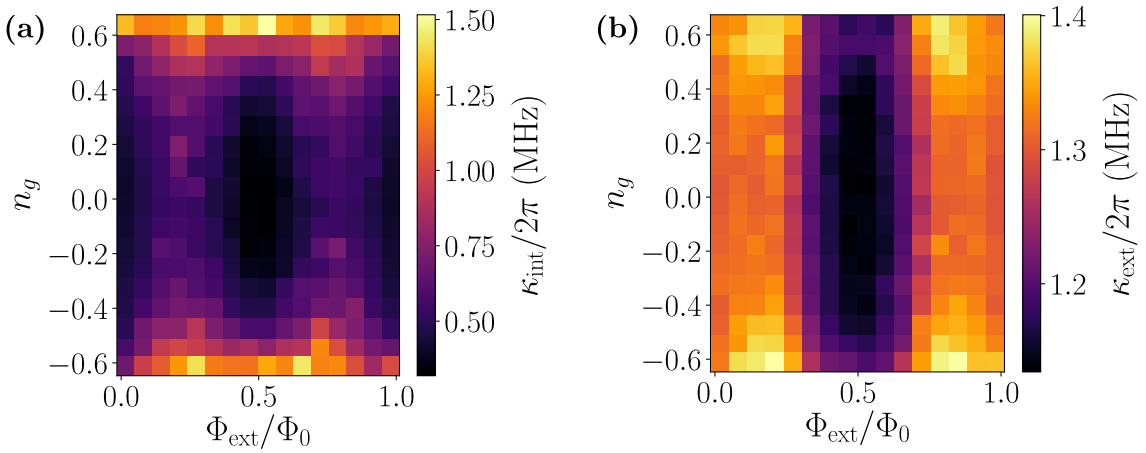

Figure 6.7: Apparent internal and external damping rates κ_{int} and κ_{ext} obtained by fitting measured traces $S_{11}(\Delta)$ to Eq. (6.17).

We first try to extract the damping rates by measuring the reflection coefficient $S_{11}(\Delta)$ and fitting to our model

$$S_{11}(\Delta) = \frac{\Delta - i\left(\kappa_{\text{int}} - \kappa_{\text{ext}}\right)/2}{\Delta - i\left(\kappa_{\text{int}} + \kappa_{\text{ext}}\right)/2} \tag{6.17}$$

derived in Section 2.3, which works well for bare $\lambda/4$ cavities. We perform this measurement as a function of n_g and Φ_{ext} to obtain the internal and external damping rates (κ_{int} and κ_{ext}) shown in Figure 6.7. Clearly, both κ_{int} and κ_{ext} appear to vary significantly with our tuning parameters n_g and Φ_{ext}.

One possible reason for this dependence on the CPT tuning parameters is an additional resistive loss channel due to transport across the CPT. In this case we would expect the damping rates to depend implicitly on the current flowing through the CPT. The current flowing through the CPT as a whole is just the average current flowing through each junction, which takes the form

$$I_{\text{CPT}} = \frac{1}{2} I_c \left[\sin(\varphi_1) + \sin(\varphi_2)\right] = I_c \sin(\overline{\varphi}) \cos(\delta\varphi). \tag{6.18}$$

Since the CPT is in its ground state, we can calculate this current as a function of

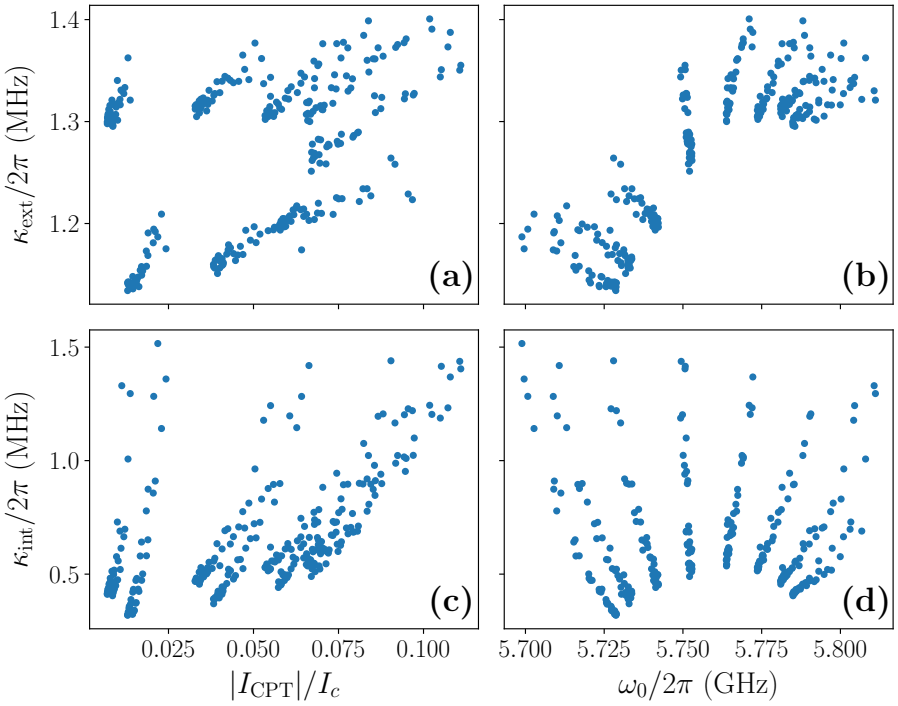

Figure 6.8: The apparent internal and external damping rates κ_{int} and κ_{ext}, taken from Figure 6.7(a) and 6.7(b) respectively, plotted parametrically vs (a,c) $I_{\text{CPT}}(n_g, \Phi_{\text{ext}})$ and (b,d) $\omega_0(n_g, \Phi_{\text{ext}})$.

gate and flux according to

$$I_{\text{CPT}}(n_g, \Phi_{\text{ext}}) = \frac{1}{2} I_c \sin\left(\frac{\pi}{\Phi_0}\Phi_{\text{ext}}\right) \left\langle \sum_{N=-\infty}^{\infty} \Big(|N+1\rangle\langle N| + |N\rangle\langle N+1| \Big) \right\rangle, \tag{6.19}$$

where the expectation value is taken with respect to the ground state of the CPT (which depends on n_g and Φ_{ext}). In Fig. 6.8(a,c) we plot κ_{int} and κ_{ext} parametrically vs I_{CPT}, but we find no implicit dependence of the damping rates on the current flowing through the CPT; for each value of I_{CPT} the damping rates take on a wide range of values.

Another possible reason for the apparent dependence of the damping rates on the CPT tuning parameters is that the physical properties of the system and/or its environment (such as characteristic impedances) could be varying with the operating frequency. In this case we would expect these quantities to depend implicitly on the resonant frequency $\omega_0(n_g, \Phi_{\text{ext}})$. In Fig. 6.8(b,d) we plot κ_{int} and κ_{ext} parametrically vs ω_0, but we find no such implicit dependence.

Thus, the damping rates of the cCPT appear to depend *explicitly* on the tuning parameters, which is unintuitive. As mentioned earlier, such tuning-dependent damping rates are commonly reported in a wide variety of tunable cavities [87, 88, 86, 89, 90, 91]. Although many have attributed this to causes specific to their devices, here we argue that the tunability itself is at least partially responsible for these observations. The line of reasoning is as follows: fluctuations in the tuning parameter will necessarily induce fluctuations in the resonant frequency. These frequency fluctuations will in turn affect the measurement of scattering matrix elements (e.g., reflection and transmission coefficients), which is a standard method for extracting the damping rates of microwave cavities [7, 8]. A similar line of reasoning holds for cavities with a Kerr nonlinearity: fluctuations in the amplitude of the intra-cavity field will lead to steady-state fluctuations in the resonant frequency, though this effect does not lead to an easily identifiable consequence in the literature as in the case of tunability.

Thus, to accurately determine the damping rates of these cavities from scattering measurements, one must account for the effect of frequency fluctuations. We proceed to develop a model for this effect, which in the case of tunable cavities both predicts the apparent dependence of the cavity's damping rates on the tuning parameter and allows one to extract the true damping rates in the presence of these frequency fluctuations. Similarly, in the case of a cavity with a Kerr nonlinearity we analyze the quantum limit of steady-state frequency fluctuations and show that the apparent damping rates can deviate significantly from their true values as the nonlinearity approaches the cavity linewidth. In both cases we provide bounds on the scale of the fluctuations necessary to yield greater than 10% inaccuracy in the apparent damping rates relative to their true values. Finally, we analyze how these two sources of fluctuations come together in the case of a tunable cavity with a Kerr nonlinearity. We expect the use of this model as a fitting function for experimental scattering measurements will allow for more accurate characterization of tunable and nonlinear cavities moving forward.

6.2.2 Average Scattering Matrix Elements

Let $S_{jk}(\Delta)$ be the scattering matrix elements of the microwave network containing the cavity [6], describing an experiment in which the cavity is driven by a sinusoidal signal on port k and measured on port j, where $\Delta = \omega - \omega_0$ is the detuning of the drive from resonance. In general, measuring these scattering matrix elements involves

a process of averaging, whether implicitly through the time-scale associated with individual measurements or explicitly through the incorporation of multiple independent measurements. The process of characterizing a cavity then consists of measuring this average value of $S_{jk}(\Delta)$ for a range of detunings around the resonant frequency and comparing these results with a theoretical model to extract the damping rates.

In the presence of fluctuations in the resonant frequency, however, $\omega_0 \rightarrow \omega_0 + \delta\omega_0(t)$ such that the detuning Δ may vary over the course of this measurement. Rather than attempting to take into account the time dependence of $\delta\omega_0$ explicitly, we treat these fluctuations as a random variable and model their effect on $S_{jk}(\Delta)$ as an ensemble average. As a result, in the presence of a fluctuating resonant frequency what will actually be measured is the convolution

$$\overline{S_{jk}}(\Delta) = \int_{-\infty}^{\infty} S_{jk}(\Delta - \Omega) P(\Omega) d\Omega \tag{6.20}$$

where $P(\Omega)$ is the probability density function (PDF) associated with drawing the value Ω from the random variable $\delta\omega_0$.

There are two generic features of this convolution worth discussing. First, the average quantity $\overline{S_{jk}}(\Delta)$ will be sensitive to those fluctuations occurring faster than the measurement time and insensitive to those occurring slower than it. For example, if we can measure $\overline{S_{jk}}(\Delta)$ faster than a given source of frequency noise then our measurement will not be influenced by this noise. Thus, $P(\Omega)$ should depend on the power spectral density of the frequency fluctuations and the time-scale associated with the measurement. In particular, since the power spectral density $S_{\omega_0\omega_0}(f)$ is simply the variance per unit frequency, the variance $\sigma^2_{\omega_0}$ of frequency fluctuations can be found by integrating over all frequencies f. For a real measurement, however, the low frequency cutoff is set by the inverse of the time T spent measuring $S_{jk}(\Delta)$ at a fixed detuning and the high frequency cutoff is set by the total linewidth of the cavity $\kappa_{\text{tot}}/2\pi$, which determines the maximum rate of cavity response, such that

$$\sigma^2_{\omega_0} = \int_{1/T}^{\kappa_{\text{tot}}/2\pi} S_{\omega_0\omega_0}(f) df. \tag{6.21}$$

We note that it may be possible to extend this simple connection using the Allan variance [93], which accounts for dead time between measurements and is well-behaved

with respect to the $1/f$ power spectra that are ubiquitous in solid state devices [81], but whose underlying formalism may not directly carry over to the scattering measurements we are considering.

Second, these scattering matrix elements $S_{jk}(\Delta)$ generally take the form of linear fractional transformations that trace out circles in the complex plane [94]. Since the convolution is essentially a convex combination of points around this circle, the shape traced out by $\overline{S_{jk}}(\Delta)$ will be smaller by comparison, corresponding to apparent changes in the damping rates. We operationalize the notion of 'apparent damping rates' by considering the best fit of the non-fluctuating model $S_{jk}(\Delta)$ to data generated by the fluctuating model $\overline{S_{jk}}(\Delta)$.

The effect of this convolution can be thought of as a form of inhomogeneous broadening, in that we are effectively averaging over the response functions of an ensemble of cavities with different resonant frequencies. Similar effects show up in a diverse range of fields, but there are two examples in the same vein as our work worth noting. First is the Doppler broadening of Lorentzian spectral lines, in which case one obtains a Voigt Profile [95, 96]. Second is the broadening of cavity lineshapes due to a linear coupling with an ensemble of spins that serve as a noisy driving field [97]. Here we apply similar methods to understand the effect of tunability and nonlinearity on the lineshapes of microwave cavities.

Although the above analysis could be applied to any microwave network containing a cavity, here we will consider the two-sided cavity that we analyzed in Section 2.3.2. The scattering matrix elements of this cavity can be written

$$S_{jk}(\Delta; \kappa_{\text{tot}}, r_{jk}) = \delta_{jk} - r_{jk}\left(1 + e^{-2i\arctan(2\Delta/\kappa_{\text{tot}})}\right) \tag{6.22}$$

where δ_{jk} is the Kronecker delta and the radii r_{jk} are given by

$$\begin{aligned} r_{12} = r_{21} &= \frac{\sqrt{\xi}}{1+\xi} \\ r_{11} = 1 - r_{22} &= \frac{\xi}{1+\xi} \end{aligned} \tag{6.23}$$

and $\xi = \kappa_{\text{ext}}/\kappa_{\text{int}}$ is the coupling ratio. This is a convenient expression for analyzing all of the scattering matrix elements at once, since they are equivalent up to translation and a rescaling of r_{jk}. It is worth noting that in order to retrieve ξ from r_{12} or r_{21} one must additionally specify whether $\xi > 1$ or $\xi < 1$, since they are invariant under $\xi \to 1/\xi$.

6.2.3 Tunable Cavity

We now consider a cavity whose resonant frequency ω_0 is a function of tuning parameter x such that $\omega_0 = \omega_0(x)$. In general, this tuning parameter can never be perfectly fixed: it will always fluctuate around its mean value. To model this effect, let $x \to \overline{x} + \delta x$, where $\overline{x}$ is the mean value of x and δx is a random variable describing fluctuations of x about $\overline{x}$, which we assume to be Gaussian with mean zero and variance σ_x^2. Expanding to lowest order in these fluctuations, we find

$$\omega_0(\overline{x} + \delta x) \approx \omega_0(\overline{x}) + \delta\omega_0(\overline{x}) \tag{6.24}$$

where the second term

$$\delta\omega_0(\overline{x}) = \frac{\partial\omega_0(\overline{x})}{\partial x}\delta x \tag{6.25}$$

is itself a Gaussian random variable with mean zero and variance $\sigma_{\omega_0}^2$ given by

$$\sigma_{\omega_0}^2 = \left|\frac{\partial\omega_0(\overline{x})}{\partial x}\right|^2 \sigma_x^2 \tag{6.26}$$

which varies with $\overline{x}$. The PDF associated with drawing the value Ω from the random variable $\delta\omega_0$ is therefore given by

$$P(\Omega) = \frac{1}{\sqrt{2\pi\sigma_{\omega_0}^2}} e^{-\Omega^2/2\sigma_{\omega_0}^2}. \tag{6.27}$$

In the presence of these fluctuations, the average scattering matrix elements are found by plugging Eqs. (6.22) and (6.27) into Eq. (6.20). This convolution results in the closed form expression

$$\overline{S_{jk}}(\Delta; \kappa_{\text{tot}}, r_{jk}, \sigma_{\omega_0}) = \delta_{jk} - r_{jk}\sqrt{\frac{\pi}{2}}\frac{\kappa_{\text{tot}}}{\sigma_{\omega_0}} w\left(\frac{i\kappa_{\text{tot}} - 2\Delta}{2\sqrt{2}\sigma_{\omega_0}}\right) \tag{6.28}$$

where $w(z)$ is the Faddeeva function, which can be written in terms of the complementary error function as $w(z) = e^{-z^2}\text{erfc}(-iz)$ [98]. As illustrated in Fig. 6.9(a), the effect of these fluctuations is a deformation of the trajectories of S_{jk} in the complex plane. Compared to $S_{jk}(\Delta; \kappa_{\text{tot}}, r_{jk})$, $\overline{S_{jk}}(\Delta; \kappa_{\text{tot}}, r_{jk}, \sigma_{\omega_0})$ is slightly oblong, its apparent radius is smaller, and it traverses its path more slowly as a function of detuning (corresponding to an apparent increase in κ_{tot}). Furthermore, although there is a systematic deviation between the closest fit of $S_{jk}(\Delta; \kappa'_{\text{tot}}, r'_{jk})$ to the trajectory

generated by $\overline{S_{jk}}(\Delta;\kappa_{\rm tot},r_{jk},\sigma_{\omega_0})$, this deviation is subtle. It is even more subtle, in fact, if one considers only the squared magnitude of S_{jk} rather than its full complex trajectory as is sometimes done [7, 17, 88].

Thus, presented with experimental data for which frequency fluctuations are significant, it is quite reasonable to believe it is well-modeled by $S_{jk}(\Delta;\kappa'_{\rm tot},r'_{jk})$. If one tries to fit this model to the data, however, one will extract damping rates that appear to vary with σ_{ω_0}, as illustrated in Fig. 6.9(b). In the case of a tunable cavity for which $\sigma_{\omega_0}=|\partial\omega_0(\overline{x})/\partial x|\sigma_x$, one will therefore find damping rates that seem to vary with $\overline{x}$, which is precisely the syndrome we set out to explain. By using this model $\overline{S_{jk}}(\Delta;\kappa_{\rm tot},r_{jk},\sigma_{\omega_0})$ as a fitting function for experimental data, however, both the true damping rates and the scale of frequency fluctuations can be determined.

We emphasize that these fluctuations will always couple into the system as given by Eqs. (6.24) - (6.26), but they will not always be significant enough to require the use of the fluctuating model $\overline{S_{jk}}(\Delta;\sigma_{\omega_0})$. The relevant frequency scale for a two-sided cavity is $\kappa_{\rm tot}$, as seen in Fig. 6.9(b): when $\sigma_{\omega_0}\ll\kappa_{\rm tot}$, the apparent and actual damping rates coincide. As a benchmark in the intermediate case, one must have $\sigma_{\omega_0}\lesssim 0.17\kappa_{\rm tot}$ in order for both the apparent $\kappa'_{\rm tot}$ and r'_{jk} to deviate from their true values $\kappa_{\rm tot}$ and r_{jk} by less than 10%.

Even when $\sigma_{\omega_0}\ll\kappa_{\rm tot}$, however, frequency fluctuations may still have a non-negligible effect on the apparent damping rates of the cavity. At maxima and minima of $\omega_0(\overline{x})$, for example, σ_{ω_0} will vanish and fluctuations in x will only affect the resonant frequency to second order such that

$$\delta\omega_0(\overline{x})=\frac{1}{2}\frac{\partial^2\omega_0(\overline{x})}{\partial x^2}\delta x^2. \tag{6.29}$$

Making the same assumption that δx is Gaussian distributed with mean zero and variance σ_x^2, these fluctuations will follow a chi squared distribution with one degree of freedom. If we define the scale associated with these fluctuations to be

$$D=\frac{\sigma_x^2}{2}\frac{\partial^2\omega_0(\overline{x})}{\partial x^2} \tag{6.30}$$

then the probability distribution associated with this random variable can be expressed as

$$P(\Omega)=\frac{1}{\sqrt{2\pi D\Omega}}e^{-\Omega/2D}\Theta(\Omega/D) \tag{6.31}$$

where Θ is the Heaviside step function, such that $P(\Omega)$ has support on either the

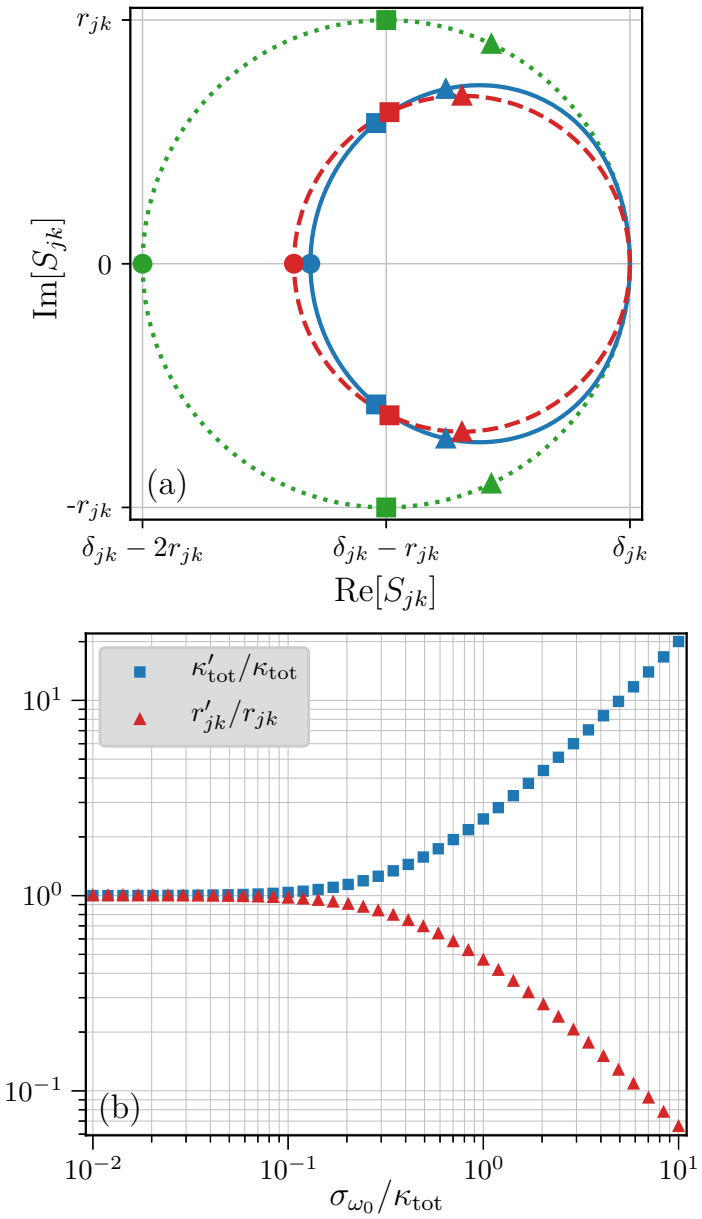

Figure 6.9: The effect of tuning fluctuations expanded to first order on the scattering matrix elements S_{jk}. (a) Visualization of the deformed resonance circle. Dotted green line: $S_{jk}(\Delta; \kappa_{\mathrm{tot}}, r_{jk})$. Solid blue line: $\overline{S_{jk}}(\Delta; \kappa_{\mathrm{tot}}, r_{jk}, \sigma_{\omega_0})$ with $\sigma_{\omega_0} = \kappa_{\mathrm{tot}}/2$. Dashed red line: best fit of $S_{jk}(\Delta; \kappa'_{\mathrm{tot}}, r'_{jk})$ to the solid blue trajectory, where $\kappa'_{\mathrm{tot}} \approx 1.6\kappa_{\mathrm{tot}}$ and $r'_{jk} \approx 0.69 r_{jk}$. Circles mark $\Delta = 0$, squares mark $\Delta = \pm\kappa_{\mathrm{tot}}/2$, and triangles mark $\Delta = \pm\kappa'_{\mathrm{tot}}/2$. (b) Results of fitting the model $S_{jk}(\Delta; \kappa'_{\mathrm{tot}}, r'_{jk})$ to data generated by $\overline{S_{jk}}(\Delta; \kappa_{\mathrm{tot}}, r_{jk}, \sigma_{\omega_0})$. The best fit parameters κ'_{tot} and r'_{jk} quantify the notion of 'apparent damping rates.'

positive or negative real axis depending on the sign of D. Performing the convolution given by Eq. (6.20) for this case, we find

$$\overline{S_{jk}}(\Delta;\kappa_{\text{tot}},r_{jk},D)=\delta_{jk}-ir_{jk}\frac{\sqrt{\pi}}{2}\frac{\kappa_{\text{tot}}}{D}\frac{w\left(i\sqrt{(i\kappa_{\text{tot}}-2\Delta)/4D}\right)}{\sqrt{(i\kappa_{\text{tot}}-2\Delta)/4D}} \tag{6.32}$$

where the branch cut can be made on the negative real axis without any issue since $\kappa_{\text{tot}}>0$.

As can be seen in Fig. 6.10(a), the effect of these fluctuations is a deformation of S_{jk} that once again leads to an increase in the apparent total damping rate κ_{tot} and a decrease in the apparent radius r_{jk}. Unlike the case of Gaussian fluctuations, however, $\overline{S_{jk}}(\Delta;\kappa_{\text{tot}},r_{jk},D)$ is now asymmetric with respect to the real axis as a result of the probability distribution only having support over the positive or negative reals, which also gives rise to an apparent shift in the resonant frequency. We have only displayed the case of $D>0$ for simplicity; the corresponding trajectory for $D<0$ can be visualized using the relationship

$$\overline{S_{jk}}(\Delta;\kappa_{\text{tot}},r_{jk},-D)=\overline{S_{jk}}(-\Delta;\kappa_{\text{tot}},r_{jk},D)^* \tag{6.33}$$

which amounts to reflecting the shape of the trajectory across the real axis and traversing it in the same clockwise orientation. As before, we obtain the apparent cavity parameters as a function of D by fitting the model $S_{jk}(\Delta';\kappa'_{\text{tot}},r'_{jk})$ to data generated by $\overline{S_{jk}}(\Delta;\kappa_{\text{tot}},r_{jk},D)$, the results of which are displayed in Fig. 6.10(b). In this case, we find that in order for the apparent κ'_{tot} and r'_{jk} to both be within 10% of their true values κ_{tot} and r_{jk}, we must have $|D|\lesssim 0.14\kappa_{\text{tot}}$.

Thus, if we tune the cavity to a point $\overline{x}_0$ where $\sigma_{\omega_0}(\overline{x}_0)=0$ and $|D(\overline{x}_0)|\ll\kappa_{\text{tot}}$, the effect of frequency fluctuations will be negligible and we can extract the correct damping rates of the cavity using the non-fluctuating model $S_{jk}(\Delta)$. In certain cases it may be sufficient to characterize the cavity only at such points, but in many cases it may be either preferable or necessary to characterize the system over a wide range of the tuning parameter $\overline{x}$. For example, if the cavity is tunable over a range of frequencies far greater than its linewidth then the physical properties of both the system and its environment (such as characteristic impedances) are likely to vary appreciably with the operating frequency $\omega_0(\overline{x})$, leading to frequency-dependent damping rates. This model for $\overline{S_{jk}}$ allows one to extract this dependence without it being obscured by the presence of frequency fluctuations.

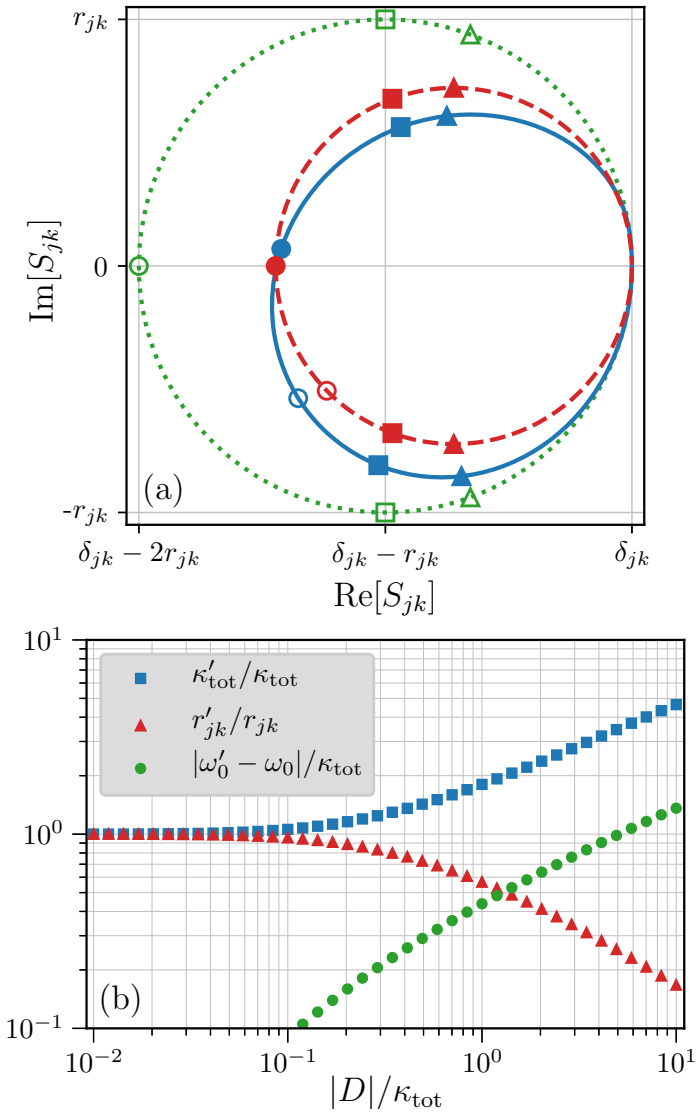

Figure 6.10: The effect of tuning fluctuations expanded to second order on the scattering matrix elements S_{jk}. (a) Visualization of the deformed resonance circle. Dotted green line: $S_{jk}(\Delta; \kappa_{\mathrm{tot}}, r_{jk})$. Solid blue line: $\overline{S_{jk}}(\Delta; \kappa_{\mathrm{tot}}, r_{jk}, D)$ with $D = \kappa_{\mathrm{tot}}/2$. Dashed red line: best fit of $S_{jk}(\Delta'; \kappa'_{\mathrm{tot}}, r'_{jk})$ to the solid blue trajectory where $\omega'_0 - \omega_0 \approx 0.29\kappa_{\mathrm{tot}}$, $\kappa'_{\mathrm{tot}} \approx 1.4\kappa_{\mathrm{tot}}$, and $r'_{jk} \approx 0.72 r_{jk}$. Hollow circles mark $\Delta = 0$, hollow squares mark $\Delta = \pm\kappa_{\mathrm{tot}}/2$, and hollow triangles mark $\Delta = \pm\kappa'_{\mathrm{tot}}/2$. Filled shapes mark the corresponding points for Δ'. (b) Results of fitting the model $S_{jk}(\Delta'; \kappa'_{\mathrm{tot}}, r'_{jk})$ to data generated by $\overline{S_{jk}}(\Delta; \kappa_{\mathrm{tot}}, r_{jk}, D)$. Values of $|\omega'_0 - \omega_0| < \kappa_{\mathrm{tot}}/10$ have been omitted for clarity.

6.2.4 Kerr Cavity

We next consider a cavity with a Kerr nonlinearity K, such that the system Hamiltonian takes the form

$$H_{\text{sys}} = \hbar\omega_0 a^\dagger a + \frac{\hbar K}{2} a^{\dagger 2} a^2. \tag{6.34}$$

The quantum Langevin equation for the operator a then becomes

$$\dot{a}(t) = -i\left[\omega_0 + K a^\dagger(t) a(t)\right] a(t) - \frac{\kappa_1 + \kappa_2}{2} a(t) + \sqrt{\kappa_1} a_1^{\text{in}}(t) + \sqrt{\kappa_2} a_2^{\text{in}}(t) \tag{6.35}$$

from which we see that the resonant frequency of the cavity depends on the state of the cavity according to

$$\omega_0(a, a^\dagger) = \omega_0 + K a^\dagger a. \tag{6.36}$$

We will restrict our focus to the regime $|K| < \kappa_{\text{tot}}$ so a semi-classical treatment is appropriate [60], and further assume that $kT \ll \hbar\omega_0$ such that the steady state response of the cavity is a coherent state to good approximation (rather than a displaced thermal state). We also assume that characterization of this system will be performed with a sufficiently weak driving field such that $|K|\langle a^\dagger a\rangle \ll \kappa_{\text{tot}}$ in the steady state [86]. In this case the cavity response will be linear to a good approximation and the scattering matrix elements (in the absence of frequency fluctuations) will be given by Eq. (6.22).

Since the scattered signal carries information about the quadratures $X_1 = a^\dagger + a$ and $X_2 = i(a^\dagger - a)$ of the intracavity field [55, 99, 100], the fluctuations in these operators are what will affect our measurement of the scattering matrix elements. We therefore express the resonant frequency as

$$\omega_0(X_1, X_2) = \omega_0 + \frac{K}{4}(X_1^2 + X_2^2) \tag{6.37}$$

where we've absorbed an overall constant into ω_0. Fluctuations $\delta X_{1,2} = X_{1,2} - \langle X_{1,2}\rangle$ of these operators in the steady state will be independent and Gaussian, each with zero mean and unit variance. The resulting frequency fluctuations $\delta\omega_0 = \omega_0(X_1, X_2) - \omega_0$ will follow a non-central chi squared distribution with two degrees of freedom, whose PDF is given by

$$P(\Omega) = \frac{2}{|K|} e^{-2(n+\Omega/K)} I_0\left(4\sqrt{n\Omega/K}\right)\Theta(\Omega/K) \tag{6.38}$$

where $n = \langle a^\dagger a \rangle = \left(\langle X_1 \rangle^2 + \langle X_2 \rangle^2\right)/4$ is the average number of photons in the cavity (assuming a coherent steady state) and $I_0(z)$ is the zeroth modified Bessel function of the first kind. Note that the number of photons n is related to the non-centrality parameter λ of the non-central chi squared distribution according to $\lambda = 4n$. There are two key downsides to working with this probability distribution. First, the convolution given by Eq. (6.20) does not readily simplify into an expression in terms of special functions (for which efficient implementations exist in most programming languages), so the numerical integration must be implemented manually. Second, if we try to fit this model (given by Eqs. (6.20) and (6.38)) to experimental data for the scattering matrix element S_{jk}, then we would have two parameters (K and n) that govern the subtle deviation of the fluctuating model $\overline{S_{jk}}(\Delta)$ from the non-fluctuating model rather than one. This may lead to overfitting problems unless either K or n can be determined independently.

It is therefore convenient to additionally work in a regime where $n \ll 1$, such that fluctuations in the resonant frequency can be approximated as

$$\delta\omega_0 \approx \frac{K}{4}\left(\delta X_1^2 + \delta X_2^2\right). \tag{6.39}$$

which will follow a central chi-squared distribution with two degrees of freedom. Since the variance of the non-central chi squared distribution increases with n and we've already taken the limit of $kT/\hbar\omega_0 \to 0$, this limit as $n \to 0$ can be thought of as the quantum limit of steady-state frequency fluctuations in a Kerr cavity. The probability of drawing the value Ω from the random variable $\delta\omega_0$ in this case is given by

$$P(\Omega) = \frac{2}{|K|} e^{-2\Omega/K}\,\Theta(\Omega/K) \tag{6.40}$$

where Θ is the Heaviside step function, such that $P(\Omega)$ has support on either the positive or negative real axis depending on the sign of K. As seen in Fig. 6.11, this approximation works very well up to $n \sim 1/8$ and accumulates significant errors by $n \sim 1/2$. For this probability distribution, Eq. (6.20) simplifies to

$$\overline{S_{jk}}(\Delta; \kappa_{\text{tot}}, r_{jk}, K) = \delta_{jk} - 2ir_{jk}\frac{\kappa_{\text{tot}}}{K} e^{(i\kappa_{\text{tot}} - 2\Delta)/K}\,\Gamma\left(0, \frac{i\kappa_{\text{tot}} - 2\Delta}{K}\right) \tag{6.41}$$

where $\Gamma(a, z) = \int_z^\infty t^{a-1}e^{-t}dt$ is the incomplete gamma function [98].

As before, the effect of these fluctuations is an apparent increase in the total

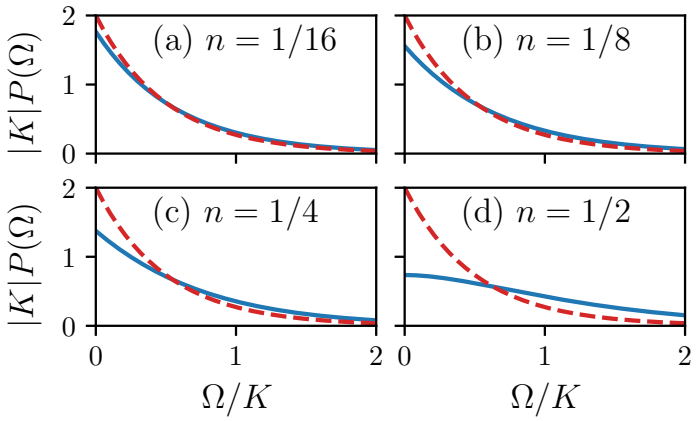

Figure 6.11: Approximating the PDF of a non-central chi squared distribution as a central chi squared distribution (both with two degrees of freedom) for increasing intracavity photon occupation $n = \langle a^\dagger a \rangle$. Solid blue lines are the exact PDF given by Eq. (6.38), dashed red lines are the approximate PDF given by Eq. (6.40).

damping rate κ_{tot} and decrease in the radius r_{jk} of the resonance circle, as seen in Fig. 6.12(a). Suprisingly, even as K approaches the cavity linewidth κ_{tot} the deviation of the resulting scattering matrix elements $\overline{S_{jk}}$ from the non-fluctuating model S_{jk} remains subtle. As such, this systematic deviation is easily obscured by measurement noise and is therefore likely to be overlooked. Just as in the case of a chi squared distribution with one degree of freedom $P(\Omega)$ only has support on either the positive or negative reals, which leads to both a shift in the apparent resonant frequency and asymmetry in the shape of the resonance circle, but these effects are slight. The case of $K > 0$ is displayed for simplicity, but the corresponding resonance circle for $K < 0$ can again be visualized by using Eq. (6.33) with the substitution $D \to K$. By fitting the model $S_{jk}(\Delta'; \kappa'_{\text{tot}}, r'_{jk})$ to data generated by $\overline{S_{jk}}(\Delta; \kappa_{\text{tot}}, r_{jk}, K)$ we have obtained the apparent values of κ'_{tot} and r'_{jk} as a function of $|K|$, which we present in Fig. 6.12(b). We find that in order for the apparent κ'_{tot} and r'_{jk} to both be within 10% of their true values κ_{tot} and r_{jk}, we must have $|K| \lesssim 0.35\kappa_{\text{tot}}$. Thus, this effect only becomes significant as $|K|$ approaches the cavity linewidth.

Another important case to consider is that of a cavity with a modest Kerr nonlinearity K driven at high enough powers such that the number of photons n in the cavity is non-negligible, a situation that is particularly important for experiments in which it is either necessary or useful to characterize the cavity using a range of input powers. In this case there is not a closed form expression for the average scattering matrix elements; instead, they must be obtained by numerically evaluating the

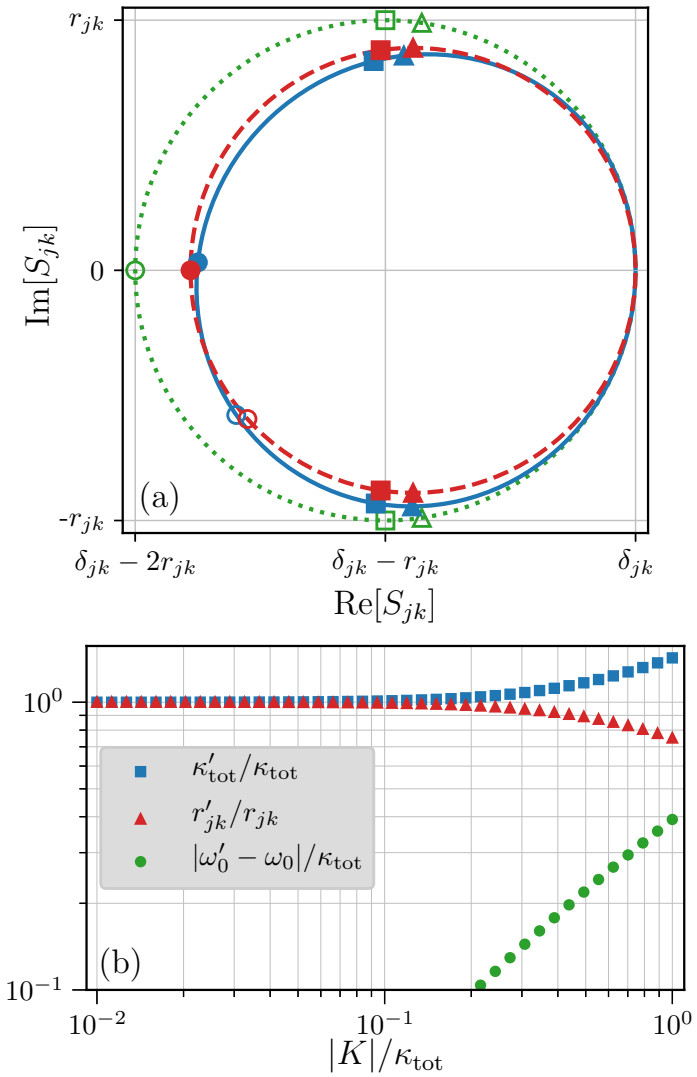

Figure 6.12: The effect of quantum fluctuations on the scattering matrix elements S_{jk} of a Kerr cavity when $n = \langle a^\dagger a \rangle \ll 1$. (a) Visualization of the deformed resonance circle. Dotted green line: $S_{jk}(\Delta; \kappa_{\mathrm{tot}}, r_{jk})$. Solid blue line: $\overline{S_{jk}}(\Delta; \kappa_{\mathrm{tot}}, r_{jk}, K)$ with $K = \kappa_{\mathrm{tot}}/2$. Dashed red line: best fit of $S_{jk}(\Delta'; \kappa'_{\mathrm{tot}}, r'_{jk})$ to the solid blue trajectory where $\omega'_0 - \omega_0 \approx 0.22\kappa_{\mathrm{tot}}$, $\kappa'_{\mathrm{tot}} \approx 1.2\kappa_{\mathrm{tot}}$, and $r'_{jk} \approx 0.89 r_{jk}$. Hollow circles mark $\Delta = 0$, hollow squares mark $\Delta = \pm\kappa_{\mathrm{tot}}/2$, and hollow triangles mark $\Delta = \pm\kappa'_{\mathrm{tot}}/2$. Filled shapes mark the corresponding points for Δ'. (b) Results of fitting the model $S_{jk}(\Delta'; \kappa'_{\mathrm{tot}}, r'_{jk})$ to data generated by $\overline{S_{jk}}(\Delta; \kappa_{\mathrm{tot}}, r_{jk}, K)$. Values of $|\omega'_0 - \omega_0| < \kappa_{\mathrm{tot}}/10$ have been omitted for clarity.

convolution

$$\overline{S_{jk}}(\Delta;\kappa_{\rm tot},r_{jk},K,n)=\int_{-\infty}^{\infty}S_{jk}(\Delta-\Omega;\kappa_{\rm tot},r_{jk})P(\Omega;K,n)d\Omega \tag{6.42}$$

where $S_{jk}(\Delta-\Omega;\kappa_{\rm tot},r_{jk})$ is given by Eq. (6.22) and $P(\Omega;K,n)$ is given by Eq. (6.38). We analyze the deformation induced by this convolution for fixed Kerr nonlinearity $K_0=\kappa_{\rm tot}/10$, for which the deformation is negligible in the limit $n\to 0$ (see Fig. 6.12(b)).

As with the previous cases, this convolution yields an apparent increase in the total damping rate $\kappa_{\rm tot}$ and decrease in the radius r_{jk} of the resonance circle, as seen in Fig. 6.13(a). Furthermore, the shape of the deformed scattering matrix element $\overline{S_{jk}}$ is qualitatively similar to that in the case of a stronger Kerr nonlinearity K and negligible cavity occupation n (compare with Fig. 6.12(a)). And, once again, the resulting deviation of the scattering matrix elements $\overline{S_{jk}}$ from the non-fluctuating model S_{jk} is subtle to the point of being easily overlooked or obscured by measurement noise. By fitting the model $S_{jk}(\Delta';\kappa'_{\rm tot},r'_{jk})$ to data generated by $\overline{S_{jk}}(\Delta;\kappa_{\rm tot},r_{jk},K_0,n)$ we have obtained the apparent values of $\kappa'_{\rm tot}$ and r'_{jk} as a function of cavity occupation $n=\langle a^\dagger a\rangle$, which we present in Fig. 6.13(b). We find that in order for the apparent $\kappa'_{\rm tot}$ and r'_{jk} to both be within 10% of their true values $\kappa_{\rm tot}$ and r_{jk} when $K=\kappa_{\rm tot}/10$, we must have $n\lesssim 2.6$. It is important to note that this effect is not scale-free; it will become stronger (weaker) for increasing (decreasing) values of $K/\kappa_{\rm tot}$, even if $nK/\kappa_{\rm tot}$ is held constant.

Thus, for cavities with even modest Kerr nonlinearities $K\gtrsim\kappa_{\rm tot}/10$ operated at the few-photon level, one will extract damping rates that differ appreciably from their true values if the effect of quantum fluctuations on the scattering matrix elements is not properly taken into account. Numerous examples of Kerr cavities in this regime are described in the literature [101, 102, 86, 16, 103, 104, 105]; based on our work, we believe that there are likely discrepancies between the reported damping rates of such cavities and their true values. The fact that these apparent damping rates vary with the cavity occupation n is particularly important to account for experimentally since it is well known that the true damping rates of microwave cavities vary with n as well, due to the two-level systems present in the dielectric substrates on which planar cavities are fabricated [106, 107, 108, 109, 110, 78, 111]. As we've shown, however, these discrepancies will persist even in the limit of zero cavity occupation. By using

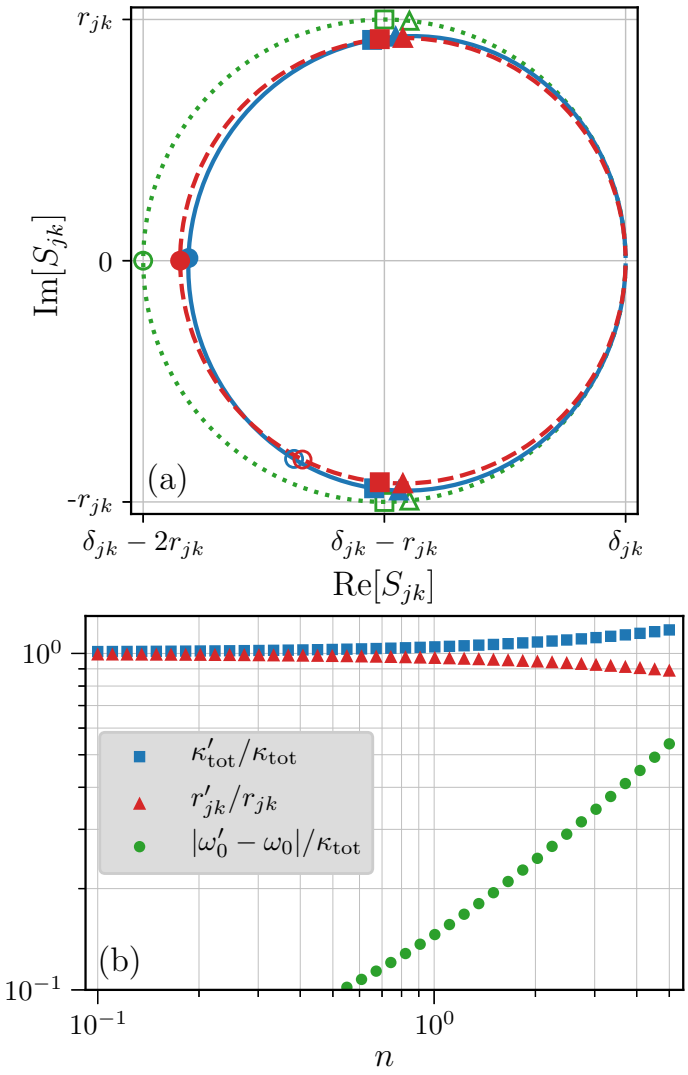

Figure 6.13: The effect of quantum fluctuations on the scattering matrix elements S_{jk} of a cavity with fixed Kerr nonlinearity $K_0 = \kappa_{\mathrm{tot}}/10$ and non-negligible cavity occupation $n = \langle a^\dagger a \rangle$. (a) Visualization of the deformed resonance circle. Dotted green line: $S_{jk}(\Delta; \kappa_{\mathrm{tot}}, r_{jk})$. Solid blue line: $\overline{S_{jk}}(\Delta; \kappa_{\mathrm{tot}}, r_{jk}, K_0, n)$ with $n = 3$ photons. Dashed red line: best fit of $S_{jk}(\Delta'; \kappa'_{\mathrm{tot}}, r'_{jk})$ to the solid blue trajectory where $\omega'_0 - \omega_0 \approx 0.34\kappa_{\mathrm{tot}}$, $\kappa'_{\mathrm{tot}} \approx 1.1\kappa_{\mathrm{tot}}$, and $r'_{jk} \approx 0.92 r_{jk}$. Hollow circles mark $\Delta = 0$, hollow squares mark $\Delta = \pm\kappa_{\mathrm{tot}}/2$, and hollow triangles mark $\Delta = \pm\kappa'_{\mathrm{tot}}/2$. Filled shapes mark the corresponding points for Δ'. (b) Results of fitting the model $S_{jk}(\Delta'; \kappa'_{\mathrm{tot}}, r'_{jk})$ to data generated by $\overline{S_{jk}}(\Delta; \kappa_{\mathrm{tot}}, r_{jk}, K_0, n)$ as a function of cavity photons n. Values of $|\omega'_0 - \omega_0| < \kappa_{\mathrm{tot}}/10$ have been omitted for clarity.

the model presented in this section, these systematic errors can be mitigated.

6.2.5 Tunable Kerr Cavity

It is useful to consider the combined effect of tunability and the Kerr nonlinearity on frequency fluctuations, since many tunable cavities contain Josephson junctions which introduce nonlinearity into the system. Making the same assumptions as in Sections 6.2.3 and 6.2.4, which led to Eqs. (6.25) and (6.39), the frequency fluctuations in this case take the form

$$\delta\omega_0 = \frac{\partial\omega_0(\overline{x})}{\partial x}\delta x + \frac{K}{4}\left(\delta X_1^2 + \delta X_2^2\right) \tag{6.43}$$

which is the sum of a Gaussian-distributed and a chi squared-distributed random variable. The resulting PDF is the convolution of a Gaussian and chi-squared distribution

$$\begin{aligned} P(\Omega) &= \int_{-\infty}^{\infty} \frac{2e^{-2\Omega'/K}}{|K|} \frac{e^{-(\Omega-\Omega')^2/2\sigma_{\omega_0}^2}}{\sqrt{2\pi\sigma_{\omega_0}^2}} \Theta(\Omega'/K) d\Omega' \\ &= e^{2\sigma_{\omega_0}^2/K^2 - 2\Omega/K} \left[\frac{1}{|K|} - \frac{\operatorname{erf}\left(\frac{\sqrt{2}\sigma_{\omega_0}}{K} - \frac{\Omega}{\sqrt{2}\sigma_{\omega_0}}\right)}{K}\right] \end{aligned} \tag{6.44}$$

where σ_{ω_0} is again given by Eq. (6.26). Working with this probability distribution has the same downsides as the non-central chi squared distribution: the convolution of Eq. (6.20) does not readily simplify in terms of special functions, and it depends on two extra free parameters rather than one. When $|K|/\sigma_{\omega_0}$ is either very small or very large, however, we can once again obtain simple expressions for the average scattering matrix elements.

When $|K| \ll \sigma_{\omega_0}$, the resulting probability distribution will be well-approximated by a Gaussian. This is most easily seen by expanding this distribution's cumulant generating function to second order in K

$$\begin{aligned} C(t) &= \frac{1}{2}\sigma_{\omega_0}^2 t^2 - \log\left(1 - \frac{Kt}{2}\right) \\ &\approx \frac{1}{2}Kt + \frac{1}{2}\left(\sigma_{\omega_0}^2 + \frac{K^2}{4}\right)t^2 \end{aligned} \tag{6.45}$$

which is identical to that of a Gaussian with mean $K/2$ and variance $\sigma_{\omega_0}^2 + K^2/4$.

More precisely, we can expand Eq. (6.44) as an Edgeworth series [112] such that

$$P(\Omega) \approx \frac{\exp\left[\dfrac{-(\Omega - K/2)^2}{2(\sigma_{\omega_0}^2 + K^2/4)}\right]}{\sqrt{2\pi(\sigma_{\omega_0}^2 + K^2/4)}} \tag{6.46}$$

to lowest order. Since the higher order cumulants will be $c_m = (K/2)^m$ for integers $m > 3$, the leading order correction to this expression will go as $K^3/(4\sigma_{\omega_0}^2 + K^2)^{3/2}$. Although this approximation is most accurate when $|K| \ll \sigma_{\omega_0}$, it actually works very well up to $|K| \approx 2\sigma_{\omega_0}$ and only begins to significantly deviate from the exact result when $|K| \gtrsim 4\sigma_{\omega_0}$, as can be seen in Fig. 6.14. Thus, for $|K| \lesssim 2\sigma_{\omega_0}$, the resonant frequency of our cavity will be shifted by $K/2$ and the average scattering matrix elements can be approximated by Eq. (6.28) with $\sigma_{\omega_0} \to \sqrt{\sigma_{\omega_0}^2 + K^2/4}$. In the opposite regime, when $|K| \gg \sigma_{\omega_0}$, the cumulants of the chi squared distribution will dominate at all orders and the scattering matrix elements can be approximated by Eq. (6.41) if $n \ll 1$, and by Eq. (6.42) otherwise.

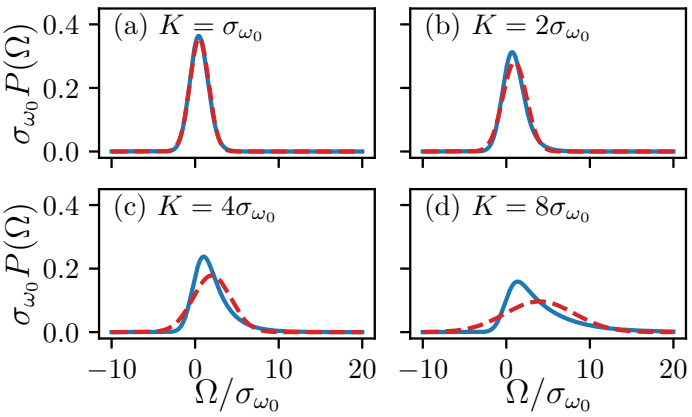

Figure 6.14: Approximating the PDF of the tunable Kerr cavity with a Gaussian for increasing values of K. Solid blue lines are the exact PDF given by Eq. (6.44), dashed red lines are the approximate Gaussian PDF given by Eq. (6.46).

6.2.6 Summary

In this section we have shown how frequency fluctuations comparable to the cavity linewidth may arise in tunable and nonlinear microwave cavities, and have presented a model for how these fluctuations deform the trajectories traced out by the scattering matrix elements in the complex plane. For tunable cavities we have shown how

fluctuations in the tuning parameter induce fluctuations in the resonant frequency, and that failing to account for these fluctuations may lead one to extract damping rates that appear to vary with the tuning parameter, which is a common observation in these systems. For Kerr cavities we have shown that quantum fluctuations in the cavity quadratures induce frequency fluctuations, which can appreciably affect the apparent damping rates of the cavity as the strength of the nonlinearity approaches the cavity linewidth. However, by using the model we have presented for the average scattering matrix elements as a fitting function for experimental data, one can extract the true damping rates even in the presence of these frequency fluctuations, allowing these cavities to be characterized more accurately moving forward.

Section 6.3
Damping Rates and Deformed Resonance Circles

In the case of the cCPT we must consider two sources of frequency fluctuations: those induced by fluctuations in the tuning parameters n_g and Φ_{ext}, and those induced by quantum fluctuations in the cavity field via the Kerr nonlinearity. To linear order in the fluctuations δn_g and $\delta\Phi_{\text{ext}}$, the frequency fluctuations they induce take the form

$$\delta\omega_0 = \frac{\partial\omega_0}{\partial n_g}\delta n_g + \frac{\partial\omega_0}{\partial\Phi_{\text{ext}}}\delta\Phi_{\text{ext}}. \tag{6.47}$$

Assuming fluctuations in the gate and flux are independent and Gaussian-distributed with mean zero and variances $\sigma^2_{n_g}$ and $\sigma^2_{\Phi_{\text{ext}}}$, respectively, then these frequency fluctuations will be Gaussian-distributed with mean zero and variance

$$\sigma^2_{\omega_0} = \left|\frac{\partial\omega_0}{\partial n_g}\right|^2 \sigma^2_{n_g} + \left|\frac{\partial\omega_0}{\partial\Phi_{\text{ext}}}\right|^2 \sigma^2_{\Phi_{\text{ext}}}. \tag{6.48}$$

In this case the average reflection coefficient takes the form [5]

$$\overline{S_{11}}(\Delta) = 1 - \sqrt{\frac{\pi}{2}}\frac{\kappa_{\text{ext}}}{\sigma_{\omega_0}} w\left(\frac{i\kappa_{\text{tot}} - 2\Delta}{2\sqrt{2}\sigma_{\omega_0}}\right) \tag{6.49}$$

where $w(z) = e^{-z^2}\text{erfc}(-iz)$ is the Faddeeva function [98].

On the other hand, the frequency fluctuations induced by quantum fluctuations

in the cavity field via the Kerr nonlinearity take the form

$$\delta\omega_0 = \frac{K}{4}(X_1^2 + X_2^2) \tag{6.50}$$

where $X_1 = a^\dagger + a$ and $X_2 = i(a^\dagger - a)$ are the quadrature operators. Assuming a coherent steady state of the cavity field, fluctuations $\delta X_{1,2} = X_{1,2} - \langle X_{1,2}\rangle$ in these operators will be independent and Gaussian, each with zero mean and unit variance. In the case of small cavity occupation $n \lesssim 1/4$, the resulting frequency fluctuations follow a chi-square distribution with two degrees of freedom to good approximation, such that the average reflection coefficient takes the form [5]

$$\overline{S_{11}}(\Delta) = 1 - 2i\frac{\kappa_{\text{ext}}}{K}e^{(i\kappa_{\text{tot}}-2\Delta)/K}\Gamma\Big(0, \frac{i\kappa_{\text{tot}} - 2\Delta}{K}\Big) \tag{6.51}$$

where $\Gamma(a, z) = \int_z^\infty t^{a-1}e^{-t}dt$ is the incomplete gamma function [98].

In general, we must consider the combined effect of these two sources of fluctuations, which leads to a complicated probability distribution that requires the convolution in Eq. (6.20) to be evaluated numerically. Of particular importance to us, however, is when the frequency fluctuations are dominated by fluctuations in the gate and flux such that $\sigma_{\omega_0} \gtrsim K/2$. In this case $\delta\omega_0$ will be Gaussian-distributed to good approximation, its variance will be renormalized by the Kerr nonlinearity according to [5]

$$\sigma_{\omega_0}^2 = \left|\frac{\partial\omega_0}{\partial n_g}\right|^2\sigma_{n_g}^2 + \left|\frac{\partial\omega_0}{\partial\Phi_{\text{ext}}}\right|^2\sigma_{\Phi_{\text{ext}}}^2 + \frac{K^2}{4} \tag{6.52}$$

and the average reflection coefficient will be given by Eq. (6.49). By fitting these models for the average reflection coefficient to our measurements, we can extract the true damping rates of the cCPT in the presence of frequency fluctuations.

As discussed in Section 6.2, in order to extract the damping rates of the cCPT we must fit our measured reflection coefficients to an appropriate model that accounts for the effects of frequency fluctuations. To this end we first study the trajectories traced out by our measured reflection coefficients and their deformation due to frequency fluctuations. This will both corroborate the presence of frequency fluctuations comparable to the cavity linewidth, as well as provide evidence of the relative magnitudes of fluctuations due to gate/flux noise and those due to quantum noise.

To study the effect of fluctuations in the tuning parameters n_g and Φ_{ext} on the resonance circle, we bias the cCPT to $(n_g, \Phi_{\text{ext}}) = (0.64, 0.27\Phi_0)$. At this point in

parameter space the resonant frequency is very sensitive to both gate and flux, since both $|\partial\omega_0/\partial n_g|$ and $|\partial\omega_0/\partial\Phi_{\text{ext}}|$ are close to their maximum values, leading to strong frequency fluctuations in accordance with Eqs. (6.47) and (6.48). Furthermore, the Kerr nonlinearity $K/2\pi = -0.03$ MHz is much smaller than the cavity linewidth at this point such that quantum fluctuations will contribute negligibly to the frequency fluctuations [5]. In Fig. 6.15 we highlight the deformation of the resonance circle at this point by fitting our measured trajectory $S_{11}(\Delta)$ to both Eq. (6.49) (which accounts for Gaussian fluctuations) and Eq. (6.17) (which does not account for any fluctuations). It is plain to see that our measured resonance circle is deformed into an oblong shape in excellent agreement with our Gaussian model for frequency fluctuations, and which cannot be explained using the non-fluctuating model. This both confirms the presence of strong frequency fluctuations comparable to the cavity linewidth, since $\sigma_{\omega_0}/\kappa_{\text{tot}} \approx 0.8$ at this point, and justifies our treatment of the underlying fluctuations in the gate and flux as Gaussian-distributed random variables. Most importantly, had we failed to account for these fluctuations we would have extracted an internal damping rate that differed from its true value by an order of magnitude.

To study the effect of quantum fluctuations on the resonance circle, we bias the cCPT to a point where the resonant frequency is insensitive to both gate and flux, but the Kerr nonlinearity is comparable to κ_{tot}. As it turns out there are two such points per period, $(n_g, \Phi_{\text{ext}}) = (0, 0)$ where $K/2\pi = -0.46$ MHz and $(n_g, \Phi_{\text{ext}}) = (0, \Phi_0/2)$ where $K/2\pi = 0.49$ MHz, such that both $|\partial\omega_0/\partial n_g|$ and $|\partial\omega_0/\partial\Phi_{\text{ext}}|$ tend toward zero at these points. In Fig. 6.16 we highlight the deformation of the resonance circle at these points by fitting our measured trajectories $S_{11}(\Delta)$ to both Eq. (6.51) (which accounts for frequency fluctuations induced by quantum fluctuations via the Kerr nonlinearity) and Eq. (6.17) (which does not account for any fluctuations). A signature of the deformation in this case is asymmetry of the trajectory with respect to reflection of $S_{11}(\Delta)$ across the real axis [5]. This arises from the chi-square distribution of the underlying fluctuations in the cavity quadratures, which only has support on either the positive or negative reals depending on the sign of K. Although it is subtle, we observe this deformation of our measured trajectories in agreement with Eq. (6.51); furthermore, the parity of this asymmetry depends on the sign of K as expected. In Fig. 6.16(b), where $K < 0$, we find that our measured trajectory $S_{11}(\Delta)$ lies outside our best fit to the nonfluctuating model at the top of the trajectory and inside it at the bottom left. In Fig. 6.16(d), where $K > 0$ on the other hand,

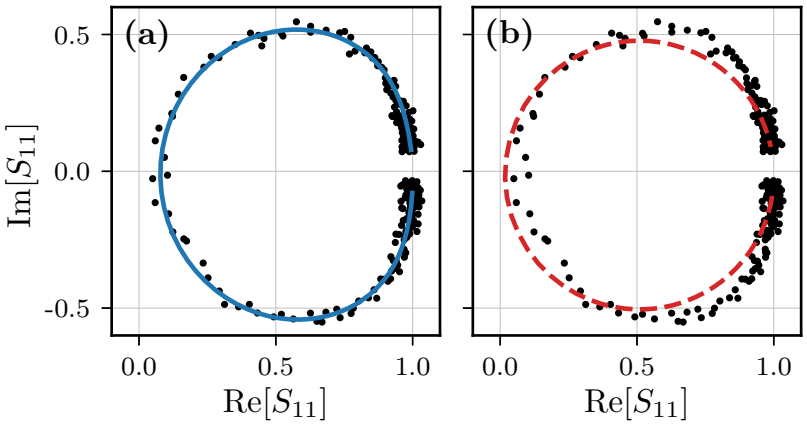

	$\kappa_{\text{int}}/2\pi$ (MHz)	$\kappa_{\text{ext}}/2\pi$ (MHz)	$\sigma_{\omega_0}/2\pi$ (MHz)
(a)	0.10 ± 0.05	1.178 ± 0.008	1.04 ± 0.02
(b)	1.40 ± 0.02	1.36 ± 0.01	

Figure 6.15: Deformation of a resonance circle due to Gaussian frequency fluctuations. The cCPT is biased to $(n_g, \Phi_{\text{ext}}) = (0.64, 0.27\Phi_0)$, where $\omega_0/2\pi = 5.751$ GHz and $K/2\pi = -0.03$ MHz. The trajectory traced out by $S_{11}(\Delta)$ is measured over a 30 MHz span around resonance, and marked by the black dots. The solid blue line in (a) is the fit to Eq. (6.49) that accounts for Gaussian frequency fluctuations, whereas the dashed red line in (b) is the fit to Eq. (6.17) that does not account for any frequency fluctuations. The best fit parameters are presented in the table above.

we find that our measured trajectory lies outside our best fit to the nonfluctuating model at the bottom of the trajectory and inside it at the top left. It is important to note that this asymmetry cannot be attributed to impedance mismatches, since additional rotation of the fit to Eq. (6.17) about the off-resonant point $S_{11} = 1$ leads to a poor fit near this point.

Across most of the parameter space spanned by n_g and Φ_{ext} we find that frequency fluctuations are dominated by Gaussian fluctuations in the gate and flux, rather than by quantum fluctuations. We therefore expect Eq. (6.49) to be an accurate model for our measured reflection coefficients $S_{11}(\Delta)$ for most bias points, where σ_{ω_0} is renormalized by the Kerr nonlinearity according to Eq. (6.52). This model breaks down in small regions near $(n_g, \Phi_{\text{ext}}) = (2m, k\Phi_0/2)$ for integers m and k, but numerically we find that if we try fitting the Gaussian model to data generated by Eq. (6.51) using the scale of the Kerr nonlinearity near these points ($|K|/\kappa_{\text{tot}} \approx 0.3$),

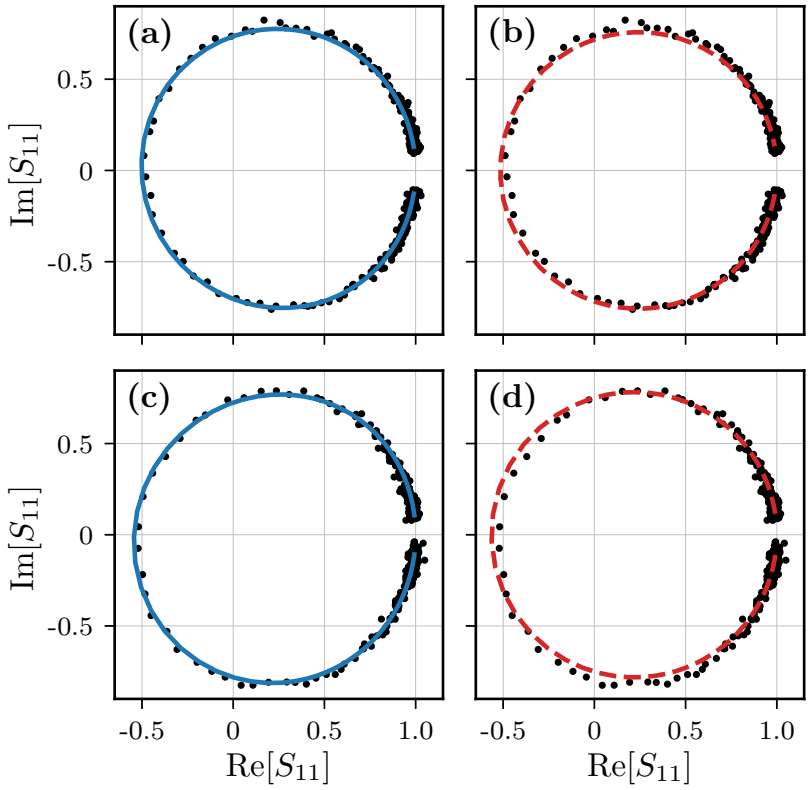

	$\kappa_{\text{int}}/2\pi$ (MHz)	$\kappa_{\text{ext}}/2\pi$ (MHz)
(a)	0.333 ± 0.005	1.295 ± 0.004
(b)	0.420 ± 0.006	1.315 ± 0.004
(c)	0.197 ± 0.005	1.081 ± 0.004
(d)	0.308 ± 0.006	1.106 ± 0.004

Figure 6.16: Deformation of two resonance circles due to quantum fluctuations. In (a) and (b) the cCPT is biased to $(n_g, \Phi_{\text{ext}}) = (0, 0)$ where $\omega_0/2\pi = 5.785$ GHz and $K/2\pi = -0.46$ kHz (obtained from Eq. (4.50)). In (c) and (d) it is biased to $(n_g, \Phi_{\text{ext}}) = (0, \Phi_0/2)$ where $\omega_0/2\pi = 5.728$ GHz and $K/2\pi = 0.49$ MHz. Each trajectory traced out by $S_{11}(\Delta)$ is measured over a 20 MHz span around resonance, and marked by the black dots. The solid blue lines in (a) and (c) are fits to Eq. (6.51) that accounts for quantum fluctuations (using the above values for K), whereas the dashed red lines in (b) and (d) are fits to Eq. (6.17) that does not account for any frequency fluctuations. The best fit parameters are presented in the table above.

we extract $\sigma_{\omega_0} \approx K/2$ to within 20% accuracy and damping rates that are accurate to within their confidence intervals. We can therefore use the Gaussian model as a fitting function for experimental data across our entire parameter space without significantly sacrificing accuracy in our model for σ_{ω_0} or in our extracted damping rates. Thus, to fully characterize the cCPT we measure $S_{11}(\Delta)$ at each point in parameter space and fit each measured trajectory to Eq. (6.49). This yields the best fit parameters $\sigma_{\omega_0}(n_g, \Phi_{\text{ext}})$, $\kappa_{\text{int}}(n_g, \Phi_{\text{ext}})$, and $\kappa_{\text{ext}}(n_g, \Phi_{\text{ext}})$, which we present in Fig. 6.17.

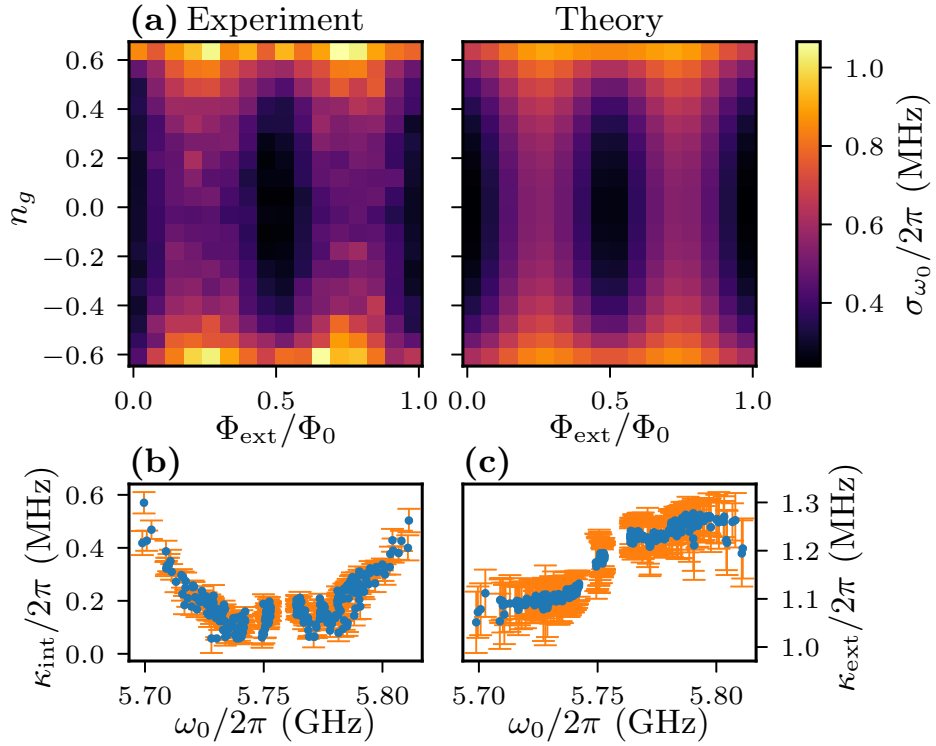

Figure 6.17: (a) Measured $\sigma_{\omega_0}(n_g, \Phi_{\text{ext}})$ and the best fit to Eq. (6.52), which includes the effects of frequency fluctuations due to charge noise, flux noise, and quantum noise. In (b) and (c), $\kappa_{\text{int}}(n_g, \Phi_{\text{ext}})$ and $\kappa_{\text{ext}}(n_g, \Phi_{\text{ext}})$ are plotted parametrically as a function of $\omega_0(n_g, \Phi_{\text{ext}})$, respectively, and their confidence intervals are shown in orange.

As shown in Fig. 6.17(a), we find excellent agreement between the measured $\sigma_{\omega_0}(n_g, \Phi_{\text{ext}})$ and the model given by Eq. (6.52). This agreement between theory and experiment further corroborates our model for the effect of frequency fluctuations on the reflection coefficient, and further demonstrates the significance of quantum fluctuations to the overall frequency fluctuations since they are crucial to the gate and flux dependence of σ_{ω_0}. From the best fit to this model we find the standard

deviations of gate and flux fluctuations to be

$$\begin{aligned} \sigma_{n_g} &= (6.1 \pm 0.2) \times 10^{-3} \text{ electrons} \\ \sigma_{\Phi_{\text{ext}}} &= (2.80 \pm 0.02) \times 10^{-3} \ \Phi_0 \end{aligned} \tag{6.53}$$

which, in general, depend on the time-scale of the individual reflection measurements used to find each value of σ_{ω_0}, as we will discuss in Section 6.4. With these we can calculate the strength of the second order couplings between the tuning and frequency fluctuations [5]

$$\begin{aligned} |D_{n_g}| &= \frac{\sigma_{n_g}^2}{2} \left| \frac{\partial^2 \omega_0}{\partial n_g^2} \right| < 2\pi \times 14 \,\text{kHz} \\ |D_{\Phi_{\text{ext}}}| &= \frac{\sigma_{\Phi_{\text{ext}}}^2}{2} \left| \frac{\partial^2 \omega_0}{\partial \Phi_{\text{ext}}^2} \right| < 2\pi \times 10 \,\text{kHz} \end{aligned} \tag{6.54}$$

where the bounds are over the full tuning range of the cCPT. Since these are both much smaller than κ_{tot}, we are justified in truncating Eq. (6.47) at linear order.

The internal damping rate $\kappa_{\text{int}}(n_g, \Phi_{\text{ext}})$ of the cCPT, obtained by fitting our measured trajectories $S_{11}(\Delta)$ to Eq. (6.49), is plotted parametrically versus $\omega_0(n_g, \Phi_{\text{ext}})$ in Fig. 6.17(b). Although κ_{int} varies somewhat at each value of ω_0, most of its variation can be attributed to an implicit dependence on the operating frequency ω_0 rather than an explicit dependence on n_g and Φ_{ext}. In Appendix A of Ref. [4] we show that the internal damping rate takes the form

$$\kappa_{\text{int}} = \frac{4\omega_{\lambda/4}}{\pi} \alpha \ell \tag{6.55}$$

where α is the attenuation constant of the cavity and ℓ is its length. Thus, one possible explanation for the implicit dependence of κ_{int} on ω_0 is the attenuation constant varying with frequency. Another possible explanation is that the metallization between the central conductor and the ground plane (which forms the CPT) affects κ_{int} in such a way that it depends on the operating frequency. It has previously been observed that similar metallization at high impedance points (e.g., the voltage antinode) yields an order unity change in a cavity's internal damping rate [113, 68]. As the resonant frequency is tuned, so too is its effective length and the impedance of the point at which the CPT is embedded. It is therefore plausible that additional loss would arise as the resonant frequency is tuned further away from its bare value, which is precisely what we observe.

The external damping rate $\kappa_{\text{ext}}(n_g, \Phi_{\text{ext}})$ of the cCPT, obtained by fitting our measured trajectories $S_{11}(\Delta)$ to Eq. (6.49), is plotted parametrically versus $\omega_0(n_g, \Phi_{\text{ext}})$ in Fig. 6.17(c). Clearly, the variation in κ_{ext} can be fully attributed to an implicit dependence on the operating frequency ω_0. In Appendix A of Ref. [4] we show that the external damping rate takes the form

$$\kappa_{\text{ext}} = \frac{4\omega_{\lambda/4}}{\pi}(\omega_0 Z_0 C_c)^2 \tag{6.56}$$

where $Z_0 = 50\Omega$ is the characteristic impedance of the transmission lines and C_c is the coupling capacitance between the cavity and the external transmission line. Although κ_{ext} depends explicitly on ω_0^2 this cannot account for its measured variation, since κ_{ext} deviates from its mean value by about 10% while ω_0 only varies from its bare value by about 1%. Rather, we attribute the variation in κ_{ext} to the characteristic impedance Z_0 of either the cavity or its environment changing with the operating frequency. Using our extracted value of $\kappa_{\text{ext}}/2\pi \approx 1.2$ MHz at $\omega_0 \approx \omega_{\lambda/4} = 2\pi \times 5.757$ GHz and the nominal value of $Z_0 = 50\Omega$, we can solve for the coupling capacitance $C_c = 7.1$ fF, which is consistent with both a first principles calculation based on the geometry of the interdigitated capacitor [114] and a simulation using Sonnet.

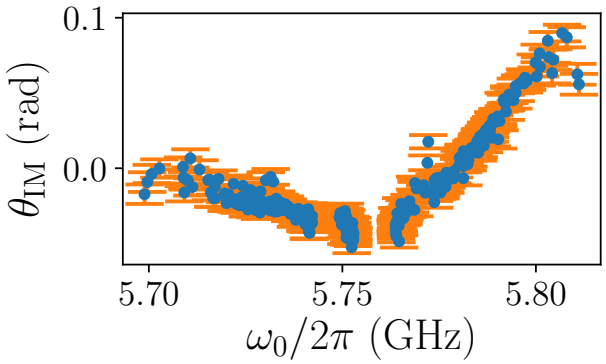

Figure 6.18: Empirical angle of rotation θ_{IM}, accounting for impedance mismatches, plotted parametrically versus ω_0.

Finally, for completeness, the empirical angle θ_{IM} accounting for impedance mismatches (see Section 5.2.2) is shown in Figure 6.18. This parameter is extracted concurrently with those presented in Figure 6.17. As you can see, it remains less than 0.1 radians in magnitude, such that impedance mismatching causes negligible errors in our extracted damping rates [79]. In addition, the variation in this parameter with

gate and flux can be attributed to an implicit dependence on ω_0.

Section 6.4

Power Spectra of Frequency Fluctuations

To corroborate the presence and strength of frequency fluctuations, as well as shed light on their underlying sources, we next perform a direct measurement of their power spectral density (PSD). We do so by driving the cCPT with a carrier signal on resonance and measuring the output PSD near ω_0 using a spectrum analyzer, as discussed in Section 5.3. This carrier signal will be modulated by the frequency fluctuations, which we assume to have PSD $S_{\Omega\Omega}(\omega)$, such that the power spectral density S_{out} of the output power at the plane of the sample is given by

$$S_{\text{out}}(\omega_0 \pm \omega) = \frac{2\kappa_{\text{ext}}^2}{\kappa_{\text{tot}}^2(\omega^2 + \kappa_{\text{tot}}^2/4)} P_{\text{in}} S_{\Omega\Omega}(\omega) \tag{6.57}$$

as shown in Section 2.4. This can be related to the power spectral density $S_{\text{out}}^{\text{SA}}$ measured by the spectrum analyzer according to

$$S_{\text{out}}^{\text{SA}}(\omega_0 \pm \omega) = \frac{2\kappa_{\text{ext}}^2}{\kappa_{\text{tot}}^2(\omega^2 + \kappa_{\text{tot}}^2/4)} \frac{G(\omega_0 \pm \omega)}{\eta_{\text{in}}} P_{\text{car}} S_{\Omega\Omega}(\omega) \tag{6.58}$$

where G is the gain of the amplifier chain, η_{in} is the input attenuation, and P_{car} is the power of the carrier signal at the fridge input.

As discussed in Section 5.2, we can measure the ratio G/η_{in} at any frequency using the off-resonant transmission magnitude $|S_{21}|$ from the input to the output port of the fridge. Having now determined the damping rates as well, we can measure $S_{\text{out}}^{\text{SA}}(\omega_0 \pm \omega)$ and invert this relationship to extract $S_{\Omega\Omega}(\omega)$. Furthermore, $S_{\Omega\Omega}$ can be expressed in terms of the PSDs of its underlying sources as

$$S_{\Omega\Omega}(\omega) = \left|\frac{\partial\omega_0}{\partial n_g}\right|^2 S_{qq}(\omega) + \left|\frac{\partial\omega_0}{\partial \Phi_{\text{ext}}}\right|^2 S_{\Phi\Phi}(\omega) + K^2 S_{nn}(\omega) \tag{6.59}$$

where S_{qq} is the PSD of fluctuations in the gate charge n_g, $S_{\Phi\Phi}$ is the PSD of fluctuations in the external flux Φ_{ext}, and S_{nn} is the PSD of quantum fluctuations in the cavity occupation $n = (X_1^2 + X_2^2 - 2)/4$. By carefully choosing the gate and flux biases at which we measure $S_{\Omega\Omega}$ we can isolate each of these contributions, which we can then compare with the results of Section 6.3.

For each of these measurements, we drive the cCPT using a carrier signal at ω_0 with power -60 dBm, slightly below the single-photon level such that the cavity response is linear to good approximation. We then measure the output power using a spectrum analyzer whose measurement window is centered at ω_0 with a span of 100 kHz and resolution bandwidth of 1 Hz. To measure the corresponding noise floor, we perform an identical measurement with the carrier signal turned off. As expected, all measured output spectra are symmetric about ω_0; we therefore calculate $S_{\Omega\Omega}(\omega)$ from the average of $S_{\text{out}}(\omega_0+\omega)$ and $S_{\text{out}}(\omega_0-\omega)$ to better resolve the fluctuations of interest from the noise floor. For convenience we express all measured PSDs in units of frequency rather than angular frequency.

6.4.1 Charge, Flux, and Quantum Noise

To measure the PSD of quantum noise, S_{nn}, we bias the cCPT to $(n_g, \Phi_{\text{ext}}) = (0, 0)$ where both $\partial\omega_0/\partial n_g = 0$ and $\partial\omega_0/\partial\Phi_{\text{ext}} = 0$. Thus, all power in excess of the noise floor near ω_0 is attributable to quantum fluctuations. Our measurement of $S_{nn}(f)$ is presented in Fig. 6.19(a), from which we see that we cannot resolve quantum fluctuations from the noise floor at these frequencies. Thus, for all subsequent measurements we assume quantum fluctuations contribute negligibly to Eq. (6.59).

To measure the PSD of charge noise, S_{qq}, we bias the cCPT to $(n_g, \Phi_{\text{ext}}) = (0.5, 0)$ where $\partial\omega_0/\partial\Phi_{\text{ext}} = 0$. Thus, all power in excess of the noise floor near ω_0 is attributable to fluctuations in the gate charge. Our measurement of $S_{qq}(f)$ is presented in Fig. 6.19(b), from which we see that it has an $f^{-\alpha}$ power law dependence. This type of charge noise is common in solid state systems, and is believed to arise due to fluctuating two-level systems in the vicinity of the CPT island [81, 82, 83]. Over the frequency range $f \lesssim 200$ Hz where the charge noise can be clearly resolved from the noise floor, we fit a power law to the charge noise in excess of the noise floor and find the best fit

$$S_{qq}(f) \approx (4.3 \times 10^{-7}) f^{-1.13} \text{ electrons}^2/\text{Hz}. \tag{6.60}$$

We note that our measured value of $S_{qq}(1\text{Hz})$ is comparable to typical values reported in the literature for single electron transistors (SETs) [115, 116, 117]. The total variance of fluctuations in the gate for a given measurement is obtained by integrating S_{qq} over the measurement bandwidth, with lower cutoff frequency set by the inverse of the measurement time $1/\tau_m$ and upper cutoff frequency set by the total damping

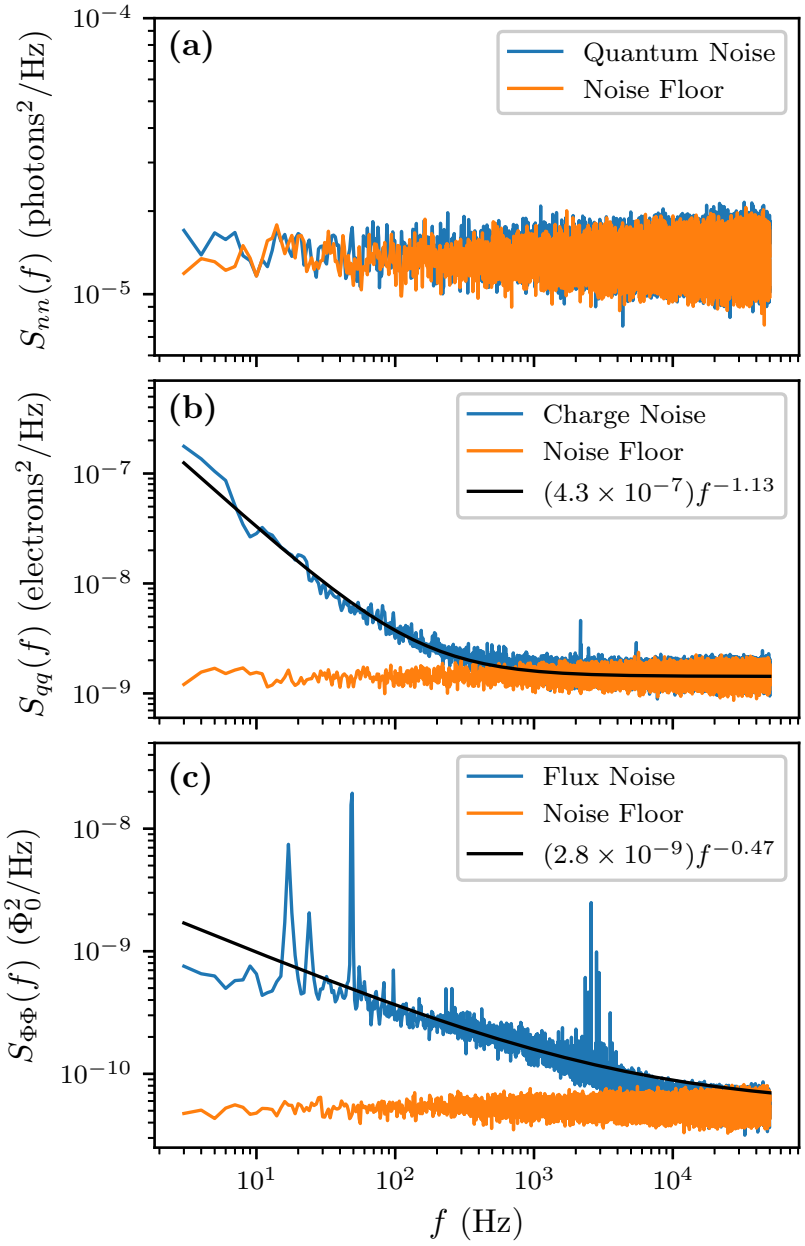

Figure 6.19: Measured power spectral densities of (a) quantum noise, (b) charge noise, and (c) flux noise. The power law fits in (b) and (c) have been offset by the mean noise floors to compare with our measured data.

rate $\kappa_{\rm tot}/2\pi$. To compare our PSD with the results of Section 6.3 we use $\tau_m = 0.03$ s. This corresponds to the total time spent measuring S_{11}, at each value of the detuning Δ, for the measurements used to determine σ_{n_g} and $\sigma_{\Phi_{\rm ext}}$ in that section. Assuming the charge noise follows the power law given by Eq. (6.60) over the full measurement bandwidth, we estimate

$$\sigma_{n_g} = \sqrt{\int_{1/\tau_m}^{\kappa_{\rm tot}/2\pi} S_{qq}(f)df} = 1.3 \times 10^{-3} \text{ electrons} \tag{6.61}$$

which is in order-of-magnitude agreement with Eq. (6.53).

To measure the PSD of flux noise, $S_{\Phi\Phi}$, we bias the cCPT to $(n_g, \Phi_{\rm ext}) = (0, \Phi_0/4)$ where $\partial\omega_0/\partial n_g = 0$. Thus, all power in excess of the noise floor near ω_0 is attributable to fluctuations in the flux threading the SQUID loop. Our measurement of $S_{\Phi\Phi}(f)$ is presented in Fig. 6.19(c), from which we see that it too has an $f^{-\alpha}$ power law dependence. This type of flux noise is ubiquitous in SQUIDs and is believed to arise from unpaired surface spins [81, 118, 84, 85]. Over the frequency range $f \lesssim 2$ kHz where the flux noise can be clearly resolved from the noise floor, we fit a power law to the flux noise in excess of the noise floor and find the best fit

$$S_{\Phi\Phi}(f) \approx (2.8 \times 10^{-9}) f^{-0.47}\ \Phi_0^2/\text{Hz}. \tag{6.62}$$

We note that our measured value of $S_{\Phi\Phi}(1\text{Hz})$ is significantly larger than typical values on the order of $(\mu\Phi_0)^2/\text{Hz}$ found in the literature [118, 84, 85], which we attribute to the large size of our SQUID loop. In addition, although the exponent $\alpha \approx 0.5$ in the $f^{-\alpha}$ dependence of $S_{\Phi\Phi}$ is on the low side of what has been reported in the literature, it is not unprecedented [85]. Following the same line of reasoning as for the charge noise, we estimate the total standard deviation of flux fluctuations (over the bandwidth of the measurement used in Section 6.3) to be

$$\sigma_{\Phi_{\rm ext}} = \sqrt{\int_{1/\tau_m}^{\kappa_{\rm tot}/2\pi} S_{\Phi\Phi}(f)df} = 3.1 \times 10^{-3}\ \Phi_0 \tag{6.63}$$

in good agreement with Eq. (6.53). The peaks in $S_{\Phi\Phi}$ from $10 - 100$ Hz and near 2.4 kHz are due to a combination of electrical and vibrational interference, primarily

from the pumps and compressors necessary to run our cryostat. We estimate that this interference contributes less than 0.5% to the total standard deviation of Φ_{ext} over the measurement bandwidth considered.

It is important to emphasize that due to limitations of this measurement and the analysis thereof, the values of σ_{n_g} and $\sigma_{\Phi_{\text{ext}}}$ obtained here should only be considered order-of-magnitude estimates for comparison with Eq. (6.53). First and foremost, the power spectra of interest disappear into the noise floor at frequencies several orders of magnitude smaller than κ_{tot}. Thus, to integrate S_{qq} and $S_{\Phi\Phi}$ over the bandwidth of the measurements used in Section 6.3 we have been forced to infer the high-frequency behavior of these power spectral densities from their low-frequency behavior. We could improve on this limitation by using a near quantum-limited first stage amplifier [119, 17, 41, 120], which would reduce our noise floor by an order of magnitude or more. Second, in deriving Eq. (6.57) we have assumed that the carrier signal is on resonance at ω_0 (see Section 2.4), where the sideband power $S_{\text{out}}(\omega_0 + \omega)$ due to frequency fluctuations $S_{\Omega\Omega}(\omega)$ is maximal. Over the course of measuring the output power at $\omega_0 + \omega$, however, the resonant frequency will fluctuate around its average value thereby reducing both the average output power at $\omega_0 + \omega$ and our estimate of $S_{\Omega\Omega}(\omega)$. Since the scale of fluctuations in the resonant frequency around its average value is comparable to but not greater than κ_{tot}, this will be an order unity effect.

6.4.2 Quasiparticle Poisoning

As discussed in Section 6.1, quasiparticle poisoning (QP) occurs when the cCPT is biased near $n_g = 0.7$. This manifests itself as random switching between two different resonant frequencies as quasiparticles tunnel onto and off of the CPT island. When measured with a VNA, this gives rise to two visible resonances as in Fig. 6.4.

To measure the power spectrum of these switching events, we bias the cCPT to $(n_g, \Phi_{\text{ext}}) = (0.7, 0.0)$. The only sources of frequency fluctuations at this point are charge noise and the random switching due to QP (ignoring the effect of quantum fluctuations as in Section 6.4 since they cannot be resolved with this measurement). Since the odd-parity resonance is effectively at $n_g = -0.3$ its resonant frequency is not very sensitive to gate noise, so the frequency fluctuations are dominated by the switching due to QP. We therefore put a carrier in at the odd-parity resonant frequency ($f_0 = 5.789$ GHz) and measure the output power spectral density near the reflected carrier, which encodes the power spectral density of frequency fluctuations. This measurement is performed with all the same parameters as the previous

measurements of the charge, flux, and quantum noise spectra.

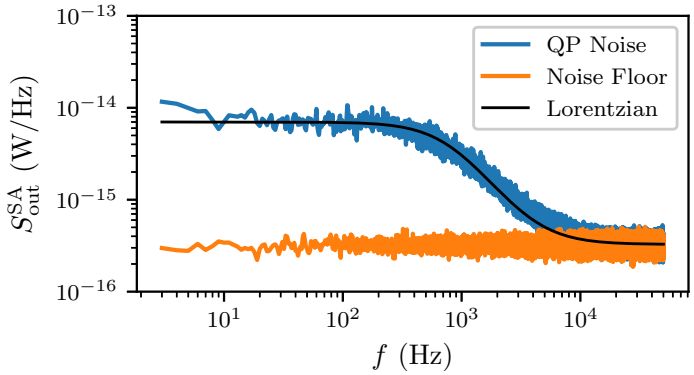

Figure 6.20: Output power spectral density at $f_0 + f$ due to frequency fluctuations induced by quasiparticle poisoning.

The results of this measurement are shown in Fig. 6.20. We find that the output power spectral density due to QP is well-modeled by a Lorentzian, as we expect for the random telegraph signal associated with QP [121, 122]. The best fit of the excess noise to a Lorentzian is

$$S_{\text{out}}^{\text{SA}}(f_0 \pm f) = \frac{6.7 \times 10^{-15}}{1 + (f/830\ \text{Hz})^2}\ \text{W/Hz}. \tag{6.64}$$

This corner frequency of 830 Hz is consistent with other measurements of QP reported in the literature [121, 122].

Section 6.5

Power Calibration via the Kerr Shift

Since many of our measurements rely on our knowledge of the number of photons in the cavity, we next study the power-dependent shift in resonant frequency due to the Kerr nonlinearity [60, 86, 59]. This will enable us to refer our input and output powers to the plane of the sample, and thereby determine the number of intracavity photons in-situ. In Appendix 2.5 we show that the resonant frequency ω_*, taken to be the frequency at which $|S_{11}|$ is minimized, is shifted from ω_0 according to

$$\omega_* = \omega_0 + Kn = \omega_0 + 4K\frac{\kappa_{\text{ext}}}{\kappa_{\text{tot}}}\frac{P_{\text{in}}}{\hbar\omega_0\kappa_{\text{tot}}} \tag{6.65}$$

where n is the number of intracavity photons on resonance and P_{in} is the input power at the plane of the sample. This can be expressed in terms of the input VNA power P_{VNA} using the input attenuation $\eta_{\text{in}} = P_{\text{VNA}}/P_{\text{in}}$. Thus, if we measure the slope

$$\frac{\partial \omega_*}{\partial P_{\text{VNA}}} = \frac{4\kappa_{\text{ext}}}{\hbar\omega_0\kappa_{\text{tot}}^2\eta_{\text{in}}}K \tag{6.66}$$

we can determine η_{in} by comparing with this theoretical model, since the resonant frequency, Kerr nonlinearity, and damping rates have already been determined. Here we have implicitly assumed that the damping rates of the cCPT do not vary with input power, which is not true in general [106, 109] but is accurate for the range of input powers we use in this measurement.

We perform this measurement by increasing P_{VNA}, finding ω_* for each input power, and determining the slope $\partial\omega_*/\partial P_{\text{VNA}}$. This is done for a full period of both n_g and Φ_{ext}, such that we can fit our results to Eq. (6.66). The results of this measurement at two different bias points, one with positive K and one with negative K, are shown in Fig. 6.21(a) and 6.21(b). Further, we repeat this process for different ranges of input VNA powers, always starting from -65 dBm and incremented on a linear scale, but ending between -56 dBm and -51 dBm. At -56 dBm, the cCPT is below the threshold of bistability (see Section 2.5) across its full tuning range but the scale of the Kerr shift is comparable to both the cavity linewidth and the jumps in frequency between measurements at different input powers (due to slow frequency fluctuations), leading to noisiness and greater uncertainty in our measured slopes. At -51 dBm, the cCPT is above the threshold of bistability across most of its tuning range, but the linear trend due to the Kerr shift is more easily resolved. In all cases we do not observe any clear signatures of bistability, such as hysteresis and sudden jumps in S_{11} as the drive frequency is swept across resonance [61], since the total scale of frequency fluctuations over the measurement time is larger than the range of frequencies over which the response is bistable for these powers. Empirically, we find that ω_* follows a linear trend with respect to P_{VNA} even into the bistable regime at the powers considered, but using larger maximum powers tends to yield slopes slightly smaller in magnitude leading to slightly larger input attenuations. This effect is illustrated by the measurements shown in Figures 6.21(a) and 6.21(b); although the magnitude of the slopes obtained using greater maximum power are not always this much less than those obtained using lower maximum power, the trend persists on average. This may be due to a slight increase in the internal damping rate at

increasing powers, but this is difficult to determine in our case due to the complexity of simulating the nonlinear reflection coefficient (see Section 2.5), in the presence of frequency fluctuations. Finally, it is worth noting that all of these effects, and our extracted input attenuations, are consistent across multiple cooldowns.

We find the best agreement between theory and experiment using a maximum input VNA power of about -54 dBm, at which the cCPT is below the bistability threshold for all but a small region around $\Phi_{\text{ext}} = \Phi_0/2$. By fitting our measured slopes $\partial\omega_*/\partial P_{\text{VNA}}$ to Eq. (6.66) we find the input attenuation

$$\eta_{\text{in}} = (1.55 \pm 0.2) \times 10^8 = 81.9 \pm 0.6\,\text{dB} \tag{6.67}$$

whose confidence interval is limited by the range of input attenuations extracted using different maximum input VNA powers. In Figure 6.21(c) we present a representative measurement of these slopes, scaled by a factor of $\hbar\omega_0\kappa_{\text{tot}}^2\eta_{\text{in}}/4\kappa_{\text{ext}}$ so they can be compared to the Kerr nonlinearity given by Eq. (4.50), and find excellent agreement between theory and experiment. The accuracy of this connection between the Kerr nonlinearity and the measured slopes depends on the accuracy of our extracted damping rates; if we had not accounted for the presence of frequency fluctuations, our extracted input attenuation would have been skewed. Our input attenuation is somewhat larger than its value of about 79 dB at room temperature, contrary to our expectations since the attenuation due to our stainless steel coaxial cables should decrease slightly at cryogenic temperatures. We believe the primary reason for this discrepancy is impedance mismatching arising at cryogenic temperatures, since all of our cables and attenuators are rated for room temperature. Based on our room temperature measurement, we estimate that η_{in} should vary from its mean value by less than ± 0.2 dB over the tuning range of ω_0, well within its confidence interval.

Although we find excellent agreement between our measured slopes and Eq. (6.66), it is worth discussing two implicit assumptions of this model. First, we have ignored the shift in ω_* due to frequency fluctuations [5], which would tend to increase the magnitude of our measured slopes and lead us to extract a smaller input attenuation. Second, we have ignored the fact that frequency fluctuations reduce the average cavity occupation in the steady state, which would tend to decrease the magnitude of our measured slopes and lead us to extract a larger input attenuation. Both of these are order unity effects that tend to cancel one another out, and modeling them rigorously would be prohibitively complex. Thus, we have neglected them.

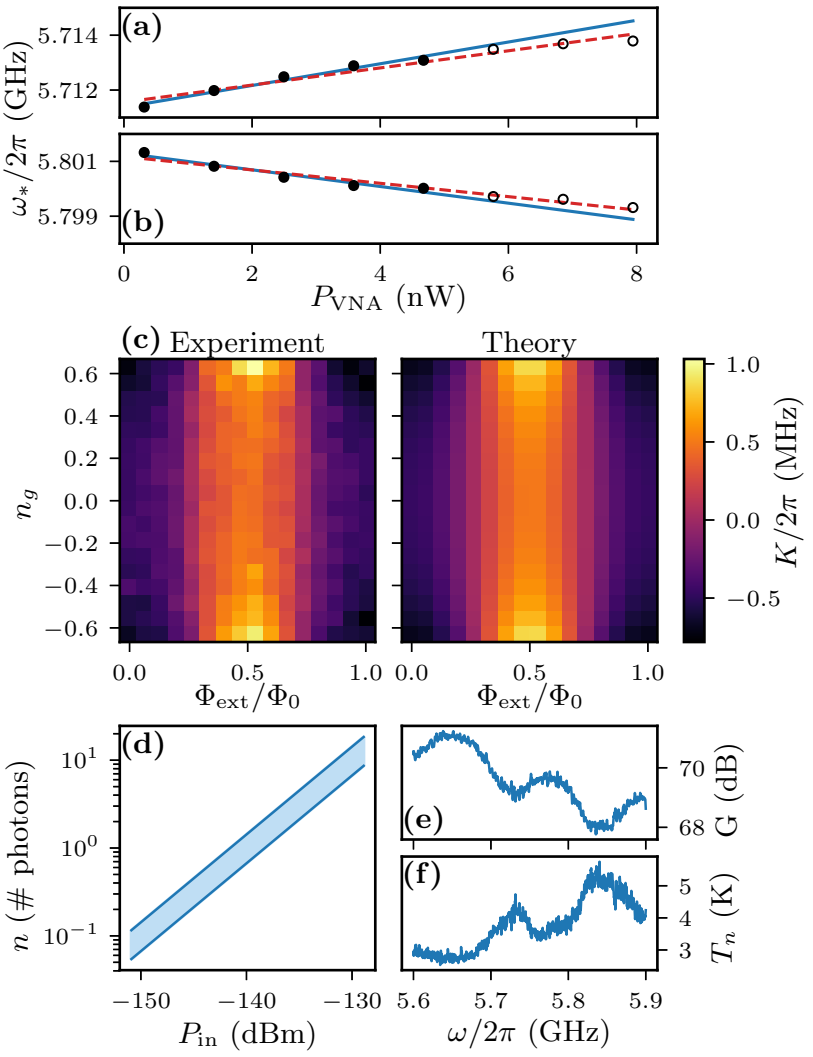

Figure 6.21: (a) Measurement of the Kerr-shifted resonant frequency ω_* (marked by black circles) as a function of P_{VNA} at $(n_g, \Phi_{\mathrm{ext}}) = (0.56, 0.53\Phi_0)$. The solid blue line is the best fit to the filled black circles (slope = 400 kHz/nW), whereas the dashed red line is the best fit to both the filled and hollow black circles (slope = 310 kHz/nW). The uncertainty in each measured $\omega_*/2\pi$ is about ± 100 kHz, smaller than the marker size. (b) Same as (a), but at $(n_g, \Phi_{\mathrm{ext}}) = (0.56, 0.0)$. The slope of the solid blue line is -300 kHz/nW, whereas the slope of the dashed red line is -240 kHz/nW. (c) Measured slopes $\partial\omega_*/\partial P_{\mathrm{VNA}}$, scaled by a factor of $\hbar\omega_0\kappa_{\mathrm{tot}}^2\eta_{\mathrm{in}}/4\kappa_{\mathrm{ext}}$, and theoretical Kerr nonlinearity given by Eq. (4.50). (d) Number of intracavity photons n at resonance as a function of P_{in} and P_{VNA}. (e) Gain and (f) system noise temperature of our amplifier chain as a function of frequency.

6.5.1 Number of Intracavity Photons

With this input attenuation, we can now refer our input VNA power P_{VNA} to the input power at the plane of the sample $P_{\mathrm{in}} = P_{\mathrm{VNA}}/\eta_{\mathrm{in}}$. Thus, we can find the average number of photons in the cavity at resonance according to

$$n = \frac{4\kappa_{\mathrm{ext}} P_{\mathrm{in}}}{\hbar\omega_0 \kappa_{\mathrm{tot}}^2}. \tag{6.68}$$

which is valid in both the linear and nonlinear response regimes, as shown in Appendices 2.3 and 2.5. This serves as an upper bound for the actual cavity occupation in the steady state, which will be reduced by both frequency fluctuations and non-zero detuning. In Fig. 6.21(d) we plot this average cavity occupation at resonance as a function of input power; the range of values at each input power is due to the variation in the damping rates as a function of operating frequency ω_0.

6.5.2 Amplifier Gain and System Noise

With this input attenuation we can also find the gain of our amplifier chain and the system noise referred to the plane of the sample. We find the gain $G(\omega)$ by measuring the magnitude of the off-resonant transmission coefficient between the input and output ports of the fridge, which takes the form

$$\left|S_{21}^{\mathrm{VNA}}(\omega)\right| = \sqrt{\frac{G(\omega)}{\eta_{\mathrm{in}}}} \tag{6.69}$$

as discussed in Section 5.2. Our measured gain profile is presented in Fig. 6.21(e). We find the system noise power spectral density $S_{\mathrm{noise}}(\omega)$ by measuring the output power spectral density at room temperature $S_{\mathrm{out}}(\omega)$, with no input drive, using a spectrum analyzer. These two quantities are related to one another according to

$$S_{\mathrm{out}}(\omega) = G(\omega) S_{\mathrm{noise}}(\omega). \tag{6.70}$$

The power spectral density of the noise (in units of W/Hz) can be converted into a system noise temperature by dividing by the Boltzmann constant k_B. Our measured system noise, shown in Figure 6.21(f), is primarily due to the added noise of our first-stage cryogenic HEMT amplifier. These results are consistent with both the specifications of the HEMT and similar results in the literature [41, 120, 10, 59], thus providing additional corroboration of our extracted value for the input attenuation.

6.5.3 Discussion

A major limitation of this method for determining the input attenuation is that we were unable to independently measure the strength of the Kerr nonlinearity, forcing us to infer its value from Eq. (4.50) using our extracted E_J and E_C given by Eq. (6.14) and $\phi_{\rm zp} = 0.176$. This same limitation exists in other work that has used the Kerr shift (or, equivalently, the Duffing shift) to determine the power at the plane of the sample in-situ [10, 86]. We have strong corroboration for the validity of this theoretical evaluation of K from the fact that the measured $\omega_0(n_g, \Phi_{\rm ext})$ is in excellent agreement with theory [Fig. 6.5(a)], the slopes $\partial\omega_*/\partial P_{\rm VNA}$ follow the same trend as our theoretical Kerr nonlinearity [Fig. 6.21(c)], and our estimate for difference between the superconducting gaps of the island and leads of the CPT is consistent with other measurements reported in the literature. However, a direct measurement of $K(n_g, \Phi_{\rm ext})$ would be preferable. We might have been able to perform such a measurement if the strength of the Kerr nonlinearity exceeded the cavity linewidth [16], in which case we could observe spectral signatures of K. Unfortunately, in our case the observable consequences of K are only sensitive to the product $P_{\rm in}K$. This is true for both the Kerr shift given by Eq. (6.65) and the bistability threshold (see Section 2.5). Within the internal logic of this methodology our uncertainty in K is determined by our confidence intervals for the best fit parameters E_J and E_C, as well as our uncertainties σ_{n_g} and $\sigma_{\Phi_{\rm ext}}$ in the gate and flux bias points due to $1/f$ noise. The total uncertainty in K varies with gate and flux, but it is typically less than about ± 15 kHz.

In addition, it is worth noting that a completely different method for determining the input attenuation would be possible if we were able to access the first excited state of the CPT and thereby operate it as a qubit. Robust methods exist for calibrating the number of photons in a cavity that is coupled to a qubit via the Jaynes-Cummings interaction. These methods make use of the Stark shift [123], a photon-number dependent shift in the qubit frequency, the coupling strength of which can be determined independently by measuring either the phase shift of a scattered signal in the case of weak coupling [124] or the vacuum Rabi splitting in the case of strong coupling [125]. Although the coupling between the qubit and cavity would be somewhat different in our case, we believe these methods could be adapted to the cCPT if not for two practical limitations. First, due to our restricted gate range $-0.65 < n_g < 0.65$, the minimum qubit frequency we can attain with the present device is $E_{0\to1}/h \approx 75$ GHz, which is beyond the range of frequencies we can access experimentally. Second,

we would expect our qubit (essentially a split Cooper pair box [126]) to have a poor coherence time, making qubit spectroscopy challenging. This could be improved if a cCPT were fabricated in the transmon regime with $E_C/E_J \ll 1$ [67], but this would then be a very different device than the one studied in the present work.

Section 6.6

Time-domain Measurements

In this section we present some time-domain measurements that shed further light on frequency fluctuations in the cCPT, but are not conducive to quantitative analysis (and therefore characterization).

6.6.1 Reflection Coefficient

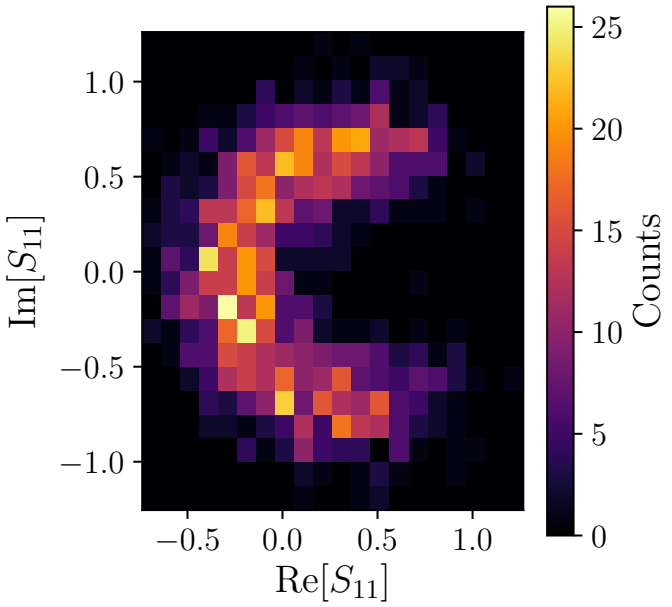

Figure 6.22: Histogram of $S_{11}(t)$, with a drive signal on resonance, at $(n_g, \Phi_{\text{ext}}) = (0.64, 0.27\Phi_0)$.

We can sample the reflection coefficient as a function of time by operating the VNA in "zero-span" mode, which fixes the frequency of the continuous-wave stimulus and records $S_{11}(t)$. To perform this measurement, we bias the cCPT to $(n_g, \Phi_{\text{ext}}) = (0.64, 0.27\Phi_0)$, where the resonant frequency is very sensitive to both gate and flux

such that σ_{ω_0} is large. First, we measure the resonant frequency ω_0 with a typical measurement of the reflection coefficient. Next, we set the stimulus frequency to ω_0 and monitor $S_{11}(t)$.

A histogram of this measurement is shown in Figure 6.22. This is clearly a sampling from the circular trajectory $S_{11}(\Delta)$ at different values of the detuning, consistent with the resonant frequency fluctuating as a function of time. However, it's not precisely the ideal trajectory since each datapoint is averaged over the measurement time (set by the IF bandwidth of the VNA). Thus, each datapoint is actually sampled from an average trajectory $\overline{S_{11}}(\Delta)$, but this sampling rate is faster than sampling the full trajectory $S_{11}(\Delta)$ so the averaging process is sensitive to a much smaller bandwidth of frequency noise (see Section 6.2). This complication makes it difficult to extract any useful quantities from this measurement.

6.6.2 Ringdown Measurements

Theory. We now consider the effect of frequency fluctuations on ringdown measurements [127, 128, 129, 130]. This type of measurement is performed by driving the cavity on resonance to a steady state amplitude, turning off the drive, and observing the subsequent decay of the intracavity field, from which the total damping rate of the cavity can be determined. Before the measurement, the average resonant frequency $\overline{\omega_0}$ must first be measured, which sets the drive frequency, after which the actual resonant frequency $\omega_0(t)$ may fluctuate from this average value by $\delta\omega_0(t) = \omega_0(t) - \overline{\omega_0}$ during the ringdown measurement. We assume that at $t = 0$ the cavity has reached a steady state, at which time the drive is abruptly turned off. Since the amplitude and phase at $t = 0$ will depend on the detuning of the drive from the true resonant frequency while the cavity approached the steady state, for $t > 0$ the average output voltage (on whichever port is to be measured) can be written

$$\langle V_{\text{out}}(t > 0)\rangle = V_0\left(\Delta_0\right) e^{-\kappa_{\text{tot}} t/2} \cos\left[\omega_0(t)t + \phi(\Delta_0)\right] \tag{6.71}$$

where Δ_0 is a function of $\delta\omega_0(t < 0)$. As we will see, the details of this dependence become irrelevant as long as care is taken in how the output signal is acquired and processed.

Since microwave signals are generally too fast to be recorded directly, they are typically mixed down to an intermediate frequency before being recorded [80]. Here we consider a homodyne IQ detection scheme, where the output signal is mixed down

to DC using a local oscillator at the drive frequency $\overline{\omega_0}$, after which both the in-phase (I) and quadrature (Q) components of the signal are recorded [99, 100]. In the presence of frequency fluctuations, these ostensibly DC signals now take the form

$$\begin{aligned} I(t) &= V_0\left(\Delta_0\right) e^{-\kappa_{\mathrm{tot}} t/2} \cos\left[\delta\omega_0(t)t + \phi(\Delta_0)\right] \\ Q(t) &= V_0\left(\Delta_0\right) e^{-\kappa_{\mathrm{tot}} t/2} \sin\left[\delta\omega_0(t)t + \phi(\Delta_0)\right] \end{aligned} \tag{6.72}$$

which remain oscillatory due to $\delta\omega_0(t)$. However, this oscillatory time dependence is not present in the amplitude of the signal

$$A(t) = \sqrt{I(t)^2 + Q(t)^2} = V_0\left(\Delta_0\right) e^{-\kappa_{\mathrm{tot}} t/2} \tag{6.73}$$

whose time dependence is a simple exponential decay from which the rate $\kappa_{\mathrm{tot}}/2$ is easily determined. Even if the noise associated with the output signal is sufficiently large that an ensemble of measurements must be performed and averaged, only the initial value of the amplitude will be affected by this process such that $\kappa_{\mathrm{tot}}/2$ can still be determined from the rate of decay. However, the ensemble-averaged amplitude will also acquire a DC offset due to the root mean square amplitude of the noise, which in practice could make it difficult to resolve the exponential decay.

To illustrate how the results of this measurement may be skewed by frequency fluctuations if the amplitude is not directly measured, we consider a single channel homodyne detection scheme in which only the in-phase part of the signal is recorded. For simplicity, we assume that V_0 and ϕ are constants independent of Δ_0, that $\phi = 0$, and that the resonant frequency doesn't fluctuate appreciably over the course of a single measurement but does fluctuate over the course of repeated measurements. In this case the in-phase part of the signal obtained from a single measurement takes the form

$$I(t) = V_0 e^{-\kappa_{\mathrm{tot}} t/2} \cos(\delta\omega_0 t). \tag{6.74}$$

Assuming $\delta\omega_0$ is a Gaussian-distributed random variable with mean zero and variance $\sigma_{\omega_0}^2$, then the average time series from an ensemble of such measurements will take the form

$$\langle I(t)\rangle = V_0 e^{-\kappa_{\mathrm{tot}} t/2} \int_{-\infty}^{\infty} \frac{e^{-\Omega^2/2\sigma_{\omega_0}^2}}{\sqrt{2\pi\sigma_{\omega_0}^2}} \cos(\Omega t) d\Omega \tag{6.75}$$

$$= V_0 e^{-\kappa_{\mathrm{tot}} t/2} e^{-\sigma_{\omega_0}^2 t^2/2}. \tag{6.76}$$

Clearly, this signal is no longer ideal for extracting κ_{tot}; if one tries to fit it to a simple exponential decay, then one will extract a total damping rate skewed by σ_{ω_0}. As before, this effect only becomes significant as σ_{ω_0} approaches κ_{tot}.

Thus, to accurately perform a ringdown measurement in the presence of frequency fluctuations, one should ideally detect the amplitude (or, equivalently, the power) of the signal directly. As we've shown, this can be accomplished with an IQ measurement, but diode detection is another feasible approach. How this is best accomplished, or if it can be accomplished at all, will depend on the specifics of the experimental device under consideration. Regardless, if the signal to noise ratio of a single measurement is sufficiently small that an ensemble of measurements is required to resolve the signal, then it is absolutely necessary to compute the amplitude of the signal prior to averaging in order to avoid the results being skewed by frequency fluctuations.

Experiment. We performed our ringdown measurements using single-channel digital homodyne detection, as discussed in Section 5.4. In this measurement, we average the IF output on the level of the sinusoidal signal rather than the amplitude, contrary to the method suggested by the above analysis. We also tried to measure the amplitude of the signal before averaging (by digitally mixing the IF signal down to DC after each measurement), but we weren't able to resolve the exponential decay in this case. We expect this is because the noise gets "baked into" the average amplitude if we average after measuring the amplitude. This means that the average output voltage increases due to the RMS noise amplitude, and the exponential decay is a tiny dip on top of this plateau. Another possible method is to measure both channels (I and Q) at the same time, calculate the amplitude ($A = \sqrt{I^2 + Q^2}$) after each sample, and average all of these values together, but this typically requires extra calibration [80] and is likely to suffer from the same noise problem.

However, it may be possible to salvage the results of this single-channel digital homodyne measurement by fitting our decaying signals to Eq. (6.76), using the values for σ_{ω_0} in Figure 6.17(a). We performed this measurement as a function of gate and flux, and we present the results of one such measurement near $(n_g, \Phi_{\text{ext}}) = (0.33, 0.51\Phi_0)$ in Figure 6.23. We perform this measurement by measuring the resonant frequency of the cCPT and then driving it with a resonant square pulse with a pulse-width of 20 μs and a pulse-period of 60 μs. We measure the reflected signal 10^6 times and average the signals together, which yields a clear signal. Finally, we locate the tail end of the pulse and fit our time-series to Eq. (6.76), where σ_{ω_0} is determined from a standard

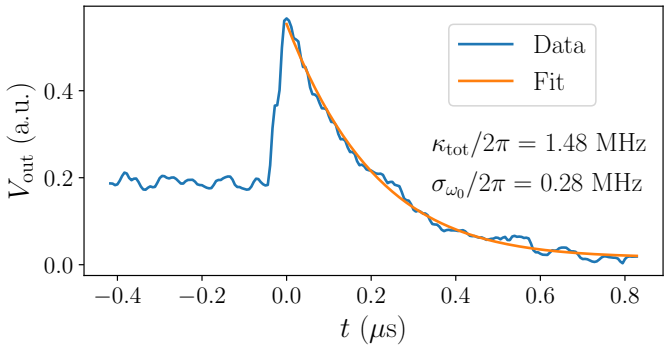

Figure 6.23: Ringdown measurement at $(n_g, \Phi_{\text{ext}}) = (0.33, -0.51\Phi_0)$ and the best fit to Eq. (6.76), which accounts for the effects of frequency fluctuations.

scattering measurement (i.e., $S_{11}(\Delta)$ measured by a VNA) performed over a similar time-scale ($\sim$ 1 minute). From the ringdown measurement we find $\kappa_{\text{tot}}/2\pi = 1.48$ MHz, whereas from the scattering measurement we find $\kappa_{\text{tot}}/2\pi = 1.32$ MHz.

This deviation between the two measurements persists as a function of gate and flux, and it is often much worse than this (some differ by a factor of 2 or more). However, these deviations are systematic in that the ringdown measurement always yields a larger value than the scattering measurement. We believe this is due to low-frequency jumps in the resonant frequency that occur after we measure ω_0 but before we start the ringdown measurement, or during the ringdown measurement itself, such that for a good portion of the measurement (10^6 pulsed measurements over a minute) the drive is off-resonant. In this case we're incorporating measurements that are sharp drops rather than genuine ring-downs, skewing our results. It may be possible to overcome this limitation by prepending a measurement of the resonant frequency to each pulse, allowing us to post-select for measurements that are on resonance, but this comes with new challenges.

Section 6.7

Discussion

In this section we've detailed the techniques used to characterize the cCPT experimentally. As we showed, the characterization process is made significantly more complex by the presence of frequency fluctuations comparable in scale to the cavity linewidth. Only by accounting for the effect of these fluctuations on the trajectories

traced out by S_{11} in the complex plane were we able to extract the true damping rates of the cCPT. In addition, we observed the key predicted signatures of both Gaussian-distributed frequency fluctuations induced by charge and flux noise, as well as chi-square-distributed frequency fluctuations induced by quantum fluctuations of the cavity field via the Kerr nonlinearity [5]. In the latter case the signature is subtle, and we are currently investigating more direct ways of observing the consequences of these quantum frequency fluctuations. We note that such nonlinearity-induced frequency fluctuations have also been studied in nanomechanical resonators [131, 132], but it is unclear whether the methods employed in this context can be applied to superconducting microwave cavities with negligible thermal occupation.

Chapter 7

Ultrasensitive Electrometry at the Single-Photon Level

Fast and ultrasensitive electrometers have been instrumental to the advancement of basic science. They have been used to detect in real time the tunneling of electrons in a quantum dot [21], determine the tunneling rates of quasiparticles in superconducting devices [22], and search for signatures of Majorana zero modes in nanowires [23]. In addition, the rapid detection of single electrons is crucial for the readout of quantum-dot-based qubits [24], for which operating at lower photon numbers reduces measurement backaction [25]. In this same vein, ultrasensitive electrometers are at the heart of many schemes for sensing the displacement of charged mechanical resonators [26, 27, 28], as well as for coherently coupling mechanical resonators to microwave cavities [3, 29, 30]. To observe and take advantage of quantum effects in such hybrid systems it is often essential that their coupling be strong at the single-photon level, a regime that has been achieved for quantum dots [31, 32] but not yet for mechanical resonators despite significant effort [33, 34, 35, 36]. Reaching the single-photon strong optomechanical coupling regime, where a single cavity photon causes sufficient radiation pressure to displace the mechanical resonator by more than its zero-point uncertainty, would enable the generation of nonclassical states of both light and motion [37, 38], as well as provide a rich platform for studying the quantum-to-classical transition and other fundamental physics [39].

Electrometers based on the single electron transistor (SET) are among the fastest and most sensitive reported in the literature to date. Radio-frequency single electron transistors (rf-SETs) are the best known of these devices, having achieved sensitivities below 1 $\mu e/\sqrt{\text{Hz}}$ [40] and bandwidths greater than 100 MHz [20]. The rf-SET

functions by encoding the charge gating the SET in the power dissipated by the SET, which is embedded in a tank circuit to enable radio-frequency readout of this dissipation. This dissipative detection typically requires picowatts of power, corresponding to hundreds of thousands of photons in the tank circuit, which renders the rf-SET unsuitable for some of the aforementioned applications and makes it impossible to integrate the rf-SET with modern near-quantum-limited parametric amplifiers [17, 41, 42] (which typically saturate well below the picowatt scale). Dispersive electrometers based on the SET have also been developed, which encode the gate charge in the resonant frequency of a tank circuit. Such electrometers have been operated using femtowatts of power [43, 22], corresponding to tens or hundreds of photons, and have achieved charge sensitivities as low as 30 $\mu e/\sqrt{\text{Hz}}$ [44]. More recently, dispersive gate-based sensors have been developed [45] that have surpassed the performance of SET-based electrometers. These devices have achieved sensitivities as low as 0.25 $\mu e/\sqrt{\text{Hz}}$ with detection bandwidths approaching 1 MHz while using only 100 attowatts of power, corresponding to hundreds of photons [46].

In this chapter we demonstrate ultrasensitive dispersive charge detection with a cavity-embedded Cooper pair transistor (cCPT) [4, 2]. Using 16 attowatts of power, corresponding to the single-photon level of the cavity, we measure a minimum charge sensitivity of 14 $\mu e/\sqrt{\text{Hz}}$. Relative to theory, we find that the cCPT operates within a factor of 5 of its quantum-limited sensitivity, this discrepancy being due to the presence of frequency fluctuations comparable to the cavity linewidth, the inherent nonlinearity of the device, and the noise of our amplifier chain. Another major limitation of the present device is quasiparticle poisoning [71], which prevents us from studying the cCPT at its theoretically-optimal operating point. Based on these results we expect an optimized sample could realistically achieve a sensitivity as low as 0.4 $\mu e/\sqrt{\text{Hz}}$, rivaling that of the best gate-based sensor [46]. This is the first ultrasensitive electrometer reported to operate at the single-photon level; for this reason, the cCPT has been proposed as a platform for reaching the single-photon strong coupling regime of optomechanics [3]. Our results support the feasibility of this proposal and represent an important step toward its realization.

It is important to note that much of this chapter is derived from our electrometry paper, Ref. [1]. Large sections of this chapter have been taken from this paper verbatim, but we've included significantly more detail in this chapter than was possible to fit into the paper due to the constraints of the letter format. In addition, we've organized the content differently so it is coherent with this thesis as a whole.

Section 7.1

Charge Sensitivity

As we showed in Chapter 4, the CPT behaves as a nonlinear Josephson inductance L_J in parallel with the cavity that can be tuned by both the number of electrons n_g gating the island and the flux Φ_{ext} threading the SQUID loop. The gate charge n_g is thus encoded in the resonant frequency ω_0 of the cavity, which can then be detected via microwave reflectometry. This device can be operated at much lower powers than comparable SET-based dispersive electrometers [22, 43, 44] for two key reasons. First, we use a distributed superconducting microwave cavity rather than a lumped-element LC circuit, yielding much lower dissipation. Second, we can tune the CPT band structure via the external flux Φ_{ext}, which provides us greater flexibility in biasing the device to an optimally-sensitive point.

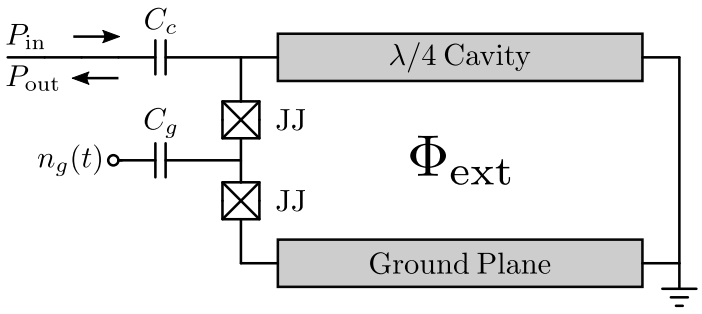

Figure 7.1: Schematic of the setup used to measure the charge sensitivity of the cCPT.

We benchmark the cCPT's performance as an electrometer by measuring its charge sensitivity, which is defined as the minimum-detectable rms charge modulation amplitude per $\sqrt{\text{Hz}}$ relative to the noise floor. To measure the charge sensitivity we drive the cCPT with a resonant carrier signal while modulating the gate about a dc bias point n_g such that $n_g(t) = n_g + \sqrt{2}(q_{\text{rms}}/e)\cos(\omega_g t)$, as depicted schematically in Figure 7.1. This charge modulation induces a frequency modulation such that $\omega_0(t) = \omega_0 + \sqrt{2}(\partial\omega_0/\partial n_g)(q_{\text{rms}}/e)\cos(\omega_g t)$. As a result, the reflected carrier signal is phase-modulated leading to output power P_{out} proportional to q_{rms}^2 at the sideband frequencies $\omega_0 \pm \omega_g$, as we showed in Section 2.4.

7.1.1 Phenomenology

We first analyze the charge sensitivity phenomenologically by considering the power at the sidebands relative to the noise floor. As we just mentioned, the power at these frequencies can be written

$$P_{\text{out}}(\omega_0 \pm \omega_g) = C q_{\text{rms}}^2 \tag{7.1}$$

for some proportionality constant C. Similarly, if the power spectral density of the noise floor is S_{noise} (in units of W/Hz) and we measure the ratio between the power at these sidebands and the noise floor using a spectrum analyzer with a resolution bandwidth B, the signal to noise ratio SNR takes the form

$$\text{SNR} = \frac{P_{\text{out}}(\omega_0 + \omega_g) + P_{\text{out}}(\omega_0 - \omega_g)}{S_{\text{noise}} \times \text{B}} = \frac{C q_{\text{rms}}^2}{S_{\text{noise}} \times \text{B}}, \tag{7.2}$$

where we've consider the total power at the two sidebands to be the signal of interest, since it is possible to combine them via homodyne mixing [40]. We can therefore solve for the constant of proportionality C

$$C = \frac{S_{\text{noise}} \times \text{B} \times \text{SNR}}{q_{\text{rms}}^2}, \tag{7.3}$$

in terms of quantities that can be determined independently.

The charge sensitivity δq of an electrometer is defined as the RMS charge amplitude per root Hz that yields a signal to noise ratio of unity, which can be written as

$$\frac{C \delta q^2}{S_{\text{noise}}} = 1. \tag{7.4}$$

Solving for δq and plugging in our expression for C, we find

$$\delta q = \frac{q_{\text{rms}}}{\sqrt{\text{B} \times \text{SNR}}} = q_{\text{rms}} \sqrt{\frac{S_{\text{noise}}}{P_{\text{out}}(\omega_0 + \omega_g) + P_{\text{out}}(\omega_0 - \omega_g)}}. \tag{7.5}$$

Thus, given the rms charge modulation amplitude q_{rms}, we can use a spectrum analyzer with resolution bandwidth B to measure both the output sideband power and the noise floor $P_{\text{noise}} = B \times S_{\text{noise}}$, from which we can extract the charge sensitivity δq.

Assuming symmetric sidebands, Eq. (7.5) can be rewritten in the more familiar

form $\delta q = q_{\mathrm{rms}}/\sqrt{2B \times 10^{\mathrm{SNR}/10}}$, where SNR is the single-sideband signal to noise ratio expressed in decibels [40, 133]. In practice, however, we observe asymmetric sidebands and therefore use Eq. (7.5) to extract the charge sensitivity from our measurements. We discuss this asymmetry in Section 7.3.3.

7.1.2 Theory

The theoretical charge sensitivity of the cCPT in this mode of operation is derived from first principles in Ref. [2]. Here we present a simple derivation based on the above phenomenological treatment and the theoretical output power

$$P_{\mathrm{out}}(\omega_0 \pm \omega_g) = \frac{2\kappa_{\mathrm{ext}}^2}{\kappa_{\mathrm{tot}}^2(\omega_g^2 + \kappa_{\mathrm{tot}}^2/4)} \left| \frac{q_{\mathrm{rms}}}{e} \frac{\partial \omega_0}{\partial n_g} \right|^2 P_{\mathrm{in}}, \tag{7.6}$$

of a frequency-modulated cavity, derived in Section 2.4. Note that this expression assumes the drive is exactly on resonance, such that $\Delta = 0$. Plugging this expression into Eq. (7.5), we obtain

$$\delta q = \frac{\kappa_{\mathrm{tot}}}{2\kappa_{\mathrm{ext}}} \sqrt{\frac{S_{\mathrm{noise}}}{P_{\mathrm{in}}} \left(\omega_g^2 + \frac{\kappa_{\mathrm{tot}}^2}{4} \right)} \left| \frac{\partial \omega_0}{\partial n_g} \right|^{-1} e. \tag{7.7}$$

The main things worth noting are that the charge sensitivity gets better with less damping, less noise, lower gate modulation frequency, greater input power, and greater slopes $\partial\omega_0/\partial n_g$. To evaluate this expression we use the sample-referred S_{noise} and P_{in} (see Section 7.2), as well as the values of κ_{ext}, κ_{tot}, and $\omega_0(n_g, \Phi_{\mathrm{ext}})$ determined from the detailed characterization of the device presented in Chapter 6. The corresponding quantum-limited sensitivity of the device is obtained by evaluating Eq. (7.7) at the quantum limit of system noise for our measurement scheme, $S_{\mathrm{noise}}^{\mathrm{QL}} = \hbar\omega$, which we discuss in Section 7.2.1.

It is important to note that both Eqs. (7.5) and (7.7) are only valid when $q_{\mathrm{rms}}/e \ll \omega_g/(\partial\omega_0/\partial n_g)$, which ensures that the amplitude of the resulting frequency modulation is small compared to ω_g and that $P_{\mathrm{out}}(\omega_0 \pm \omega_g)$ is proportional to q_{rms}^2. In all of our measurements we use sufficiently small q_{rms} to satisfy this constraint. Furthermore, Eq. (7.7) is most accurate in the linear response regime for which $n \ll \kappa_{\mathrm{tot}}/|K|$, where $n = 4\kappa_{\mathrm{ext}}P_{\mathrm{in}}/\hbar\omega_0\kappa_{\mathrm{tot}}^2$ is the average number of intracavity photons and K is the Kerr nonlinearity of the cCPT [4]. Experimentally, we find that for $n \ll \kappa_{\mathrm{tot}}/|K|$ the output sideband power grows linearly with P_{in} as expected from

Eq. (7.6), but as n approaches $\kappa_{\text{tot}}/|K|$ this trend becomes sub-linear. Near this threshold, $P_{\text{out}}(\omega_0 \pm \omega_g)$ begins to decrease with increasing P_{in}. We therefore use sufficiently small input powers such that $n \lesssim 1$ in all of our measurements, since $\kappa_{\text{tot}}/|K| > 1.7$ for all values of n_g and Φ_{ext} [4]. We discuss the power-dependence of the charge sensitivity in Section 7.3.2.

The detection bandwidth of the device, which determines the maximum rate at which the cavity can respond to changes in the gate charge n_g, is set by κ_{tot} and is on the order of 1 MHz. This can be improved by using a larger coupling capacitance C_c, thereby increasing κ_{ext}, but this improved bandwidth also affects the charge sensitivity. Restricting ourselves to single-photon-level operation and assuming negligible internal loss such that $\kappa_{\text{tot}} \approx \kappa_{\text{ext}}$, Eq. (7.7) becomes

$$\delta q = \frac{1}{2}\sqrt{\kappa_{\text{tot}}\frac{S_{\text{noise}}}{\hbar\omega_0}}\left|\frac{\partial\omega_0}{\partial n_g}\right|^{-1} e \tag{7.8}$$

for $\omega_g \ll \kappa_{\text{tot}}$. Thus, the bandwidth can be improved at the expense of sensitivity, and vice versa.

7.1.3 Effect of Frequency Fluctuations

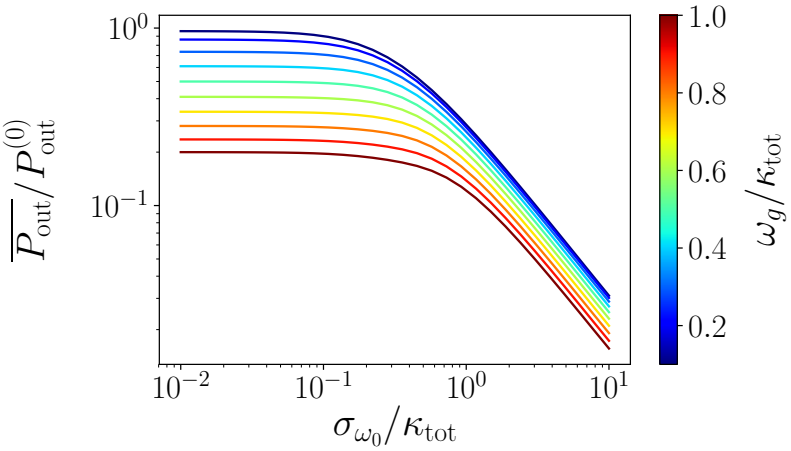

Figure 7.2: Average output sideband power (Eq. 7.10) as a function of σ_{ω_0} and ω_g. The power is scaled by $P_{\text{out}}^{(0)}$, which is the the ideal sideband power (Eq. 7.6) evaluated for $\Delta \to 0$ and $\omega_g \to 0$.

We account for the effect of frequency fluctuations by performing the same analysis as in Section 2.4, but allow for a non-zero detuning. Following the same line of

reasoning, we find that the outgoing power at the sideband frequencies takes the form

$$P_{\text{out}}(\omega \pm \omega_g) = \frac{1}{[\Delta^2 + \kappa_{\text{tot}}^2/4]\,[(\Delta \pm \omega_g)^2 + \kappa_{\text{tot}}^2/4]} \frac{\kappa_{\text{ext}}^2}{2} \left| \frac{q_{\text{rms}}}{e} \frac{\partial \omega_0}{\partial n_g} \right|^2 P_{\text{in}}. \tag{7.9}$$

In the presence of frequency fluctuations, the average power at these sidebands will be an average over a distribution of detunings around our ideal operating point of $\Delta = 0$. For example, if the fluctuations are Gaussian-distributed with variance $\sigma_{\omega_0}^2$, our average power will take the form

$$\overline{P_{\text{out}}}(\omega \pm \omega_g) = \frac{\kappa_{\text{ext}}^2}{2} \left| \frac{q_{\text{rms}}}{e} \frac{\partial \omega_0}{\partial n_g} \right|^2 P_{\text{in}} \int_{-\infty}^{\infty} \frac{\exp\!\left(-\Delta^2/2\sigma_{\omega_0}^2\right)/\sqrt{2\pi\sigma_{\omega_0}^2}}{[\Delta^2 + \kappa_{\text{tot}}^2/4]\,[(\Delta \pm \omega_g)^2 + \kappa_{\text{tot}}^2/4]} d\Delta. \tag{7.10}$$

Mathematica actually gives a closed form expression for this integral, but it's far too messy to present or use in any meaningful way. Rather, we evaluate this integral numerically.

The results of simulating this average output sideband power are shown in Figure 7.2. As expected, the average sideband power decreases significantly as $\sigma_{\omega_0} \to \kappa_{\text{tot}}$. Thus, frequency fluctuations will cause a degradation of the charge sensitivity of the cCPT, on average.

Section 7.2

Measurement Setup

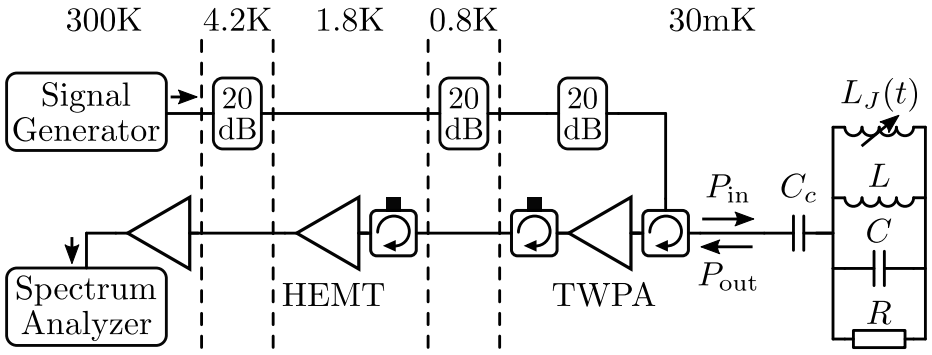

Figure 7.3: Schematic of the circuitry used to measure the charge sensitivity of the cCPT.

The charge sensitivity of the cCPT is measured using the circuitry depicted

schematically in Fig. 7.3, which is nearly identical to that described in Chapter 5. The one difference here is that we use a near quantum-limited TWPA [41] as a first-stage amplifier, followed by a cryogenic HEMT amplifier and room temperature amplifier.

7.2.1 System Noise

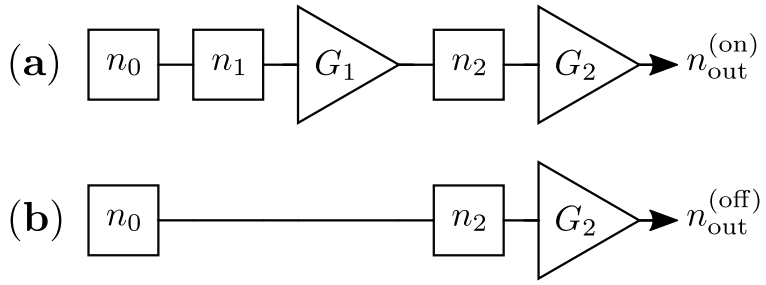

Figure 7.4: Schematic of the measurement used to isolate the TWPA added noise, with (a) the pump on and (b) the pump off. All quantities depend on frequency.

We use the techniques described in Section 6.5 to refer all input and output powers, as well as the system noise $S_{\text{noise}}(\omega)$, to the plane of the sample. We determine the noise added by the TWPA and HEMT independently by measuring the gain of the amplifier chain and total system noise twice: once with the TWPA pump on and once with it off. A schematic of this measurement, using units of photons, is presented in Fig. 7.4. Here G_1 and n_1 represent the TWPA gain and added noise, respectively, G_2 and n_2 model the rest of the amplifier chain (HEMT, room temperature amp, cable attenuation), and $n_0 = 1/2$ is the vacuum noise in the transmission line. We note that the added noise n_1 of the TWPA is not included in Fig. 7.4(b). This is because the TWPA behaves as a lossy transmission line when the pump is off and it is mounted in the mixing chamber, which means it attenuates n_0 by a certain amount and then adds exactly that same amount of noise, leaving the total input-referred noise unchanged (see Yurke's chapter in Ref. [134] for the beam-splitter model of an attenuator). In addition, although the HEMT is located at the 1K pot stage (with a temperature of about 1.7 K), the coaxial cable connecting from the TWPA output to the HEMT is made of Niobium, which should have minimal loss and therefore should add a negligible amount of additional noise referred to the HEMT input relative to n_2.

Using the transmission measurements we can determine both G_1 and G_2 (see Section 6.5). The noise measurements are then described by the equations

$$\begin{aligned} n_{\text{out}}^{(\text{on})} &= G_1 G_2 (n_0 + n_1) + G_2 n_2 \\ n_{\text{out}}^{(\text{off})} &= G_2 (n_0 + n_2). \end{aligned} \tag{7.11}$$

Measuring the output noise in these two cases therefore enables us to determine

$$n_1 = \frac{n_{\text{out}}^{(\text{on})} - n_{\text{out}}^{(\text{off})}}{G_1 G_2} - n_0 \left(1 - \frac{1}{G_1}\right), \tag{7.12}$$

$$n_2 = \frac{n_{\text{out}}^{(\text{off})}}{G_2} - n_0. \tag{7.13}$$

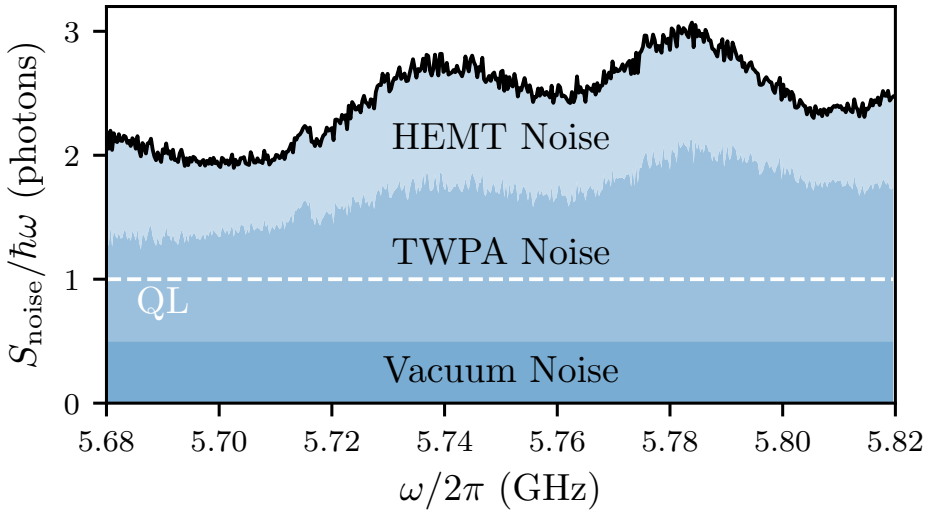

Figure 7.5: System noise referred to the sample plane (solid black line). Shaded areas show the contribution of each noise source. The dashed white line is the quantum limit.

The measured system noise, shown in Fig. 7.5, is due to the half-photon of vacuum noise $S_{\text{vac}} = \hbar\omega/2$ in the input/output transmission line [55] and the added noise of our amplifier chain S_{amp}, such that $S_{\text{noise}} = S_{\text{vac}} + S_{\text{amp}}$. For all of the charge sensitivity measurements we report, the noise floor near the sideband frequencies is dominated by this system noise, which is why we use the same notation for these two quantities. At sufficiently low gate modulation frequencies, however, the noise floor is dominated by $1/f$ charge noise [81]. In our case this regime is below about 1 kHz [4]. Over the working range of resonant frequencies of the cCPT (between 5.68 GHz and 5.82 GHz), the TWPA contributes 1.2 photons of noise (50% of total) while the

HEMT contributes 0.7 photons (30% of total) on average. The room temperature amplifier contributes negligibly to S_{noise}. The quantum limit of noise in this system is one photon, such that $S_{\text{noise}}^{\text{QL}} = \hbar\omega$, since phase-insensitive amplifiers must add at least a half-photon of noise [119]. Thus, our average system noise is only a factor of 2.4 greater than the quantum limit for this measurement scheme, such that the theoretical sensitivity (Eq. 7.7) is only a factor of $\sqrt{2.4}$ greater than the quantum-limited sensitivity.

7.2.2 Gate Attenuation

Just as we had to measure the input attenuation to determine the number of photons in the cavity, we must now measure the gate attenuation to determine the rms charge modulation amplitude q_{rms} at the plane of the sample. We measure the gate attenuation using two methods. First, we directly measure the attenuation on the RF gate line with a combination of room temperature and cryogenic measurements. Second, we modulate the gate at varying strengths and measure the resulting variance of the induced frequency fluctuations using the techniques developed in Chapter 6. As we will see, these two techniques yield results that are in good agreement with one another.

Direct Measurement. We first measure the gate attenuation at room temperature, since we do not expect the attenuation at low frequencies ($\lesssim$ 1 MHz) to change significantly at cryogenic temperatures. The one thing we do expect to change at cryogenic temperatures is the rolloff frequency of the high pass filter built into the RF port of the bias tee. Without this extra attenuation due to the bias tee, the gate attenuation is about 64.1 dB. We measure the attenuation of the bias tee as a function of frequency at 4K, the results of which are shown in Figure 7.6.

Frequency Fluctuation Measurement. We next determine the gate attenuation in-situ by modulating the gate and measuring the resulting variance of the induced frequency fluctuations. When the gate is modulated with a sinusoidal voltage with amplitude V_g, the resulting variance of the resonant frequency can be written

$$\sigma_{\omega_0}(V_g)^2 = \sigma_{\omega_0}(0)^2 + \frac{1}{2}\left|\frac{\partial\omega_0}{\partial V_g}\right|^2 V_g^2. \tag{7.14}$$

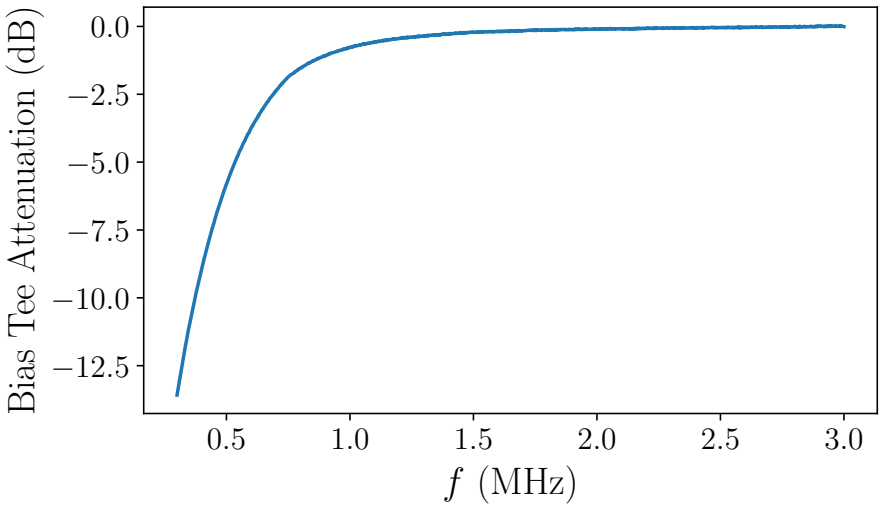

Figure 7.6: Gate attenuation due to the bias tee, measured at 4K.

Thus, if we can measure the slopes $\partial\omega_0/\partial V_g$ and $\partial(\sigma_{\omega_0}^2)/\partial(V_{g,300\mathrm{K}}^2)$, we can determine the ratio $\eta_g = V_{g,300\mathrm{K}}/V_g$ corresponding to the gate attenuation.

We perform this measurement by first biasing to a charge-sensitive point (the precise point is irrelevant). We then linearly sweep the DC gate voltage, measuring the resonant frequency, and determine the slope $\partial\omega_0/\partial V_g$. Finally, we modulate the gate at 350 kHz, sweep the gate modulation power on a linear scale, measure the reflection coefficient, fit to the average reflection coefficient (deformed resonance circle) using the model that assumes Gaussian frequency fluctuations, and determine the slope $\partial(\sigma_{\omega_0}^2)/\partial(V_{g,300\mathrm{K}}^2)$. This last step is a bit hand-wavy, since we're using a model that assumes Gaussian frequency fluctuations but this is not precise for a sinusoidally-modulated resonant frequency. As such, we only expect our results to be accurate to within a factor of unity.

The results of these measurements are shown in Figure 7.7. From these slopes we determine the gate attenuation to be 74.4 dB at 350 kHz. Without the extra cryogenic attenuation of the bias tee this corresponds to an attenuation of 63.3 dB, which differs from our direct measurement by only 20% or so. Due to the limitations of this measurement mentioned above, we err on the side of caution and use our direct measurement of the gate attenuation to analyze our experimental results for the charge sensitivity.

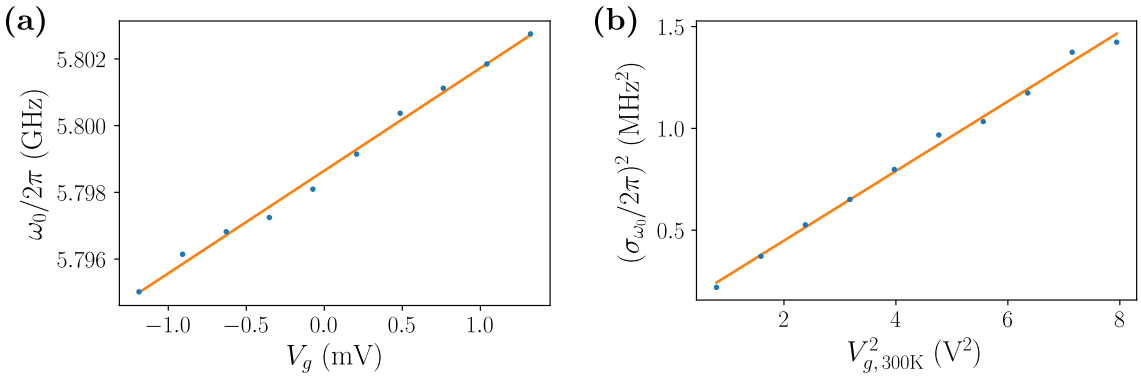

Figure 7.7: Measurements used to extract the gate attenuation in-situ. (a) Resonant frequency versus DC gate bias voltage. (b) Variance in the resonant frequency versus room temperature gate modulation voltage $V_{g,300\mathrm{K}}$.

Section 7.3

Results

7.3.1 Gate/Flux Crosstalk

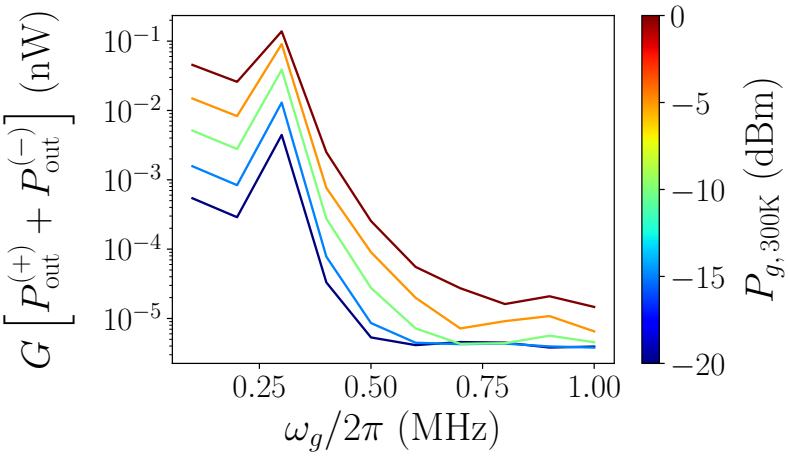

Figure 7.8: Anomalous sideband power as a function of gate modulation power and frequency. $P^{(\pm)}_{\mathrm{out}} = P_{\mathrm{out}}(\omega_0 \pm \omega_g)$ is the sideband power at the plane of the sample, G is the gain of the amplifier chain, $P_{g,300\mathrm{K}}$ is the gate modulation power at room temperature, and ω_g is the gate modulation frequency.

In our experiments, we observe crosstalk between our gate and flux lines at low

frequencies, which requires some care to avoid. To measure this crosstalk we bias the cCPT to $(n_g, \Phi_{\text{ext}}) = (0.0, \Phi_0/4)$, where the resonant frequency is sensitive to flux but insensitive to charge. We then perform our usual charge sensitivity measurement by modulating the gate at a frequency ω_g with room-temperature power $P_{g,\,300\text{K}}$ and measuring the output power at the sidebands. Any sideband power here can be attributed to an unwanted flux-modulation induced by the gate modulation via crosstalk.

The results of this measurement are shown in Figure 7.8. As you can see, this cross-talk drops off at higher frequencies and low gate modulation powers. In all of our subsequent measurements we use these results to make sure the effects of crosstalk are negligible.

7.3.2 Dependence on Input Power

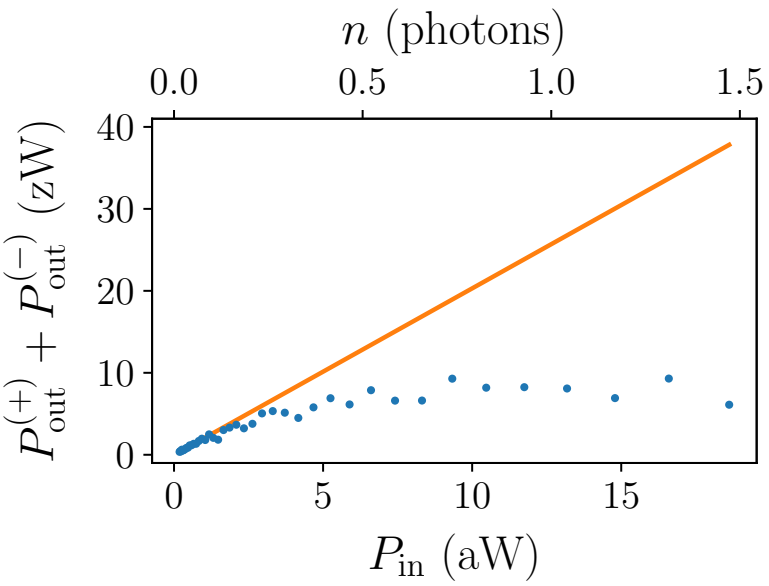

Figure 7.9: Combined output sideband power ($P_{\text{out}}^{(\pm)} = P_{\text{out}}(\omega_0 \pm \omega_g)$) as a function of input power P_{in}. This measurement was performed at $(n_g, \Phi_{\text{ext}}) = (0.6, 0.0)$, which is near the optimal bias point, with a gate modulation frequency $\omega_g/2\pi = 500$ kHz and $q_{\text{rms}} = 8.7 \times 10^{-4}e$. The line is the best fit to the low-power data.

Theoretically, we expect the output sideband power to grow linearly with the input power. Experimentally, however, this is only true for very low powers. As

the number of photons in the cavity approaches unity, the nonlinearity of the cCPT becomes important and causes a sublinear dependence of the output sideband power on the input power, as shown in Figure 7.9. The line is the best fit to the low-power data, which represents our extrapolated theoretical expectations. At $P_{\text{in}} = 16$ attowatts, our experimental and theoretical output powers differ by a factor of about 3.6.

7.3.3 Sideband Asymmetry

Experimentally, we often observe asymmetric sidebands when we modulate the gate charge n_g. This is a consequence of the sideband power's dependence on detuning

$$P_{\text{out}}(\omega \pm \omega_g) = \frac{1}{[\Delta^2 + \kappa_{\text{tot}}^2/4]\,[(\Delta \pm \omega_g)^2 + \kappa_{\text{tot}}^2/4]} \frac{\kappa_{\text{ext}}^2}{2} \left| \frac{q_{\text{rms}}}{e} \frac{\partial \omega_0}{\partial n_g} \right|^2 P_{\text{in}}. \tag{7.15}$$

As the detuning Δ deviates from zero, one sideband gets larger and one gets smaller due to the factor of $\Delta \pm \omega_g$ in the denominator. This effect is negligible for $\omega_g \ll \kappa_{\text{tot}}$, but in our case we're forced to use $\omega_g \lesssim \kappa_{\text{tot}}$ due to gate/flux crosstalk and the cryogenic attenuation of our bias tee. Thus, it is worth exploring the consequences of this effect.

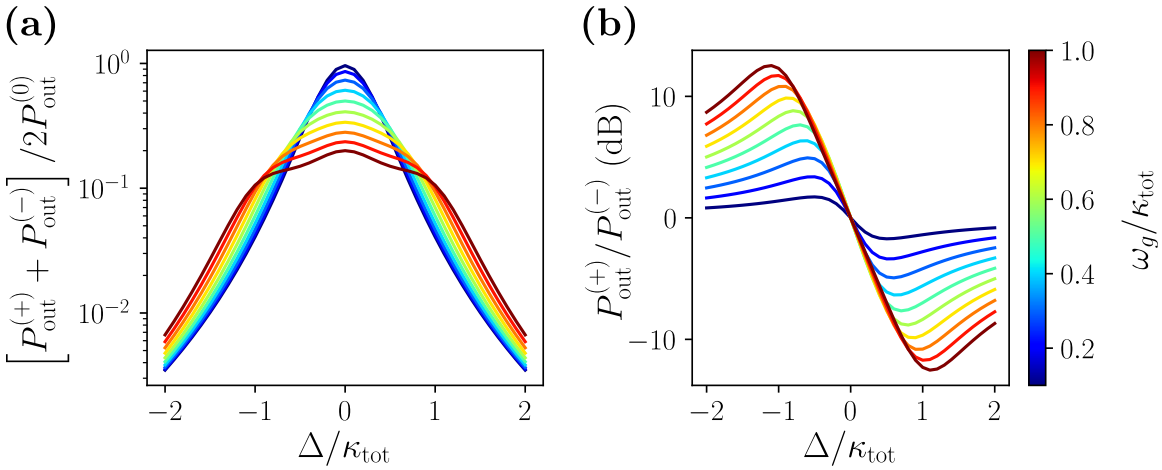

Figure 7.10: Effects of non-zero detuning on the output sideband power ($P_{\text{out}}^{(\pm)} = P_{\text{out}}(\omega_0 \pm \omega_g)$). (a) Combined sideband power as a function of detuning. The power is scaled by $P_{\text{out}}^{(0)}$, which is the the ideal sideband power (Eq. 7.6) evaluated for $\Delta \to 0$ and $\omega_g \to 0$. (b) Asymmetry between the left and right sidebands as a function of detuning.

We are primarily interested in answering two questions: how does the total side-

band power (sum of left and right) depend on the detuning, and how does the asymmetry between the two sidebands depend on the detuning. The results of simulating the total sideband power and sideband asymmetry as functions of detuning (via Eq. 7.15) are shown in Figure 7.10, (a) and (b) respectively. We find that at lower gate modulation frequencies ω_g we can achieve greater output power overall, but we are also more susceptible to deviations away from zero detuning. And, as expected, the asymmetry between the left and right sidebands is negligible for small ω_g.

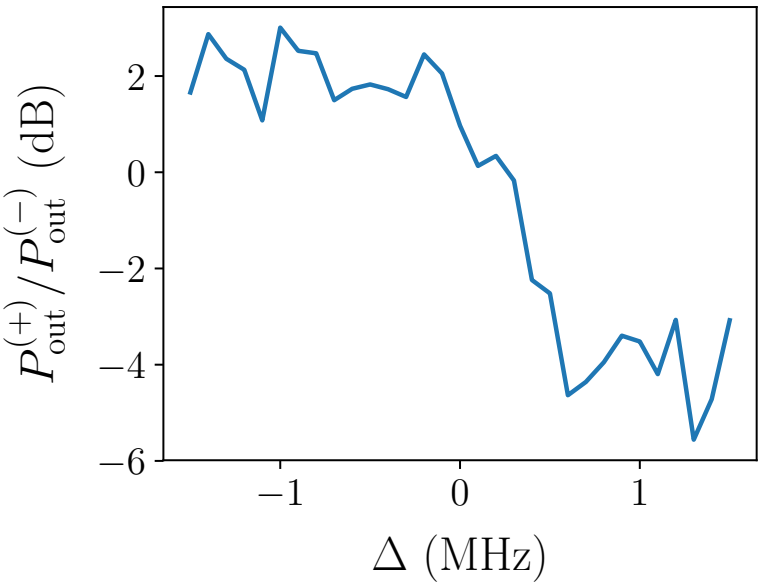

Figure 7.11: Measured asymmetry between the left and right sidebands as a function of detuning.

We can measure this asymmetry by biasing to a charge-sensitive point, sweeping the detuning of the carrier, and measuring the resulting output power when the gate is modulated sinusoidally. The results of one such measurement are shown in Figure 7.11. As expected, the right sideband is larger than the left at negative detunings, and vice versa for positive detunings. It's difficult to get a very clean measurement of this asymmetry due to frequency jumps occuring over the course of the sweep.

7.3.4 Dependence on Gate and Flux

In order to compare the cCPT's charge sensitivity with its theoretical performance, given by Eq. (7.7), we first measure δq as a function of both the gate charge n_g and external flux Φ_{ext}. Although we can access a full period of Φ_{ext} (from 0 to the

magnetic flux quantum Φ_0), we can only access the gate range $-0.65 < n_g < 0.65$ due to quasiparticle poisoning [4]. We perform this measurement using an input power $P_{\text{in}} = -141$ dBm ≈ 8 aW and gate modulation amplitude $q_{\text{rms}} = 10^{-3}e$. Ideally we would set ω_g to be significantly less than $\kappa_{\text{tot}}/2 \approx 2\pi \times 700$ kHz to minimize Eq. (7.7), but due to the cross-talk between our gate and flux lines we use $\omega_g/2\pi = 800$ kHz, such that the gate modulation does not also induce a flux modulation. To measure the reflected power and noise floor at $\omega_0 \pm \omega_g$ we use a resolution bandwidth $B = 1$ Hz.

The results of this measurement are shown in Fig. 7.12(a). We find that the variation of δq with n_g and Φ_{ext} is in good agreement with our theory, but our measured sensitivities are about 3 times worse than theory. We attribute this discrepancy to two factors. First and foremost, the resonant frequency fluctuates due to $1/f$ charge and flux noise [4, 5] over the course of each measurement, which means our carrier is not always on resonance. On average, this reduces the output sideband power yielding worse charge sensitivity than expected. Second, we used a sufficiently high input power that $P_{\text{out}}(\omega_0 \pm \omega_g)$ scales sublinearly with P_{in} due to the Kerr nonlinearity. Although this improves the sensitivity overall and was necessary to resolve the sidebands over a large area of the gate/flux parameter space, it causes the measured sensitivity to diverge from theory since the latter assumes proportionality between P_{in} and $P_{\text{out}}(\omega_0 \pm \omega_g)$. Finally, accounting for the fact that $S_{\text{noise}}/S_{\text{noise}}^{\text{QL}} \approx 2.4$, the factor of 3 discrepancy between theory and experiment means our measured sensitivities are within a factor of 5 of the quantum limit. In this measurement we find a minimum charge sensitivity of 24 $\mu e/\sqrt{\text{Hz}}$ at $(n_g, \Phi_{\text{ext}}) = (0.63, 0.0)$, whereas our predicted theoretical and quantum-limited sensitivities at this point are 9 $\mu e/\sqrt{\text{Hz}}$ and 6 $\mu e/\sqrt{\text{Hz}}$, respectively.

7.3.5 Optimal Sensitivity

In order to optimize δq we narrow our search to the gate range $0.6 \leq |n_g| \leq 0.65$ and the flux points $\Phi_{\text{ext}} = 0, \Phi_0/2$. At these flux points the resonant frequency of the cCPT is insensitive to flux, so we can reduce our gate modulation frequency to $\omega_g/2\pi = 350$ kHz without the gate/flux cross-talk interfering with our results. To maintain a small frequency modulation amplitude relative to ω_g, we also reduce q_{rms} to $5 \times 10^{-4}e$. For this measurement we use a resolution bandwidth $B = 10$ Hz.

We find a minimum charge sensitivity of 14 $\mu e/\sqrt{\text{Hz}}$ at $(n_g, \Phi_{\text{ext}}) = (0.625, 0.0)$ using an input power $P_{\text{in}} = -138$ dBm ≈ 16 aW. Under these conditions our pre-

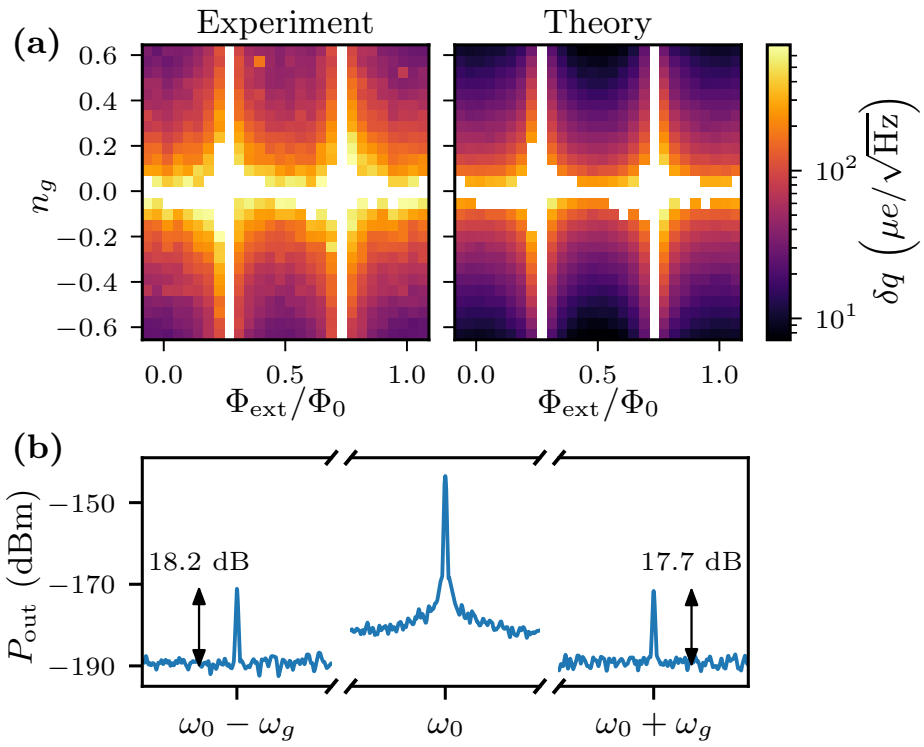

Figure 7.12: (a) Measured and theoretical charge sensitivities, obtained using Eqs. (7.5) and (7.7) respectively, as a function of gate and flux. Data is omitted where the sidebands could not be resolved from the noise floor. (b) Sample-referred spectrum analyzer trace of the optimal charge sensitivity measurement, corresponding to $\delta q = 14\ \mu e/\sqrt{\text{Hz}}$. The carrier frequency is $\omega_0/2\pi = 5.806$ GHz, the gate modulation frequency is $\omega_g/2\pi = 350$ kHz, the span of each segment is 1 kHz, and the resolution bandwidth is $B = 10$ Hz. The noise floor near the carrier is due to $1/f$ charge noise [4, 81].

dicted theoretical and quantum-limited sensitivities are 5 $\mu e/\sqrt{\text{Hz}}$ and 3 $\mu e/\sqrt{\text{Hz}}$, respectively. The spectrum analyzer trace of this optimal measurement is shown in Fig. 7.12(b). At this bias point the resonant frequency is $\omega_0/2\pi = 5.806$ GHz, the external damping is $\kappa_{\text{ext}}/2\pi = 1.24$ MHz, and the total damping is $\kappa_{\text{tot}}/2\pi = 1.62$ MHz, such that the number of intracavity photons is $n = 4\kappa_{\text{ext}}P_{\text{in}}/\hbar\omega_0\kappa_{\text{tot}}^2 \approx 1$.

Section 7.4

Discussion

This is the first ultrasensitive electrometer reported to operate at the single-photon level. Furthermore, its sensitivity is rivaled only by gate-based sensors [46], rf-SETs

[40], and carbon nanotube-based rf-SETs [135]. In Table 7.1 we compare the performance of the cCPT to a representative set of fast (detection bandwidth $\gtrsim 1$ MHz) and ultrasensitive ($\delta q < 10^{-3} e/\sqrt{\text{Hz}}$) electrometers. Clearly, the cCPT is unparalleled in its ability to operate at low powers and photon numbers. As discussed earlier, this makes it ideal for mediating an optomechanical interaction that reaches the single-photon strong coupling regime [3].

As we mentioned earlier, the factor of 3 discrepancy between theory and experiment is primarily attributable to frequency fluctuations and the inherent nonlinearity of the cCPT. Using our results from Section 7.1.3, we estimate that frequency fluctuations accounts for a factor of about $\sqrt{1.6}$ discrepancy between theory and experiment for the optimal measurement. Using our results from Section 7.3.2, we estimate that the nonlinearity of the cCPT accounts for a factor of about $\sqrt{3.6}$ discrepancy. Thus, the two combined account for a factor of about 2.4. We believe the remaining $\sim 20\%$ of the discrepancy is primarily due to the insertion loss of circulators and interconnects between the sample and TWPA (as well as between the TWPA and HEMT to a lesser degree), which would decrease our SNR relative to theory.

There remains significant room for improving the sensitivity of the cCPT, with two distinct approaches for doing so. The most promising approach is to reduce quasiparticle poisoning (QP) [71], which prevents us from operating at gate biases above $|n_g| \approx 0.65$ [4]. If we were able to operate the present device at $(n_g, \Phi_{\text{ext}}) = (0.9, \Phi_0/2)$ we would expect to attain a charge sensitivity of $\delta q \approx 0.4\ \mu e/\sqrt{\text{Hz}}$, assuming the same factor of 3 discrepancy with theory as we observe experimentally. The present device was designed with a 9 nm thick CPT island [4] to suppress QP [69], but other fabrication techniques could be employed to reduce it further. These include oxygen-doping the CPT island [71] and embedding quasiparticle traps near the CPT [136].

The other approach is to mitigate the discrepancy between our measured sensitivities and the quantum limit of sensitivity for the cCPT. One such improvement would be to use a truly quantum-limited amplifier, which would improve our sensitivities by a factor of $\sqrt{S_{\text{noise}}/\hbar\omega} \approx \sqrt{2.4}$. Another such improvement would be to stabilize the resonant frequency using a Pound-locking loop [139], thereby reducing the scale of frequency fluctuations induced by $1/f$ noise, which we expect would substantially improve the sensitivity of the cCPT.

Finally, it may be possible to improve the sensitivity of the cCPT by employing more sophisticated charge detection schemes. For example, the cCPT can be driven to its bifurcation point, set by the Kerr nonlinearity, where the slope of the cavity

Electrometer	δq ($\mu e/\sqrt{\text{Hz}}$)	P_{in} (aW)	# photons
cCPT*	14	16	1
Best gate sensor[46]*	0.25	100	190
Best rf-SET[40]	0.9	6×10^6	2×10^5
Andresen et al.[135]	2.3	3×10^8	2×10^6
L-SET[44]*	30	1×10^4	70
Naaman et al.[22]*	52	2×10^3	150
Bell et al.[137]*	70	3×10^7	2×10^5
rf-QPC[138]	200	1×10^9	7×10^7

Table 7.1: Comparison of the cCPT with a representative set of fast and ultrasensitive electrometers. Asterisks indicate dispersive electrometers.

response with respect to detuning diverges. At this point the charge modulation would induce a stronger modulation of the reflected signal and thus improved sensitivity [140, 141]. It is difficult to operate at this point, however, since frequency fluctuations blur the sharp cavity response. We analyze this nonlinear charge detection scheme in depth in Appendix A and conclude that it is only practical if the relative size of frequency fluctuations ($\sigma_{\omega_0}/\kappa_{\text{tot}}$) can be reduced. This may be possible in our sample by using Pound-locking, as mentioned above, or in a new sample by increasing κ_{ext}.

Another possible method to enhance the charge sensitivity of the cCPT is to incorporate parametric pumping of the flux at $2\omega_0$. If biased near the threshold of parametric oscillation, small changes in the gate charge would yield huge changes in the oscillation amplitude. Such a scheme has previously been used to achieve single-shot readout of a superconducting qubit [10].

Chapter 8

Summary and Outlook

In this thesis we presented the results of two projects involving the cavity embedded Cooper pair transistor (cCPT). The first project consisted of a detailed characterization of the cCPT, which had both theoretical [5] and experimental [4] components. On the theoretical side, we developed a model for how frequency fluctuations comparable to the cavity linewidth may arise in tunable and nonlinear microwave cavities (due to classical fluctuations in the tuning parameters and quantum fluctuations in the intracavity field, respectively), and how these frequency fluctuations affect the measurement of scattering matrix elements (such as the reflection and transmission coefficients). Since the measurement of scattering matrix elements is a standard method for extracting the damping rates of microwave cavities [7, 8], one must use this model that accounts for the effect of frequency fluctuations to accurately determine the damping rates of these cavities. On the experimental side, we used this theoretical model to characterize the cCPT. We observed key signatures of frequency fluctuations predicted by our model, and described in detail the experimental techniques used to measure and corroborate the effects of frequency fluctuations. We expect this work to be broadly relevant to the community working on tunable and nonlinear microwave cavities, which have become ubiquitous in the field of circuit quantum electrodynamics. By using our theoretical model for the effect of frequency fluctuations on measurements of scattering matrix elements, we expect that these devices can be characterized more accurately moving forward.

The second project was a careful benchmarking of the cCPT's performance as a dispersive electrometer. We demonstrated ultrasensitive dispersive charge detection with the cCPT: using 16 attowatts of power, corresponding to the single-photon level of the cavity, we measured a minimum charge sensitivity of 14 $\mu e/\sqrt{\text{Hz}}$. This is

the first ultrasensitive electrometer reported to operate at the single-photon level and its sensitivity is comparable to rf-SETs [20], which typically require picowatts of power. Relative to theory, we found that the cCPT operates within a factor of 5 of its quantum-limited sensitivity. The sensitivity of the cCPT is rivaled only by gate-based sensors [46], rf-SETs [40], and carbon nanotube-based rf-SETs [135]. As for its ability to operate at low powers and photon numbers, it is unrivaled. Our demonstration of ultrasensitive charge detection at the single-photon level thus advances the state of the art of electrometry. As we discussed in Chapter 7, this low-power operation enables the cCPT to be integrated with near quantum-limited amplifiers and could help facilitate the multiplexed readout of quantum-dot-based qubits. Furthermore, our results support the feasibility of using the cCPT to mediate an optomechanical interaction that reaches the single-photon strong coupling regime [3].

Looking forward, there are many opportunities for new projects stemming from this work. For example, there are multiple ways we might improve upon the charge sensitivity of the cCPT. First, we might exploit the nonlinearity of the cCPT to enhance the charge sensitivity. One way of doing so would be to drive the cCPT to its bifurcation point, set by the Kerr nonlinearity, where the slope of the cavity response with respect to detuning diverges. At this point the charge modulation would induce a stronger modulation of the reflected signal and thus improved sensitivity [140, 141]. It is difficult to operate at this point, however, since frequency fluctuations blur the sharp cavity response. We analyze this nonlinear charge detection scheme in depth in Appendix A and conclude that it is only practical if the relative size of frequency fluctuations ($\sigma_{\omega_0}/\kappa_{\rm tot}$) can be reduced. This may be possible in our sample by using Pound-locking to stabilize the resonant frequency against $1/f$ noise, as our labmate Sisira is currently working on implementing, or in a new sample by increasing $\kappa_{\rm ext}$. Another possible method to enhance the charge sensitivity of the cCPT is to incorporate parametric pumping of the flux at $2\omega_0$. If biased near the threshold of parametric oscillation, small changes in the gate charge would yield huge changes in the oscillation amplitude. Such a scheme has previously been used to achieve single-shot readout of a superconducting qubit [10]. A possible pitfall of this approach is that we'd have to bias the cCPT to a point where the resonant frequency is sensitive to flux, such that it would also be susceptible to $1/f$ flux noise. However, it may also be possible to simply pump the gate charge at $2\omega_0$ rather than the flux.

Another interesting project is to study parametric resonance in the cCPT at a point where the Kerr nonlinearity vanishes. Since the Kerr nonlinearity is generally

understood to be the primary factor limiting the steady-state amplitude of parametric oscillation [142, 143], this would mean exploring a new regime of parametric resonance and the dynamical Casimir effect [13, 14, 15]. This ability to tune the nonlinearity to zero while parametrically pumping the flux line is a novel feature of the cCPT; for comparable systems that have been used to study parametric resonance [144, 86], there is a minimum value of the magnitude of the Kerr nonlinearity. We present some preliminary experimental results on this topic in Appendix B.

Appendix A

Nonlinear Dispersive Sensing

In this Appendix we show how a cavity's Kerr nonlinearity can be exploited to improve detection of a dispersively-coupled signal. Our particular interest is in dispersive charge sensing with the cavity-embedded Cooper pair transitor (cCPT) [4, 1, 2], but our analysis can easily be translated to model other systems as well. We begin by briefly contextualizing our treatment of dispersive sensing. We then present a simple analysis in the linear regime, followed by the same analysis in the nonlinear regime. Our focus is on determining the additional gain one can obtain in the nonlinear regime compared to the linear regime, and the bandwidth of this gain. Finally, we analyze the effects of both frequency fluctuations and Kerr fluctuations on this gain, and discuss methods of mitigating these effects in the cCPT. We find that increasing the coupling between the cavity and the input/output transmission line is a straightforward way to reduce the relative scale of frequency fluctuations in the cCPT, which should allow the Kerr nonlinearity to be exploited for improved charge sensitivity.

Section A.1

Dispersive Sensing

We consider a cavity dispersively coupled to a classical gate charge n_g, in units of numbers of electrons, such that the cavity's resonant frequency $\omega_0 = \omega_0(n_g)$. The cavity is probed by reflection measurements, such that the input and output voltages are related by the reflection coefficient $S_{11}(\Delta)$ according to

$$V_{\text{out}}(t) = S_{11}(\Delta) V_{\text{in}} e^{i\omega t} \tag{A.1}$$

where $\Delta = \omega - \omega_0$ is the detuning of the drive from resonance. When driven near resonance, changes in the gate charge n_g lead to changes in ω_0, which in turn lead to changes in the phase and/or amplitude of the reflected signal. In particular, if the resonant frequency changes according to $\omega_0 \to \omega_0 + \Omega(t)$, then the change in output voltage is

$$\delta V_{\text{out}}(t) = -\frac{\partial S_{11}}{\partial \Delta}\Omega(t) V_{\text{in}} e^{i\omega t}, \tag{A.2}$$

to linear order in the dispersive shift $\Omega(t)$. In general, the output voltage will change in both amplitude and phase. The combined effect of these changes is captured by the quantity $|\partial S_{11}/\partial \Delta|$, which we call the "dispersive response" and will be using as a metric for analyzing detection sensitivity.

This treatment is similar to that in Ref. [141], and it is particularly convenient for analyzing the nonlinear cavity response. However, it glosses over the dynamics of the intracavity field and is therefore only accurate when the changes in frequency $\Omega(t)$ occur much slower than the total damping rate κ_{tot} of the cavity (i.e., there is an implicit assumption that the cavity can instantaneously respond to changes in its resonant frequency). Obviously, another important aspect of a sensor is how changes in the sensed quantity (charge, for example) give rise to a dispersive shift, but this is not our main interest in these notes. Rather, we are interested in how well the cavity converts a change in resonant frequency into a change in output voltage, and how this conversion depends on operating conditions (input power, detuning, etc.).

Section A.2

Linear Regime

The reflection coefficient S_{11} of a linear two-sided cavity takes the form

$$S_{11}(\Delta) = \frac{\Delta - i(\kappa_{\text{int}} - \kappa_{\text{ext}})/2}{\Delta - i(\kappa_{\text{int}} + \kappa_{\text{ext}})/2} \tag{A.3}$$

as derived in Section 2.3, where $\Delta = \omega - \omega_0$ is the detuning of the drive from resonance. This is an accurate model for the reflection coefficient of a $\lambda/4$ microwave cavity with internal loss rate κ_{int}, external coupling rate κ_{ext} to the input/output transmission line, and total damping rate $\kappa_{\text{tot}} = \kappa_{\text{int}} + \kappa_{\text{ext}}$. In this case the dispersive response takes the form

$$\left|\frac{\partial S_{11}}{\partial \Delta}\right| = \frac{\kappa_{\text{ext}}}{\Delta^2 + \kappa_{\text{tot}}^2/4}. \tag{A.4}$$

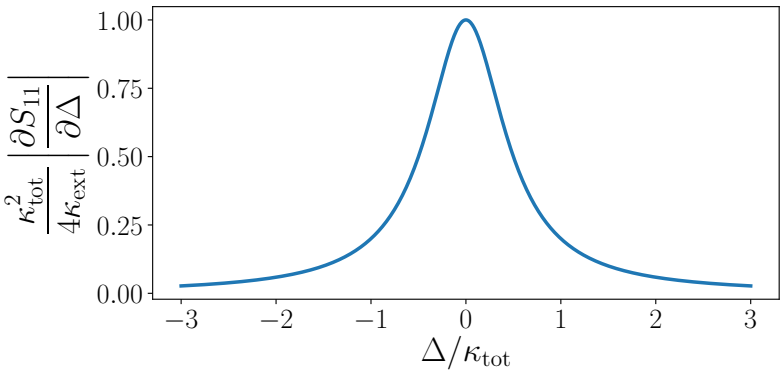

Figure A.1: Dispersive response in the linear regime.

This is a Lorentzian whose maximum value of $4\kappa_{\text{ext}}/\kappa_{\text{tot}}^2$ is obtained at $\Delta = 0$ and whose linewidth is κ_{tot}, as depicted in Figure A.1. This maximum value is what we will use as a basis of comparison with the nonlinear response regime.

Section A.3

Nonlinear Regime

We first briefly reiterate some of the results of Section 2.5. As we showed, the reflection coefficient of a cavity with Kerr nonlinearity K is given by

$$S_{11}^{\text{Kerr}}(\Delta) = \frac{\Delta - Kn - i(\kappa_{\text{int}} - \kappa_{\text{ext}})/2}{\Delta - Kn - i(\kappa_{\text{int}} + \kappa_{\text{ext}})/2}, \tag{A.5}$$

which is identical to the linear reflection coefficient (A.3) evaluated at the shifted detuning $\Delta - Kn$. In this expression $n(\Delta)$ is the number of intracavity photons as a function of detuning, obtained by solving the cubic equation

$$K^2 n^3 - 2\Delta K n^2 + \left[\Delta^2 + \frac{\kappa_{\text{tot}}^2}{4}\right] n - \kappa_{\text{ext}} \frac{P_{\text{in}}}{\hbar\omega_0} = 0, \tag{A.6}$$

where P_{in} is the input power of the drive. In general, this cubic equation for the cavity response has three solutions; if only one solution is real then it is stable and the unique physical solution, whereas if all three solutions are real then one solution will be unstable and there will be bistability in the cavity response as a function of

detuning [60]. The onset of bistability occurs at the critical power and detuning

$$P_c = \frac{\sqrt{3}}{9}\frac{\hbar\omega_0\kappa_{\text{tot}}^3}{|K|\kappa_{\text{ext}}}, \tag{A.7}$$

$$\Delta_c = \text{sign}(K)\frac{\sqrt{3}\kappa_{\text{tot}}}{2}. \tag{A.8}$$

It is worth noting that all of these results are obtained using a semiclassical approach, which is only appropriate when $|K| < \kappa_{\text{tot}}$. To simulate this nonlinear response it is convenient to write Eq. (A.6) in non-dimensional form

$$N^3 - 2\delta N^2 + \left(\delta^2 + \frac{1}{4}\right)N - \frac{\sqrt{3}}{9}\rho_{\text{in}} = 0, \tag{A.9}$$

$$N = |K|n/\kappa_{\text{tot}}, \tag{A.10}$$

$$\delta = (\Delta/\kappa_{\text{tot}})\text{sign}(K), \tag{A.11}$$

$$\rho_{\text{in}} = P_{\text{in}}/P_c. \tag{A.12}$$

The simulated curve $N(\delta)$ is shown in Figure A.2. At the bifurcation point $\rho_{\text{in}} = 1$, the slope of $N(\delta)$ diverges.

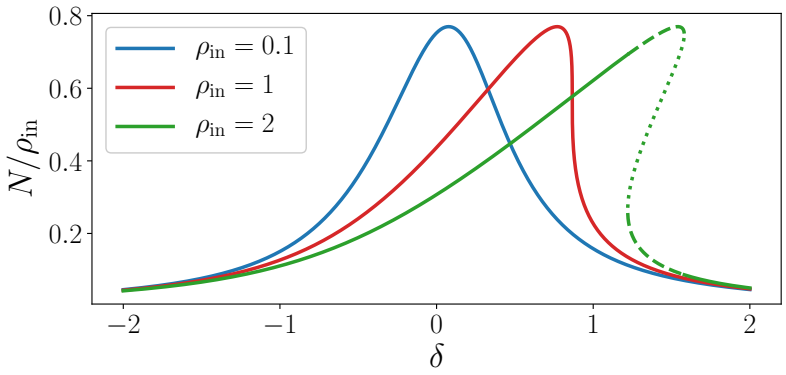

Figure A.2: Number of photons in the Kerr cavity as a function of detuning at different input powers. Solid lines indicate monostable solutions, dashed lines indicate bistable solutions, and dotted lines indicate unstable solutions.

We now turn to the dispersive response of the Kerr cavity, which can be written

$$\left|\frac{\partial S_{11}^{\text{Kerr}}}{\partial\Delta}\right| = \frac{\kappa_{\text{ext}}}{(\Delta - Kn)^2 + \kappa_{\text{tot}}^2/4}\left|1 - K\frac{\partial n}{\partial\Delta}\right|, \tag{A.13}$$

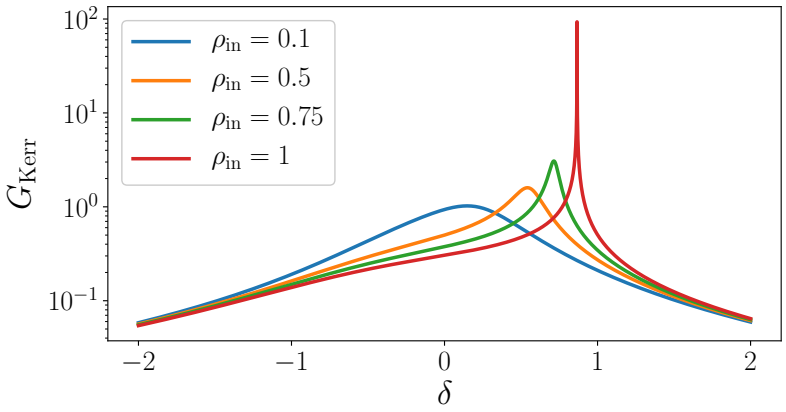

Figure A.3: Additional dispersive response gain due to the Kerr nonlinearity.

which is simple to evaluate except for the term $\partial n/\partial\Delta$. Rather than numerically differentiating our numerical solution to $n(\Delta)$, we differentiate Eq. (A.6) with respect to Δ and solve for $\partial n/\partial\Delta$, which takes the form

$$\frac{\partial n}{\partial \Delta} = -\frac{2n(\Delta - Kn)}{3K^2n^2 - 4\Delta Kn + \Delta^2 + \kappa_{\mathrm{tot}}^2/4}. \tag{A.14}$$

We next define the Kerr gain G_{Kerr} as the ratio of the nonlinear dispersive response $|\partial S_{11}^{\mathrm{Kerr}}/\partial\Delta|$ to the maximum linear dispersive response $4\kappa_{\mathrm{ext}}/\kappa_{\mathrm{tot}}^2$. Plugging back into Eq. (A.13) and rewriting in terms of the nondimensional parameters introduced above, we find

$$G_{\mathrm{Kerr}} = \left| \frac{1}{12N^2 - 16\delta N + 4\delta^2 + 1} \right|. \tag{A.15}$$

Since this method of dispersive detection (monitoring a continuously-varying resonant frequency) only makes sense below the bifurcation point, we limit our analysis of this gain to $\rho_{\mathrm{in}} \leq 1$. Our simulation of G_{Kerr} for input powers leading up to the bifurcation point is shown in Figure A.3. Since this gain is a function of the slope of $N(\delta)$, it diverges as the bifurcation point $\rho_{\mathrm{in}} = 1$ is approached.

Another important feature of G_{Kerr} is its bandwidth BW_{Kerr}, which we take to be the full width at half maximum (FWHM). We've plotted both this bandwidth and the maximum gain as a function of ρ_{in} in Figure A.4. As the bifurcation is approached, we see that the bandwidth goes to zero while the maximum gain diverges.

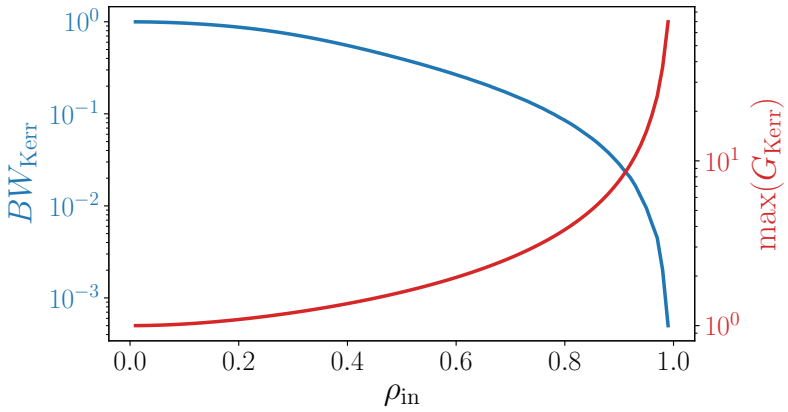

Figure A.4: FWHM and maximum gain of G_{Kerr} as a function of ρ_{in}.

Section A.4

Frequency and Kerr Fluctuations

We next consider how G_{Kerr} is affected by a fluctuating resonant frequency and Kerr nonlinearity. Essentially, frequency fluctuations prevent us from operating at a precise value of the detuning (when $\omega_0 \to \omega_0 + d\omega$, $\delta \to \delta - d\omega/\kappa_{\mathrm{tot}}$), and Kerr fluctuations prevent us from operating at a precise value of ρ_{in} (when $K \to K + dK$, $\rho_{\mathrm{in}} \to \rho_{\mathrm{in}}(1 + dK/K)$). We analyze the effect of these fluctuations on G_{Kerr} by posing the following question: for each value of ρ_{in}, if we can stabilize δ to within $\pm\sigma_\delta$ of the detuning δ_{max} where G_{Kerr} is maximized, what is the average gain we can expect? The result of our simulation addressing this question is presented in Figure A.5.

As expected, the smaller σ_δ is and the closer to $\rho_{\mathrm{in}} = 1$ we can operate, the larger average gain we can achieve. In particular, to achieve an average gain of $\overline{G_{\mathrm{Kerr}}} > 10$, we must have $\rho_{\mathrm{in}} \gtrsim 0.92$ and $\sigma_\delta \lesssim 0.01$. The optimal strategy in the presence of these fluctuations is to aim for $\delta = \delta_{\mathrm{max}}$ and $\rho_{\mathrm{in}} = 1 - dK/K$ (so that we always remain below the bifurcation point). Thus, for a rule of thumb, to achieve appreciable gain we can tolerate frequency fluctuations less than about 1% of κ_{tot} and Kerr fluctuations less than about 5% of K.

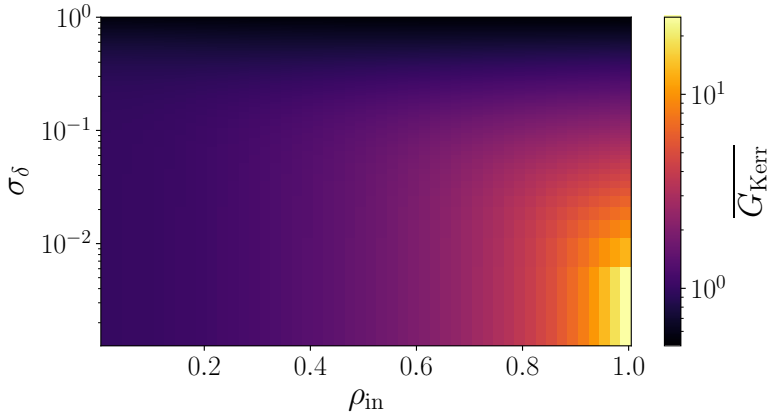

Figure A.5: Average gain $\overline{G_{\text{Kerr}}}$ over the interval $\delta_{\text{max}} \pm \sigma_\delta$, as a function of σ_δ and ρ_{in}. The average is taken over uniformly-sampled detunings in the interval $\delta_{\text{max}} \pm \sigma_\delta$, with uniform weighting.

Section A.5

Discussion

With these results in hand, we next discuss the implications for the cCPT. We first consider our experimental realization of the device [4, 1]. The sources of frequency fluctuations in this device are $1/f$ charge noise, $1/f$ flux noise, and quantum fluctuations of the intracavity field coupling to the resonant frequency via the Kerr nonlinearity [5], whereas the sources of Kerr fluctuations are primarily the $1/f$ charge and flux noise. We quantify these fluctuations by their associated variances $\sigma^2_{\omega_0}$ and σ^2_K, which generally depend on the time-scale over which the quantities are sampled (over longer periods of time, these quantities will be sensitive to fluctuations occurring at lower frequencies, leading to larger variances). These variances can be expressed as

$$\sigma^2_{\omega_0} = \left|\frac{\partial \omega_0}{\partial n_g}\right|^2 \sigma^2_{n_g} + \left|\frac{\partial \omega_0}{\partial \Phi_{\text{ext}}}\right|^2 \sigma^2_{\Phi_{\text{ext}}} + \frac{K^2}{4}, \tag{A.16}$$

$$\sigma^2_K = \left|\frac{\partial K}{\partial n_g}\right|^2 \sigma^2_{n_g} + \left|\frac{\partial K}{\partial \Phi_{\text{ext}}}\right|^2 \sigma^2_{\Phi_{\text{ext}}}, \tag{A.17}$$

where $\sigma^2_{n_g}$ and $\sigma^2_{\Phi_{\text{ext}}}$ are the variances of the $1/f$ charge and flux noise, respectively. At the point of optimal charge sensitivity $(n_g, \Phi_{\text{ext}}) \approx (0.63, 0.0)$ where $K/2\pi \approx -0.7$ MHz and $\kappa_{\text{tot}}/2\pi \approx 1.6$ MHz, the standard deviations of frequency and Kerr

fluctuations are

$$\sigma_{\omega_0} \approx 2\pi \times 0.7\,\text{MHz} \approx \kappa_{\text{tot}}/2, \tag{A.18}$$

$$\sigma_K \approx 2\pi \times 6\,\text{kHz} \approx |K|/100, \tag{A.19}$$

assuming a sampling time-scale on the order of seconds. These Kerr fluctuations are tolerable, but the frequency fluctuations are far too large to achieve appreciable gain. The only way to reduce the scale of frequency fluctuations in the present device is to implement a feedback loop, such as Pound-locking. Feedback of some kind is likely to be necessary in any realistic implementation of the cCPT as an electrometer anyway, to deal with slow drift of the gate charge as well as sudden jumps that occur infrequently (every 8-12 hours, typically). Even if such a feedback loop could stabilize the resonant frequency against most of the $1/f$ charge noise it is unlikely to stabilize it against quantum fluctuations, which are not sharply peaked at low frequencies. Thus, although stabilizing against $1/f$ noise would be beneficial in numerous ways, it is unlikely to provide sufficient stability to achieve appreciable gain via the cavity's nonlinear response.

However, for a new realization of the device the relative size of these frequency fluctuations can be reduced considerably by simply increasing κ_{ext} (by increasing the size of the interdigitated capacitor coupling the cavity to the input/output transmission line). Since this change would have other consequences, it's useful to return to the theoretical equation for the charge sensitivity of the cCPT in the linear response regime [1, 2]

$$\delta q = \frac{\kappa_{\text{tot}}}{4}\sqrt{\frac{S_{\text{noise}}}{P_{\text{in}}}}\left|\frac{\partial\omega_0}{\partial n_g}\right|^{-1} e, \tag{A.20}$$

where we've assumed that κ_{int} is negligible and that the gate signal of interest is slow compared to $\kappa_{\text{tot}} \approx \kappa_{\text{ext}}$. Plugging in the critical power (A.7), this expression reduces to

$$\delta q = \frac{1}{4}\sqrt{3\sqrt{3}|K|\frac{S_{\text{noise}}}{\hbar\omega_0}}\left|\frac{\partial\omega_0}{\partial n_g}\right|^{-1} e. \tag{A.21}$$

We therefore see that increasing κ_{tot} has no effect on the sensitivity, since it also allows us to use higher input powers due to the smaller ratio of $|K|/\kappa_{\text{tot}}$. If one needs to operate at the single-photon level, however, this is no longer the case as δq will scale as $\sqrt{\kappa_{\text{tot}}}$. Including the nonlinear gain, the charge sensitivity further improves by a factor of $1/G_{\text{Kerr}}$. Thus, increasing κ_{tot} to somewhere between 10 and 50 MHz

is a straightforward way of improving the device: the relative scale of frequency fluctuations will decrease, the nonlinear gain will improve the charge sensitivity, and the detection bandwidth will increase. That being said, this may make operating the device more difficult in other ways; for instance, the tunability range of ω_0 would no longer be much greater than the linewidth, which could make it harder to pinpoint the bias point of the cCPT.

This analysis changes somewhat if we consider a device without quasiparticle poisoning (QP), which prevents us from operating above $|n_g| > 0.65$ in the present device [4]. If we were able to operate up to $n_g = 0.9$, for example, then the most sensitive point would be at $(n_g, \Phi_{\text{ext}}) \approx (0.9, \Phi_0/2)$, where $K/2\pi \approx 6$ MHz, $\sigma_K/2\pi \approx 0.8$ MHz, and $\sigma_{\omega_0}/2\pi \approx 10$ MHz. In this case the Kerr fluctuations would limit our nonlinear gain to $G_{\text{Kerr}} \lesssim 3$ on average, and that's only if $\sigma_{\omega_0}/\kappa_{\text{tot}} \lesssim 0.05$; this would require increasing the total damping rate to $\kappa_{\text{tot}}/2\pi \approx 200$ MHz, which would in turn lead to significant additional charge noise (see below). However, in the absence of QP the charge sensitivity would improve by about an order of magnitude, due to $|\partial\omega_0/\partial n_g|$ increasing by a factor of 35 and $|K|$ increasing by a factor of 10. Thus, eliminating QP is another straightforward way to significantly improve upon the present device. Given this improvement, it may also be possible to achieve a nonlinear gain of order unity, but only by significantly increasing κ_{tot}.

We conclude by discussing one detrimental consequence of increasing the external damping rate. When the dynamics of the cCPT are derived from first-principles [2], we find that there is a direct coupling between the gate and the field in the input/output transmission line, which takes the form

$$n_g^{\text{in}}(t) = \frac{C_g C_c}{2C_J} \frac{V_{\text{in}}(t)}{e}, \tag{A.22}$$

where we've assumed symmetric junctions and $C_g \ll C_J$. This term can be found in Ref. [2] below Eq. (28) and in Eq. (34), although here we use slightly different notation. Assuming we operate the present device at its optimal point using an input power corresponding to the bifurcation point, and also account for the input power due to vacuum noise in the transmission line (power spectral density of $\hbar\omega/2$) integrated over the cavity bandwidth, the rms amplitude of this gate drive is

$$\sqrt{\left\langle (n_g^{\text{in}})^2 \right\rangle} \approx 3.3 \times 10^{-5}, \tag{A.23}$$

which is much smaller than $\sigma_{n_g} \approx 6 \times 10^{-3}$ and is therefore negligible. However, since $\kappa_{\text{ext}} \propto C_c^2$ and $P_c \propto \kappa_{\text{tot}}^2$, this rms amplitude scales as $\kappa_{\text{tot}}^{3/2}$. Thus, κ_{tot} can only be increased by a factor of about 30 before this effect becomes important. This corresponds to a maximum value of $\kappa_{\text{max}}/2\pi \approx 50$ MHz and $\sqrt{2}$ times more charge noise than the present device.

Appendix B

Parametric Resonance

Section B.1

Theory

Due to its tunability, we can operate the cCPT as a parametric oscillator. In this mode of operation, we drive the flux at $\omega_p = 2(\omega_0 + \Delta)$ for small detuning Δ such that

$$\Phi_{\text{ext}}(t) = \Phi_{\text{ext}} + \delta\Phi\cos(\omega_p t). \tag{B.1}$$

The RWA Hamiltonian in this case takes the form

$$H = \hbar\omega_0 a^\dagger a + \frac{1}{2}\hbar K a^{\dagger 2}a^2 + \frac{\hbar}{4}\frac{\partial\omega_0}{\partial\Phi_{\text{ext}}}\delta\Phi\left(a^2 e^{i\omega_p t} + a^{\dagger 2}e^{-i\omega_p t}\right) \tag{B.2}$$

giving rise to the quantum Langevin equation

$$\dot{a} = \left[-i(\omega_0 + Ka^\dagger a) - \frac{\kappa_{\text{tot}}}{2}\right]a - \frac{i}{2}\frac{\partial\omega_0}{\partial\Phi_{\text{ext}}}\delta\Phi e^{-i\omega_p t}a^\dagger + \sqrt{\kappa_{\text{ext}}}a_{\text{in}}(t) + \sqrt{\kappa_{\text{int}}}b_{\text{in}}(t). \tag{B.3}$$

We now take the expectation value of this equation, assuming no external drives such that $\langle a_{\text{in}}\rangle = \langle b_{\text{in}}\rangle = 0$, and make the ansatz $\langle a(t)\rangle = \alpha e^{-i(\omega_0+\Delta)t}$ such that the above equation simplifies to

$$\left[-i(\Delta - K|\alpha|^2) - \frac{\kappa_{\text{tot}}}{2}\right]\alpha = -\frac{i}{2}\frac{\partial\omega_0}{\partial\Phi_{\text{ext}}}\delta\Phi\alpha^*. \tag{B.4}$$

Multiplying both sides by their complex conjugates, we find

$$\left[(\Delta - Kn)^2 + \frac{\kappa_{\text{tot}}^2}{4} - \epsilon^2\right] n = 0 \tag{B.5}$$

where we've introduced the average intra-cavity photon number $n = |\alpha|^2$ and defined the pump strength

$$\epsilon = \frac{1}{2}\frac{\partial \omega_0}{\partial \Phi_{\text{ext}}}\delta\Phi. \tag{B.6}$$

At this point our analysis basically coincides with that of Ref. [143]. A non-zero cavity response becomes possible above the threshold $\epsilon > \kappa_{\text{tot}}/2$, in which case we can solve for the number of intra-cavity photons

$$n = \frac{1}{K}\left(\Delta \pm \sqrt{\epsilon^2 - \frac{\kappa_{\text{tot}}^2}{4}}\right). \tag{B.7}$$

The region in the ϵ/Δ plane for which $n > 0$ defines the parametric oscillation domain. As with other treatments, we include the pump-induced detuning after the fact. This arises due to the expansion to second order in the pump strength, which oscillates rapidly and averages out to a static shift of the resonant frequency for a given pump strength. The term in the Hamiltonian takes the form

$$H_{\text{pump}}^{(2)} = \frac{\hbar}{2}\frac{\partial^2 \omega_0}{\partial \Phi_{\text{ext}}^2}\delta\Phi^2 \cos^2(\omega_p t) \tag{B.8}$$

which, when averaged over a full period, gives rise to the resonant frequency shift

$$\Delta_{\text{pump}} = \frac{1}{4}\frac{\partial^2 \omega_0}{\partial \Phi_{\text{ext}}^2}\delta\Phi^2 \tag{B.9}$$

that is proportional to both ϵ^2 and K (since the second derivative of ω_0 with respect to the external flux is proportional to K).

Introducing the dimensionless parameter β defined by $\Delta_{\text{pump}} = 2\beta\epsilon^2/\kappa_{\text{tot}}$, the solution for the number of intracavity photons now takes the form

$$n = \frac{1}{K}\left(\Delta - \frac{2\beta}{\kappa_{\text{tot}}}\epsilon^2 \pm \sqrt{\epsilon^2 - \frac{\kappa_{\text{tot}}^2}{4}}\right). \tag{B.10}$$

We can now solve for the edges of the parametric resonance domain by setting $n = 0$

and solving for ϵ, which results in

$$\epsilon_{\pm} = \frac{\kappa_{\text{tot}}}{2\sqrt{2}\beta}\sqrt{1 - 4\beta\frac{\Delta}{\kappa_{\text{tot}}} \pm \sqrt{1 - 4\beta\left(\beta + 2\frac{\Delta}{\kappa_{\text{tot}}}\right)}}. \tag{B.11}$$

This is equivalent to Ref. [86], where the damping rate Γ they use is related to ours by $\Gamma = \kappa_{\text{tot}}/2$.

Section B.2

Kerr-free Stabilization

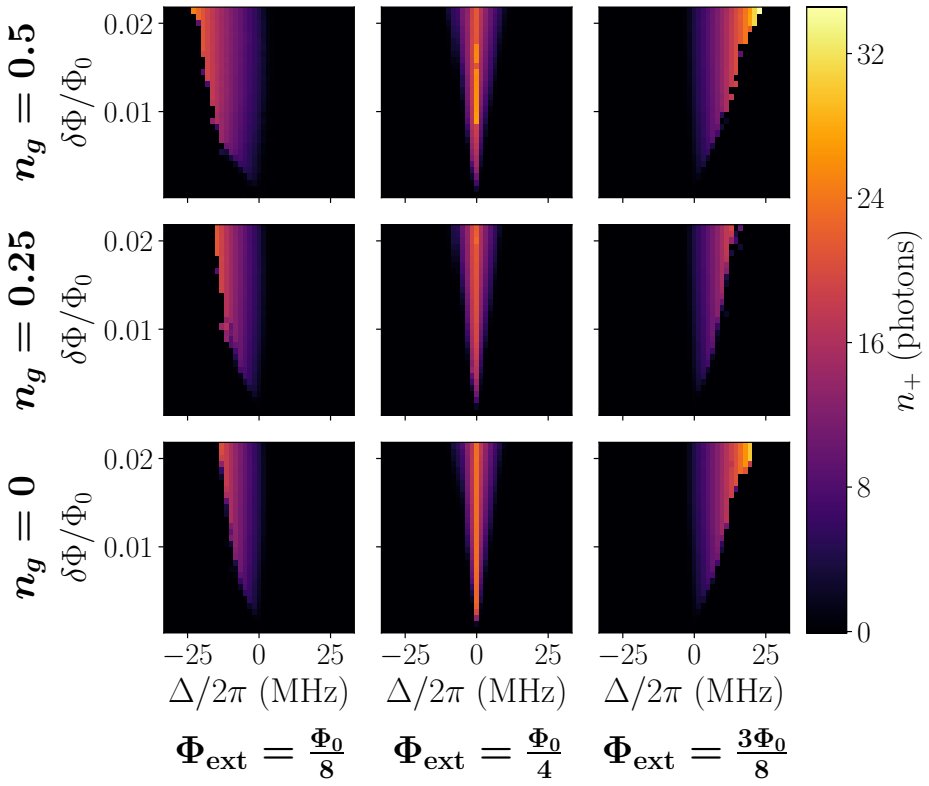

Figure B.1: Parametric resonance region near $\Phi_{\text{ext}} = \Phi_0/4$ where the Kerr nonlinearity becomes negligibly small. n_+ is the number of intra-cavity photons when the detuning is swept forward.

The above analysis indicates that the number of intra-cavity photons is limited by the Kerr nonlinearity. Interestingly, in our case the Kerr nonlinearity vanishes near $(n_g, \Phi_{\text{ext}}) = (0.0, \Phi_0/4)$, at which point $\partial\omega_0/\partial\Phi_{\text{ext}}$ is maximized such that we

can achieve parametric oscillation. When we perform this measurement, however, we do not see as drastic increase in the output power as we might expect (see Figure B.1). We do, however, see other signs of the Kerr nonlinearity becoming negligibly small, such as the parametric resonance region becoming symmetric in Δ (due to negligibly small pump-induced detuning), the parametric response becoming non-hysteretic (see Figure B.2), and the Kerr shift becoming negligibly small (see Figure B.3). This indicates the Kerr nonlinearity is not the bottleneck limiting the number of intracavity photons.

One mechanism that may account for the stabilization of the number of intracavity photons is nonlinear damping, the significance of which has been appreciated in related systems [60, 17] but not in parametric oscillators (to my knowledge). That is, the internal damping rate may be increasing with the number of photons in the cavity (we don't expect the external damping rate to vary appreciably with power) at such a rate as to balance the exponential growth of the cavity field due to the parametric pump. However, we can measure the internal damping rate over a wide range of input powers at the bias point where the Kerr nonlinearity vanishes, and the internal damping rate never gets much larger than its single-photon-level value (see Figure B.4). Thus, we don't believe nonlinear damping can account for the stabilization of the intracavity field at this point. At this point we believe the stabilization is due to fluctuations in the Kerr nonlinearity due to $1/f$ flux noise, but more work needs to be done on the theoretical front here.

It is worth noting that the Kerr nonlinearity has recently been pointed out as a key factor limiting the performance of parametric amplifiers and other pumped processes (see the introduction of [42] for a brief summary and many good references). We expect there's a good tie-in here.

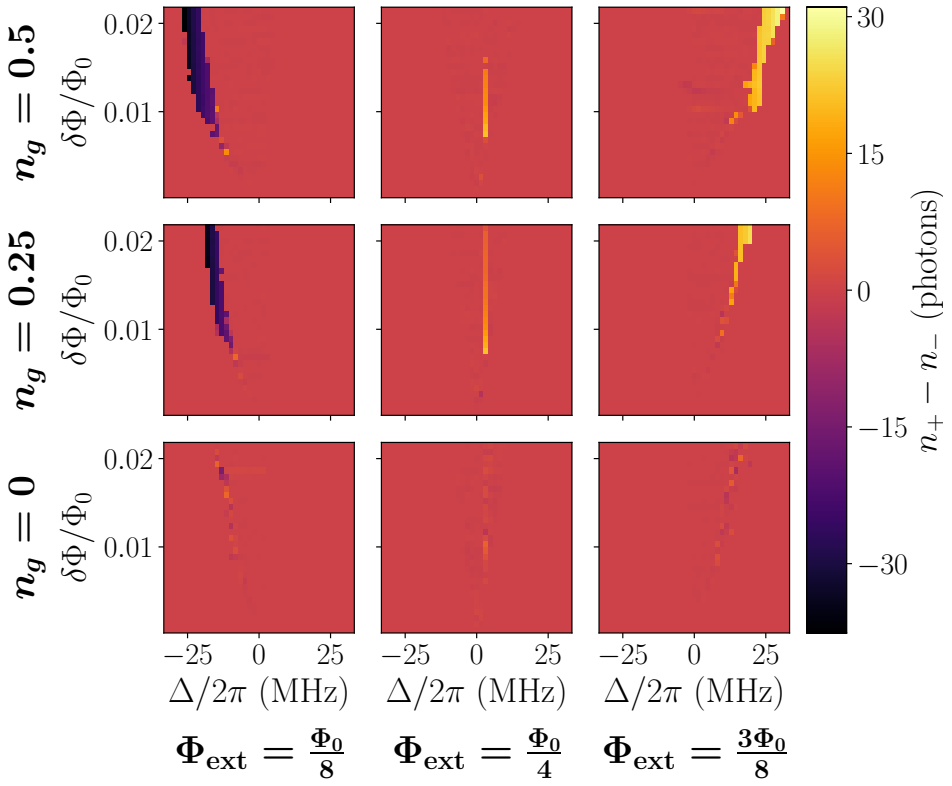

Figure B.2: Hysteresis in the parametric response near $\Phi_{\text{ext}} = \Phi_0/4$ where the Kerr nonlinearity becomes negligibly small. n_+ is the number of photons in the cavity when the detuning is swept forward, n_- is the number of photons when the detuning is swept backwards. The hysteresis disappears when the Kerr nonlinearity vanishes.

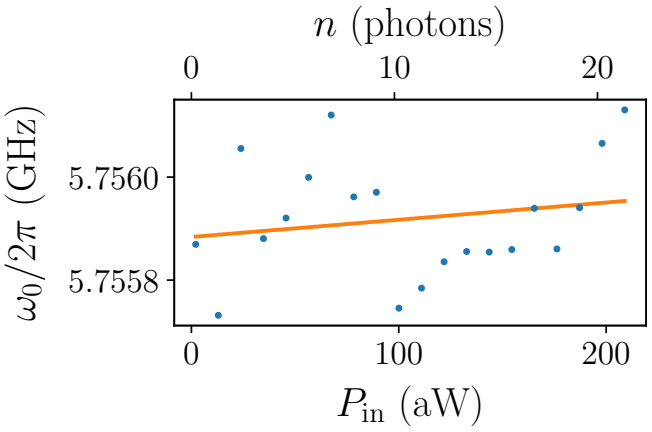

Figure B.3: Kerr shift measurement with negligible Kerr nonlinearity, at $(n_g, \Phi_{\text{ext}}) = (0.0, \Phi_0/4)$. From the best fit slope, we extract a Kerr nonlinearity of $K/2\pi \approx 3$ kHz, but clearly this data is not linear. We attribute the fluctuations in ω_0 to $1/f$ flux noise, which causes small stochastic jumps between consecutive measurements.

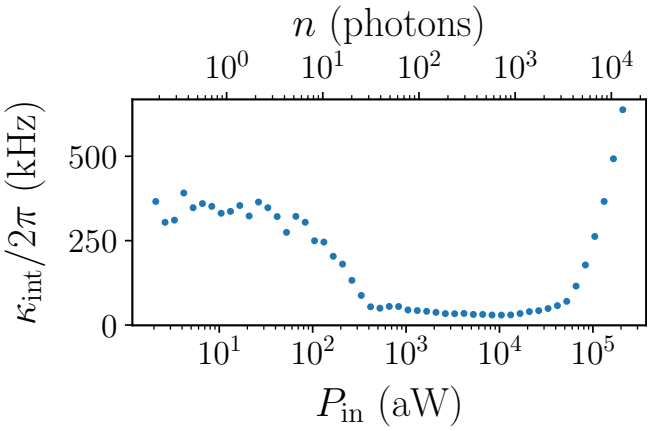

Figure B.4: Internal damping rate κ_{int} as a function of P_{in}, at $(n_g, \Phi_{\text{ext}}) = (0.0, \Phi_0/4)$ where $K \approx 0$. Over a very wide range of input powers, κ_{int} does not get much larger than its single-photon-level value.

Appendix C

Miscellaneous Measurements

When operated at powers even modestly above the single-photon level, the cCPT response becomes nonlinear due to the Kerr nonlinearity K. The number of intracavity photons as a function of detuning must then be found by solving the cubic equation

$$K^2 n^3 - 2\Delta K n^2 + \left[\Delta^2 + \frac{\kappa_{\text{tot}}^2}{4}\right] n - \kappa_{\text{ext}} \frac{P_{\text{in}}}{\hbar\omega_0} = 0 \tag{C.1}$$

to find n as a function of detuning Δ, which then allows us to find the reflection coefficient

$$S_{11} = \frac{\Delta - Kn - i(\kappa_{\text{int}} - \kappa_{\text{ext}})/2}{\Delta - Kn - i(\kappa_{\text{int}} + \kappa_{\text{ext}})/2} \tag{C.2}$$

as shown in Appendix C of the characterization paper.

Section C.1
Deformed Nonlinear Reflection Coefficient

This treatment, however, doesn't account for frequency fluctuations, which give rise to the highly deformed trajectory seen in Figure C.1. As you can see, the reflection coefficient varies rapidly over the very narrow window of the bistability region, which has branches on both sides of the resonance circle. Even though we are well into the bistable regime, the bistability region is smaller than the scale of frequency fluctuations (almost solely due to quantum fluctuations here, since the resonant frequency is not very sensitive to gate or flux at this point). As such, when we measure S_{11} we sample from both branches, which causes a significant contraction of the measured trajectory. The nonlinear rate of traversal of the ideal resonance circle also

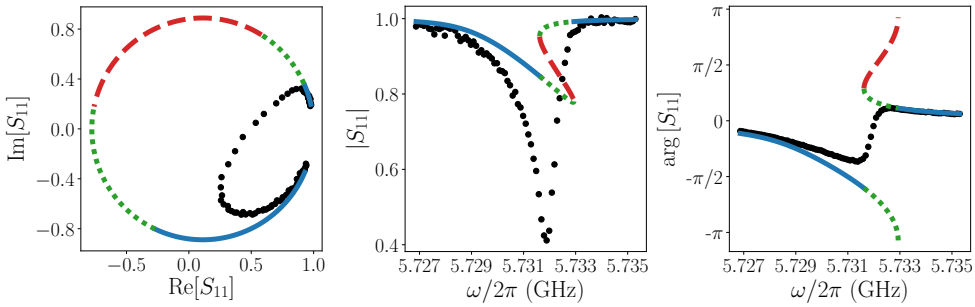

Figure C.1: Nonlinear response of the cCPT. The black circles are measured data and the lines are the theoretical response not taking frequency fluctuations into account. The solid blue line is the unique solution in the monostable regime, the dotted green lines are the two solutions in the bistable regime, and the dashed red line is the unstable solution in the bistable regime. The cCPT was biased to $(n_g, \Phi_{\text{ext}}) = (-0.04, 0.53)$ where $\omega_0/2\pi = 5.730$ GHz, $\kappa_{\text{int}}/2\pi = 0.14$ MHz, $\kappa_{\text{ext}} = 1.10$ MHz, and $K/2\pi = 0.51$ MHz. The input power at the plane of the sample was -132.9 dBm or 51.9 aW, corresponding to about 6.2 intracavity photons at resonance.

leads to significant asymmetry (some asymmetry due to the chi-square distributed fluctuations as well). Furthermore, key signatures of this bistability such as sharp jump phenomena from the lower to the upper branch (or vice versa depending on the direction in which the frequency probe is swept) and hysteresis are washed out.

Section C.2

Hysteresis in the cCPT

However, when we increase the power substantially we can still observe jump phenomena and hysteresis, as can be seen in Figure C.2.

Section C.3

Josephson Parametric Amplification

Due to its strong Kerr nonlinearity, we can operate the cCPT as a Josephson parametric amplifier (JPA). In this mode of operation, the cCPT is driven by a pump tone at the power and frequency (ω_p) corresponding to the bifurcation point (see Appendix C of characterization paper) and a signal tone is put in at a nearby frequency ω_s. As

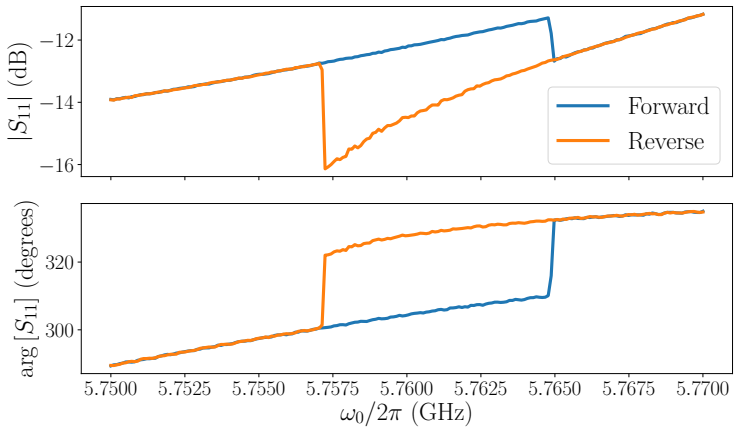

Figure C.2: Hysteresis due to the Kerr nonlinearity. We measured S_{11} by sweeping the drive frequency forward, then in reverse. When the edge of the bistable region is reached we observe sharp jump phenomena. This measurement was done in the small fridge with the SLUG, and we don't have sufficient data to remove the background reflection coefficient or refer powers to the plane of the sample. We also just picked a random point in parameter space. We used −20 dBm at room temperature, which is about equivalent to −30 dBm in the big fridge due to different attenuations, if we are remembering correctly. As an order of magnitude estimate, there are probably hundreds of photons in the cavity here.

a result of the pump and signal tones being mixed by the nonlinearity, the signal is parametrically amplified and an image (or idler) tone is generated at $\omega_i = 2\omega_p - \omega_s$ [60, 17, 145]. We have observed precisely this effect in the cCPT, and have achieved

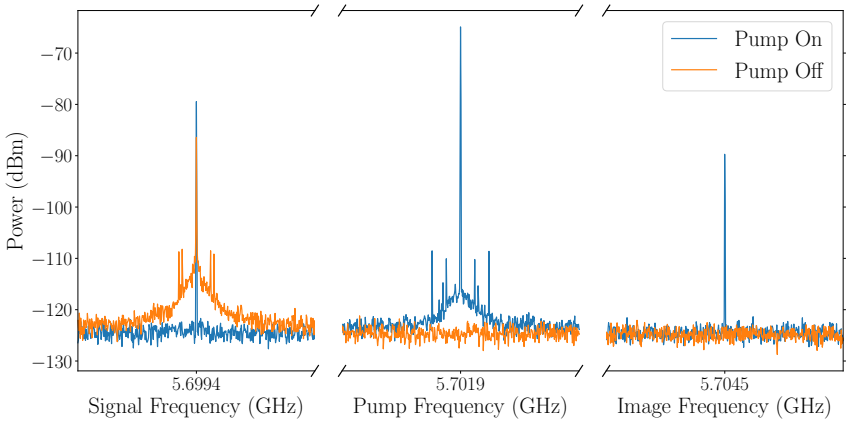

Figure C.3: Operating the cCPT as a JPA. We obtain a signal gain of about 7 dB.

a signal gain of about 7dB. This is merely a proof-of-principle measurement and is nowhere near optimized. Obviously, targeting the bifurcation point precisely requires accurate characterization of the cCPT damping rates and calibration of the input power at the plane of the sample. Note that powers here are not referred to the plane of the sample. The span of each spectrum analyzer segment is 1 kHz and the resolution bandwidth is 1 Hz.

Appendix D

Open cCPT Hamiltonian

In this chapter we present a rigorous derivation of the open system Hamiltonian of our cCPT coupled to a semi-infinite transmission line from first principles. We take a slightly different approach than Ref. [2], which is more detailed than our analysis. For instance, in Ref. [2] the gate voltage is treated as time-dependent from the start, which yields an additional noise term missing from the derivation presented in this chapter. As discussed in Appendix A, this noise term would become significant if we fabricated a sample with a larger coupling capacitance. In the following derivation we generally follow the quantization method described in Ref. [53].

Section D.1

Equations of Motion

To derive the equations of motion governing the dynamics of the cCPT coupled to a semi-infinite transmission line, we use the schematic representation of our system depicted in Fig. D.1. We begin by considering the cavity, for which Kirchhoff's laws yield the telegrapher equations

$$\begin{aligned} \frac{\partial V(x,t)}{\partial x} &= -\mathcal{L}\frac{\partial I(x,t)}{\partial t} \\ \frac{\partial I(x,t)}{\partial x} &= -\mathcal{C}\frac{\partial V(x,t)}{\partial t} \end{aligned} \tag{D.1}$$

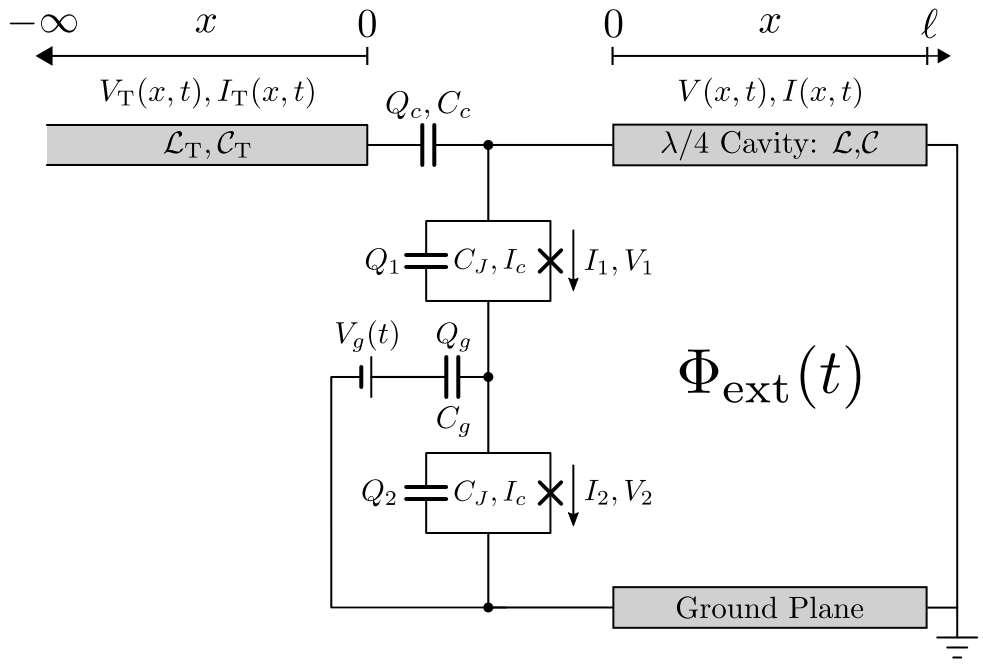

Figure D.1: Schematic of the open-system cCPT, consisting of a Cooper pair transistor connected between the voltage antinode and ground plane of a superconducting $\lambda/4$ cavity. The system is capacitively coupled to a semi-infinite transmission line extending from $-\infty$ to 0 along the x axis. A gate voltage $V_g(t)$ is applied to the island between the JJs via the capacitance C_g. An external flux $\Phi_{\mathrm{ext}}(t)$ is threaded through the superconducting loop formed by the series combination of the cavity and the CPT. The JJs are assumed to be identical, each having capacitance C_J and critical current I_c. The cavity is characterized by its inductance per unit length $\mathcal{L}$, its capacitance per unit length $\mathcal{C}$, and its length ℓ.

in the bulk of the cavity ($0 < x < \ell$). We again introduce a flux variable

$$\phi(x,t) = \int_{-\infty}^{t} V(x,t')dt' \tag{D.2}$$

and, assuming all voltages and currents vanish as $t \to -\infty$, these differential equations can be written concisely as

$$\frac{\partial^2\phi(x,t)}{\partial t^2} = v^2\frac{\partial^2\phi(x,t)}{\partial x^2} \quad ; \quad 0 < x < \ell \tag{D.3}$$

which is a wave equation for $\phi(x,t)$ with phase velocity $v = 1/\sqrt{\mathcal{LC}}$. The cavity is shorted at $x = \ell$ so we can impose the boundary condition $V(\ell,t) = 0$ (or equivalently $\phi(\ell,t) = 0$), but the boundary condition at $x = 0$ dictates the coupling to the CPT and cannot be strictly imposed, as we will see. Similarly, Kirchhoff's laws in the semi-infinite transmission line yield the telegrapher equations

$$\begin{aligned} \frac{\partial V_{\mathrm{T}}(x,t)}{\partial x} &= -\mathcal{L}_{\mathrm{T}} \frac{\partial I_{\mathrm{T}}(x,t)}{\partial t} \\ \frac{\partial I_{\mathrm{T}}(x,t)}{\partial x} &= -\mathcal{C}_{\mathrm{ext}} \frac{\partial V_{\mathrm{T}}(x,t)}{\partial t} \end{aligned} \tag{D.4}$$

in the bulk of the line ($x < 0$). Defining an analogous flux variable $\phi_{\mathrm{T}}(x,t)$ in this transmission line, these equations can be written concisely as

$$\frac{\partial^2 \phi_{\mathrm{T}}(x,t)}{\partial t^2} = v_{\mathrm{T}}^2 \frac{\partial^2 \phi_{\mathrm{T}}(x,t)}{\partial x^2} \quad ; \quad x < 0 \tag{D.5}$$

where $v_{\mathrm{T}} = 1/\sqrt{\mathcal{L}_{\mathrm{T}}\mathcal{C}_{\mathrm{T}}}$.

As for the rest of the circuit, Kirchhoff's voltage law yields the equations

$$V_1 - \frac{Q_1}{C_J} = 0 \tag{D.6}$$

$$V_2 - \frac{Q_2}{C_J} = 0 \tag{D.7}$$

$$V_g(t) - \frac{Q_g}{C_g} - \frac{Q_2}{C_J} = 0 \tag{D.8}$$

$$\frac{Q_1}{C_J} + \frac{Q_2}{C_J} + \int_0^{\ell} \frac{\partial V(x,t)}{\partial x} dx - \dot{\Phi}_{\mathrm{ext}}(t) = 0 \tag{D.9}$$

$$V_{\mathrm{T}}(0,t) - \frac{Q_c}{C_c} - \frac{Q_1}{C_J} - \frac{Q_2}{C_J} = 0 \tag{D.10}$$

and Kirchhoff's current law yields the equations

$$\dot{Q}_1 + I_1 + \dot{Q}_g - \dot{Q}_2 - I_2 = 0 \tag{D.11}$$

$$\dot{Q}_c - I(0,t) - \dot{Q}_1 - I_1 = 0 \tag{D.12}$$

$$I_{\mathrm{T}}(0,t) - \dot{Q}_c = 0 \tag{D.13}$$

from which we see that the boundary conditions of both the cavity and transmission line at $x = 0$ couple into the dynamics of the JJs. It is convenient at this point to

express the voltages and currents at the boundary $x = 0$ of the cavity in terms of the flux field. The voltages at the boundary take the form

$$\int_0^\ell \frac{\partial V(x,t)}{\partial x} dx = -V(0,t) = -\dot{\phi}(0,t) \tag{D.14}$$

$$V_{\mathrm{T}}(0,t) = \dot{\phi}(0,t) \tag{D.15}$$

where we've used the boundary condition $V(\ell, t) = 0$, and the currents at the boundary can be written

$$I(0,t) = -\frac{1}{\mathcal{L}}\phi'(0,t) \tag{D.16}$$

$$I_{\mathrm{T}}(0,t) = -\frac{1}{\mathcal{L}_{\mathrm{T}}}\phi'_{\mathrm{T}}(0,t) \tag{D.17}$$

using the telegrapher equations.

We now impose the Josephson relations on the currents through and voltages across each JJ

$$\begin{aligned} I_i &= I_c \sin(\varphi_i) \\ V_i &= \frac{\Phi_0}{2\pi}\frac{\partial \varphi_i}{\partial t} \end{aligned} \tag{D.18}$$

where φ_i is the gauge invariant phase across the i'th JJ and $\Phi_0 = h/2e$ is the magnetic flux quantum. Plugging back in to Eqs. (D.6)-(D.8), we can express the charge variables in terms of the phases across the JJs according to

$$Q_1 = C_J \frac{\Phi_0}{2\pi}\dot{\varphi}_1 \tag{D.19}$$

$$Q_2 = C_J \frac{\Phi_0}{2\pi}\dot{\varphi}_2 \tag{D.20}$$

$$Q_g = C_g V_g(t) - C_g \frac{\Phi_0}{2\pi}\dot{\varphi}_2. \tag{D.21}$$

Plugging these expressions into Eq. (D.9), we find

$$\frac{\partial}{\partial t}\left[\frac{\Phi_0}{2\pi}(\varphi_1 + \varphi_2) - \phi(0,t) - \Phi_{\mathrm{ext}}(t)\right] = 0 \tag{D.22}$$

which we recognize as the condition that the flux around a closed superconducting loop is constant. Integrating this equation, and absorbing the constant of integration

(an integer multiple of Φ_0) into Φ_{ext} as a DC offset, we find

$$\frac{\Phi_0}{2\pi}\left(\varphi_1+\varphi_2\right)=\phi(0,t)+\Phi_{\text{ext}}(t). \tag{D.23}$$

Plugging this result into Eq. (D.10), we can solve for the charge on the coupling capacitor

$$Q_c=C_c\left(\dot{\phi}_{\text{T}}(0,t)-\dot{\phi}(0,t)-\dot{\Phi}_{\text{ext}}(t)\right) \tag{D.24}$$

in terms of which Eq. (D.13) takes the form

$$C_c\left(\ddot{\phi}_{\text{T}}(0,t)-\ddot{\phi}(0,t)-\ddot{\Phi}_{\text{ext}}(t)\right)+\frac{1}{\mathcal{L}_{\text{T}}}\phi'_{\text{T}}(0,t)=0. \tag{D.25}$$

We now plug all these results into Eqs. (D.11) and (D.12), and add the latter to the former, to find

$$(C_J+C_g)\frac{\Phi_0}{2\pi}\ddot{\varphi}_2+I_c\sin(\varphi_2)-C_g\dot{V}_g-C_c\left(\ddot{\phi}_{\text{T}}(0,t)-\ddot{\phi}(0,t)-\ddot{\Phi}_{\text{ext}}\right)-\frac{1}{\mathcal{L}}\phi'(0,t)=0 \tag{D.26}$$

$$C_J\frac{\Phi_0}{2\pi}\ddot{\varphi}_1+I_c\sin(\varphi_1)-C_c\left(\ddot{\phi}_{\text{T}}(0,t)-\ddot{\phi}(0,t)-\ddot{\Phi}_{\text{ext}}\right)-\frac{1}{\mathcal{L}}\phi'(0,t)=0. \tag{D.27}$$

Introducing the average and relative phase coordinates

$$\begin{aligned}\bar{\varphi}&=\frac{\varphi_1+\varphi_2}{2}\\ \delta\varphi&=\frac{\varphi_1-\varphi_2}{2}\end{aligned} \tag{D.28}$$

we can express Eqs. (D.26) and (D.27) as

$$-C_J\frac{\Phi_0}{2\pi}\ddot{\delta\varphi}+I_c\sin(\bar{\varphi}-\delta\varphi)-C_c\left(\ddot{\phi}_{\text{T}}(0,t)-\ddot{\phi}(0,t)-\ddot{\Phi}_{\text{ext}}\right)-\frac{1}{\mathcal{L}}\phi'(0,t)-C_g\dot{V}_g=0 \tag{D.29}$$

$$C_J\frac{\Phi_0}{2\pi}\ddot{\delta\varphi}+I_c\sin(\bar{\varphi}+\delta\varphi)-C_c\left(\ddot{\phi}_{\text{T}}(0,t)-\ddot{\phi}(0,t)-\ddot{\Phi}_{\text{ext}}\right)-\frac{1}{\mathcal{L}}\phi'(0,t)=0 \tag{D.30}$$

where we've used the relationship

$$\bar{\varphi}=\frac{\pi}{\Phi_0}\left[\phi(0,t)+\Phi_{\text{ext}}(t)\right] \tag{D.31}$$

from Eq. (D.23) and the fact that $C_g \ll C_J \ll C_c$ to drop sub-leading-order terms. Taking the sum of and difference between Eqs. (D.26) and (D.27), and dividing both by 2, we find

$$I_c \sin(\bar{\varphi})\cos(\delta\varphi) - C_c\left(\ddot{\phi}_{\mathrm{T}}(0,t) - \ddot{\phi}(0,t) - \ddot{\Phi}_{\mathrm{ext}}\right) - \frac{1}{\mathcal{L}}\phi'(0,t) - \frac{1}{2}C_g\dot{V}_g = 0 \quad \text{(D.32)}$$

$$C_J\frac{\Phi_0}{2\pi}\ddot{\delta\varphi} + I_c\cos(\bar{\varphi})\sin(\delta\varphi) + \frac{1}{2}C_g\dot{V}_g = 0 \quad \text{(D.33)}$$

which are our final expressions for these equations. To summarize, the equations of motion governing the dynamics of the open-system cCPT are Eqs. (D.3), (D.5), (D.25), (D.32), and (D.33). To be clear, $\bar{\varphi}$ is not an independent variable; it is a function of the cavity flux coordinate at $x = 0$, as given by Eq. (D.31).

Section D.2

Lagrangian

These equations of motion can be derived from the Lagrangian density

$$\begin{aligned}\mathscr{L} = &\left(\Theta(x) + \Theta(\ell - x) - 1\right)\left[\frac{\mathcal{C}}{2}\dot{\phi}(x,t)^2 - \frac{1}{2\mathcal{L}}\phi'(x,t)^2\right] \\ &+ \left(1 - \Theta(x)\right)\left[\frac{\mathcal{C}_{\mathrm{T}}}{2}\dot{\phi}_{\mathrm{T}}(x,t)^2 - \frac{1}{2\mathcal{L}_{\mathrm{T}}}\phi'_{\mathrm{T}}(x,t)^2\right] \\ &+ \delta(x)\Bigg[C_J\left(\frac{\Phi_0}{2\pi}\right)^2\dot{\delta\varphi}^2 + \frac{\Phi_0}{2\pi}C_gV_g\dot{\delta\varphi} + \frac{C_c}{2}\left(\dot{\Phi}_{\mathrm{ext}} + \dot{\phi}(x,t) - \dot{\phi}_{\mathrm{T}}(x,t)\right)^2 \\ &\qquad - \frac{C_gV_g}{2}\dot{\phi}(x,t) + 2E_J\cos\left(\frac{\pi}{\Phi_0}\phi(x,t) + \frac{\pi}{\Phi_0}\Phi_{\mathrm{ext}}\right)\cos(\delta\varphi)\Bigg]\end{aligned} \quad \text{(D.34)}$$

where $\Theta(x)$ is the Heaviside step function. Next we will integrate this density to find the full Lagrangian and perform a Legendre transformation to arrive at the Hamiltonion of our system, but first it is useful to express the cavity and transmission line fields in terms of their normal mode coordinates.

Cavity Modes. The general solution of the cavity flux field $\phi(x,t)$, given the boundary condition $\phi(\ell,t)=0$, can be written

$$\phi(x,t)=\sum_{n=1}^{\infty}\left[\Phi_n^+(t)\cos\left(k_n^+x\right)+\Phi_n^-(t)\sin\left(k_n^-x\right)\right] \tag{D.35}$$

where

$$\begin{aligned} k_n^+ &= \frac{(2n-1)\pi}{2\ell} \\ k_n^- &= \frac{n\pi}{\ell} \\ n &= 1,2,3,... \end{aligned} \tag{D.36}$$

and the pluses/minuses indicate even/odd solutions. As we can see from Eq. (D.34), however, only the even modes will couple into the dynamics of the CPT. Furthermore, as we will later show when we consider the open system dynamics, these are also the only modes that will couple into the external transmission line, so these odd modes cannot be driven. Thus, we make an approximate normal mode expansion

$$\phi(x,t)\approx\sum_{n=1}^{\infty}\Phi_n(t)\cos(k_nx) \tag{D.37}$$

in terms of the even modes alone, where

$$k_n=\frac{(2n-1)\pi}{2\ell}\quad;\quad n=1,2,3,... \tag{D.38}$$

which is the normal mode expansion for the bare $\lambda/4$ cavity. Note that if we don't make this approximation here, then when we integrate over the Lagrangian density we will obtain cross terms between the modes since the sines and cosines above are not orthogonal.

Using these mode coordinates, the term in the Lagrangian associated with the

bare cavity can be expressed

$$\begin{aligned} L_{\text{Cavity}} &= \int_{-\infty}^{\infty} dx\, (\Theta(x) + \Theta(\ell - x) - 1) \left[\frac{\mathcal{C}}{2} \dot{\phi}(x,t)^2 - \frac{1}{2\mathcal{L}} \phi'(x,t)^2 \right] \\ &= \int_{0}^{\ell} dx \sum_{n,m=1}^{\infty} \left[\frac{\mathcal{C}}{2} \dot{\Phi}_n \dot{\Phi}_m \cos(k_n x) \cos(k_m x) - \frac{k_n k_m}{2\mathcal{L}} \Phi_n \Phi_m \sin(k_n x) \sin(k_m x) \right] \\ &= \sum_{n=1}^{\infty} \left[\frac{\mathcal{C}\ell}{4} \dot{\Phi}_n^2 - \frac{k_n^2 \ell}{4\mathcal{L}} \Phi_n^2 \right] \end{aligned} \tag{D.39}$$

where we've used the fact that

$$\int_0^{\ell} \cos(k_n x) \cos(k_m x) dx = \int_0^{\ell} \sin(k_n x) \sin(k_m x) dx = \frac{\ell}{2} \delta_{nm}. \tag{D.40}$$

Finally, we introduce the effective inductances and capacitances

$$L_n = \frac{2\mathcal{L}}{k_n^2 \ell} = \frac{8\ell\mathcal{L}}{\pi^2 (2n-1)^2} \tag{D.41}$$

$$C_n = \frac{\ell \mathcal{C}}{2} \tag{D.42}$$

in terms of which the cavity Lagrangian can be expressed

$$L_{\text{Cavity}} = \sum_{n=1}^{\infty} \left(\frac{C_n}{2} \dot{\Phi}_n^2 - \frac{1}{2L_n} \Phi_n^2 \right). \tag{D.43}$$

Transmission Line Modes. As was the case for the cavity, only those modes in the transmission line that have flux antinodes at $x = 0$ will couple into our system. Thus, our general solution for the field in the transmission line can be approximated as

$$\phi_{\text{T}}(x,t) \approx \int_0^{\infty} d\omega \cos\left(\frac{\omega x}{v_{\text{T}}} \right) \Phi_{\text{T}}(\omega, t) \tag{D.44}$$

which is the continuous version of the mode decomposition used for the cavity. Note that the mode coordinates $\Phi_{\text{T}}(\omega, t)$ have units of flux per unit bandwidth. Using these mode coordinates, the term in the Lagrangian corresponding to the bare transmission

line can be expressed

$$\begin{aligned} L_{\text{Bath}} &= \int_{-\infty}^{\infty} dx\,(1-\Theta(x))\left[\frac{\mathcal{C}_{\text{T}}}{2}\dot{\phi}_{\text{T}}(x,t)^2 - \frac{1}{2\mathcal{L}_{\text{T}}}\phi'_{\text{T}}(x,t)^2\right] \\ &= \int_{-\infty}^{0} dx \int_{0}^{\infty} d\omega \int_{0}^{\infty} d\omega' \left[\frac{\mathcal{C}_{\text{T}}}{2}\dot{\Phi}_{\text{T}}(\omega)\dot{\Phi}_{\text{T}}(\omega')\cos\left(\frac{\omega x}{v_{\text{T}}}\right)\cos\left(\frac{\omega' x}{v_{\text{T}}}\right)\right. \\ &\qquad\qquad \left. - \frac{\omega\omega'}{2\mathcal{L}_{\text{T}}v_{\text{T}}^2}\Phi_{\text{T}}(\omega)\Phi_{\text{T}}(\omega')\sin\left(\frac{\omega x}{v_{\text{T}}}\right)\sin\left(\frac{\omega' x}{v_{\text{T}}}\right)\right] \\ &= \int_{0}^{\infty} d\omega \left(\frac{\pi\mathcal{C}_{\text{T}}v_{\text{T}}}{4}\dot{\Phi}_{\text{T}}(\omega)^2 - \frac{\pi\omega^2}{4\mathcal{L}_{\text{T}}v_{\text{T}}}\Phi_{\text{T}}(\omega)^2\right) \end{aligned} \tag{D.45}$$

where we've used the fact that

$$\int_{-\infty}^{0}\cos\left(\frac{\omega x}{v_{\text{T}}}\right)\cos\left(\frac{\omega' x}{v_{\text{T}}}\right)dx = \int_{-\infty}^{0}\sin\left(\frac{\omega x}{v_{\text{T}}}\right)\sin\left(\frac{\omega' x}{v_{\text{T}}}\right)dx = \frac{\pi v_{\text{T}}}{2}\delta(\omega'-\omega). \tag{D.46}$$

This term in the Lagrangian can be expressed more simply as

$$L_{\text{Bath}} = \frac{\pi}{4\mathcal{Z}_{\text{T}}}\int_{0}^{\infty} d\omega \left(\dot{\Phi}_{\text{T}}(\omega)^2 - \omega^2\Phi_{\text{T}}(\omega)^2\right) \tag{D.47}$$

where we've introduced the characteristic impedance $\mathcal{Z}_{\text{T}} = \sqrt{\mathcal{L}_{\text{T}}/\mathcal{C}_{\text{T}}}$ of the transmission line.

Lagrangian. Using these solutions we can now integrate the Lagrangian density over all space to find the total Lagrangian of our system

$$\begin{aligned}
L =& \int_{-\infty}^{\infty} \mathscr{L} dx \\
=& \sum_{n=1}^{\infty} \left(\frac{C_n}{2} \dot{\Phi}_n^2 - \frac{1}{2L_n} \Phi_n^2 \right) + \frac{\pi}{4\mathcal{Z}_\mathrm{T}} \int_0^{\infty} d\omega \left(\dot{\Phi}_\mathrm{T}(\omega)^2 - \omega^2 \Phi_\mathrm{T}(\omega)^2 \right) \\
&+ \frac{C_c}{2} \left(\dot{\Phi}_\mathrm{ext} + \sum_{n=1}^{\infty} \dot{\Phi}_n - \int_0^{\infty} d\omega \dot{\Phi}_\mathrm{T}(\omega) \right)^2 - \frac{C_g V_g}{2} \sum_{n=1}^{\infty} \dot{\Phi}_n \\
&+ C_J \left(\frac{\Phi_0}{2\pi} \right)^2 \dot{\delta\varphi}^2 + \frac{\Phi_0}{2\pi} C_g V_g \dot{\delta\varphi} + 2E_J \cos\left(\frac{\pi}{\Phi_0} \sum_{n=1}^{\infty} \Phi_n + \frac{\pi}{\Phi_0} \Phi_\mathrm{ext} \right) \cos(\delta\varphi).
\end{aligned} \tag{D.48}$$

This can be written in a somewhat more useful form as

$$\begin{aligned}
L =& \sum_{n=1}^{\infty} \left(\frac{C_n}{2} \dot{\Phi}_n^2 - \frac{1}{2L_n} \Phi_n^2 \right) + \frac{\pi}{4\mathcal{Z}_\mathrm{T}} \int_0^{\infty} d\omega \left(\dot{\Phi}_\mathrm{T}(\omega)^2 - \omega^2 \Phi_\mathrm{T}(\omega)^2 \right) \\
&+ \frac{C_c}{2} \sum_{n,m=1}^{\infty} \dot{\Phi}_n \dot{\Phi}_m + \frac{C_c}{2} \int_0^{\infty} d\omega \int_0^{\infty} d\omega' \dot{\Phi}_\mathrm{T}(\omega) \dot{\Phi}_\mathrm{T}(\omega') \\
&+ \left(C_c \dot{\Phi}_\mathrm{ext} - \frac{C_g V_g}{2} \right) \sum_{n=1}^{\infty} \dot{\Phi}_n - C_c \dot{\Phi}_\mathrm{ext} \int_0^{\infty} d\omega \dot{\Phi}_\mathrm{T}(\omega) - C_c \int_0^{\infty} d\omega \dot{\Phi}_\mathrm{T}(\omega) \sum_{n=1}^{\infty} \dot{\Phi}_n \\
&+ C_J \left(\frac{\Phi_0}{2\pi} \right)^2 \dot{\delta\varphi}^2 + \frac{\Phi_0}{2\pi} C_g V_g \dot{\delta\varphi} + 2E_J \cos\left(\frac{\pi}{\Phi_0} \sum_{n=1}^{\infty} \Phi_n + \frac{\pi}{\Phi_0} \Phi_\mathrm{ext} \right) \cos(\delta\varphi).
\end{aligned} \tag{D.49}$$

where we've expanded the coupling term involving the transmission line modes and dropped an overall constant term. We now note that if we were to transform into a frame rotating at the resonant frequency of any mode of the cavity, then the term $\dot{\Phi}_n \dot{\Phi}_m$ would be highly off-resonant whenever $n \neq m$, and would therefore be dropped when we apply the rotating wave approximation. The terms that would be stationary in the rotating frame are those with $n = m$, in which case they would renormalize the effective cavity capacitance from $C_n/2$ to $C_n/2 + C_J/4$. However, we know that $C_J \ll C_n$ so this renormalization is negligible and we drop these terms as well.

Furthermore, so long as we are not driving the gate $V_g(t)$ or external flux $\Phi_{\text{ext}}(t)$ near the resonant frequency of the mode of interest (the fundamental mode in our case), then the terms linear in $\dot{\Phi}_n$ will be off-resonant in the RWA and they can be absorbed into the quadratic terms by completing the square. A similar line of reasoning applies to the extra terms involving the modes in the transmission line, where we are generally only interested in frequencies in a narrow range around the mode of interest. In light of this, our Lagrangian takes the form

$$\begin{aligned} L = &\sum_{n=1}^{\infty}\left(\frac{C_n}{2}\dot{\Phi}_n^2 - \frac{1}{2L_n}\Phi_n^2\right) + \frac{\pi}{4\mathcal{Z}_{\text{T}}}\int_0^{\infty} d\omega\left(\dot{\Phi}_{\text{T}}(\omega)^2 - \omega^2\Phi_{\text{T}}(\omega)^2\right) \\ &+ C_J\left(\frac{\Phi_0}{2\pi}\right)^2\dot{\delta\varphi}^2 + \frac{\Phi_0}{2\pi}C_g V_g\dot{\delta\varphi} + 2E_J\cos\left(\frac{\pi}{\Phi_0}\sum_{n=1}^{\infty}\Phi_n + \frac{\pi}{\Phi_0}\Phi_{\text{ext}}\right)\cos(\delta\varphi) \\ &- C_c\int_0^{\infty} d\omega\dot{\Phi}_{\text{T}}(\omega)\sum_{n=1}^{\infty}\dot{\Phi}_n. \end{aligned} \tag{D.50}$$

Note that if we don't get rid of these cross terms here, then we get conjugate momenta that depend on one another in a recursive way that can be expanded in orders of C_J/C_n. This yields a perturbative coupling between all modes, that only disappears within the RWA to lowest order in the expansion. It may eventually become necessary to include these terms perturbatively, but it's unlikely since $C_J/C_n \sim 10^{-3}$.

Section D.3

Hamiltonian

We now find the Hamiltonian by determining the canonical momenta and performing a Legendre transformation. For the cavity mode Φ_n the conjugate momentum is the charge coordinate

$$Q_n = \frac{\partial L}{\partial\dot{\Phi}_n} = C_n\dot{\Phi}_n - C_c\int_0^{\infty} d\omega\dot{\Phi}_{\text{T}}(\omega) \tag{D.51}$$

for the transmission line mode $\Phi_{\mathrm{T}}(\omega)$ the conjugate momentum is the charge coordinate

$$Q_{\mathrm{T}}(\omega) = \frac{\partial L}{\partial \dot{\Phi}_{\mathrm{T}}(\omega)} = \frac{\pi}{2\mathcal{Z}_{\mathrm{T}}}\dot{\Phi}_{\mathrm{T}}(\omega) - C_c \sum_{n=1}^{\infty} \dot{\Phi}_n \tag{D.52}$$

and for the phase difference $\delta\varphi$ between the JJs the conjugate momentum is

$$p_{\delta\varphi} = \frac{\partial L}{\partial \dot{\delta\varphi}} = 2C_J \left(\frac{\Phi_0}{2\pi}\right)^2 \dot{\delta\varphi} + \frac{\Phi_0}{2\pi} C_g V_g. \tag{D.53}$$

As we might have expected the cavity and transmission line momenta couple to one another, leading to recursive solutions for $\dot{\Phi}_n$ and $\dot{\Phi}_{\mathrm{T}}(\omega)$ in terms of the Q_n's and $Q_{\mathrm{T}}(\omega)$'s. We truncate these relationships to leading order in the coupling strength, yielding the solutions

$$\dot{\Phi}_n = \frac{Q_n}{C_n} + \frac{2\mathcal{Z}_{\mathrm{T}}}{\pi}\frac{C_c}{C_n}\int_0^{\infty} Q_{\mathrm{T}}(\omega)d\omega + \mathcal{O}\left(C_c^2\right) \tag{D.54}$$

$$\dot{\Phi}_{\mathrm{T}}(\omega) = \frac{2\mathcal{Z}_{\mathrm{T}}}{\pi} Q_{\mathrm{T}}(\omega) + \frac{2\mathcal{Z}_{\mathrm{T}}}{\pi}\frac{C_c}{C_n}\sum_{n=1}^{\infty} Q_n + \mathcal{O}\left(C_c^2\right). \tag{D.55}$$

Performing the Legendre transformation, we find the Hamiltonian to be

$$\begin{aligned}
H =&\dot{\delta\varphi}\frac{\partial L}{\partial \dot{\delta\varphi}} + \sum_{n=1}^{\infty}\dot{\Phi}_n\frac{\partial L}{\partial \dot{\Phi}_n} + \int_0^{\infty}\dot{\Phi}_{\mathrm{T}}(\omega)\frac{\partial L}{\partial \dot{\Phi}_{\mathrm{T}}(\omega)}d\omega - L \\
=&\sum_{n=1}^{\infty}\left(\frac{C_n}{2}\dot{\Phi}_n^2 + \frac{1}{2L_n}\Phi_n^2\right) + \frac{\pi}{4\mathcal{Z}_{\mathrm{T}}}\int_0^{\infty}d\omega\left(\dot{\Phi}_{\mathrm{T}}(\omega)^2 + \omega^2\Phi_{\mathrm{T}}(\omega)^2\right) \\
&+ \frac{1}{4C_J}\left(\frac{2\pi}{\Phi_0}p_{\delta\varphi} - C_gV_g\right)^2 - 2E_J\cos\left(\frac{\pi}{\Phi_0}\sum_{n=1}^{\infty}\Phi_n + \frac{\pi}{\Phi_0}\Phi_{\mathrm{ext}}\right)\cos(\delta\varphi) \\
&- C_c\int_0^{\infty}d\omega\dot{\Phi}_{\mathrm{T}}(\omega)\sum_{n=1}^{\infty}\dot{\Phi}_n \qquad \text{(D.56)} \\
=&\sum_{n=1}^{\infty}\left(\frac{1}{2C_n}Q_n^2 + \frac{1}{2L_n}\Phi_n^2\right) + \frac{1}{2}\int_0^{\infty}d\omega\left(\frac{2\mathcal{Z}_{\mathrm{T}}}{\pi}Q_{\mathrm{T}}(\omega)^2 + \omega^2\frac{\pi}{2\mathcal{Z}_{\mathrm{T}}}\Phi_{\mathrm{T}}(\omega)^2\right) \\
&+ \frac{1}{4C_J}\left(\frac{2\pi}{\Phi_0}p_{\delta\varphi} - C_gV_g\right)^2 - 2E_J\cos\left(\frac{\pi}{\Phi_0}\sum_{n=1}^{\infty}\Phi_n + \frac{\pi}{\Phi_0}\Phi_{\mathrm{ext}}\right)\cos(\delta\varphi) \\
&+ \frac{2\mathcal{Z}_{\mathrm{T}}}{\pi}\sum_{n=1}^{\infty}\frac{C_c}{C_n}\int_0^{\infty}d\omega Q_{\mathrm{T}}(\omega)\sum_{n=1}^{\infty}Q_n.
\end{aligned}$$

to lowest order in the coupling strength. We note that the conjugate momenta obey the canonical commutation relations

$$[\Phi_n, Q_m] = i\hbar\delta_{nm} \qquad \text{(D.57)}$$

$$[\Phi_{\mathrm{T}}(\omega), Q_{\mathrm{T}}(\omega')] = i\hbar\delta(\omega - \omega') \qquad \text{(D.58)}$$

$$[\delta\varphi, p_{\delta\varphi}] = i\hbar. \qquad \text{(D.59)}$$

For convenience, we split the Hamiltonian into four parts

$$H = H_{\text{Cavity}} + H_{\text{Bath}} + H_{\text{CPT}} + H_{\text{Int}} \tag{D.60}$$

$$H_{\text{Cavity}} = \sum_{n=1}^{\infty} \left(\frac{1}{2C_n} Q_n^2 + \frac{1}{2L_n} \Phi_n^2 \right) \tag{D.61}$$

$$H_{\text{Bath}} = \frac{1}{2} \int_0^{\infty} d\omega \left(\frac{2\mathcal{Z}_{\text{T}}}{\pi} Q_{\text{T}}(\omega)^2 + \omega^2 \frac{\pi}{2\mathcal{Z}_{\text{T}}} \Phi_{\text{T}}(\omega)^2 \right) \tag{D.62}$$

$$H_{\text{CPT}} = \frac{1}{4C_J} \left(\frac{2\pi}{\Phi_0} p_{\delta\varphi} - C_g V_g \right)^2 - 2E_J \cos\left(\frac{\pi}{\Phi_0} \sum_{n=1}^{\infty} \Phi_n + \frac{\pi}{\Phi_0} \Phi_{\text{ext}} \right) \cos(\delta\varphi) \tag{D.63}$$

$$H_{\text{Int}} = \frac{2\mathcal{Z}_{\text{T}}}{\pi} \frac{C_c}{C_n} \int_0^{\infty} d\omega Q_{\text{T}}(\omega) \sum_{n=1}^{\infty} Q_n \tag{D.64}$$

and consider each separately.

CPT Hamiltonian. Using techniques of Chapter 3, the CPT Hamiltonian can be expressed

$$H_{CPT} = 4E_C \sum_{N\in\mathbb{Z}} \left(N - \frac{n_g}{2} \right)^2 |N\rangle\langle N| - E_J \cos\left(\bar{\phi}/2\right) \sum_{N\in\mathbb{Z}} \Big(|N+1\rangle\langle N| + |N\rangle\langle N+1| \Big) \tag{D.65}$$

where we've reintroduced the total phase coordinate

$$\bar{\phi} = \frac{2\pi}{\Phi_0} \left[\sum_{n=1}^{\infty} \Phi_n + \Phi_{\text{ext}}(t) \right] \tag{D.66}$$

for notational convenience.

Bath and Interaction Hamiltonians. We now want to express the bath and interaction Hamiltonians in terms of creation and annihilation operators. To this end, we define

$$b(\omega) = \frac{1}{\sqrt{2\hbar}} \left(\sqrt{\frac{\pi\omega}{2\mathcal{Z}_{\text{T}}}} \Phi_{\text{T}}(\omega) + i \sqrt{\frac{2\mathcal{Z}_{\text{T}}}{\pi\omega}} Q_{\text{T}}(\omega) \right) \tag{D.67}$$

$$b^{\dagger}(\omega) = \frac{1}{\sqrt{2\hbar}} \left(\sqrt{\frac{\pi\omega}{2\mathcal{Z}_{\text{T}}}} \Phi_{\text{T}}(\omega) - i \sqrt{\frac{2\mathcal{Z}_{\text{T}}}{\pi\omega}} Q_{\text{T}}(\omega) \right) \tag{D.68}$$

which obey the commutation relation

$$[b(\omega), b^\dagger(\omega')] = \delta(\omega - \omega'). \tag{D.69}$$

For completeness, the inverse transformation is given by

$$\Phi_{\mathrm{T}}(\omega) = \sqrt{\frac{\hbar \mathcal{Z}_{\mathrm{T}}}{\pi\omega}} \left(b^\dagger(\omega) + b(\omega)\right) \tag{D.70}$$

$$Q_{\mathrm{T}}(\omega) = \frac{i}{2}\sqrt{\frac{\pi\hbar\omega}{\mathcal{Z}_{\mathrm{T}}}} \left(b^\dagger(\omega) - b(\omega)\right). \tag{D.71}$$

In terms of these operators, the bath Hamiltonian can be written

$$H_{\mathrm{Bath}} = \int_0^\infty \hbar\omega b^\dagger(\omega) b(\omega) d\omega \tag{D.72}$$

where we've dropped an overall constant (albeit infinite) term arising from the commutation relations. Similarly, the interaction term in the Hamiltonian becomes

$$H_{\mathrm{Int}} = i\sqrt{\frac{\hbar\mathcal{Z}_{\mathrm{T}}}{\pi}} \frac{C_c}{C_n} \int_0^\infty d\omega \sqrt{\omega} \left(b^\dagger(\omega) - b(\omega)\right) \sum_{n=1}^\infty Q_n. \tag{D.73}$$

Further analysis and simplification of this interaction term is possible, but we hold off on this until after we introduce the creation and annihilation operators associated with the cavity modes.

From here our analysis proceeds in the same way as in Chapter 4: we adiabatically eliminate the CPT degree of freedom, expand the cavity flux coordinates about their equilibria, restrict our attention to the fundamental mode, and quantize. The main difference in this analysis is the interaction Hamiltonian, which couples the cavity to the external transmission line.

Section D.4

Coupling to the Transmission Line

We now consider the interaction Hamiltonian coupling the fundamental mode to the transmission line. Starting from the total interaction Hamiltonian of Eq. (D.73)

restricted to the fundamental mode

$$H_{\text{Int}} = i\frac{C_c}{C}\sqrt{\frac{\hbar\mathcal{Z}_{\text{T}}}{\pi}}\int_0^\infty d\omega\sqrt{\omega}\left(b^\dagger(\omega) - b(\omega)\right)Q \tag{D.74}$$

we can express the charge mode operator Q in terms of the creation and annihilation operators, yielding the expression

$$H_{\text{Int}} = -\frac{\hbar}{\sqrt{2\pi}}\frac{C_c}{C}\sqrt{\frac{\mathcal{Z}_{\text{T}}}{Z_{\text{tot}}}}\int_0^\infty d\omega\sqrt{\omega}\left(b^\dagger(\omega) - b(\omega)\right)\left(a^\dagger - a\right), \tag{D.75}$$

where $Z_{\text{tot}} = \sqrt{L_{\text{tot}}/C}$ is the characteristic impedance of the fundamental mode of the cCPT (see Chapter 4). Applying the RWA and extending the limits of integration to $-\infty$ on the lower end (justified by assuming we'll enter a rotating frame in which negative frequencies have physical meaning), this becomes

$$H_{\text{Int}} = \frac{\hbar}{\sqrt{2\pi}}\frac{C_c}{C}\sqrt{\frac{\mathcal{Z}_{\text{T}}}{Z_{\text{tot}}}}\int_{-\infty}^\infty d\omega\sqrt{\omega}\left(b^\dagger(\omega)a + b(\omega)a^\dagger\right) \tag{D.76}$$

which we want to connect up with the standard form of the interaction used in input-output theory

$$H_{\text{Int}} = \frac{\hbar}{\sqrt{2\pi}}\int_{-\infty}^\infty \sqrt{\kappa(\omega)}\left(b^\dagger(\omega)a + b(\omega)a^\dagger\right)d\omega, \tag{D.77}$$

as we used in Section 2.2.

Thus, we find that the coupling rate between the fundamental cavity mode and the transmission line is given by

$$\kappa(\omega) = \left(\frac{C_c}{C}\right)^2\frac{\mathcal{Z}_{\text{T}}}{Z_{\text{tot}}}\omega. \tag{D.78}$$

Since our frequencies of interest are a narrow band around the effective resonant frequency of the fundamental mode we can make a Markov approximation by setting $\omega \approx \omega_0$, in terms of which our coupling rate becomes

$$\kappa(\omega_0) = \frac{4}{\pi}C_c^2\mathcal{Z}\mathcal{Z}_{\text{T}}\omega_{\lambda/4}\omega_0^2 \tag{D.79}$$

where we've also expressed C and Z_{tot} in terms of the characteristic cavity impedance $\mathcal{Z}$, the bare fundamental frequency $\omega_{\lambda/4}$, and the effective fundamental frequency $\omega_0(n_g, \varphi_{\text{ext}})$. This coupling rate agrees with a derivation using a lumped-element-circuit model [4].

References

[1] B. L. Brock, Juliang Li, S. Kanhirathingal, B. Thyagarajan, M. P. Blencowe, and A. J. Rimberg. A fast and ultrasensitive electrometer operating at the single-photon level. *arXiv preprint arXiv:2102.05362*, 2021. URL: https://arxiv.org/abs/2102.05362.

[2] S. Kanhirathingal, B. L. Brock, A. J. Rimberg, and M. P. Blencowe. Quantum-limited linear charge detection with a cavity-embedded cooper pair transistor. *arXiv preprint arXiv:2012.12313*, 2020. URL: https://arxiv.org/abs/2012.12313.

[3] A J Rimberg, M P Blencowe, A D Armour, and P D Nation. A cavity-cooper pair transistor scheme for investigating quantum optomechanics in the ultra-strong coupling regime. *New Journal of Physics*, 16(5):055008, 2014. URL: http://stacks.iop.org/1367-2630/16/i=5/a=055008.

[4] B.L. Brock, Juliang Li, S. Kanhirathingal, B. Thyagarajan, William F. Braasch, M.P. Blencowe, and A.J. Rimberg. Nonlinear charge- and flux-tunable cavity derived from an embedded cooper-pair transistor. *Physical Review Applied*, 15(4), apr 2021. doi:10.1103/physrevapplied.15.044009.

[5] B. L. Brock, M. P. Blencowe, and A. J. Rimberg. Frequency fluctuations in tunable and nonlinear microwave cavities. *Phys. Rev. Applied*, 14:054026, 2020. URL: https://doi.org/10.1103/PhysRevApplied.14.054026.

[6] D.M. Pozar. *Microwave Engineering*. Wiley, 2004. URL: https://books.google.com/books?id=4wzpQwAACAAJ.

[7] P. J. Petersan and S. M. Anlage. Measurement of resonant frequency and quality factor of microwave resonators: Comparison of methods. *Journal of Applied Physics*, 84(6):3392–3402, 1998. URL: https://doi.org/10.1063/1.368498.

[8] S. Probst, F. B. Song, P. A. Bushev, A. V. Ustinov, and M. Weides. Efficient and robust analysis of complex scattering data under noise in microwave resonators. *Review of Scientific Instruments*, 86(2):024706, 2015. URL: https://doi.org/10.1063/1.4907935.

[9] Z.R. Lin, K. Inomata, K. Koshino, W.D. Oliver, Y. Nakamura, J.S. Tsai, and T. Yamamoto. Josephson parametric phase-locked oscillator and its application to dispersive readout of superconducting qubits. *Nature Communications*, 5(1):4480, 2014. URL: https://doi.org/10.1038/ncomms5480.

[10] Philip Krantz, Andreas Bengtsson, Michaël Simoen, Simon Gustavsson, Vitaly Shumeiko, W. D. Oliver, C. M. Wilson, Per Delsing, and Jonas Bylander. Single-shot read-out of a superconducting qubit using a josephson parametric oscillator. *Nature Communications*, 7:11417 EP –, May 2016. Article. URL: https://doi.org/10.1038/ncomms11417.

[11] L. Casparis, N. J. Pearson, A. Kringhøj, T. W. Larsen, F. Kuemmeth, J. Nygård, P. Krogstrup, K. D. Petersson, and C. M. Marcus. Voltage-controlled superconducting quantum bus. *Physical Review B*, 99:085434, Feb 2019. URL: https://doi.org/10.1103/PhysRevB.99.085434.

[12] T. J. Clark, V. Vadakkumbatt, F. Souris, H. Ramp, and J. P. Davis. Cryogenic microwave filter cavity with a tunability greater than 5 GHz. *Review of Scientific Instruments*, 89(11):114704, 2018. URL: https://doi.org/10.1063/1.5051042.

[13] C. M. Wilson, G. Johansson, A. Pourkabirian, M. Simoen, J. R. Johansson, T. Duty, F. Nori, and P. Delsing. Observation of the dynamical casimir effect in a superconducting circuit. *Nature*, 479(7373):376–379, 2011. URL: https://doi.org/10.1038/nature10561.

[14] P. Lähteenmäki, G. S. Paraoanu, J. Hassel, and P. J. Hakonen. Dynamical casimir effect in a josephson metamaterial. *Proceedings of the National Academy of Sciences*, 110(11):4234–4238, 2013. URL: https://doi.org/10.1073/pnas.1212705110.

[15] I-M. Svensson, M. Pierre, M. Simoen, W. Wustmann, P. Krantz, A. Bengtsson, G. Johansson, J. Bylander, V. Shumeiko, and P. Delsing. Microwave photon generation in a doubly tunable superconducting resonator. *Journal of*

Physics: Conference Series, 969:012146, 2018. URL: https://doi.org/10.1088/1742-6596/969/1/012146.

[16] Gerhard Kirchmair, Brian Vlastakis, Zaki Leghtas, Simon E. Nigg, Hanhee Paik, Eran Ginossar, Mazyar Mirrahimi, Luigi Frunzio, S. M. Girvin, and R. J. Schoelkopf. Observation of quantum state collapse and revival due to the single-photon kerr effect. *Nature*, 495(7440):205–209, mar 2013. URL: https://doi.org/10.1038/nature11902.

[17] M. A. Castellanos-Beltran and K. W. Lehnert. Widely tunable parametric amplifier based on a superconducting quantum interference device array resonator. *Applied Physics Letters*, 91(8):083509, 2007. URL: https://doi.org/10.1063/1.2773988.

[18] M. A. Castellanos-Beltran, K. D. Irwin, G. C. Hilton, L. R. Vale, and K. W. Lehnert. Amplification and squeezing of quantum noise with a tunable josephson metamaterial. *Nature Physics*, 4(12):929–931, oct 2008. URL: https://doi.org/10.1038/nphys1090.

[19] N. Bergeal, F. Schackert, M. Metcalfe, R. Vijay, V. E. Manucharyan, L. Frunzio, D. E. Prober, R. J. Schoelkopf, S. M. Girvin, and M. H. Devoret. Phase-preserving amplification near the quantum limit with a josephson ring modulator. *Nature*, 465(7294):64–68, may 2010. URL: https://doi.org/10.1038/nature09035.

[20] R. J. Schoelkopf, P. Wahlgren, A. A. Kozhevnikov, P. Delsing, and D. E. Prober. The radio-frequency single-electron transistor (rf-set): A fast and ultrasensitive electrometer. *Science*, 280(5367):1238–1242, 1998. URL: http://science.sciencemag.org/content/280/5367/1238, arXiv: http://science.sciencemag.org/content/280/5367/1238.full.pdf, doi: 10.1126/science.280.5367.1238.

[21] Wei Lu, Zhongqing Ji, Loren Pfeiffer, K. W. West, and A. J. Rimberg. Real-time detection of electron tunnelling in a quantum dot. *Nature*, 423(6938):422–425, 2003. URL: https://doi.org/10.1038/nature01642.

[22] O. Naaman and J. Aumentado. Time-domain measurements of quasiparticle tunneling rates in a single-cooper-pair transistor. *Phys. Rev. B*,

73:172504, May 2006. URL: https://link.aps.org/doi/10.1103/PhysRevB.73.172504, doi:10.1103/PhysRevB.73.172504.

[23] David M. T. van Zanten, Deividas Sabonis, Judith Suter, Jukka I. Väyrynen, Torsten Karzig, Dmitry I. Pikulin, Eoin C. T. O'Farrell, Davydas Razmadze, Karl D. Petersson, Peter Krogstrup, and Charles M. Marcus. Photon-assisted tunnelling of zero modes in a majorana wire. *Nature Physics*, 16(6):663–668, 2020. URL: https://doi.org/10.1038/s41567-020-0858-0.

[24] J. R. Petta, A. C. Johnson, J. M. Taylor, E. A. Laird, A. Yacoby, M. D. Lukin, C. M. Marcus, M. P. Hanson, and A. C. Gossard. Coherent manipulation of coupled electron spins in semiconductor quantum dots. *Science*, 309(5744):2180–2184, 2005. URL: https://doi.org/10.1126/science.1116955.

[25] B. D'Anjou and Guido Burkard. Optimal dispersive readout of a spin qubit with a microwave resonator. *Physical Review B*, 100(24):245427, 2019. URL: https://doi.org/10.1103/physrevb.100.245427.

[26] Robert G. Knobel and Andrew N. Cleland. Nanometre-scale displacement sensing using a single electron transistor. *Nature*, 424(6946):291–293, 2003. URL: https://doi.org/10.1038/nature01773.

[27] M. D. LaHaye, O. Buu, B. Camarota, and K. C. Schwab. Approaching the quantum limit of a nanomechanical resonator. *Science*, 304(5667):74–77, 2004. URL: https://doi.org/10.1126/science.1094419.

[28] A. Naik, O. Buu, M. D. LaHaye, A. D. Armour, A. A. Clerk, M. P. Blencowe, and K. C. Schwab. Cooling a nanomechanical resonator with quantum back-action. *Nature*, 443(7108):193–196, 2006. URL: https://doi.org/10.1038/nature05027.

[29] T. T. Heikkilä, F. Massel, J. Tuorila, R. Khan, and M. A. Sillanpää. Enhancing optomechanical coupling via the josephson effect. *Phys. Rev. Lett.*, 112:203603, May 2014. URL: https://link.aps.org/doi/10.1103/PhysRevLett.112.203603, doi:10.1103/PhysRevLett.112.203603.

[30] J.-M. Pirkkalainen, S.U. Cho, F. Massel, J. Tuorila, T.T. Heikkilä, P.J. Hakonen, and M.A. Sillanpää. Cavity optomechanics mediated by a quantum

two-level system. *Nature Communications*, 6(1):6981, 2015. URL: https://doi.org/10.1038/ncomms7981.

[31] X. Mi, J. V. Cady, D. M. Zajac, P. W. Deelman, and J. R. Petta. Strong coupling of a single electron in silicon to a microwave photon. *Science*, 355(6321):156–158, 2016. URL: https://doi.org/10.1126/science.aal2469.

[32] X. Mi, M. Benito, S. Putz, D. M. Zajac, J. M. Taylor, Guido Burkard, and J. R. Petta. A coherent spin–photon interface in silicon. *Nature*, 555(7698):599–603, 2018. URL: https://doi.org/10.1038/nature25769.

[33] D. Zoepfl, M. L. Juan, C. M. F. Schneider, and G. Kirchmair. Single-photon cooling in microwave magnetomechanics. *Physical Review Letters*, 125(2):023601, 2020. URL: https://doi.org/10.1103/physrevlett.125.023601.

[34] Philip Schmidt, Mohammad T. Amawi, Stefan Pogorzalek, Frank Deppe, Achim Marx, Rudolf Gross, and Hans Huebl. Sideband-resolved resonator electromechanics based on a nonlinear josephson inductance probed on the single-photon level. *Communications Physics*, 3(1):233, 2020. URL: https://doi.org/10.1038/s42005-020-00501-3.

[35] Marios Kounalakis, Yaroslav M. Blanter, and Gary A. Steele. Flux-mediated optomechanics with a transmon qubit in the single-photon ultrastrong-coupling regime. *Physical Review Research*, 2(2):023335, 2020. URL: https://doi.org/10.1103/physrevresearch.2.023335.

[36] Tanmoy Bera, Sourav Majumder, Sudhir Kumar Sahu, and Vibhor Singh. Large flux-mediated coupling in hybrid electromechanical system with a transmon qubit. *Communications Physics*, 4(1):12, 2021. URL: https://doi.org/10.1038/s42005-020-00514-y.

[37] A. Nunnenkamp, K. Børkje, and S. M. Girvin. Single-photon optomechanics. *Phys. Rev. Lett.*, 107:063602, Aug 2011. URL: https://link.aps.org/doi/10.1103/PhysRevLett.107.063602, doi:10.1103/PhysRevLett.107.063602.

[38] P. Rabl. Photon blockade effect in optomechanical systems. *Physical Review Letters*, 107(6):063601, 2011. URL: https://doi.org/10.1103/physrevlett.107.063601.

[39] Markus Aspelmeyer, Tobias J. Kippenberg, and Florian Marquardt. Cavity optomechanics. *Reviews of Modern Physics*, 86(4):1391–1452, 2014. URL: https://doi.org/10.1103/revmodphys.86.1391.

[40] Henrik Brenning, Sergey Kafanov, Tim Duty, Sergey Kubatkin, and Per Delsing. An ultrasensitive radio-frequency single-electron transistor working up to 4.2 k. *Journal of Applied Physics*, 100(11):114321, 2006. doi:10.1063/1.2388134.

[41] C. Macklin, K. O'Brien, D. Hover, M. E. Schwartz, V. Bolkhovsky, X. Zhang, W. D. Oliver, and I. Siddiqi. A near–quantum-limited josephson traveling-wave parametric amplifier. *Science*, 350(6258):307–310, 2015. URL: http://science.sciencemag.org/content/350/6258/307, arXiv:http://science.sciencemag.org/content/350/6258/307.full.pdf, doi:10.1126/science.aaa8525.

[42] V.V. Sivak, N.E. Frattini, V.R. Joshi, A. Lingenfelter, S. Shankar, and M.H. Devoret. Kerr-free three-wave mixing in superconducting quantum circuits. *Physical Review Applied*, 11(5):054060, 2019. URL: https://doi.org/10.1103/physrevapplied.11.054060.

[43] Mika A. Sillanpää, Leif Roschier, and Pertti J. Hakonen. Inductive single-electron transistor. *Physical Review Letters*, 93(6):066805, 2004. URL: https://doi.org/10.1103/physrevlett.93.066805.

[44] Mika A. Sillanpää, Leif Roschier, and Pertti J. Hakonen. Charge sensitivity of the inductive single-electron transistor. *Applied Physics Letters*, 87(9):092502, 2005. URL: https://doi.org/10.1063/1.2034096.

[45] M. F. Gonzalez-Zalba, S. Barraud, A. J. Ferguson, and A. C. Betz. Probing the limits of gate-based charge sensing. *Nature Communications*, 6(1):6084, 2015. URL: https://doi.org/10.1038/ncomms7084.

[46] S. Schaal, I. Ahmed, J. A. Haigh, L. Hutin, B. Bertrand, S. Barraud, M. Vinet, C.-M. Lee, N. Stelmashenko, J. W. A. Robinson, J. Y. Qiu, S. Hacohen-Gourgy,

I. Siddiqi, M. F. Gonzalez-Zalba, and J. J. L. Morton. Fast gate-based readout of silicon quantum dots using josephson parametric amplification. *Physical Review Letters*, 124(6):067701, 2020. URL: https://doi.org/10.1103/physrevlett.124.067701.

[47] C. Gerry and P. Knight. *Introductory Quantum Optics*. Cambridge University Press, 2005. URL: https://books.google.com/books?id=CgByyoBJJwgC.

[48] W.P. Schleich. *Quantum Optics in Phase Space*. Wiley, 2011. URL: https://books.google.com/books?id=2jUjQPW-WXAC.

[49] Juliang Li. *Near Quantum Limited Charge Detector and Beyond*. PhD thesis, Dartmouth College, 2018.

[50] M. Devoret. Quantum fluctuations in electrical circuits. In *Quantum Fluctuations, Les Houches Session LXIII*, pages 351–386. Elsevier, 1997.

[51] Uri Vool and Michel Devoret. Introduction to quantum electromagnetic circuits. *International Journal of Circuit Theory and Applications*, 45(7):897–934, jun 2017. doi:10.1002/cta.2359.

[52] L. S. Bishop. *Circuit Quantum Electrodynamics*. PhD thesis, Yale University, 2010.

[53] Bernard Yurke and John S. Denker. Quantum network theory. *Physical Review A*, 29(3):1419–1437, mar 1984. doi:10.1103/physreva.29.1419.

[54] C. Gardiner and P. Zoller. *Quantum Noise: A Handbook of Markovian and Non-Markovian Quantum Stochastic Methods with Applications to Quantum Optics*. Springer Series in Synergetics. Springer, 2004. URL: https://books.google.com/books?id=a_xsT8oGhdgC.

[55] A. A. Clerk, M. H. Devoret, S. M. Girvin, Florian Marquardt, and R. J. Schoelkopf. Introduction to quantum noise, measurement, and amplification. *Reviews of Modern Physics*, 82(2):1155–1208, apr 2010. URL: https://doi.org/10.1103/revmodphys.82.1155.

[56] Peter D. Drummond and Zbigniew Ficek, editors. *Quantum Squeezing*. Springer Berlin Heidelberg, 2004. doi:10.1007/978-3-662-09645-1.

[57] C. W. Gardiner and M. J. Collett. Input and output in damped quantum systems: Quantum stochastic differential equations and the master equation. *Phys. Rev. A*, 31:3761–3774, 1985. URL: https://link.aps.org/doi/10.1103/PhysRevA.31.3761, doi:10.1103/PhysRevA.31.3761.

[58] M. Sillanpaa. *Quantum Device Applications of Mesoscopic Superconductivity*. PhD thesis, Helsinki University of Technology, 2005.

[59] P. Krantz. *The Josephson Parametric Oscillator - From Microscopic Studies to Single-shot Qubit Readout*. PhD thesis, Chalmers University of Technology, 2016.

[60] Bernard Yurke and Eyal Buks. Performance of cavity-parametric amplifiers, employing kerr nonlinearites, in the presence of two-photon loss. *J. Lightwave Technol.*, 24(12):5054–5066, Dec 2006. URL: http://jlt.osa.org/abstract.cfm?URI=jlt-24-12-5054.

[61] A.H. Nayfeh and D.T. Mook. *Nonlinear Oscillations*. Wiley Classics Library. Wiley, 2008. URL: https://books.google.com/books?id=sj3ebg7jRaoC.

[62] T.P. Orlando and K.A. Delin. *Foundations of Applied Superconductivity*. Electrical Engineering Series. Addison-Wesley, 1991. URL: https://books.google.com/books?id=7yRRAAAAMAAJ.

[63] M. Tinkham. *Introduction to Superconductivity: Second Edition*. Dover Books on Physics. Dover Publications, 2004. URL: https://books.google.com/books?id=JOQoAwAAQBAJ.

[64] A. Cottet. *Implementation of a Quantum Bit in a Superconducting Circuit*. PhD thesis, University of Paris, 2002.

[65] P. Joyez. *The Single Cooper Pair Transistor: A Macroscopic Quantum System*. PhD thesis, University of Paris, 1995.

[66] J. J. Sakurai and Jim Napolitano. *Modern Quantum Mechanics*. Cambridge University Press, sep 2017. doi:10.1017/9781108499996.

[67] Jens Koch, Terri M. Yu, Jay Gambetta, A. A. Houck, D. I. Schuster, J. Majer, Alexandre Blais, M. H. Devoret, S. M. Girvin, and R. J. Schoelkopf. Charge-insensitive qubit design derived from the cooper pair box. *Physical Review A*, 76(4), oct 2007. doi:10.1103/physreva.76.042319.

[68] Fei Chen. *The Cavity-Embedded Cooper Pair Transistor*. PhD thesis, Dartmouth College, 2013.

[69] T. Yamamoto, Y. Nakamura, Yu. A. Pashkin, O. Astafiev, and J. S. Tsai. Parity effect in superconducting aluminum single electron transistors with spatial gap profile controlled by film thickness. *Applied Physics Letters*, 88(21):212509, 2006. URL: https://doi.org/10.1063/1.2207555.

[70] N A Court, A J Ferguson, and R G Clark. Energy gap measurement of nanostructured aluminium thin films for single cooper-pair devices. *Superconductor Science and Technology*, 21(1):015013, 2007. URL: https://doi.org/10.1088/0953-2048/21/01/015013.

[71] J. Aumentado, Mark W. Keller, John M. Martinis, and M. H. Devoret. Nonequilibrium quasiparticles and 2e periodicity in single-cooper-pair transistors. *Physical Review Letters*, 92(6):066802, 2004. URL: https://doi.org/10.1103/physrevlett.92.066802.

[72] Fei Chen, Juliang Li, A. D. Armour, E. Brahimi, Joel Stettenheim, A. J. Sirois, R. W. Simmonds, M. P. Blencowe, and A. J. Rimberg. Realization of a single-cooper-pair josephson laser. *Physical Review B*, 90(2):020506(R), 2014. URL: https://doi.org/10.1103/physrevb.90.020506.

[73] D.S. Betts. *An Introduction to Millikelvin Technology*. Cambridge Studies in Low Temperature Physics. Cambridge University Press, 1989. URL: https://books.google.com/books?id=-s7UBIdy0fsC.

[74] O.V. Lounasmaa. *Experimental principles and methods below 1 K*. Academic Press, 1974. URL: https://books.google.com/books?id=8AdRAAAAMAAJ.

[75] F. Pobell. *Matter and methods at low temperatures*. Springer-Verlag, 1992. URL: https://books.google.com/books?id=grrvAAAAMAAJ.

[76] A. Fukushima, A. Sato, A. Iwasa, Y. Nakamura, T. Komatsuzaki, and Y. Sakamoto. Attenuation of microwave filters for single-electron tunneling experiments. *IEEE Transactions on Instrumentation and Measurement*, 46(2):289–293, 1997. URL: https://doi.org/10.1109/19.571834.

[77] N. A. Masluk. *Reducing the losses of the fluxonium artificial atom*. PhD thesis, Yale University, 2012.

[78] A. Megrant, C. Neill, R. Barends, B. Chiaro, Yu Chen, L. Feigl, J. Kelly, Erik Lucero, Matteo Mariantoni, P. J. J. O'Malley, D. Sank, A. Vainsencher, J. Wenner, T. C. White, Y. Yin, J. Zhao, C. J. Palmstrøm, John M. Martinis, and A. N. Cleland. Planar superconducting resonators with internal quality factors above one million. *Applied Physics Letters*, 100(11):113510, 2012. URL: https://doi.org/10.1063/1.3693409.

[79] M. S. Khalil, M. J. A. Stoutimore, F. C. Wellstood, and K. D. Osborn. An analysis method for asymmetric resonator transmission applied to superconducting devices. *Journal of Applied Physics*, 111(5):054510, 2012. URL: https://doi.org/10.1063/1.3692073.

[80] D. I. Schuster. *Circuit Quantum Electrodynamics*. PhD thesis, Yale University, 2007.

[81] E. Paladino, Y. M. Galperin, G. Falci, and B. L. Altshuler. 1/f noise: Implications for solid-state quantum information. *Reviews of Modern Physics*, 86(2):361–418, apr 2014. URL: https://doi.org/10.1103/revmodphys.86.361.

[82] O. Astafiev, Yu. A. Pashkin, Y. Nakamura, T. Yamamoto, and J. S. Tsai. Temperature square dependence of the low frequency $1/f$ charge noise in the josephson junction qubits. *Physical Review Letters*, 96(13):137001, 2006. URL: https://doi.org/10.1103/physrevlett.96.137001.

[83] S. Kafanov, H. Brenning, T. Duty, and P. Delsing. Charge noise in single-electron transistors and charge qubits may be caused by metallic grains. *Physical Review B*, 78(12):125411, 2008. URL: https://doi.org/10.1103/physrevb.78.125411.

[84] S. Sendelbach, D. Hover, A. Kittel, M. Mück, John M. Martinis, and R. McDermott. Magnetism in SQUIDs at millikelvin temperatures. *Physical Review Letters*, 100(22):227006, 2008. URL: https://doi.org/10.1103/physrevlett.100.227006.

[85] P. Kumar, S. Sendelbach, M. A. Beck, J. W. Freeland, Zhe Wang, Hui Wang, Clare C. Yu, R. Q. Wu, D. P. Pappas, and R. McDermott. Origin and reduction of $1/f$ magnetic flux noise in superconducting devices. *Phys. Rev.*

Appl., 6:041001, 2016. URL: https://doi.org/10.1103/PhysRevApplied.6.041001.

[86] P. Krantz, Y. Reshitnyk, W. Wustmann, J. Bylander, S. Gustavsson, W. D Oliver, T. Duty, V. Shumeiko, and P. Delsing. Investigation of nonlinear effects in josephson parametric oscillators used in circuit quantum electrodynamics. *New Journal of Physics*, 15(10):105002, 2013. URL: https://doi.org/10.1088/1367-2630/15/10/105002.

[87] A. Palacios-Laloy, F. Nguyen, F. Mallet, P. Bertet, D. Vion, and D. Esteve. Tunable resonators for quantum circuits. *Journal of Low Temperature Physics*, 151(3-4):1034–1042, 2008. URL: https://doi.org/10.1007/s10909-008-9774-x.

[88] M. Sandberg, C. M. Wilson, F. Persson, T. Bauch, G. Johansson, V. Shumeiko, T. Duty, and P. Delsing. Tuning the field in a microwave resonator faster than the photon lifetime. *Applied Physics Letters*, 92(20):203501, 2008. URL: https://doi.org/10.1063/1.2929367.

[89] M. R. Vissers, J. Hubmayr, M. Sandberg, S. Chaudhuri, C. Bockstiegel, and J. Gao. Frequency-tunable superconducting resonators via nonlinear kinetic inductance. *Applied Physics Letters*, 107(6):062601, 2015. URL: https://doi.org/10.1063/1.4927444.

[90] O.W. Kennedy, J. Burnett, J.C. Fenton, N.G.N. Constantino, P.A. Warburton, J.J.L. Morton, and E. Dupont-Ferrier. Tunable Nb superconducting resonator based on a constriction nano-squid fabricated with a Ne focused ion beam. *Physical Review Applied*, 11:014006, 2019. URL: https://doi.org/10.1103/PhysRevApplied.11.014006.

[91] B. Ferdinand, D. Bothner, R. Kleiner, and D. Koelle. Tunable superconducting two-chip lumped-element resonator. *Physical Review Applied*, 11:034050, 2019. URL: https://doi.org/10.1103/PhysRevApplied.11.034050.

[92] M P Silveri, J A Tuorila, E V Thuneberg, and G S Paraoanu. Quantum systems under frequency modulation. *Reports on Progress in Physics*, 80(5):056002, apr 2017. URL: https://doi.org/10.1088/1361-6633/aa5170.

[93] D.W. Allan. Statistics of atomic frequency standards. *Proceedings of the IEEE*, 54(2):221–230, 1966. URL: https://doi.org/10.1109/proc.1966.4634.

[94] J.E. Marsden and M.J. Hoffman. *Basic Complex Analysis*. W. H. Freeman, 1999.

[95] B.H. Armstrong. Spectrum line profiles: The voigt function. *J. Quant. Spectrosc. Radiat. Transfer*, 7(1):61–88, jan 1967. doi:10.1016/0022-4073(67)90057-x.

[96] Paul Siddons, Charles S Adams, and Ifan G Hughes. Off-resonance absorption and dispersion in vapours of hot alkali-metal atoms. *Journal of Physics B: Atomic, Molecular and Optical Physics*, 42(17):175004, aug 2009. URL: https://doi.org/10.1088/0953-4075/42/17/175004.

[97] I. Diniz, S. Portolan, R. Ferreira, J. M. Gérard, P. Bertet, and A. Auffèves. Strongly coupling a cavity to inhomogeneous ensembles of emitters: Potential for long-lived solid-state quantum memories. *Physical Review A*, 84(6):063810, dec 2011. URL: https://doi.org/10.1103/physreva.84.063810.

[98] Frank W. Olver, Daniel W. Lozier, Ronald F. Boisvert, and Charles W. Clark. *NIST Handbook of Mathematical Functions*. Cambridge University Press, New York, NY, USA, 1st edition, 2010.

[99] Marcus P. da Silva, Deniz Bozyigit, Andreas Wallraff, and Alexandre Blais. Schemes for the observation of photon correlation functions in circuit QED with linear detectors. *Physical Review A*, 82(4):043804, oct 2010. URL: https://doi.org/10.1103/physreva.82.043804.

[100] C. Eichler, D. Bozyigit, and A. Wallraff. Characterizing quantum microwave radiation and its entanglement with superconducting qubits using linear detectors. *Physical Review A*, 86(3):032106, sep 2012. URL: https://doi.org/10.1103/physreva.86.032106.

[101] A. J. Hoffman, S. J. Srinivasan, S. Schmidt, L. Spietz, J. Aumentado, H. E. Türeci, and A. A. Houck. Dispersive photon blockade in a superconducting circuit. *Physical Review Letters*, 107(5):053602, jul 2011. URL: https://doi.org/10.1103/physrevlett.107.053602.

[102] Eva Zakka-Bajjani, François Nguyen, Minhyea Lee, Leila R. Vale, Raymond W. Simmonds, and José Aumentado. Quantum superposition of a single microwave photon in two different 'colour' states. *Nature Physics*, 7(8):599–603, jul 2011. URL: https://doi.org/10.1038/nphys2035.

[103] Ida-Maria Svensson, Andreas Bengtsson, Philip Krantz, Jonas Bylander, Vitaly Shumeiko, and Per Delsing. Period-tripling subharmonic oscillations in a driven superconducting resonator. *Physical Review B*, 96(17):174503, nov 2017. URL: https://doi.org/10.1103/physrevb.96.174503.

[104] Andreas Bengtsson, Philip Krantz, Michaël Simoen, Ida-Maria Svensson, Ben Schneider, Vitaly Shumeiko, Per Delsing, and Jonas Bylander. Nondegenerate parametric oscillations in a tunable superconducting resonator. *Physical Review B*, 97(14):144502, apr 2018. URL: https://doi.org/10.1103/physrevb.97.144502.

[105] Zhaoyou Wang, Marek Pechal, E. Alex Wollack, Patricio Arrangoiz-Arriola, Maodong Gao, Nathan R. Lee, and Amir H. Safavi-Naeini. Quantum dynamics of a few-photon parametric oscillator. *Physical Review X*, 9(2):021049, jun 2019. URL: https://doi.org/10.1103/physrevx.9.021049.

[106] John M. Martinis, K. B. Cooper, R. McDermott, Matthias Steffen, Markus Ansmann, K. D. Osborn, K. Cicak, Seongshik Oh, D. P. Pappas, R. W. Simmonds, and Clare C. Yu. Decoherence in josephson qubits from dielectric loss. *Physical Review Letters*, 95(21):210503, nov 2005. URL: https://doi.org/10.1103/physrevlett.95.210503.

[107] R. Barends, N. Vercruyssen, A. Endo, P. J. de Visser, T. Zijlstra, T. M. Klapwijk, P. Diener, S. J. C. Yates, and J. J. A. Baselmans. Minimal resonator loss for circuit quantum electrodynamics. *Applied Physics Letters*, 97(2):023508, 2010. URL: https://doi.org/10.1063/1.3458705.

[108] M. R. Vissers, J. Gao, D. S. Wisbey, D. A. Hite, C. C. Tsuei, A. D. Corcoles, M. Steffen, and D. P. Pappas. Low loss superconducting titanium nitride coplanar waveguide resonators. *Applied Physics Letters*, 97(23):232509, dec 2010. URL: https://doi.org/10.1063/1.3517252.

[109] Jeremy M. Sage, Vladimir Bolkhovsky, William D. Oliver, Benjamin Turek, and Paul B. Welander. Study of loss in superconducting coplanar waveguide

resonators. *Journal of Applied Physics*, 109(6):063915, mar 2011. URL: https://doi.org/10.1063/1.3552890.

[110] Moe S. Khalil, F. C. Wellstood, and Kevin D. Osborn. Loss dependence on geometry and applied power in superconducting coplanar resonators. *IEEE Transactions on Applied Superconductivity*, 21(3):879–882, jun 2011. URL: https://doi.org/10.1109/tasc.2010.2090330.

[111] A. Bruno, G. de Lange, S. Asaad, K. L. van der Enden, N. K. Langford, and L. DiCarlo. Reducing intrinsic loss in superconducting resonators by surface treatment and deep etching of silicon substrates. *Applied Physics Letters*, 106(18):182601, may 2015. URL: https://doi.org/10.1063/1.4919761.

[112] David L. Wallace. Asymptotic approximations to distributions. *The Annals of Mathematical Statistics*, 29(3):635–654, sep 1958. URL: https://doi.org/10.1214/aoms/1177706528.

[113] Fei Chen, A. J. Sirois, R. W. Simmonds, and A. J. Rimberg. Introduction of a dc bias into a high-q superconducting microwave cavity. *Applied Physics Letters*, 98(13):132509, 2011. URL: https://doi.org/10.1063/1.3573824.

[114] K.C. Gupta, R. Garg, I. Bahl, and P. Bhartia. *Microstrip Lines and Slotlines*. Artech House, 1996. URL: https://books.google.com/books?id=gqeHQgAACAAJ.

[115] S. M. Verbrugh, M. L. Benhamadi, E. H. Visscher, and J. E. Mooij. Optimization of island size in single electron tunneling devices: Experiment and theory. *Journal of Applied Physics*, 78(4):2830–2836, 1995. URL: https://doi.org/10.1063/1.360083.

[116] A. B. Zorin, F.-J. Ahlers, J. Niemeyer, T. Weimann, H. Wolf, V. A. Krupenin, and S. V. Lotkhov. Background charge noise in metallic single-electron tunneling devices. *Physical Review B*, 53(20):13682–13687, 1996. URL: https://doi.org/10.1103/PhysRevB.53.13682.

[117] T. F. Li, Yu. A. Pashkin, O. Astafiev, Y. Nakamura, J. S. Tsai, and H. Im. Low-frequency charge noise in suspended aluminum single-electron transistors. *Applied Physics Letters*, 91(3):033107, 2007. URL: https://doi.org/10.1063/1.2759260.

[118] F. C. Wellstood, C. Urbina, and J. Clarke. Low-frequency noise in dc superconducting quantum interference devices below 1 k. *Appl. Phys. Lett.*, 50(12):772–774, 1987. URL: https://doi.org/10.1063/1.98041.

[119] Carlton M. Caves. Quantum limits on noise in linear amplifiers. *Phys. Rev. D*, 26:1817–1839, Oct 1982. URL: https://link.aps.org/doi/10.1103/PhysRevD.26.1817, doi:10.1103/PhysRevD.26.1817.

[120] T. C. White, J. Y. Mutus, I.-C. Hoi, R. Barends, B. Campbell, Yu Chen, Z. Chen, B. Chiaro, A. Dunsworth, E. Jeffrey, J. Kelly, A. Megrant, C. Neill, P. J. J. OMalley, P. Roushan, D. Sank, A. Vainsencher, J. Wenner, S. Chaudhuri, J. Gao, and John M. Martinis. Traveling wave parametric amplifier with josephson junctions using minimal resonator phase matching. *Applied Physics Letters*, 106(24):242601, 2015. URL: https://doi.org/10.1063/1.4922348.

[121] L. Sun, L. DiCarlo, M. D. Reed, G. Catelani, Lev S. Bishop, D. I. Schuster, B. R. Johnson, Ge A. Yang, L. Frunzio, L. Glazman, M. H. Devoret, and R. J. Schoelkopf. Measurements of quasiparticle tunneling dynamics in a band-gap-engineered transmon qubit. *Physical Review Letters*, 108(23):230509, 2012. URL: https://doi.org/10.1103/PhysRevLett.108.230509.

[122] D. Ristè, C. C. Bultink, M. J. Tiggelman, R. N. Schouten, K. W. Lehnert, and L. DiCarlo. Millisecond charge-parity fluctuations and induced decoherence in a superconducting transmon qubit. *Nature Communications*, 4(1):1913, 2013. URL: https://doi.org/10.1038/ncomms2936.

[123] D. I. Schuster, A. Wallraff, A. Blais, L. Frunzio, R.-S. Huang, J. Majer, S. M. Girvin, and R. J. Schoelkopf. ac stark shift and dephasing of a superconducting qubit strongly coupled to a cavity field. *Physical Review Letters*, 94(12):123602, 2005. URL: https://doi.org/10.1103/physrevlett.94.123602.

[124] A. Palacios-Laloy. *Superconducting qubit in a resonator: test of the Leggett-Garg inequality and single-shot readout*. PhD thesis, Quantronics Group, SPEC-CEA Saclay, 2010.

[125] A. Wallraff, D. I. Schuster, A. Blais, L. Frunzio, R.-S. Huang, J. Majer, S. Kumar, S. M. Girvin, and R. J. Schoelkopf. Strong coupling of a single photon to a superconducting qubit using circuit quantum electrodynamics. *Nature*, 431:162 EP –, Sep 2004. URL: https://doi.org/10.1038/nature02851.

[126] Y. Nakamura, Yu. A. Pashkin, and J. S. Tsai. Coherent control of macroscopic quantum states in a single-cooper-pair box. *Nature*, 398(6730):786–788, 1999. URL: https://doi.org/10.1038/19718.

[127] Matthew Reagor, Hanhee Paik, Gianluigi Catelani, Luyan Sun, Christopher Axline, Eric Holland, Ioan M. Pop, Nicholas A. Masluk, Teresa Brecht, Luigi Frunzio, Michel H. Devoret, Leonid Glazman, and Robert J. Schoelkopf. Reaching 10 ms single photon lifetimes for superconducting aluminum cavities. *Applied Physics Letters*, 102(19):192604, may 2013. URL: https://doi.org/10.1063/1.4807015.

[128] P. Bhupathi, Peter Groszkowski, M. P. DeFeo, Matthew Ware, Frank K. Wilhelm, and B. L. T. Plourde. Transient dynamics of a superconducting nonlinear oscillator. *Physical Review Applied*, 5(2):024002, feb 2016. URL: https://doi.org/10.1103/PhysRevApplied.5.024002.

[129] D. Hall. *New Insights into the Limitations on the Efficiency and Achievable Gradients in Nb3Sn SRF Cavities*. PhD thesis, Cornell University, 2017.

[130] A. K. Sinclair, E. Schroeder, D. Zhu, M. Colangelo, J. Glasby, P. D. Mauskopf, H. Mani, and K. K. Berggren. Demonstration of microwave multiplexed readout of DC-biased superconducting nanowire detectors. *IEEE Transactions on Applied Superconductivity*, 29(5):1–4, aug 2019. URL: https://doi.org/10.1109/tasc.2019.2899329.

[131] Yaxing Zhang, J. Moser, J. Güttinger, A. Bachtold, and M. I. Dykman. Interplay of driving and frequency noise in the spectra of vibrational systems. *Physical Review Letters*, 113(25):255502, 2014. URL: https://doi.org/10.1103/PhysRevLett.113.255502.

[132] Olivier Maillet, Xin Zhou, Rasul Gazizulin, Ana Maldonado Cid, Martial Defoort, Olivier Bourgeois, and Eddy Collin. Nonlinear frequency transduction of nanomechanical brownian motion. *Physical Review B*, 96(16):165434, 2017. URL: https://doi.org/10.1103/PhysRevB.96.165434.

[133] A. Aassime, D. Gunnarsson, K. Bladh, P. Delsing, and R. Schoelkopf. Radio-frequency single-electron transistor: Toward the shot-noise limit. *Applied Physics Letters*, 79(24):4031–4033, 2001. URL: https://doi.org/10.1063/1.1424477.

[134] P.D. Drummond, Z. Ficek, and Z. Spicek. *Quantum Squeezing*. Physics and Astronomy Online Library. Springer, 2004. URL: https://books.google.com/books?id=OmvY7-lKLgUC.

[135] S. E. S. Andresen, F. Wu, R. Danneau, D. Gunnarsson, and P. J. Hakonen. Highly sensitive and broadband carbon nanotube radio-frequency single-electron transistor. *Journal of Applied Physics*, 104(3):033715, 2008. URL: https://doi.org/10.1063/1.2968123.

[136] Sukumar Rajauria, L. M. A. Pascal, Ph. Gandit, F. W. J. Hekking, B. Pannetier, and H. Courtois. Efficiency of quasiparticle evacuation in superconducting devices. *Physical Review B*, 85(2):020505, 2012. URL: https://doi.org/10.1103/physrevb.85.020505.

[137] Matthew T. Bell, Lev B. Ioffe, and Michael E. Gershenson. Microwave spectroscopy of a cooper-pair transistor coupled to a lumped-element resonator. *Physical Review B*, 86(14):144512, 2012. URL: https://doi.org/10.1103/physrevb.86.144512.

[138] M. C. Cassidy, A. S. Dzurak, R. G. Clark, K. D. Petersson, I. Farrer, D. A. Ritchie, and C. G. Smith. Single shot charge detection using a radio-frequency quantum point contact. *Applied Physics Letters*, 91(22):222104, 2007. URL: https://doi.org/10.1063/1.2809370.

[139] T. Lindström, J. Burnett, M. Oxborrow, and A Ya. Tzalenchuk. Pound-locking for characterization of superconducting microresonators. *Review of Scientific Instruments*, 82(10):104706, 2011. URL: https://doi.org/10.1063/1.3648134.

[140] C. Laflamme and A. A. Clerk. Quantum-limited amplification with a nonlinear cavity detector. *Physical Review A*, 83(3):033803, 2011. URL: https://doi.org/10.1103/physreva.83.033803.

[141] L. Tosi, D. Vion, and H. le Sueur. Design of a cooper-pair box electrometer for application to solid-state and astroparticle physics. *Physical Review Applied*, 11(5), may 2019. doi:10.1103/physrevapplied.11.054072.

[142] M. I. Dykman, C. M. Maloney, V. N. Smelyanskiy, and M. Silverstein. Fluctuational phase-flip transitions in parametrically driven oscillators. *Physical Re-*

view E, 57(5):5202–5212, 1998. URL: https://doi.org/10.1103/physreve.57.5202.

[143] Waltraut Wustmann and Vitaly Shumeiko. Parametric resonance in tunable superconducting cavities. *Physical Review B*, 87(18), may 2013. doi:10.1103/physrevb.87.184501.

[144] C. M. Wilson, T. Duty, M. Sandberg, F. Persson, V. Shumeiko, and P. Delsing. Photon generation in an electromagnetic cavity with a time-dependent boundary. *Physical Review Letters*, 105(23):233907, 2010. URL: https://doi.org/10.1103/physrevlett.105.233907.

[145] Erik A. Tholén, Adem Ergül, Evelyn M. Doherty, Frank M. Weber, Fabien Grégis, and David B. Haviland. Nonlinearities and parametric amplification in superconducting coplanar waveguide resonators. *Applied Physics Letters*, 90(25):253509, jun 2007. doi:10.1063/1.2750520.